Elastic properties characterization of nuclear fuels under extreme conditions

Mara Marchetti

THÈSE POUR OBTENIR LE GRADE DE DOCTEUR DE L'UNIVERSITÉ DE MONTPELLIER

En Électronique

École doctorale I2S- Information, Structures, Systèmes

Unité de recherche Matériaux, Micro-capteurs et Acoustique

PROPRIÉTÉS ÉLASTIQUES DES COMBUSTIBLES NUCLÉAIRES SOUS CONDITIONS EXTRÊMES

Présentée par Mara MARCHETTI
Le 27 novembre 2017

Sous la direction de Gilles Despaux et Didier Laux

Devant le jury composé de

Marc LETHIECQ, Professeur des Universités, Université François-Rabelais de Tours	[Rapporteur]
Frédérico GARRIDO, Professeur des Universités, Université Paris-sud	[Rapporteur]
Rodrigue LARGENTON, Ingénieur, EDF R&D	[Examinateur]
Emmanuel LE CLÉZIO, Professeur des Universités, Université de Montpellier	[Président]
Thierry WISS, Ingénieur, European Commission-JRC-Karlsruhe	[Examinateur]
Didier LAUX, Maître de conférences, Université de Montpellier	[Co-Directeur de Thèse]
Gilles DESPAUX, Professeur des Universités, Université de Montpellier	[Directeur de Thèse]
Philippe MARTIN, Ingénieur, CEA Marcoule	[Membre invité]

UNIVERSITÉ DE MONTPELLIER

THÈSE POUR OBTENIR LE GRADE DE DOCTEUR DE L'UNIVERSITÉ DE MONTPELLIER

En Électronique

École doctorale I2S- Information, Structures, Systèmes

Unité de recherche Matériaux, Micro-capteurs et Acoustique

PROPRIÉTÉS ÉLASTIQUES DES COMBUSTIBLES NUCLÉAIRES SOUS CONDITIONS EXTRÊMES

Présentée par Mara MARCHETTI
Le 27 novembre 2017

Sous la direction de Gilles Despaux et Didier Laux

Devant le jury composé de

Marc LETHIECQ, Professeur des Universités, Université François-Rabelais de Tours	[Rapporteur]
Frédérico GARRIDO, Professeur des Universités, Université Paris-sud	[Rapporteur]
Rodrigue LARGENTON, Ingénieur, EDF R&D	[Examinateur]
Emmanuel LE CLÉZIO, Professeur des Universités, Université de Montpellier	[Président]
Thierry WISS, Ingénieur, European Commission-JRC-Karlsruhe	[Examinateur]
Didier LAUX, Maître de conférences, Université de Montpellier	[Co-Directeur de Thèse]
Gilles DESPAUX, Professeur des Universités, Université de Montpellier	[Directeur de Thèse]
Philippe MARTIN, Ingénieur, CEA Marcoule	[Membre invité]

UNIVERSITÉ DE MONTPELLIER

Résumé

Ce travail de recherche vise à étudier les propriétés élastiques par microscopie acoustique du combustible nucléaire dans trois situations particulières : combustible en utilisation normale en réacteur nucléaire, combustible stocké après la période d'irradiation et combustible en conditions extrêmes suite à un accident nucléaire. Les mesures réalisées sur les échantillons irradiés ont conduit à plusieurs résultats majeurs : validation d'une loi corrélant la vitesse des ondes de Rayleigh à la densité du dioxyde d'uranium irradié ou frais ; détermination de la porosité dans le combustible irradié ; évaluation du gonflement de la matrice en fonction du taux de combustion dans la gamme 0-100 GWd$\cdot$ t^{-1}M ; développement d'un modèle empirique capable de prévoir la variation de module de Young en fonction du taux de combustion en prenant même en compte la teneur en dopants (Gd_2O_3, CeO_2) ; quantification de l'évolution du module de Young du combustible suite à l'endommagement en stockage ; premières mesures sur du corium. Enfin, grâce au lien entre les propriétés thermiques et élastiques, différentes propriétés thermiques de l'UO_2 ont été calculées en mesurant la vitesse de l'onde de surface de Rayleigh seule.

Mots-clés : *Microscopie acoustique, combustible nucléaire, propriétés élastiques, propriétés mécaniques, dégâts par rayonnement, corium*

Laboratoire : Institut d'Électronique et des Systèmes

Abstract

The focus of the present thesis is the determination of the elastic properties of nuclear fuel using high frequency acoustic microscopy. The nuclear fuel is considered under three different conditions: during its normal life in reactor, after its discharge and disposal in interim or long-term storage and subsequently to its severe degradation caused by a nuclear accident. Measurements performed on irradiated fuels allowed to validate a law between the density of fresh and irradiated fuel and the Rayleigh wave velocity; the determination of the irradiated fuel porosity and matrix swelling in the broad burnup range 0-100 GWd$\cdot$ t^{-1}M; the development of an empirical model capable of predicting the evolution of Young's modulus versus burnup correcting also for the additives content (Gd_2O_3, CeO_2); Young's modulus evolution due to alpha-decay damage as in-storage condition; first corium measurements. Moreover, several UO_2 thermal parameters were calculated only by means of the Rayleigh wave velocity thanks to the link between thermal and elastic properties.

Title: Elastic properties characterization of nuclear fuels under extreme conditions

Key words: *Acoustic microscopy, nuclear fuel, elastic properties, mechanical properties, radiation damage, corium*

Institution: European Commission-Joint Research Centre-Directorate for Nuclear Safety and Security

Ai riverberi sonori della memoria.

Le piogge di maggio
raccogli impetuoso
fiume Mogami.
M.Bashō

Acknowledgements

The research presented in this thesis was financially supported by the European Commission through the Training and Mobility of Researchers program in the frame of Horizon 2020. It was carried out at the Joint Research Centre Karlsruhe, former Institute for Transuranium Elements, in collaboration with the University of Montpellier.
This thesis was made possible by the contributions of different people who helped me in solving problems or simply making possible the experimental research work, fighting next to me against technical issues, limited working hours, ventilation shutdowns. I wish to express my gratitude towards my supervisor, Dr. Thierry Wiss, for his continued encouragement and suggestions during this work, a person with an amicable and positive disposition, always ready to give his advice. My results could not be achievable without the contribution of my Head of Department Dr. Vincenzo Rondinella and my Head of Unit Dr. Joseph Somers. Both they were always ready in giving support and scientific advices, despite their busy schedule.
At the same level I must convey my gratefulness to my thesis directors Gilles Despaux and Didier Laux: both always ready to clarify my doubts and to give support after the frequent laboratory closures.
This research work exists especially thanks to the contribution of Ernesto Fontana, who had the patience to listen to all my complains and who was substaining my mood through conversation on literature, art, Japanese culture. The annealing in hot-cell was possible thanks to his perseverance and tecnical capabilities. Thank you very much Ernesto.
I am also grate to all the Unit: Dimitri Papaioannou for the samples selections, the communications with NFIR and in general for the support given, Gianni Paperini and Ralf Gretter who prepared the samples I measured, Gérard Montagnier who searched for the samples I was looking for, Abdelilah El Abjani for the support during the bag-in, Jurgen Hillenbrand and Michael Spreizenbarth, for the support with the electrical system. Thank you very much Yvan Kintz for having helped me in obtaining the possibility to use the cold set-up.
Special thanks are for Lorenzo Fongaro and his image analysis explanations and for Oliver Dieste Blanco, in particular for the great time I

had during the German lessons.
Special thanks are conveyed also to Matthias and Klaus for the swift technical support (sometimes instantaneous).
I would like to express my immense gratitude to Antonio Bulgheroni, because his intervention was critical for the continuation of my experimental research work and also because he was always available in giving a scientific advice. Then, Rafael Alvarez Sarandez and Paul Carbol, for the selection of the FARO samples and the support during densities measurements. I am deeply grateful to Dragos Staicu, Paul Van Uffelen, Arndt Schubert and David Bottomley for their scientific advices, discussions and time; they were really precious for the development of the present manuscript. I would like to thank also Co Boshoven, Eckhard Dahms, Daniel Bouexière and Philippe Raison, respectively for the annealings outside the hot-cell and for having given support during the XRD measurements. I cannot forget also the professionality of Madame Corinne Brossard when I needed to ship FARO samples to the University of Montpellier: she followed and took care of the transport. Thank you Tony and Joseph for the manipulators technical maintenance. Thank you very much Anna Matthei Socha, for your efforts in creating a unit team. Thank you very much Fanny May for the Pubsy explanations. I would like also to thank the Director Dr. Maria Betti, for having allowed the continuation of this experimental work.
I convey my gratefulness to Areva GmbH and NFIR for having given the permission to publish the experimental results obtained. I would like to conclude expressing my deep gratitude towards all the people who selected me during the interview of January 2014, because they really made possible my professional development; in this context I would like to mention also Prof. Dr. Thomas Fanghänel.
I will bring this experience in my heart for my life. Thank you.

Résumé

Ce travail de recherche vise à étudier la variation des propriétés élastiques du combustible nucléaire dans trois situations particulières. Une première concerne l'ensemble des opérations du combustible en réacteur nucléaire, la deuxième la gestion du combustible irradié après la période d'irradiation et la troisième étudie les conditions extrêmes du combustible suite à un accident nucléaire. S'agissant de l'exploitation en réacteur, nous avons distingué les conditions normales et celles en situation accidentelle.
De nos jours, 440 centrales nucléaires commerciales, distribuées dans environ 31 pays, fournissent 11% de l'énergie électrique mondiale. L'énergie produite en réacteur nucléaire est générée par les fissions induites dans le combustible nucléaire, en particulier par la perte d'énergie des fragments de fission. Pour les réacteurs à eau légère, qui sont considérés dans le cadre de la présente thèse, le combustible est généralement de l'UO_2 enrichi en ^{235}U (2-5 %) ou un mélange d'oxydes (MOX) qui est constitué par UO_2 et environ 5% de PuO_2. Le PuO_2 provient du retraitement des combustibles usés à travers une série de procédés chimiques visant à séparer des déchets les éléments potentiellement valorisables, dont communément l'uranium et le plutonium .
Dans les technologies liées à l'énergie nucléaire, la fraction du combustible qui est consommée pendant les processus de fission en réacteur peut être indiquée en termes de pourcentage d'atomes qui ont subi une fission nucléaire (%FIMA ou fissions par atome de métal initial), ou par l'énergie fournie, exprimée en gigawatt-jour par tonne de métal (GWd·t^{-1}M en anglais).
En conséquence de l'irradiation, la structure cristalline de la matrice combustible est sujette à la formation de défauts. Lorsqu'une particule (ion), caractérisée par une certaine vitesse, pénètre la matière elle perd progressivement son énergie en interagissant avec le milieu. La perte d'énergie est décrite par son pouvoir d'arrêt, qui est fonction de la distance parcourue par la particule (ion). Différents types d'interactions particules chargées-matière peuvent avoir lieu. Dans le cas des particules lourdes de haute énergie, la plus grande partie de l'énergie est

perdue par collisions inélastiques avec les électrons du milieu, tandis que lorsque la vitesse est basse les collisions élastiques avec les noyaux deviennent dominantes. La perte d'énergie peut donc être électronique ou nucléaire, selon que l'interaction soit entre la particule incidente et les électrons ou avec les noyaux du milieu traversé. Par effet de l'interaction entre une particule d'une certaine énergie avec la matière, différent types des défauts peuvent être générés : défauts ponctuels (lacune ou atome interstitiel), dislocations et défauts planaires ou de volume. Les trois derniers types appartiennent au groupe plus général des défauts étendus. L'irradiation détermine l'accumulation de défauts dans les matériaux : si l'interaction est élastique les dommages produits dans la matrice peuvent être quantifiés en utilisant le concept de dpa (déplacement par atome), si l'interaction est inélastique cette unité de mesure ne décrit pas de manière satisfaisante les dommages crées dans les matériaux par l'irradiation.
Pendant l'irradiation en réacteur à eau légère, plusieurs phénomènes physiques interviennent : au début, l'irradiation est responsable de la diminution de la porosité initiale provenant du frittage, puis elle réaugmente (à partir d'environ 10-15 GWd·t^{-1}M) et le volume du combustible croît (gonflement). Ce phénomène résulte de la précipitation des produits de fission insolubles dans la matrice du combustible et dans une moindre mesure d'une expansion du paramètre de maille provoquée par les dommages radio-induits.
L'augmentation du volume pose des problèmes liés à la sûreté nucléaire ; en effet l'espace entre la gaine et les pastilles de combustible, qui normalement doit être maintenu, se réduit jusqu'au contact des deux. Les interactions pastille-gaine de nature chimique et mécanique, affectent l'intégrité de la gaine ; qui dans un cas extrême peut se rompre et provoquer un relâchement des produits de fission.
Quand le taux de combustion moyen est supérieur à $\sim$ 50 GWd·t^{-1}M, la périphérie de la pastille présente la formation d'une nouvelle structure : les grains qui initialement avaient une dimension autour de 10 μm se subdivisent en grains de 0.1 - 0.3 μm, le gaz qui était présent dans la matrice migre dans des pores de $\sim 1\mu$m et la porosité augmente exponentiellement à la périphérie jusqu'à atteindre une valeur de l'ordre de 20%. Cette nouvelle structure a été appelée *High Burnup Structure* (HBS). Différentes théories ont été développées pour expliquer le mécanisme de formation de la HBS, mais la littérature a trouvé un accord sur les causes qui conduisent à la nouvelle structure, en particulier la co-existence d'une basse température d'irradiation à la périphérie de la

pastille (600-800K) et le haut taux de fissions causé par la formation de ^{239}Pu par capture résonante de ^{238}U. Les propriétés mécaniques de la pastille de combustible varient de manière hétérogène le long du rayon et la détermination locale de ces propriétés devient fondamentale pour l'évaluation des performances du combustible nucléaire et des facteurs influençant la sûreté nucléaire.

Après quelques années en réacteur (typiquement trois ans), le combustible nucléaire est déchargé des réacteurs, stocké temporairement dans une piscine dédiée à assurer les critères de radioprotection et de dissipation thermique, en attendant que les radionucléides de demi-vie brève décroissent. Dans un second temps, le combustible irradié est placé dans un site d'entreposage qui peut être sous eau ou à sec. La destination finale du combustible usé peut être une couche géologique profonde.

Une fois déchargé du réacteur le combustible contient $\sim 1\%$ d'actinides (Np, Pu, Am and Cm) qui sont sujets à désintégration alpha. La particule alpha émise et le noyau fils issu de la désintégration, produisent des dommages dans la matrice du combustible, qui s'accumulent et provoquent des changements des propriétés mécaniques (e.g. augmentation de la dureté). L'endommagement contribue ultérieurement au gonflement du combustible usé (soit par expansion du volume de la maille cristalline, soit par la production des bulles d'hélium). Les propriétés physiques et mécaniques évoluent pendant le stockage ; le combustible usagé, en comparaison avec le combustible en opération, est caractérisé par une température inférieure (T max = 673 K) qui rend la diffusion thermique moins efficace et empêche le recuit des défauts. L'accumulation d'hélium en dehors de la matrice de combustible augmente potentiellement la pression qui favorise le processus de détérioration de la gaine qui est déjà plus fragile en raison des dommages produits par l'irradiation ; tous ces phénomènes compliquent le conditionement et le transport du combustible usé.

Le viellissement du combustible usé continue pendant des milliers d'années et il est extrêmement important de pouvoir quantifier aujourd'hui l'évolution de ses proprietés physiques et mécaniques et en particulier leur effet sur l'intégrité du combustible. Les conséquences d'une perte d'intégrité seraient l'accroissement de la surface de combustible exposée à l'eau en cas de rupture de barrières de confinement et donc du relâchement de radionuclides dans la géosphère.

La troisième partie de la thèse est dédiée à l'étude des proprietés élastiques du matériau produit à la suite d'un accident nucléaire. À ce jour

les accidents nucléaires les plus graves ont été : l'accident à l'unité 2 à Three Mile Island (TMI-2), l'accident de Chernobyl et l'accident à Fukushima ; les deux derniers accidents ayant été classifiés au maximum du niveau de sévérité (7) dans l'échelle internationale des événements nucléaires (INES). Pendant un accident nucléaire grave, les matériaux qui constituent le coeur du réacteur sont sujets à oxydation ; particulièrement lorsque la gaine est en Zircaloy, son oxydation conduit à la production de chaleur du fait du caractère exothermique de la réaction. Le comportement du coeur du réacteur après chauffage dépend par exemple de la témperature de fusion de chaque composant et aussi de la formation d'eutectiques qui ont une témperature de fusion inférieure et peuvent causer des dysfonctionnements précoces : l'oxydation du Zircaloy produit de l'hydrogène et la température augmente jusqu'à atteindre la fusion du combustible. Le matériau produit suite à un accident nucléaire est appelé *corium* et sa composition est fortement dépendante du réacteur et du combustible utilisé. À la suite d'un accident nucléaire il est extrêmement important de restituer une situation pré-accidentelle. Le démantèlement et la remise du site dans son état original sont les objectifs primaires à obtenir après un accident sévère : ils permettent de rétablir les conditions originales de l'environnement et des conditions de vie des personnes qui ont été affectés par l'accident. Dans le démantèlement d'une centrale nucléaire non endommagée, il est nécessaire de prendre une série de mesures afin d'assurer l'enlèvement du combustible en toute sécurité permettant d'optimiser les opérations de décontamination. Le démantèlement post-accidentel présente lui une situation complètement différente : l'état des installations, du combustible et des différents équipements est inconnu et déterminer les opérations nécessaires est extrêmement plus compliqué et coûteux.

Au jour d'aujourd'hui aucune des trois centrales nucléaire accidentées n'a pu être démantelée : sur le site de Three Mile Island l'unitée endommagée ne sera démantelée que d'ici vingt ans, l'unité 4 de Tchernobyl est actuellement en condition de stockage sécurisé et le plan est de terminer son démantèlement pour 2050, pour Fukushima Daiichi NPP les premières conditions ne sont pas encore atteintes, mais le plan est de réaliser l'enlèvement du combustible fondu le plus tôt possible et d'assurer un stockage en toute sécurité.

Pour optimiser l'enlèvement du combustible il est nécessaire de concevoir des outils adaptés aux conditions particulières du corium de Fukushima ; l'expérience de TMI-2 a montré que les propriétés élastiques

du corium sont extrêmement importantes afin de réaliser l'opération. Fukushima peut compter sur l'expérience de TMI-2, mais certaines différences doivent être considérées : la différence entre le type de réacteur (réacteur à eau pressurisée dans le cas de TMI-2 et réacteur à eau bouillante dans le cas de Fukushima), les différences entre les cinétiques accidentelles et le fait que pour Fukushima l'eau de mer a été utilisée pour refroidir les cœurs des réacteurs.
Dans le cadre de la thèse, les propriétés élastiques du combustible après irradiation en réacteur, après avoir subi une auto-irradiation en stockage ou suite à un accident nucléaire, ont été étudiés par microscopie acoustique haute fréquence.
La propagation du son dans la matière, spécifiquement des ondes longitudinales et transverses, est strictement liée aux propriétés élastiques du matériau, par conséquent le module de Young, le module d'élasticité isostatique et le module de cisaillement (les paramètres de Lamé) peuvent être calculés en mesurant la vitesse de propagation des ondes transverses et longitudinales dans le matériau.
L'existence des ondes de surface et de relations mathématiques entre les vitesses de propagation des ondes transverses et longitudinales et la vitesse de l'onde de surface de Rayleigh permet de calculer les propriétés élastiques en utilisant simplement la vitesse de propagation de l'onde de Rayleigh.
Pour déterminer les propriétés élastiques, la technique de la signature acoustique a été utilisée : le capteur est approché graduellement de l'échantillon de manière à ce que le signal reçu soit produit par l'interférence entre l'onde normale réfléchie sur l'échantillon et l'onde de Rayleigh qui se propage sur la surface de ce même échantillon. La résolution spatiale à 100 MHz est ~ 125 μm. Dans la première partie de la thèse, le cas du combustible en réacteur a été consideré. Pour évaluer l'impact de l'irradiation en réacteur nucléaire, une campagne de mesures expérimentales a été réalisée à la fois sur des disques d'irradiation spéciaux et à la fois sur des échantillons de combustible provenant de réacteurs à eau préssurisé (REP) commerciaux, dans une gamme de taux de combustion de 0-100 GWd$\cdot$ t^{-1}M. Les disques, différement des pastilles commerciales, sont caractérisés par l'homogénéité de la distribution en température et du taux de combustion le long du rayon du disque : le taux de combustion moyen correspond au taux de combustion local. Les mesures réalisées sur ces échantillons ont conduit à l'obtention de quatre résultats importants :

- La validation d'une loi permettant de corréler la vitesse des ondes

de Rayleigh à la densité du dioxyde d'uranium frais et irradié ;

- La détermination de la porosité dans le combustible de dioxyde d'uranium irradié ;
- L'évaluation du gonflement de la matrice en fonction du taux de combustion dans la gamme 0-100 GWd· t^{-1}M ;
- Le développement d'un modèle empirique capable de prévoir la variation de module de Young en fonction du taux de combustion en considérant la teneur en dopants (Gd_2O_3, CeO_2).

L'existence d'une loi permettant de calculer la densité locale du combustible irradié offre de nombreux avantages, surtout en considérant la difficulté d'examens post-irradiation, qui comportent des temps extrêmement longs et des risques radiologiques : les hautes doses d'irradiation nécéssitent la mise en œuvre des protections adéquates. Le temps est une contrainte importante lors du travail avec du combustible irradié, réduire le temps nécessaire à la caractérisation permet de réduire indirectement les coûts.
Les lois trouvées consistent à obtenir avec une mesure unique de la vitesse de l'onde de Rayleigh, à la fois la densité locale, la porosité et le module de Young. À travers la valeur de la vitesse de l'onde de Rayleigh il est également possible d'estimer le taux de combustion moyen et inconnu d'un combustible irradié.
Le module de Young, corrigé pour l'effet de la teneur en dopants, décroît de $\sim 33\%$ dans l'intervale 0-100 GWd· t^{-1}M et la loi empirique proposée ajuste les données expérimentales et de la littérature de manière satisfaisante.
En étudiant l'évolution de la densité de la matrice de UO_2, la porosité locale de deux pastilles irradiées a été évaluée à partir de la vitesse de l'onde de Rayleigh seule. La variation de la densité de la matrice en fonction du taux de combustion donne également la possibilité d'estimer le gonflement du combustible dans l'intervale 0-100 GWd· t^{-1}M.
En étudiant la variation locale de taux de combustion entre environ 57 et 120 GWd· t^{-1}M une diminution plus forte du module de Young est observée dans la région intermédiaire entre le centre et la périphérie de la pastille ; dans la région où la structure standard de UO_2 coexiste avec la HBS. Ce résultat expérimental laisse penser que la décroissance du module de Young est plus importante dans les régions intermédiaires, qui sont une transition entre la structure originale et son évolution en HBS.
Afin d'étendre les champs d'application du microscope acoustique, le

rapport entre la micro-dureté de Vickers et le module de Young a été calculé pour deux échantillons de combustible commercial REP, grâce à une campagne expérimentale de mesure de dureté réalisée en parallèle sur les mêmes échantillons. Le rapport entre la micro-dureté Vickers et le module de Young dans une gamme de taux de combustion de 60-113 GWd· t^{-1}M, est demeuré constant, mais près de 100% plus élevé que le rapport mesuré sur du combustible non irradié ou sur des ersatz simulant chimiquement le combustible irradié. Cet écart démontre que les dopants chimiques ne peuvent pas représenter complètement le comportement du combustible irradié : en particulier l'augmentation de la porosité et les défauts ponctuels et étendus sont absents, ainsi que les variations de microstructure.
La première partie de la thèse a été aussi consacrée à la détermination des relations entre vitesses de propagation des ondes et propriétés thermiques du matériau. Dans ce contexte une pastille de UO_2 vierge et un échantillon avec un taux de combustion simulé de 60 GWd·t^{-1}M ont été mesurés par microscopie acoustique de haute fréquence et les vitesses des ondes de Rayleigh des échantillons avec un taux de combustion simulé de 30 et 80 GWd·t^{-1}M ont été considérées.
Dans le modèle à simple paramètre développé par Debye, toutes les ondes acoustiques se propagent à la même vitesse et la vitesse moyenne du son est directement liée à la température de Debye et à la chaleur spécifique du matériau.
La température de Debye et la chaleur spécifique peuvent être calculées si les vitesses de propagation des ondes transversales et longitudinales dans la matière sont connues, donc si la vitesse de l'onde de Rayleigh est connue.
Si la description quantique de l'interaction sonore dans la matière est considérée, les phonons sont aussi responsables du transport de la chaleur, en particulier la conductivité thermique dépend d'un facteur B lié à la diffusion phonons-phonons ; B est par conséquence lié à la vitesse de propagation des ondes.
Dans le cadre de la thèse, la température de Debye, la capacité thermique à volume constant et à pression constante et le paramètre de Grüneisen ont été calculés à partir de la vitesse de Rayleigh. En plus, en utilisant le modèle développé par Leibfried and Schlömann et révisé par Slack, le facteur B a été estimé pour les derniers échantillons.
Les valeurs de température de Debye et de paramètre de Grüneisen sont en accord avec la littérature, la valeur de la capacité thermique présente un écart de $\sim 8\%$ avec des valeurs recommandées en littérature et le

paramètre B a en général un écart de 15%-30% avec celui obtenu avec des mesures de diffusivité thermique. Les écarts, peuvent être expliqués par le fait que le coefficient de Poisson n'a pas été mesuré, mais pris dans la littérature pour UO_2 vierge ; une autre considération à faire est que le modèle de Debye fournit une description du phénomène de transmission de la chaleur surtout à basse température.
La deuxième partie de la thèse a visé à étudier le combustible dans les conditions de stockage. La variation de paramètre de maille et de module de Young due aux dommages produits par les désintégrations alpha ont été plus particulièrement considérés. Suite à l'endommagement le paramètre de maille augmente du fait des défauts ponctuels qui s'accumulent. Quand le taux de formation de défauts est égal au taux de recuit des défauts (normalement pour des temps longs), le paramètre de maille arrive à saturation. La variation du paramètre de maille et la prodution d'hélium induisent une augmentation du volume (diminution de la densité) qui impacte le module de Young.
La variation du module de Young, par effet de l'auto-irradiation alpha, a été approchée de deux manières différentes : en déterminant la variation du module de Young intrinsèque (module de Young corrigé par la porosité) en fonction des dommages alpha cumulés pendant le stockage et en mesurant le module de Young avant et après des traitements thermiques.
A ce stade les conditions du combustible âgé ont été simulées en dopant des échantillons de UO_2 avec ^{238}Pu, qui produit un endommagement (au moment de l'étude) comparable à celui d'un combustible REP commercial de taux de combustion approximativement 40 GWd·t^{-1}M, après plus de 30 000 ans de stockage. L'endommagement a aussi été évalué en déterminant les dommages produits dans un combustible commercial REP après 23 ans de stockage et des échantillons MOX après 18 ans. Le module de Young a été corrigé pour la porosité, de manière à obtenir sa valeur intrinsèque et pour la variation qui peut être causée par l'addition de Pu ou des produits de fission. Le module de Young a enfin été évalué en fonction du nombre de déplacements par atome (dpa) générés pendant le stockage.
La valeur intrinsèque du module de Young décroit avec l'accumulation des dommages alpha, au moins jusqu'à une certaine valeur, mais à 5 dpa le module de Young obtenu est supérieur à celui du combustible de dioxyde d'uranium frais. Cette augmentation peut être causée par une saturation de défauts étendus qui induit une relaxation des propriétés élastiques. La variation du module de Young du fait de l'auto-

irradiation alpha trouve son explication à la fois dans la variation des distances inter-atomiques (du fait de la présence de défauts) et à la variation du volume du cristal générée partiellement par l'augmentation du paramètre de maille (qui cause le gonflement de la matrice de UO_2) et partiellement à l'accumulation des bulles d'hélium qui contribuent à une diminution de la densité et, par conséquence, à une diminution du module de Young.
L'effet de l'auto-irradiation a aussi été étudié en réalisant un traitemant thermique sur un échantillon irradié avec un taux de combustion moyen de 80 GWd· t^{-1}M : une moitié de sa section longitudinale a été polie et mesurée immédiatement par microscopie acoustique à haute fréquence (60 MHz) et une moité a été chauffée à 850 K, température qui permet de recuire la majorité des défauts du réseau cristallin, tel que rapporté dans la littérature et confirmé parallèlement dans une campagne de mesure dans cette étude. Les mesures réalisées après recuit donnent une valeur de module de Young généralement plus élevée, par rapport à des mesures réalisées sur la moité de pastille qui n'a pas été traitée, alors même que des différences significatives (en dehors des barres d'erreur) sont détectées principalement vers la périphérie de la pastille. Si on mesure la distribution de plutonium le long du rayon d'une pastille irradiée, on peut observer que sa concentration est supérieure vers la périphérie, en conséquence de la réaction de capture résonante sur ^{238}U. Cet effet peut expliquer le profil de la variation du module de Young après le traitement thermique : la région avec une concentration supérieure de Pu montre une plus forte augmentation du module de Young qui peut être interprétée par une restauration de ses propriétées élastiques initiales. La variation du module de Young dans le combustible usé n'est donc pas uniforme le long du rayon d'une pastille et cet aspect doit être pris en considération si l'intégrité de la gaine doit être préservée.
L'effet des dommages sur le module de Young a été étudié aussi en considérant des défauts produits par l'irradiation en réacteur, en particulier l'effet des traces générées par les produits de fission le long de leurs parcours a été consideré. A ce stade, un échantillon implanté avec des ions ^{238}U caracterisés par une énergie moyenne de 2.7 GeV et une fluence de $5 \cdot 10^{10}$ ions·cm^{-2} a été selectionné. Le parcours des ions dans le dioxyde d'uranium a été estimé à près du double de la pénétration de l'onde de Rayleigh dans l'échantillon si une fréquence de 100 MHz est utilisée. Cette différence assure que l'onde de Rayleigh interagisse seulement dans l'épaisseur endommagée. La mesure a été

realisée en dehors de la cellule en utilisant l'éthanol comme liquide de couplage, qui produit une atténuation plus forte, en comparaison avec le méthanol, mais qui a permit d'obtenir une signature acoustique avec plus de trois oscillations : donc une vitesse de l'onde de Rayleigh avec une bonne précision. Les ions de ^{238}U avec une énergie moyenne de 2.7 GeV ont une perte d'énergie (inélastique) de 67 MeV$\cdot\mu m^{-1}$ dans UO_2 99% TD, qui est trois fois plus grande que le pouvoir d'arrêt des produits de fission. Cette implantation produit des traces visibles dans l'échantillon qui ont été observées dans des études précédentes.
La valeur du module de Young dans la couche implantée est plus basse en comparaison avec celle obtenue en mesurant la surface vierge de l'échantillon et qui présente un module de Young comparable avec celui d'un échantillon frais ; ainsi ce résultat indiquerait une baisse du module de Young dans le cas d'oxyde d'uranium causée par l'irradiation avec les ions ^{238}U à haute énergie. En réacteur les produits de fission ont une perte d'énergie plus basse en comparaison avec cette expérience, les masses et les vitesses étant également plus basses ; la production de traces dans le dioxyde d'uranium a été observée comme étant un effet de seuil, qui est une fonction de l'énergie d'irradiation.
La troisième et dernière partie de la thèse traite des propriétés élastiques du corium qui a une composition extrêmement variable et complexe, dépendante du réacteur et de la dynamique de l'accident. Par exemple pour l'accident de Tchernobyl le combustible a interagi avec la gaine de Zircaloy et avec l'acier, le béton et le sable pour générer un produit qui a été appelé "lava" de Tchernobyl .
Le but de ce travail consiste à produire une base de données pour concevoir les outils pour récupérer le combustible fondu et optimiser les opérations de démantèlement.
Pour évaluer le module de Young du corium, le premier cas considéré a été celui du corium synthétisé ou provenant d'accidents simulés ; en particulier deux échantillons provenant par la série d'expériences FARO, réalisé par le Joint Research Centre Ispra afin d'étudier l'interaction entre le corium et l'eau, ont été sélectionnés. Les échantillons FARO ont une composition de 80 wt% UO_2 and 20 wt% ZrO_2, les synthétisés par le Joint Research Centre Karlsruhe ont une composition respectivement de 45 mol% UO_2-55 mol% ZrO_2 et 20 mol% UO_2- 80 mol% ZrO_2. Le corium avec une composition contrôlée offre l'avantage de pouvoir étudier séparément les effets . Le coefficient de Poisson a été mesuré pour les échantillons FARO et une valeur comparable avec le dioxyde d'uranium a été trouvé. Le module de Young du dioxyde de zirconium

a été corrigé par la porosité et les valeurs obtenues montrent une chute en fonction du contenu en ZrO_2, jusqu'à 80 mol%. La valeur du module de Young pour le corium produit au Joint Research Centre Karlsruhe, avec une composition approximativement équimolaire peut être comparée avec les valeurs de module de Young obtenu en mesurant les échantillons qui correspondent au cœur fondu du réacteur Three Mile Island, unité 2 (TMI-2). Les échantillons avaient été caractérisés dans le passé grâce à une collaboration entre des laboratoires internationaux. Les échantillons de corium prélevés dans le cœur du réacteur fondu ont en général des modules de Young proches, même lorsque les densités sont très différentes. Deux échantillons TMI-2 contiennent des phases ferreuses et si on considère les barres d'erreurs, ils ont une valeur similaire du module de Young. Aux examens post-irradiation l'échantillon avec la plus haute densité ne contient pas de phases ferreuses. L'effet de phases ferreuses doit être étudiés plus en détail.
In fine, un échantillon de lave de Tchernobyl a été mesuré par microscopie acoustique. Dans ce cas la valeur du coefficient de Poisson n'a pas été mesurée : en considérant que ce type de lave est principalement constituée de SiO_2, sa valeur du coefficient de Poisson publiée dans la littérature, a été utilisé. Le module de Young de la lave de Tchernobyl est environ la moitié du module de Young des échantillons TMI-2 ; son module de Young correspond à la valeur du verre.
Ce travail de thèse a pu montrer la pertinence de la miscroscopie acoustique pour mesurer et exploiter les propriétés élastiques du combustible irradié. En particulier il a pu être souligné les avantages apportés par cette technique : la possibilité d'évaluer simultanément le module élastique, la densité et la porosité et d'estimer la dureté de l' UO_2 (ou du MOX) en mesurant la vitesse de l'onde de surface de Rayleigh seule. Les résultats obtenus ont montré que le module de Young du combustible irradié décroît d'environ 33 % entre 0 et 100 GWd·t^{-1}M et que la décroissance du module de Young est plus importante dans les régions de la pastille de combustible où la microstructure est partiellement caractérisée par la formation de la structure HBS (ou High burnup Structure, HBS, en anglais dans le texte). Cette zone en périphérie de la pastille de combustible irradiée présente un taux de combustion local accru par rapport au taux de combustion moyen et une réorganisation de la microstructure avec des propriétés particulières pouvant impacter le comportement sous irradiation. Un autre résultat important obtenu est la liaison entre les propriétés thermiques et élastiques de l'UO_2, qui permet d'estimer différentes propriétés thermiques en mesurant la vi-

tesse de l'onde de surface de Rayleigh seule. Les conséquences de cette relation consiste en la possibilité d'affiner le modèle décrivant l'évolution des propriétés élastiques pendant l'irradiation de façon cohérente avec la variation de conductivité thermique, particulièrement en considérant la tenue en additifs et des défauts ponctuels et étendus.
Le présent travail répond aux premières questions concernant la dégradation des propriétés élastiques due aux défauts produits par l'irradiation de particules et des ions : le module de Young diminue si on considère une gamme de dommages produits par interaction élastique où par les traces d'ions d'énergie très élevée. La question reste ouverte sur la variation du module de Young si on augmente le niveau d'endommagement (les déplacements par atome), en particulier si l'énergie des ions et leur masse sont comparables avec celles des produits de fission. Dans les études futures il sera nécéssaire de comparer les résultats entre différentes irradiations singularisées par des énergies et des fluences variées ainsi que de quantifier l'endommagement de manière à comparer différents phénomènes (i.e. interactions élastiques et interactions inélastiques). La variation du module de Young suite à l'interaction radiation-matière a été exploitée plus en détail par rapport à la première partie de ce travail dédiée à l'étude de cette variation avec le taux de combustion.
Le dernier chapitre a montré que la microscopie acoustique peut fournir des informations importantes sur les propriétés élastiques du corium et du combustible dégradé. Dans ce domaine les questions ouvertes restent l'évaluation de la constante de Poisson en fonction de la composition du corium, l'effet des phases ferreuses et des composants de la structure sur le module de Young et le module de Young de la lave de Tchernobyl. Les perspectives de cette étude particulière porte sur la mesure des propriétés élastiques du corium qui a interagi avec l'eau, spécialement avec l'eau de mer ; en outre l'évolution du module de Young en fonction de la stœchiométrie et de la concentration en ZrO_2 présente un grand intérêt dans le but de qualifier les outils qui seront utilisés pour le démantèlement de la centrale nucléaire accidentée. De manière générale cette thèse a pu démontrer l'utilité de la microscopie acoustique pour déterminer les propriétés élastiques des céramiques du nucléaire tout au long du cycle du combustible. Les paramètres microstructuraux en particulier ceux liés à l'endommagement en cours d'irradiation en réacteur nucléaire ont été abordés et une étude par effets séparés tel que l'irradiation par des ions permettrait de quantifier et d'interpréter plus précisément les variations du module élastique en fonction du

taux de combustion mais aussi de l'historique de l'irradiation. L'aval du cycle électronucléaire revêt une importance capitale s'agissant de la prédiction de l'évolution des propriétés mécaniques. La microscopie acoustique appliquée à des analogues de combustibles usagés a permis de noter une chute du module de Young suivie d'une remontée importante pour des équivalences en terme d'endommagement alpha correspondant à des temps de stockage de plusieurs milliers d'années. Les analyses en situation opérationnelle normale ont été complétées par une étude sur des corium synthétiques, trois fragments de corium de Three Mile Island et même par une mesure d'un morceau de lave de Tchernobyl.

Abstract

The focus of the present thesis is the determination of the elastic properties of nuclear fuel using high frequency acoustic microscopy. The nuclear fuel is considered under three different conditions: during its normal life in reactor, after its discharge and disposal in interim or long-term storage and subsequently to its severe degradation caused by a nuclear accident.
In reactor, nuclear fuel is subjected to accumulation of fission products and fission damage which contributes increasing the fuel volume, affecting several safety-relevant properties. Moreover, the fuel pellet is subjected to radial gradients of the burnup and irradiation temperature, which in turn cause a substantial modification of the fuel local morphology, with porosity increase especially toward the pellet periphery. These phenomena cause the mechanical properties to vary heterogeneously along the radius of the pellet, affecting both fuel performance and fuel-safety during the in-pile operations. Moreover, the evolution of the elastic properties of nuclear fuel during the irradiation in reactor has a direct consequence on its thermo-mechanical behaviour.
The first part of the thesis is oriented to the determination of an empirical model able to describe the evolution of the fuel Young's modulus as a function of burnup. The second parallel scope of this first part is the extension of the range of applications of high frequency acoustic microscopy in the post irradiation examination. In fact, examination of irradiated nuclear fuel requires various techniques to be used and implies different samples treatments/transports with enhancement of the contamination risk. Thanks to the study performed in the present research work, high frequency acoustic microscopy would enable determining different micro-structural features with a single acoustic measurement performed on the available surface of the sample.
The second part of the thesis deals with the degradation of the fuel elastic properties after several years from the end of irradiation; in fact due to the necessity of discharging, transporting and placing irradiated nuclear fuel in interim or long-term storage, the determination of the

evolution of the elastic properties is fundamental. After discharge, the damage caused by the alpha-decays of radionuclides produced during in-reactor irradiation accumulates. The determination of spent fuel elastic properties is fundamental to ensure the fuel safe disposal on a geological time-scale. This problem was tackled by measuring stored irradiated nuclear fuel samples and specimens reproducing in laboratory the alpha damage accumulated after thousands of years.
The third part of the thesis treats the case of nuclear accident. During a nuclear accident the extreme conditions conduct to the fuel melting and to its interaction with all the surrounding materials, generating a new material whose properties are strictly related to the nuclear reactor type and nuclear accident dynamic (*corium*). Severely degraded fuel after a nuclear accident is extremely complex and present different phases, hence the determination of its mechanical properties is not straightforward; however, the removal of this material is extremely important if the pre-accidental conditions have to be restored. To conceive the appropriate tools for debris and corium removal, fundamental is the determination of the severely degraded fuel elastic properties.
Application of the high frequency acoustic microscopy to determine spent fuel and severely degraded fuel elastic properties is pioneering, hence this thesis provides a first set of data and interpretations which will find further developments in future.

List of Abbreviations

DBA . . . . . Design Basis Accident
EDF . . . . . Électricité de France
EPMA . . . . Electron Probe Microanalysis
FIMA . . . . . Fission of Initial Metallic Atoms
FPs . . . . . Fission products
HBRP . . . . . High Burnup Rim Project
HBS . . . . . High Burnup Structure
LOCA . . . . . Loss of Coolant Accident
LWR . . . . . Light Water Reactor
MOX . . . . . Mixed Oxide fuel
NFIR . . . . . Nuclear Fuel Industry Research
NPP . . . . . Nuclear Power Plant
PWR . . . . . Pressurised Water Reactor
SEM . . . . . Scanning Electron Microscopy
SNF . . . . . Spent Nuclear Fuel
TD . . . . . Theoretical Density
TEM . . . . . Transmission Electron Microscopy
TMI-2 . . . . . The Three Mile Island Unit 2 reactor
XRD . . . . . X-Ray Diffraction

Nomenclature

α	Thermal expansion coefficient
β	Thermal compressibility
γ	Grüneisen parameter
λ	Lamé's parameter
λ_c	Thermal conductivity
μ	Lamé's parameter
ν	Poisson's ratio
ρ	Density
σ_{ik}	Stress tensor
Θ	Debye's temperature
ε_{ik}	Strain tensor
a	Lattice parameter
C_p	Specific heat capacity at constant pressure
C_v	Specific heat capacity at constant volume
c_{ikjl}	Elastic stiffness constants
dpa	Displacement per atom
E	Young's modulus
H	Hardness
K	Bulk's modulus

k	Thermal conductivity
k_B	Boltzmann's constant
N_a	Avogadro constant
R	gas constant
s_{ikjl}	Elastic compliances
v_l	Longitudinal wave velocity
v_R	Rayleigh wave velocity
v_t	Transverse wave velocity

Contents

List of Figures

List of Tables

Chapter 1

Nuclear fuels in normal and off-normal conditions

Contents

1.1 Introduction

Currently (2017), ~ 31 countries use nuclear energy, running about 440 commercial nuclear power reactors which provide approximately 11% of the world's electricity [1]. Sixteen countries depend on nuclear power for about 25% of their electricity; for instance France gets $\sim$ 80% of its electricity thanks to the 58 commercial nuclear power reactors. Italy and Denmark, which are not hosting active nuclear power plants, get almost 10% of their power from nuclear, through import. A detailed comparison of the percentage of nuclear in electricity production for each country in 2014 and 2015 is showed in Figure 1.1.

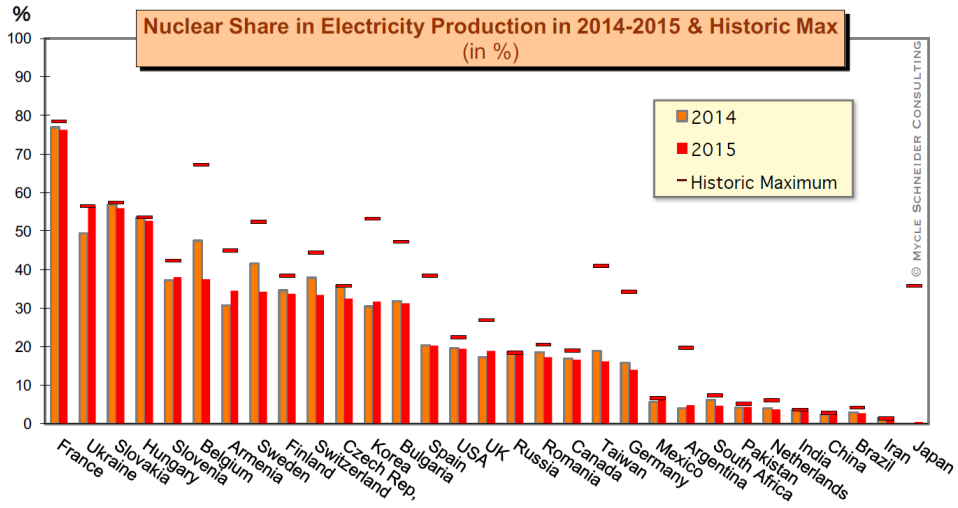

Figure 1.1 – Annual nuclear share in electricity mix by country and historical maximum [2]

1.2 Nuclear fuel

Energy in a nuclear reactor is produced by the fission events inside the nuclear fuel. The nuclear fuel is, thus, constituted of fissile material contained in a matrix which is generally a ceramic compound or a metallic alloy. The characteristics that a nuclear fuel must satisfy can be summarised as follows [3]:

- The neutron capture cross section should be low for the non fissile nuclei, to optimise the number of neutrons available for fissioning (neutron economy)
- The density of the heavy atoms must be as high as possible to minimise the reactor core size

- Absence of chemical reactions with the materials constituting its surrounding
- High thermal conductivity and melting point. This because the transmission of heat between fuel and coolant must be good enough to avoid the risk of fuel melting (margin to melt, i.e. the difference between the operating and the melting temperatures which is higher in oxide fuels in comparison with metal fuels).
- High thermo-mechanical stability and very good resistance to radiation damage.

The series of processes and operations related to the production of nuclear fuel, its irradiation in nuclear reactor and storage or reprocessing is identified as *Nuclear fuel cycle*. Uranium is the element most widely used to fabricate nuclear fuel. Its natural composition is about 99.28 wt% ^{238}U, 0.71 wt% ^{235}U and 0.005 wt% ^{234}U [4]; among these the fissile isotope is ^{235}U. Uranium is extracted from the ore which usually contain 0.1% - 0.5% of uranium by means of: underground mining ($\sim$38% of total), open pit mining ($\sim$23%), in situ leaching-ISL ($\sim$28%), co-product or by-product recovery from copper and gold operations ($\sim$8%) and other methods ($\sim$3%) ([4] and [5]). Once extracted, it is chemically treated in order to obtain an uranium concentrate which is commonly called *yellowcake*, because of its yellow colour. Uranium concentrate is then converted to uranium hexafluoride (UF_6) or metal uranium in case of fuel based on metallic uranium alloy.
Many compounds of uranium have been studied as nuclear fuel, mainly oxides, metal alloys, carbides and nitrides. Most nuclear power reactors use uranium dioxide enriched in ^{235}U to about 2-5% , or uranium dioxide with about 5% of PuO_2, which is commonly known as mixed oxide fuel (MOX). The enrichment of uranium is mainly achieved via gaseous diffusion or centrifugation of uranium hexafluoride, which are both based on the mass and mobility difference among uranium isotopes.
Table 1.1 describes the possible type of reactors around the world, the fuel, the coolant and the moderator that are used. The fuel consists, with few exceptions, of a stack of cylindrical fuel pellets encapsulated in a cladding tube. For instance, in a 900 MW pressurised water reactor (PWR), 272 sintered pellets of uranium dioxide in a Zr alloy, form a 3.85 m long rod. About 264 rods are bundled together in a fuel assembly and then 157 of these assemblies form the core of the reactor [6]. Figure 1.2 (a) shows a schematic of a fuel rod . Between the pellets and the cladding a gap filled with He is present. The purpose of this gap is to accommodate the gaseous fission products and the thermal expansion of the pellets. In Figure 1.2 (b) is shown the structure of typical PWR assembly of fuel rods. A schematic representation of the nuclear fuel cycle is depicted in Figure 1.3.

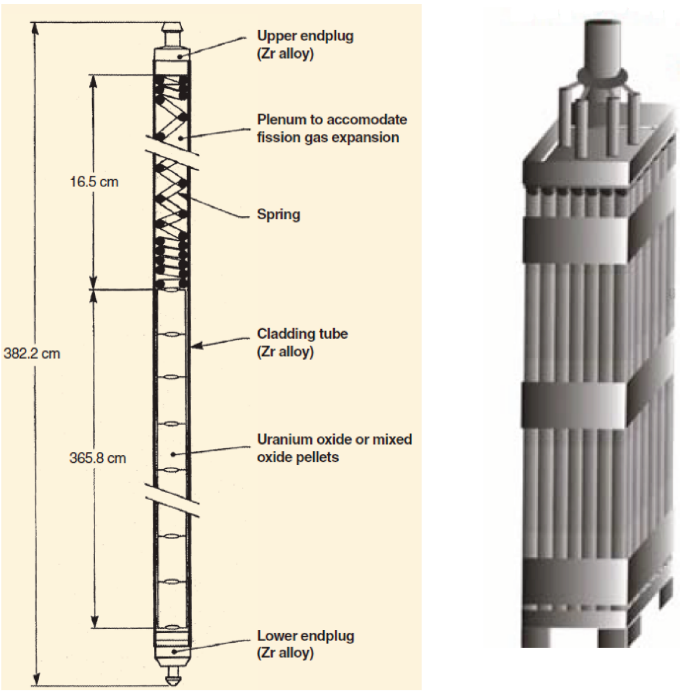

(a) (b)

Figure 1.2 – (a)PWR fuel rod schematic. The dimensions are characteristic of a 900 MW PWR fuel rod. The free space left between the top of the pellet stack and the welded end plugs is called *Plenum*, which is meant to accommodate the release of the fission gases [7]. (b) Schematic illustration of a PWR assembly [4]

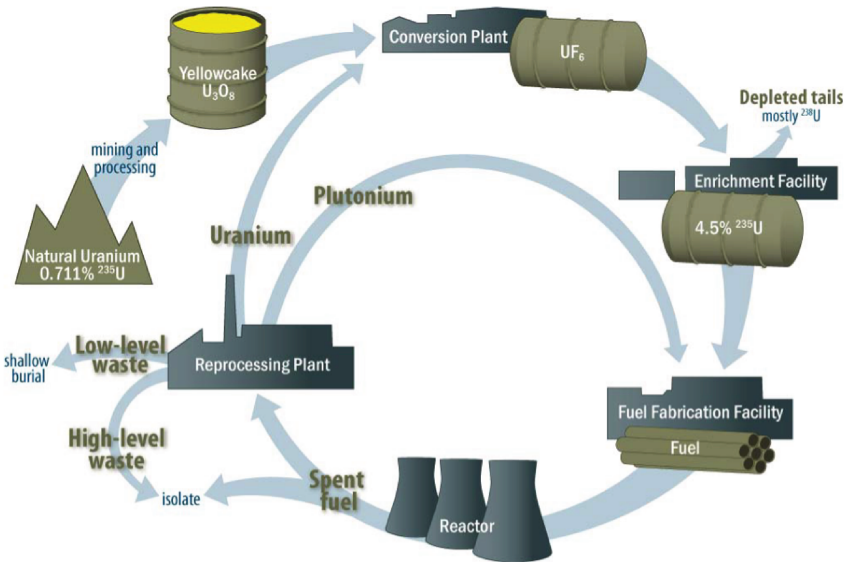

Figure 1.3 – Schematic of a nuclear fuel cycle with both open and closed (plutonium reprocessing) options. (Congressional Research Service, 2011)

Table 1.1 – Nuclear Power Plants in use in 2008 [4] [8]

Reactor type	**Fuel**	**Coolant**	**Moderator**
Light Water Reactor (LWR): Pressurised Water Reactor (PWR) | Boiling Water Reactor (BWR)	UO_2/MOX	H_2O	H_2O
Graphite Moderated Light Water Cooled Reactors (RBMK)	UO_2/MOX	H_2O	Graphite
Pressurised Heavy Water Reactor (PHWR)	UO_2	D_2O	D_2O
Advanced Gas Reactor (AGR)	UO_2	CO_2	Graphite
Magnesium non oxidizing (MAGNOX)	U	CO_2	Graphite
High Temperature Reactor (HTR)	UO_2	He	Graphite
Fast Reactor (FR)	MOX	Na	-

1.2.1 Production of uranium dioxide nuclear fuel pellets

The chemical form of uranium during enrichment is UF_6; different conversion processes are used in order to transform the uranium hexafluoride into uranium dioxide powder. These processes are generally subdivided in two categories: wet process, which is a precipitation based method and dry process. The dry process consists in a reaction between vaporised UF_6 and H_2O vapour, with consequent UO_2F_2 formation, reduced successively in presence of H_2 and steam to UO_2 [9] [8]. Figure 1.4 shows a schematic of the dry processes followed to manufacture an uranium dioxide pellet starting from uranium hexafluoride. In order to obtain a density ∼95 % of the theoretical density TD (TD = 10960 kg $\cdot$ m^{-3}) U_3O_8 is mixed together with pore formers. This very fine U_3O_8 powder is obtained by calcination (oxidation of UO_2 in air at about 623 K) of scraps from former fabricated batches. A lubricant (generally zinc stearate) is added to help the pressing stage. The "green" pellets after pressing have a density of about 60 % TD [8]. Sintering is performed at 1973 K in H_2 atmosphere in order to obtain a O/M ratio the closest as possible to 2.00, optimising the thermal conductivity properties of the fuel. At the end of the process the pellets are visually examined in order to ensure fulfillment of

the requirements; in particular metallographs are performed to ensure the particle grain size to be about 10 μm in standard grain fuels.

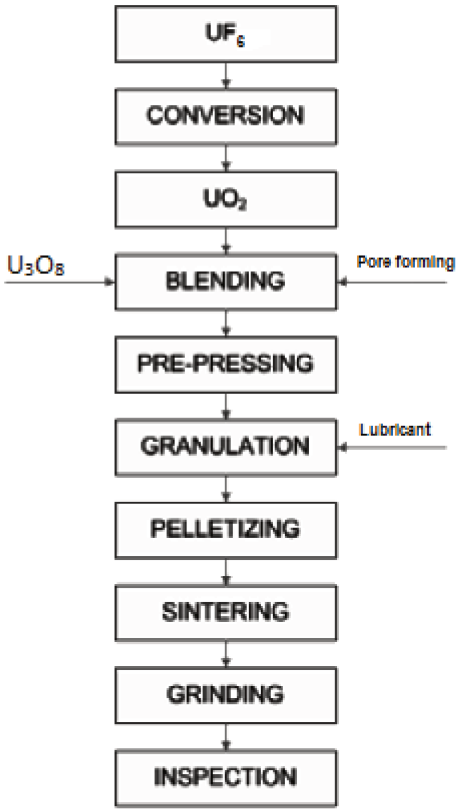

Figure 1.4 – Flowsheet of a typical uranium dioxide synthesis from UF_6 [10]

1.2.2 Production of MOX fuel pellets

Mixed oxide pellets for LWR or FR are also fabricated by powder metallurgy. In this case PuO_2 powder, which comes from reprocessing plants (Figure 1.3) must be intimately mixed with UO_2 powder. For the fabrication of MOX pellets for LWR, the MIMAS process (see Figure 1.5) is the most used commercially : this process consists in an intimate milling of UO_2 powder together with the PuO_2 powder

to obtained the "Micronized MASter-blend" with a Pu content between 25 and 30 %. This master-blend is then diluted in the remaining UO_2 powder to obtain the required plutonium content ($\sim$ 5-10%), through a blending operation. After pressing, MOX pellets as UO_2 pellets are sintered during 4 hours at 1973 K, in a slightly moist argon hydrogen mixture to obtain a condition close to stochiometry. In MOX MIMAS pellet Pu is not homogeneously distributed [8].

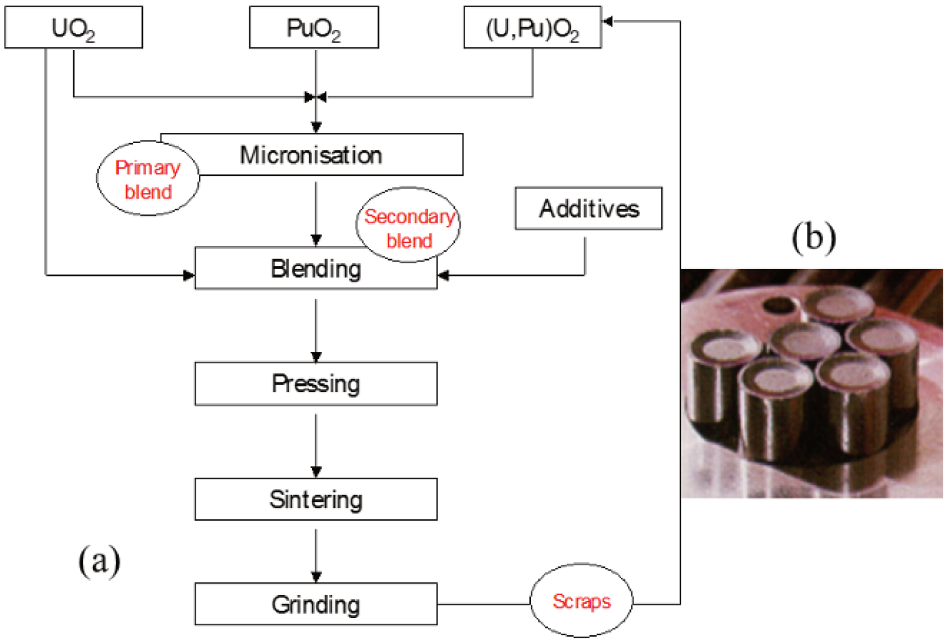

Figure 1.5 – (a) Flowsheet of MOX synthesis via MIMAS (b) MOX pellets.

1.3 Irradiation of nuclear fuel

Each ^{235}U fission produces two new nuclei (stable or radioactive) whose atomic mass is centred around 95 and 139. In order to avoid the release of the fission products (FPs) in the coolant, the fuel pellet is contained in a metallic cladding; both the fuel and the cladding act as a first barrier, ensuring the confinement of the fission products. The fission products accumulating in the nuclear fuel during its life in reactor core can be classified, according to Kleykamp [11], in four categories: 1) fission gases and other volatile fission products e.g. Kr, Xe, Br, I; 2) metallic precipitates e.g. Mo,Tc, Ru, Rh, Pd, Ag, Cd, In, Sn, Sb, Te; 3) oxide precipitates e.g. Rb, Cs, Ba, Zr, Nb, Mo, Te; 4) fission products dissolved

as oxides in the matrix e.g. Sr, Zr, Nb, and the rare earths Y, La, Ce, Pr, Nd, Pm, Sm. Some of the FPs can be present in different forms, depending on the local chemical conditions (e.g. oxygen potential). The accumulation of the fission products is responsible for the modification of the chemistry of the fuel; the new elements are accommodated in the fuel matrix, precipitate as oxides or metals or can accumulate in bubbles. The composition of the fuel changes also because of the neutron capture of uranium nuclei and the subsequent decays which determine the formation of transuranium elements such as Np, Pu, Am and Cm.
Radiation damage is another important consequence of nuclear fission: the fission fragments, in fact, dissipate their kinetic energy by transferring it to the neighbouring atoms. A smaller, but not completely negligible, contribution to the damage is determined by the alpha decays of the abovementioned transuranium elements.

1.3.1 Interaction between charged particles and matter

It is possible to classify the interacting particles in light or heavy particles, considering as heavy those characterised by a rest mass greater than the electron rest mass, while light particles are e.g. electrons and positrons. For practical purposes we describe in this section only the interaction of heavy charged particles with matter.
Inelastic collisions with target's bound atomic electrons, and their consequent excitation and ionisation, are the main mechanisms responsible for the loss of kinetic energy during the interaction of swift[1] charged particles with matter. Another important mechanism is the inelastic collision with a nucleus which determines a deflection of the charged particle[2]. The charged particle can interact with matter also by means of elastic collisions with nuclei or with electrons, determining in both cases a non radiative deflection of the charged particle. In the elastic collisions with electrons energy and momentum are conserved and the energy transfer is smaller than the lowest electrons excitations potential. Elastic collisions with atomic electrons are relevant only for very low energy electrons [12].
Swift heavy charged particles lose a large fraction of their kinetic energy by means of ionisations and excitations, whereas the elastic nuclear scattering becomes relevant when the projectile has become a slow heavy particle with a very large nuclear charge, e.g. a fission product. The total energy E (keV) loss per unit path x (μm), during the penetration of matter, is called Stopping power. The stopping

[1] If the velocity of the charged particle is higher than the mean quadratic velocity of its electrons: $v_0 Z_1^{2/3} (v_0 = e^2/\hbar)$

[2] in case the charged particle is an electron, the energy lost during the deceleration is converted in X-ray radiation (Bremsstrahlung)

power (-dE/dx) can be expressed as:

$$-\frac{dE}{dx} = (-\frac{dE}{dx})_{electronic} + (-\frac{dE}{dx})_{nuclear} \tag{1.1}$$

If the velocity of the projectile is lower than the mean quadratic velocity of its electrons, the loss of energy due to collisions with nuclei, dominated by the charge neutralisation, is not negligible, hence the nuclear stopping power must be considered [13]. The theory of the nuclear stopping power was firstly developed by Niels Bohr and then extended by a group of Danish theoreticians (Lindhart, Scharff and Schiott, LSS). The nuclear stopping power can be expressed in terms of the the reduced stopping power S_n [14]:

$$S_n = 0.5\frac{ln(1+\varepsilon)}{(\varepsilon + 0.10718\varepsilon^{0.37544})} \tag{1.2}$$

where:

$$\varepsilon = \frac{32.53 m_2 E}{[Z_1 Z_2 (m_1+m_2)(Z_1^{2/3}+Z_2^{2/3})^{1/2}]} \tag{1.3}$$

E is the particle energy in keV, Z_1 and Z_2 the ion and target atomic numbers, m_1 and m_2 the ion and target masses in u. Figure 1.6 shows the reduced stopping power S_n versus ϵ.

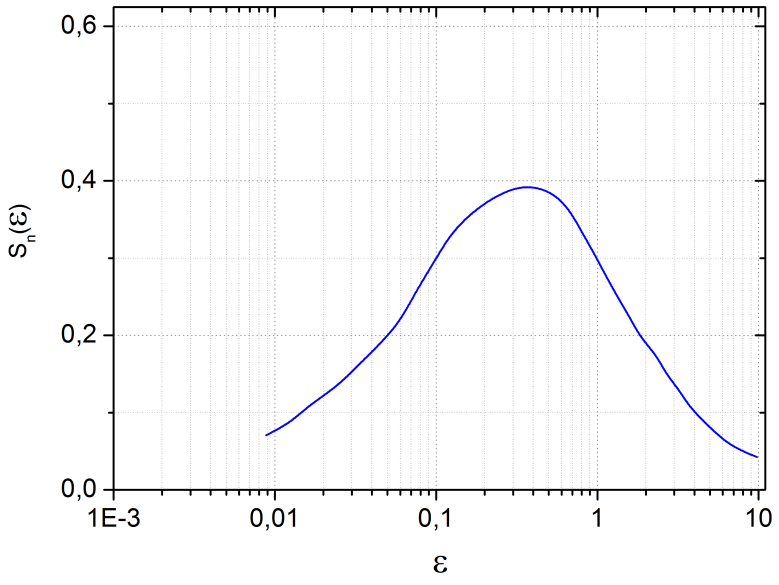

Figure 1.6 – Reduced nuclear stopping power as a function of ϵ parameter, for the model developed by Lindhart, Scharff and Schiott.

If the particle penetrating matter with velocity v has rest mass >> electron's rest mass m_e, the energy transferred as ionisations and excitations in the element path dx, can be determined by the Bethe and Bloch formula [15]:

$$-\frac{dE}{dx} = 4\pi N_a r_e^2 m_e c^2 \rho \frac{Z_1^2 Z_2}{A_2 \beta^2} \cdot (ln\frac{E_{max}}{I} - \beta^2 - \frac{\varepsilon}{2} - \frac{C}{Z_2}) \tag{1.4}$$

where N_a is the Avogadro constant;
β= v/c with c = speed of light in vacuum;
r_e and m_e are, respectively, the electron classical radius and rest mass;
Z_1 is the charge of the projectile, Z_2 and A_2 are the material atomic number and mass;
E_{max} is the maximum energy transferable during the collision;
I indicates the geometric mean of all the excitation and ionisation potentials of the absorbing atom.
The last two terms are correction factors: ε is a function of the electron density and applies at high energies, when polarization of electrons by the electric field of the moving charged particle shields distant electrons. C takes into account the fact that at low energies the collision is non-adiabatic [15]: it is termed *shell correction* and it is function of the electrons orbital velocities. The Bethe and Bloch equation contains a term depending on the material and a term which is function of the projectile's properties. In particular:

$$-\frac{dE}{dx} \propto \frac{AZ_1^2}{E_{ion}} \tag{1.5}$$

Thus, the higher the kinetic energy of the heavy charged particle (E_{ion}), the lower is the rate of energy loss. If the term $\beta \to 0$, the energy loss rate increases abruptly and the charge state of the particle decreases due to the capture of orbital electrons of the material. These two phenomena determine the particle to lose the majority of its energy at the end of its range. Figure 1.7 shows a comparison between the nuclear and electronic components of stopping power for ^{4}He at 5 MeV, and for the low energy recoil ^{237}Np generated during the alpha-decay of ^{241}Am, in UO_2 with 97% of theoretical density TD (TD = 10960 $kg \cdot m^{-3}$). The nuclear component of the stopping power is negligible for a swift charged particle like He, whilst is dominant in the loss of energy of the slow recoil (kinetic energy $\sim$ 100 keV), as showed in Figure 1.7 (b). The peak noticeable for the electronic stopping power in Figure 1.7 (a), at the end of the particle's range, is called *Bragg's peak*.
If the energy of the particle is low enough to justify the elastic collisions with nuclei, the atoms are displaced from the lattice site and the knock-on atoms can generate new collisions and displacements.

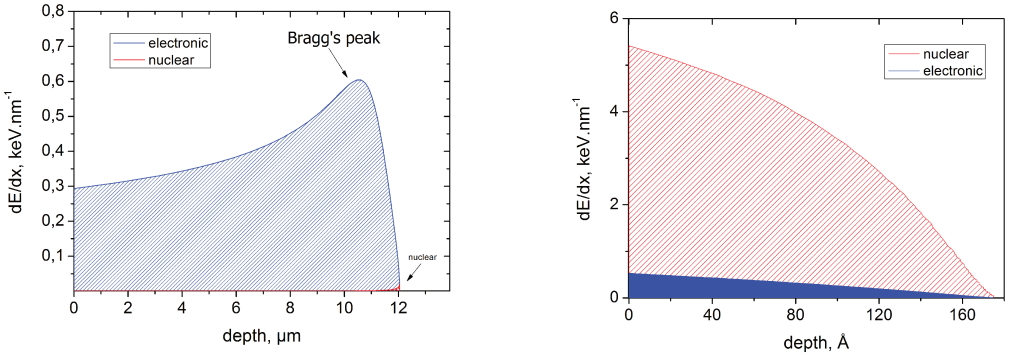

(a) (b)

Figure 1.7 – (a)Electronic stopping power (blue) and nuclear stopping power (red) of a ^{4}He nucleus with energy of 5 MeV in UO_2 with 97% of theoretical density. (b) Electronic stopping power (blue) and nuclear stopping power (red) of the low energy recoil ^{237}Np generated during alpha-decay of ^{241}Am nucleus. The Stopping powers were calculated using the code SRIM [16].

If the initial projectile has enough energy the result of the process can be a collision cascade: each knock-on atom collides with another atom, transferring sufficient energy to determine a successive collision and so forth. Typically an energy of 40 eV and 20 eV is required to displace an U and an O atom, respectively.
Figure 1.8 shows and compares the defects produced during the alpha decay of the ^{241}Am and the fission of ^{235}U. In the first case the greater number of defects is generated by the recoil, whilst in the second the majority of defects is produced by the heaviest of the two fission fragments.
In the case of fission, in addition to the ballistic displaced atoms, electronic energy loss can result in thermal spikes due to electrons-phonons coupling. The consequences of the above-mentioned phenomenon include fission-enhanced diffusion, fission enhanced-creep, resolution of fission gas from small bubbles, etc [17].

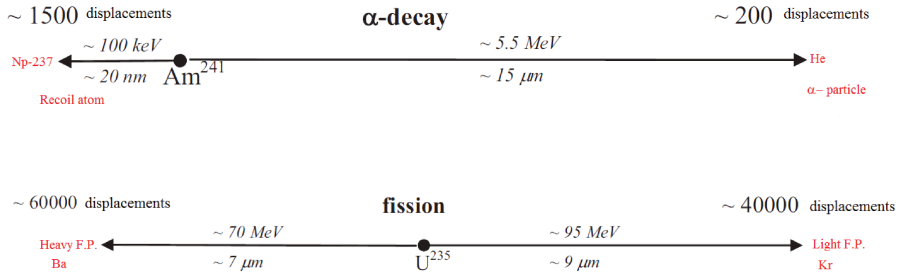

Figure 1.8 – Schematic of the energies and ranges and damages produced by nuclear fission of ^{235}U and ^{241}Am alpha-decay [6].

1.3.2 Radiation damage

Irradiation of a material produces defects in its crystalline structure. These can be grouped into four categories [18, 19]:

- Point defects, i.e. missing atoms, incorrectly positioned atoms or dopants.
- Line defects or dislocations. The dislocation line has a central core of atoms located away from the regular crystallographic site.
- Planar defects, which extend in two dimensions and are essentially atomic in the ortogonal direction. Examples of planar defects are grain boundaries, stacking faults, inversion domains, and twins.
- Volume defects, i.e. three dimensional aggregates of atoms, secondary-phase particles or precipitates and voids formed by aggregation of vacancies or bubbles formed by gas atoms.

Point defects

Point defects are present in real crystals, even under thermal equilibrium conditions. The displacement of an atom from its lattice site to an interstitial position produces a type of point defect which is termed Frenkel pair. If the atom, removed from an inner lattice site migrates to a lattice site belonging to the surface of the crystal, the point defect produced is called Schottky defect . A schematic of these two different point defects are depicted in Figures 1.9 and 1.10.

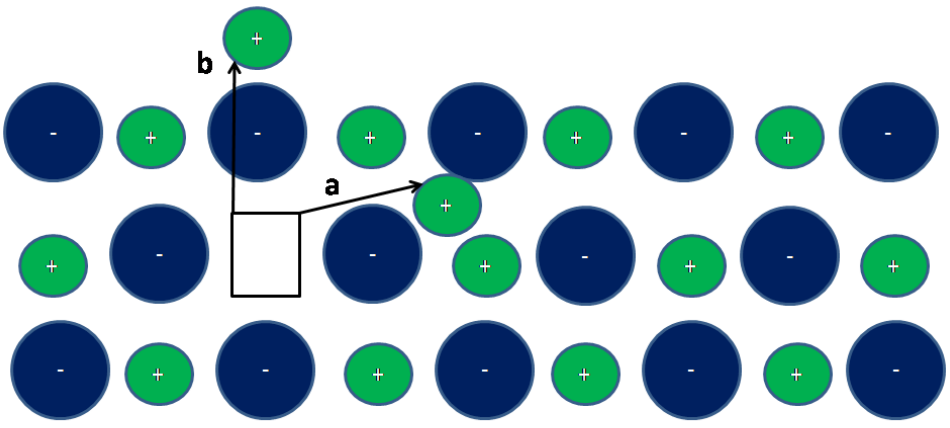

Figure 1.9 – Frenkel pairs (a) and Schottky defect (b) in an ionic crystal. In the first case the ion migrates to an interstitial position, in the second the ion moves to the surface of the crystal.

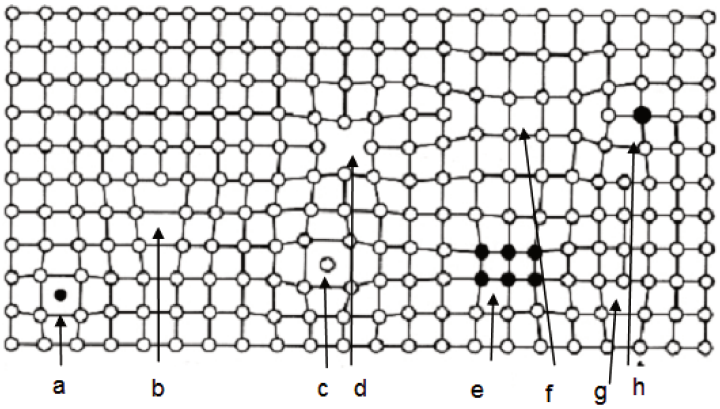

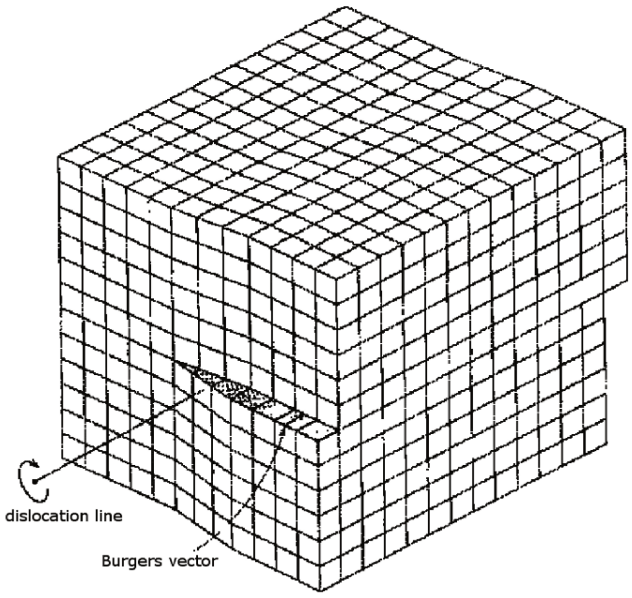

i

Figure 1.10 – Possible crystal defects: (a) interstitial impurity atom, (b) edge dislocation, (c) self-interstitial atom, (d) vacancy, (e) precipitate of impurity atoms, (f) vacancy-type dislocation loop, (g) interstitial-type dislocation loop, (h) substitutional impurity atom. (i) screw dislocation [20]

In ionic crystal the formation of an equal number of positive and negative vacancies, hence the local neutrality of the crystal, is energetically favourable.

Extended defects

Linear, planar and volume defects belong to the bigger group of extended defects. Dislocations are line imperfections in the crystal which determine a misfit within it; they are usually described by a line and an associated misfit vector which is

called Burgers vector [21]. The most common dislocation types are: edge, screw or mixed dislocations. The first one can be easily visualised as an extra plane or half plane of atoms in the crystalline lattice; in this case the Burgers vector is perpendicular to the slip direction (Figure 1.10 b). Screw dislocations (Figure 1.10 i), described by a Burgers vector parallel to the slip direction, can be imagined as a cut in the crystal determining a consequent shear parallel to the cut direction [22]. In the mixed dislocations, characteristics typical of screw and edge dislocations can be found, in particular for these dislocations the relative direction between slip and Burgers vector is neither purely perpendicular nor purely parallel.
Planar defects are determined by irregularities in the crystalline lattice across a planar surface of the crystal. When a single plane of atoms within the crystalline lattice is out of order a *stacking fault* is generated. An example of stacking fault in the cubic close packed structure, which normally has an ABCABC stacking order, is the ABCABABC stacking order [20]. Other planar defects are *twin boundaries* and *Grain boundaries*. The first occur when a stacking fault re-orient the rest of the crystal and a grain boundary derives from the coupling of two or more single crystals with different orientation. Other types of planar defects are *vacancies* and *Self-interstitial dislocation loops*.
Three dimensional defects are clusters of point defects: clusters of vacancies forming empty volumes in the material determine a type of three dimensional defect known as *voids*. Clusters of atoms different from the matrix material form *precipitates*.
Figure 1.11 shows an image of dislocation loops in $^{233}UO_2$ acquired by means of a Transmission Electron microscope (TEM).

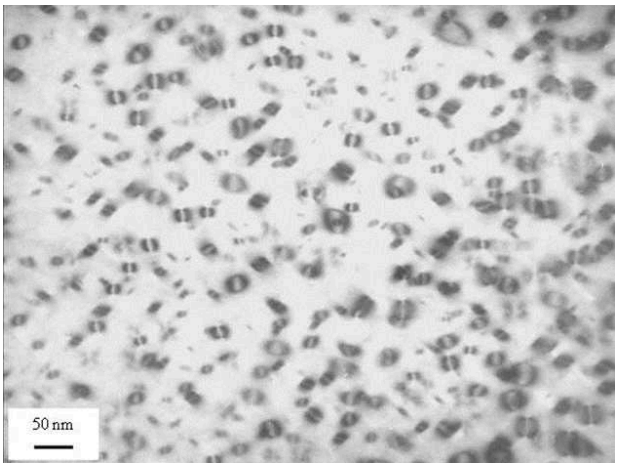

Figure 1.11 – Dislocation loops $^{233}UO_2$ acquired by means of a Transmission Electron microscope (TEM).

An international measurement of radiation damage in materials is given by the displacement per atom (dpa) unit which enables the comparison among damages

produced by different irradiating particles in a wide range of materials. The idea behind the dpa concept is that energetic particles travel along straight paths in the material, colliding randomly in a binary-system mode and transferring energy to lattice atoms.
If the energy transferred to a lattice atom, in a binary collision, is smaller than the binding energy of the atom in the lattice, the atom is not displaced from its original position and defects are not produced. If the energy is larger than the binding energy, the atom can acquire sufficient kinetic energy, move through the lattice and produce more defects. Such considerations led to the formulation of the Kinchin-Pease model, which enables the calculation of the produced defects number (N_d) [23]:

$$N_d = \begin{cases} 0 & \text{if } E_t < E_d \\ 1 & \text{if } E_d < E_t < 2E_d \\ \frac{E_t}{2E_d} & \text{if } 2E_d < E_t < \infty \end{cases} \tag{1.6}$$

where E_t is the energy transferred during the collision and available for damage production, E_d is the threshold displacement energy, higher than the cohesive energy of the atom in the lattice. This model was successively refined by Norgett, Robinson and Torrens by taking account of possible recombinations (NRT). Once calculated the number of defects produced by means of the Kinchin-Pease model or the NRT, in a considered volume of material (V), the dpa can be determined by [23]:

$$dpa = \frac{number\ of\ displaced\ atoms\ in\ V}{number\ of\ material\ atoms\ in\ V} \tag{1.7}$$

The displacement per atoms unit is quite inaccurate in the description of complex differences in primary damage production for energetic displacement cascade conditions, in comparison to isolated Frenkel pair production [24].
When a material is irradiated, the atoms surrounding the induced defects accommodate by slightly displacing from their original lattice positions (lattice relaxation), determining an elastic strain field whose extent is greater than the defect chemical size. As a consequence of this phenomenon, the mechanical properties of the material are subjected to a variation [18].
UO_2 has a fluorite crystalline structure type: U atoms, with charge +IV, form a face-centred structure with O atoms (charge -II), settled inside each tetrahedral U site (Figure 1.12). In uranium dioxide the formation of vacancies is related to that of interstitials and vice versa. A vacancy in the anion sub-lattice with consequent migration to the surface, would determine a surface negatively charged and an interior with a net positive charge, with a violation of the local electrical neutrality. Hence, in UO_2 two anion vacancies must be created for each cation

vacancy (Schottky trio) [17]. The most probable defect in ideally stoichiometric uranium dioxide is the production of anion Frenkel pairs [17].

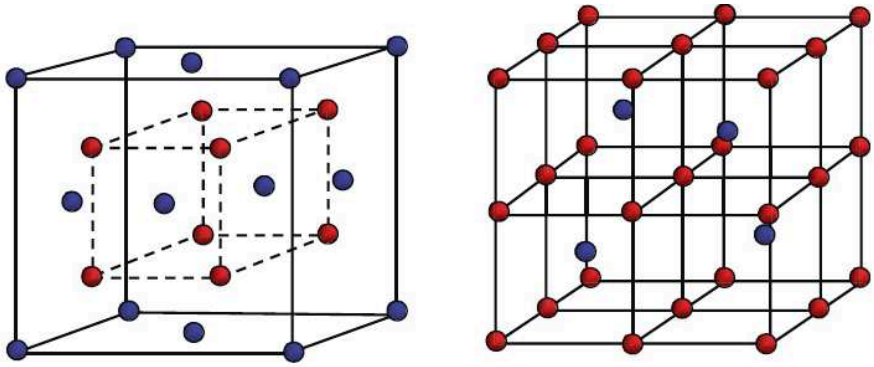

Figure 1.12 – Uranium dioxide crystalline structure. On the left the unit cell and on the right the oxygen lattice. Uranium atoms are in blue, oxygen atoms in red [3].

Figure 1.13 shows the trend followed by the uranium and oxygen vacancies as a function of penetration depth of the ^{4}He nucleus in UO_2 for the alpha decay of ^{238}Pu. The observed peak corresponds to the zone, close to the end of the projectile's path, where the nuclear stopping power starts increasing.

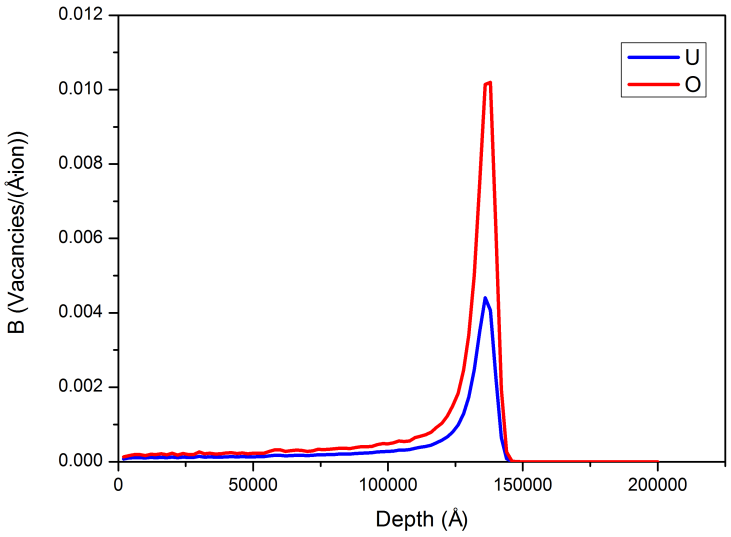

Figure 1.13 – Uranium and oxygen vacancies variation with depth for penetration of ^{4}He nucleus in UO_2 due to alpha decay of ^{238}Pu calculated with SRIM [16].

During irradiation the free interstitial atoms can assemble and form interstitial loops, while vacancies tend to form voids. The formation energy of a cationic

interstitial is greater than that of a vacancy [25].
During the uranium dioxide irradiation, the depleted zone created in collision cascades may act as nucleation sites for voids generation. Voids nucleation and growth are sequential events: the number of voids increases with time during the nucleation period, whilst voids size increases during the growth step. The void growth is controlled by diffusion of vacancies and interstitials from the bulk of the solid to the void surface [17]. Voids lead to the fuel swelling phenomenon: the crystal lattice volume increases and the effect has an impact on the global fuel volume. To a larger extent fuel volume increases due to the insoluble fission products precipitation [26]. The fuel volume increase during irradiation is treated in subsection 1.3.3.

Defects annealing

For every type of defect exists a threshold temperature above which diffusion is favourable and the defects (e.g. vacancy/interstitial) could recombine or anneal. Matzke and co-workers [27] studied formation and recovery of radiation damage by irradiating UO_2 and UN single crystals with ions of rare gases (Kr and Xe) and volatiles FPs (Te, I, Rb, Cs) at different irradiation doses and energies. The implanted samples were then annealed in furnace up to temperatures of 2070 K. They observed the dependence of the anneling on both the temperature and the irradiation dose. In uranium dioxide they found as threshold temperature for uranium dioxide vacancy annealing 850 K. For volatiles implantation, they obtained annealing of the uranium vacancies at 890 K. For the rare gas implantantion, at high defects concentration, they observed a shift of the first stage of annealing, but a complete recovery at temperatures of about 1700 K.
Weber [28] performed isochronal and isothermal annealing to study the behaviour of lattice defects produced by irradiating UO_2 single crystals with a semi-infinite $^{238}PuO_2$ source. After the annealing he measured the lattice parameter evaluating the percentage of recovery. Based on this study, three recovery steps have been observed for the lattice parameter (Figure 1.15): 573 K, 850 K and 1198 K. A direct correlation with the produced defects was not studied, but on the basis of the work performed by Nakae et al. (5), Weber [28] suggested that the first stage of recovering is related to the migration of oxygen vacancies and the second stage to the migration of uranium vacancies. Stage III was observed only in single crystals and Weber, making considerations on the temperature and activation energies, interpreted this stage as the trapped helium release from the vacancies, via migration or dissociation of the vacancy-He complexes.

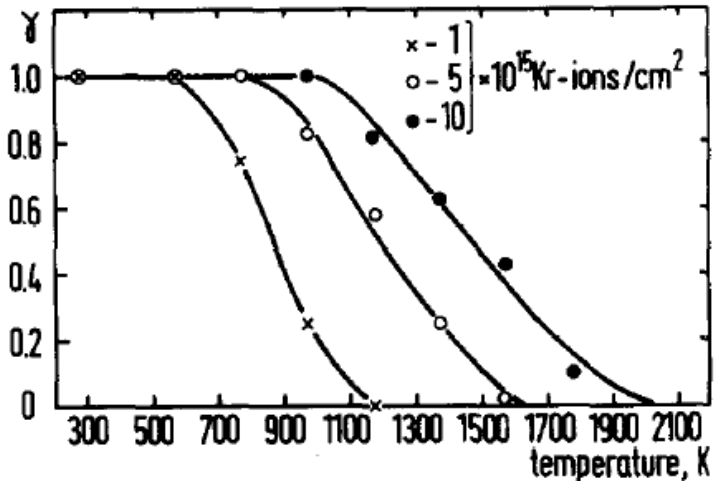

Figure 1.14 – Annealing stages of <100> UO_2 single crystal as a function of Kr-ions irradiation fluence [27].

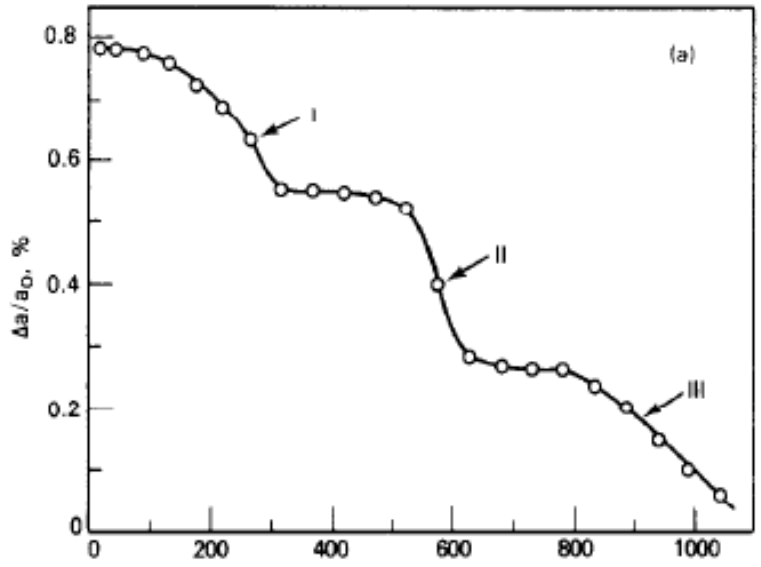

Figure 1.15 – Recovery effect determined by the heating of uranium dioxide single crystals, irradiated by a semi-infinite source of $^{238}PuO_2$. The annealing of the defects appears at three different temperature stages [28].

1.3.3 Nuclear fuel swelling

During the irradiation, the uranium dioxide volume is subjected to a variation with the burnup[3]. At the beginning, the initial porosity of the sintered pellets decreases as a consequence of the possible fragments-driven vacancies ejection from the pores. Some of the vacancies migrate from pores to sinks, e.g. to grain boundaries or dislocations, where they annihilate and determine a global volume decrease [29]. This process saturates quickly and after about 15 $GWd \cdot t^{-1}M$, the volume starts increasing with further increase of the burnup, determining the fuel swelling effect. The main consequence is the fuel-cladding gap progressive reduction until contact, which determines mechanical and chemical interactions between the nuclear fuel and the cladding. The fuel swelling is determined by an increase in the fuel matrix volume and an increase of the nuclear fuel porosity.
The matrix swelling is mainly due to insoluble fission products precipitation (solid or gaseous), in intragranular bubbles or in bubbles settled at grain boundaries [30]. Solid fission products contribute to matrix swelling for 0.32% per 10 $GWd \cdot t^{-1}M$. The largest contribution to the matrix swelling derives from the formation of fission gas filled bubbles (especially intergranular) which contribute to give a total matrix swelling between 0.8% and 1% per 10$GWd \cdot t^{-1}M$ [29–31]. Spino and coworkers [32] observed a total matrix swelling in the above-mentioned range, up to a threshold burnup ($\sim$ 70 $GWd \cdot t^{-1}M$), after which the swelling rate decreases, being dominated by solid FPs swelling, while the fuel matrix becomes gradually depleted in gaseous FPs.
Another important component is the lattice expansion due to the production of defects within the lattice. This effect that usually overrides the lattice contraction caused by the soluble fission products [32, 33].
Figure 1.16 shows the study performed by Weber on lattice expansion of uranium dioxide single crystals, irradiated with alpha particles produced during the decay of a $^{238}PuO_2$ source. He observed that the variation of the lattice parameter, as a function of the irradiation fluence, was following an exponential ingrowth behaviour consistent with the model of constant rate production of Frenkel defects and recombination rate proportional to the defects concentration [34].
Figure 1.17 shows the variation of lattice parameter experienced by actinides-doped UO_2, MOX and PuO_2 samples published by Wiss et al. [35], who determined an analogue behaviour of the lattice parameter due to defects accumulation in the lattice, with a saturation value $\sim$ 0.63%.

[3]Burnup is either defined as the ratio between the number of fissions and the initial number of heavy metal atoms (in % sometimes spelled out as FIMA) or as the thermal energy released by fuel containing 1 ton of heavy-metal atoms ($GWd \cdot t^{-1}M$). Approximately 1 at% corresponds to 10 $GWd \cdot t^{-1}M$.

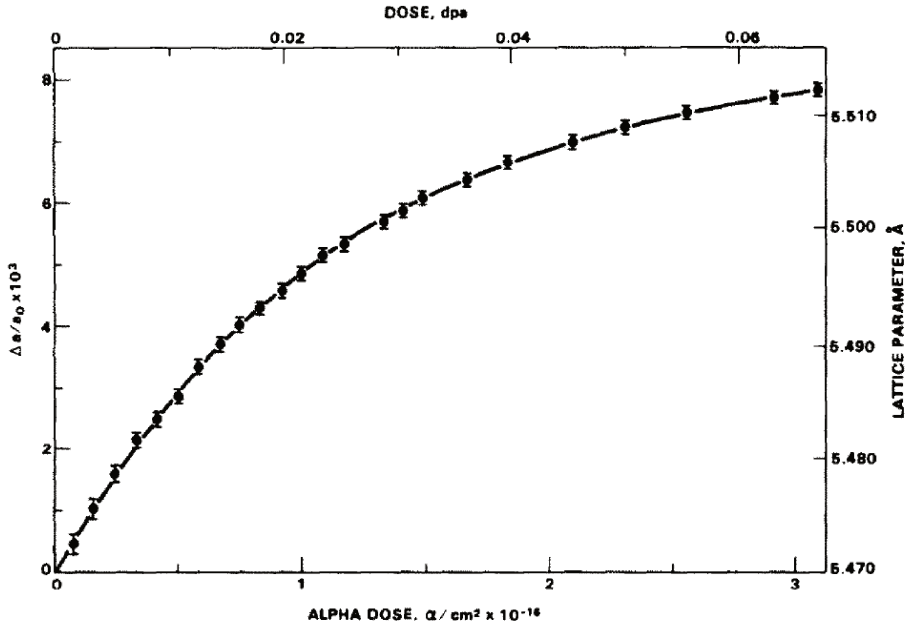

Figure 1.16 – Variation of lattice parameter of uranium dioxide single crystals due to alpha irradiation [34]. Weber experiments lead to the conclusion that the phenomenon saturates at 0.80%

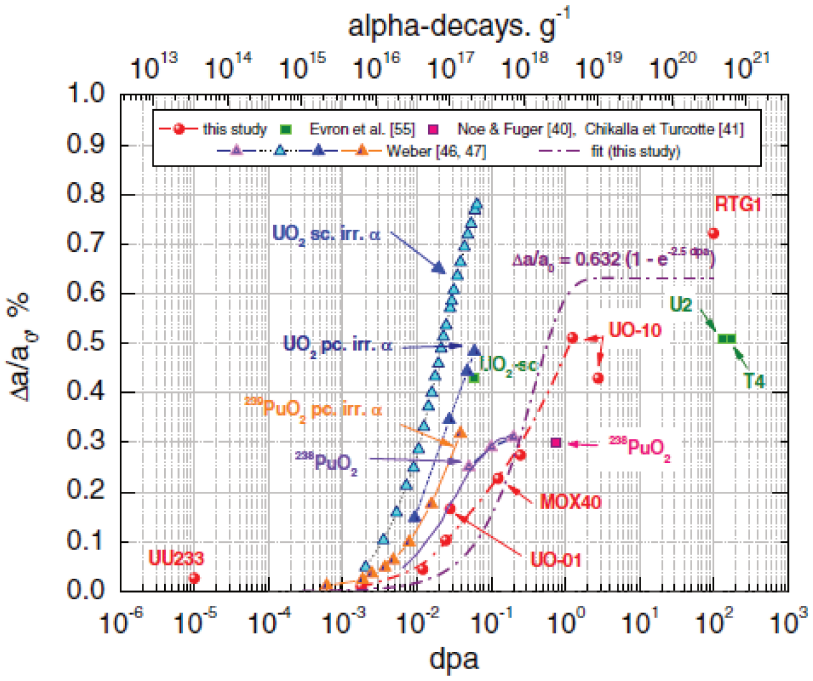

Figure 1.17 – Evolution of lattice parameter in actinides-doped UO_2, MOX and PuO_2, determined by Wiss et al. [35]

1.3.4 High burnup structure

In order to optimise the nuclear fuel usage, reducing costs, the life of the LWR fuels in reactor can be prolonged, with the consequent increase of the average burnup at the end of fuel life. Post irradiation examinations of uranium dioxide fuel with average burnup greater than 40-50 GWd $\cdot$ t^{-1}M detailed the formation of a porous and fine grained microstructure at the pellet periphery (rim), characterised by the original $\sim$ 10 μm grains subdivided into sub-micron grains (0.1-0.3 μm), a high concentration of micron-sized closed pores and an exponential increase of the local porosity which could reach values of about 20% [36]. Figure 1.18 compares the morphology of fresh uranium dioxide fuel and the characteristic high burnup structure at the periphery of an uranium dioxide pellet (local burnup $\sim$ 75 GWd $\cdot$ t^{-1}M).

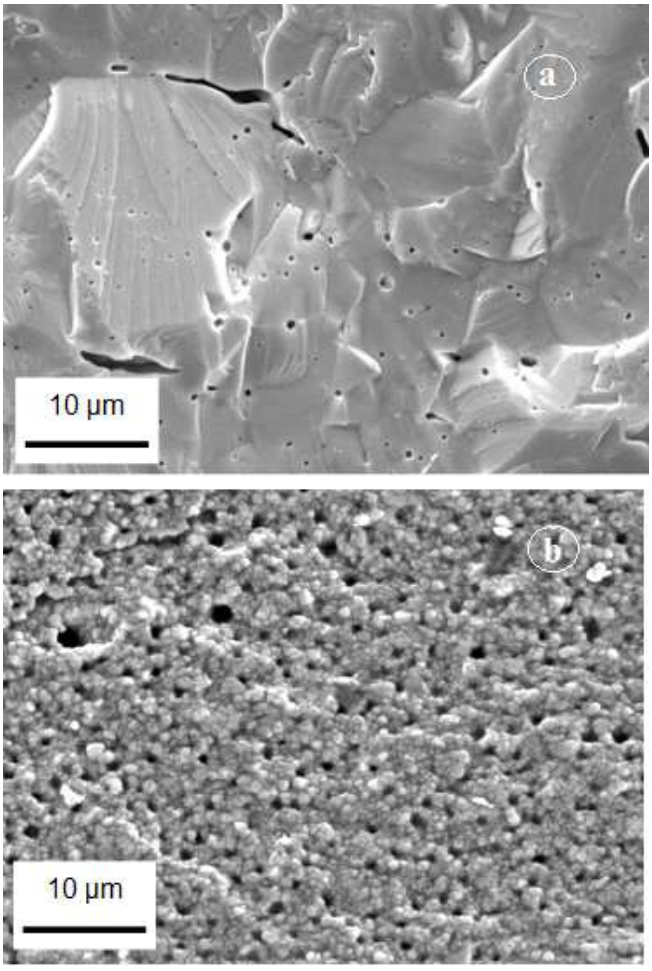

Figure 1.18 – Scanning Electron Microscopy micrographs: a) fresh uranium dioxide fuel of typical 10 μm sized grain b) irradiated uranium dioxide fuel with local burnup of about 75 GWd $\cdot$ t^{-1}M characterised by the high burnup structure [36]

The variation of the local porosity along the radius is depicted in Figure 1.19, for three different uranium dioxide pellets with respectively 40.3, 56.9 and 66.6 GWd $\cdot$ t^{-1}M average burnup. All of them are characterised by a steep increase of porosity at the rim ($r/r_0 \geq 0.9$), while higher porosities are observed for the pellets with higher average burnup. The rim or high burnup structure (HBS) is a consequence of the combined effect of the high local burnup and the relatively low temperature. In fact, the typical operating temperatures of the LWR fuels at the pellet rim are $\sim$ 600-800 K whereas $\sim$ 1300-1500 K are reached at the pellet centre. The high local burnup is caused by the epithermal neutron resonance absorption in ^{238}U nuclei at the rim of the UO_2 fuel pellet, which enriches this area in fissile plutonium determining higher local fission density. The local burnup at the rim of the pellet could be 2-3 times higher than the average burnup, depending on the flux spectrum in the reactor [37].

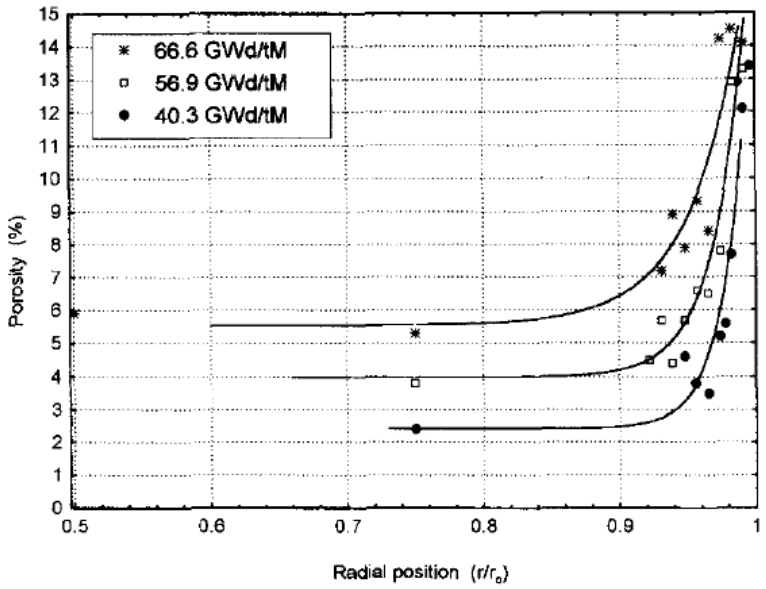

Figure 1.19 – Porosity radial profile of three irradiated fuels with increasing average burnup. The porosity increases exponentially at the rim of the pellet; the increase starts earlier for the pellet with highest average burnup which has, as well, the highest porosity [38].

Another characteristic of the rim zone is the depletion of xenon in the matrix that has been observed by electron probe microanalysis in different experimental campaigns [39–42]. The depletion of Xe in matrix at the pellet edge is shown in Figure 1.20: Walker and co-workers [42] measured the Xe-concentration along the radius of an uranium dioxide pellet with average burnup of 65 GWd $\cdot$ t^{-1}M using both secondary ion mass spectrometry (SIMS) and Electron probe microanalysis (EPMA). They observed a relocation of Xe in the pores and a depletion in the matrix in proximity of the pellet periphery. The rim region thickness in commercial

fuels increases with the burnup and can reach about 200 μm; adjacent to this fully restructured zone an intermediate region, not fully restructured, has been observed. The depth of this mixed region depends on the average burnup and might extend deeply into the pellet [43]. Several experimental campaigns were performed and specific programmes were established in order to study mechanisms and characteristics of the HBS (a review is availble in references [36] and [44]). With the purpose of determining the conditions of the rim structure formation as a function of burnup and temperature and to investigate physical and chemical properties of the HBS, the High Burnup Rim Project (HBRP) [45] [46] [47] was established. In the frame of this project, special irradiation discs of UO_2, enriched to 26 wt% in ^{235}U, were irradiated in the Halden reactor for 2.5 years, reaching very high burnup (about 100 $GWd \cdot t^{-1}M$), under controlled temperature conditions. The formation of the HBS poses questions on the impact of the restructuring on the fuel performance and safety; in particular, the fission gas behaviour, the mechanical interaction between fuel and cladding and the impact on the thermal conductivity are of interest. Figure 1.21 shows the Vickers microhardness (H_v) radial profile of three LWR UO_2 fuels with 40, 67 and 80 $GWd \cdot t^{-1}M$ average burnup as experimentally determined by Spino and co-workers [48]. The graph shows that along the pellet radius the hardness appears approximately constant, whereas at the rim the hardness reduces gradually toward the pellet edge. This implies that softening is caused by the high burnup structure. The rim softening guarantees, indeed, tolerable mechanical stresses on the cladding [36].

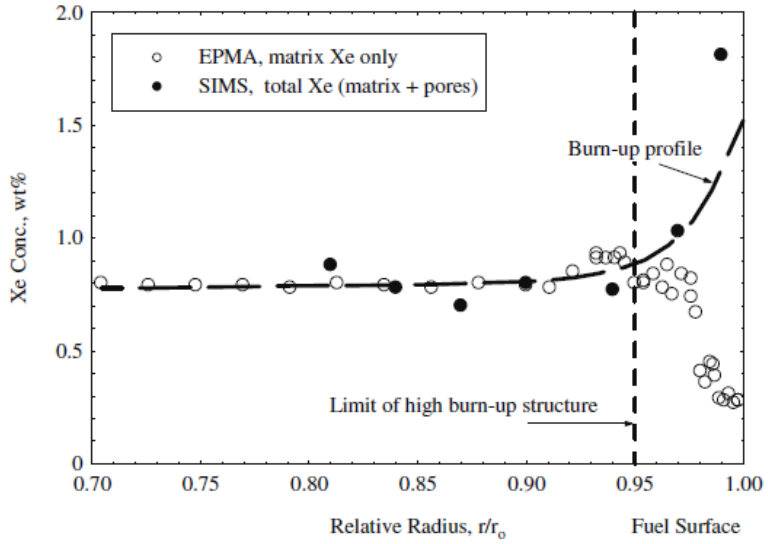

Figure 1.20 – Concentration of Xe along the radius of a UO_2 pellet with 65 $GWd \cdot t^{-1}M$ average burnup, from a commercial PWR. Black circles indicate the total Xe concentration as measured by SIMS both in the matrix and in the pores of the sample. White circles refer to the concentration of Xe measured in the matrix by EPMA. A progressive depletion of Xe in the matrix and enrichment in the pores at the rim of the pellet was observed [42].

During the last 20 years several models have been developed to explain formation and evolution of HBS: some of them considered recrystallisation as the main mechanism of formation of the HBS; others focused onto the polygonalisation mechanisms (subdivision of the original grain); different approaches were also used to individuate the driving force generating the new structure. A schematic summary of the HBS models are available in [36] and [49].

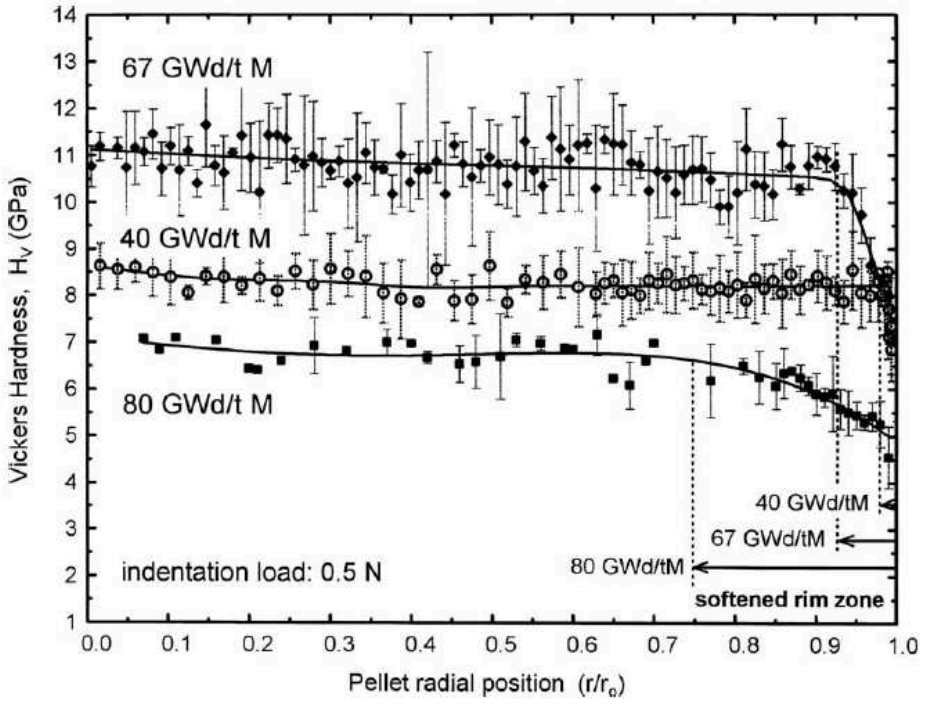

Figure 1.21 – Fuel Vickers hardness profile for fuels with different average burnup. The radial width of the softened region increases with the burnup increase [48].

1.4 Spent fuel

After several years of life in reactor, typically three, the nuclear fuel is removed from the core and becomes spent nuclear fuel (SNF). It is usually discharged and subsequently stored for several years under water to achieve thermal cooling and short-lived radionuclides decay. After the cooling period two different strategies are considered: reprocessing to extract reusable material (uranium and plutonium) or disposing as a waste. As of today, France, Russia, Japan, India and China reprocess most of their spent fuel, while the USA, Canada, Finland and Sweden have currently chosen direct disposal. Many countries have not yet decided their

strategy [50]. The nuclear waste disposal includes two different interim storage possibilities: wet storage in pools or dry storage in vaults and/or casks. Figure 1.22 shows the pool at the CLAB wet storage facility in Sweden and Figure 1.23 the casks of the dry repository of ZWILAG in Switzerland.

Figure 1.22 – Wet storage: CLAB pool for wet storage in Sweden [50].

Figure 1.23 – Dry storage: casks at the ZWILAG facility in Switzerland [51].

In pool storage facilities the presence of water must be permanent and its chemical composition must be monitored to avoid corrosion phenomena and radioactive leaks: normally, boric acid is flushed into the pool to capture neutrons emitted from the spent fuel and pH is mantained in the range 4.5-7; attention must be also paid to control the effects of radiolysis [52]. In dry storage, the spent fuel is locked within a container, which protects it and acts as a confinement barrier; therefore its resistance to degradation must be accurately studied [52]. Moreover, it is important to assess the behaviour of the fuel under the increasing pressure due to helium accumulation as a consequence of alpha-decay of the actinides.
To assess the geologic fuel repositories performance it is necessary to consider the radiotoxicity of the individual radionuclides, therefore its content, its activity and its spatial distribution in spent fuel must be studied. Uranium dioxide nuclear fuel contains, at the end of the irradiation, about 95 wt% of UO_2 and 1% of heavier actinides (Np, Pu, Am and Cm) and 4% of fission products. Due to the ingrowth of ^{239}Pu and ^{240}Pu during irradiation, plutonium is the heavy metal element with the second highest concentration in the SNF [53]. Because of the alpha decays taking place within the fuel, helium concentration increases with time determining gas pressure and lattice parameter increase [34] [35] which are responsible for the spent nuclear fuel swelling. The properties of the spent fuel subjected to alpha autoirradiation may vary, including stress increase due to the fuel swelling and will depend on the defects recombination or evolution into extended defects.

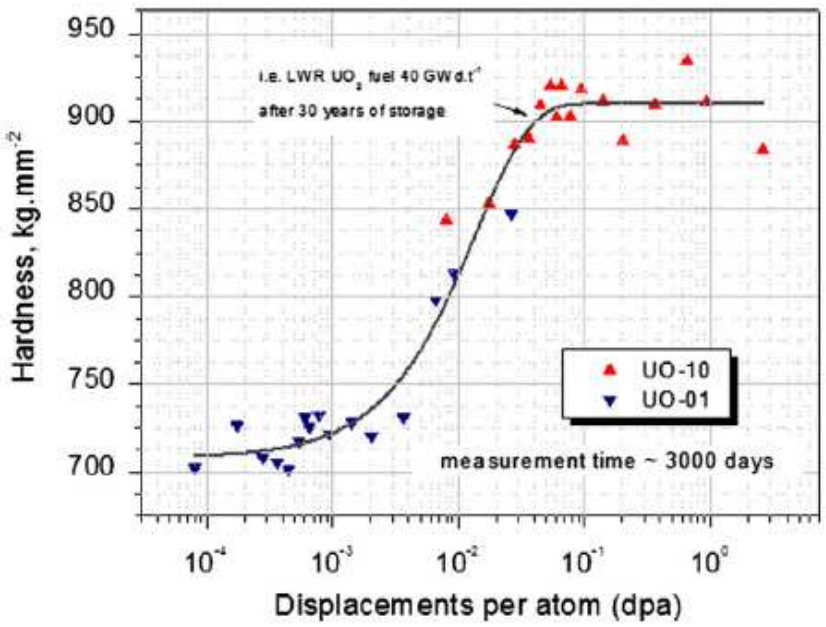

Figure 1.24 – Hardness variation of ^{238}Pu-doped uranium dioxide samples, as a function of the displacements per atom (dpa) resulting from cumulated alpha-decay.

In addition to lattice parameter variation due to alpha decay, Wiss et al. [35] have studied microhardness evolution of the spent fuel by using UO_2 samples doped with strong alpha-emitters (e.g.^{238}Pu) and they have observed an increase of the doped uranium dioxide hardness up to $\sim 4 \cdot 10^{-2}$ dpa followed by a saturation for further increasing values of cumulated alpha-damage (Figure 1.24).
The increase of the average fuel burnup corresponds to higher decay heat and specific activity at the discharge; the high burnup nuclear fuel mechanical properties tend to be more degraded, which makes the spent fuel management even more challenging [54]. In this scenario, the determination of the aging effects affecting the spent fuel assumes a primary role in the prediction of the behaviour of the spent fuel during handling, transport before and after long-term storage. The conditions of the spent fuel after few years of storage are not representative of the state of aged fuel after thousands of years; consideration must be performed based on a geological time scale[4].
Figure1.25 shows the alpha activity trend during 10 000 years after the discharge of uranium dioxide PWR fuel with 70 GWd $\cdot$ t^{-1}M average burnup and initial enrichment of 3.8% ^{235}U, calculated with webKORIGEN code [55] and Decay Engine++ tool of Nucleonica [56][5]. The alpha activity of ^{244}Cm and ^{243}Cm contributes up to 1000 years, while the alpha activity of to ^{241}Am increases in the first 100 years due to the beta-decay of ^{241}Pu ($t_{1/2}$ = 14.325 years [57]). The rest of radionulides considered continue contributing to the damage for a longer time.
The integrated damage produced by auto-irradiation of high burnup PWR commercial fuels (3.5% ^{235}U), during a 10 000 years of storage is illustrated in Figure 1.26, where the dpa produced by the alpha-decays in a spent uranium dioxide fuel with average burnup of 45 GWd $\cdot$ t^{-1}M are compared with those produced by a fuel with the same characterists but higher burnup (100 GWd $\cdot$ t^{-1}M) with the aid of SRIM[6] code [16]. After 10 000 years, the lower burnup fuel accumulates approximately 3 dpa, while the higher burnup about 8 dpa.
Auto-irradiation and the consequent helium build-up in SNF increase the pressure and enhance the fuel cladding degradation and radiation-induced embrittlement phenomena. Fuel pellets fracturing or cladding failure make the repackaging and transportation of the fuel to a final disposal site, challenging operations.

[4]The possible nececessity to retrieve spent fuel implies the necessity to study time scales ranging from few centuries to million of years

[5]WebKORIGEN allows the determination of the radionuclides inventory of the irradiated fuel. Decay Engine++ tool enables the determination of different parameters at the time of examination, e.g. the alpha-particles accumulated.

[6]SRIM code calculates the interaction of ions with matter and among the available outputs is the number of displacements per ion.

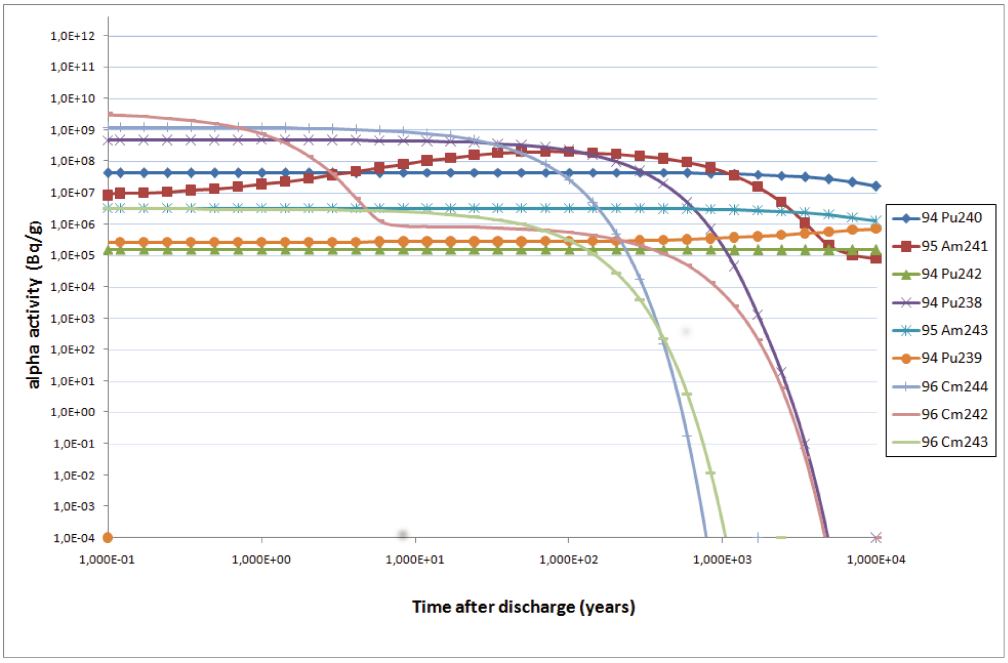

Figure 1.25 – Specific alpha activity for a UO_2 fuel with 70 $GWd \cdot t^{-1}M$ average burnup and initial enrichment of 3.8% of ^{235}U calculated with webKORIGEN code [55] and Decay Engine++ tool of Nucleonica [56].

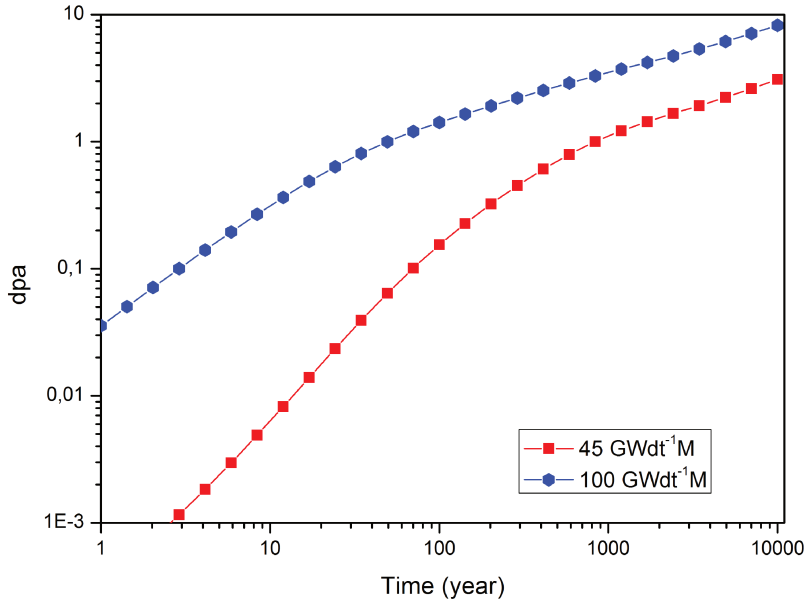

Figure 1.26 – Displacements per atom produced in UO_2 fuels with 45 $GWd \cdot t^{-1}M$ (red curve) and 100 $GWd \cdot t^{-1}M$ (blue curve) average burnup and initial enrichment of 3.5% of ^{235}U calculated with webKORIGEN code [55], Decay Engine++ tool of NUCLEONICA [56] and SRIM [16].

1.5 Severely degraded Fuels

1.5.1 Safety in Light Water Reactors

The principal safety aim in Nuclear Power Plants (NPPs) is to ensure that the nuclear facilities will not cause hazard or increase the population health risks by release of radionuclides into the environment. All the events deviating from the NPPs normal operation conditions are classified on the basis of the International Nuclear and Radiological Event Scale (INES scale), which was introduced in the 1990 by IAEA and OECD Nuclear Energy Agency (OECD/NEA). The events (Figure 1.27) are grouped into seven categories, four of them (4-7) are indicated as accident. The accident at the Chernobyl nuclear power plant (1986) has been classified at Level 7 of the INES scale, because of the large impact on people and environment while the 1979 accident at the Three Mile Island nuclear power plant is rated at Level 5 on INES. An accident causing a single human death is classified at level 4 [58]. The Fukushima accident was initially classified as accident level 4, but it was successively upgraded to 7, even though the aerea of the Chernobyl radioactivity release was much larger than that for the Fukushima.

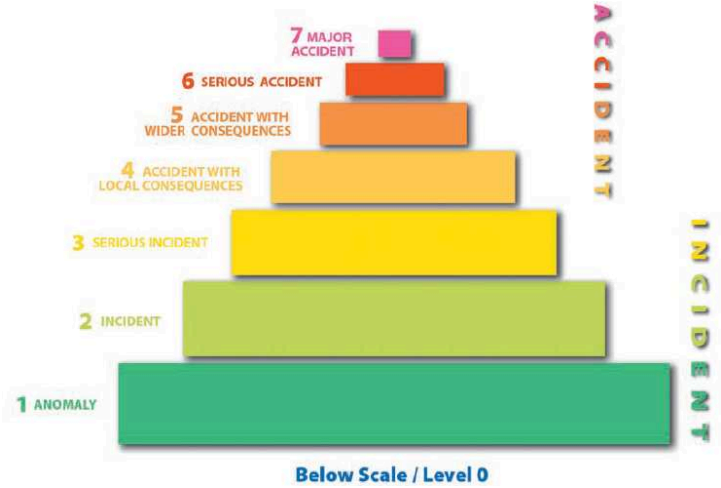

Figure 1.27 – International Nuclear and Radiological Event Scale (INES scale) [58]

One of the design basis accidents (DBA) for water cooled reactors is the loss of coolant accident (LOCA) caused by the failure of a large coolant pipe. The large LOCA causes a removal of water from the primary system resulting in a very fast uncovering of the reactor core, which must be recovered at very high rate, in order to fill the vessel and submerge the core of the reactor. This recovery operation

must be fast as a temperature increase above the threshold for exothermic Zircaloy steam oxidation reaction must be avoided, to prevent cladding and fuel melting which would cause a severe nuclear accident.
During a severe nuclear accident in a LWR, the materials constituting the reactor core are subjected to oxidation which in the case of Zircaloy produces heat. The behaviour of the core under heating depends on its configuration and composition, i.e. it would depend on the melting temperature of each single constituent material, but the chemical reactions occurring in the core might cause a lower melting temperature, because of the production of eutectics, especially between Zircaloy cladding and stainless steel components (e.g. Fe, Ni), which lead to liquefaction of components. In case of Zircaloy cladding, the presence of steam enables the Zircaloy oxidation and the exponential increase of the Zircaloy oxidation rate (with hydrogen release). This is responsible for a further temperature increase, above the Zircaloy melting point (2100 K) [59]. The total amount of oxidation energy added to the core can be mitigated e.g. by the availability of steam in the core and by the diffusion rate of oxygen through zirconium dioxide to the metallic Zircaloy. The ZrO_2 layer reduces the diffusion rate at constant temperature, but its protective role is practically completed disabled by the sharp temperature increase which leads to a complete cladding oxidation. The material produced after the core meltdown has been termed *corium*; its composition depends strongly on the type of reactor, its design, the fuel used and the accident dynamics.
Different international experimental programmes were started in the past and are still ongoing, in order to simulate accidental conditions and to investigate behaviour of corium during the accident, or simply to characterise its physical, chemical and mechanical properties. For the sake of brevity we mention only those that have been considered in the framework of this work: Phébus PF project [60] and FARO [61]. The purpose of Phébus PF project was to study fission products release and behaviour from irradiated uranium dioxide fuel in a PWR bundle under typical loss of coolant accident conditions [60]. The FARO LWR research programme was launched in JRC Ispra at the beginning of the 1990s with the purpose of obtaining data on the effect of mixing and quenching in water of large masses of corium [62]. It consisted of twelve experiments and the composition of the corium is, with the exception of L-11 experiment, 80 wt% UO_2 - 20 wt% ZrO_2. Corium from the experiments L-19 and L-24 was shipped to the Joint Research Centre Karlsruhe for characterization of the material before and after the interaction with water, with the aim to understand the possible mechanisms responsible for hydrogen production [61]
In the following paragraphs severe accidents occured around the world are briefly described.

1.5.2 Severe accidents

Three Mile Island unit-2 accident

The first nuclear core melt down accident occurred in the second unit of the Three Mile Island (TMI-2) NPP in 1979. The accident was generated by the loss of feed water to the steam generators, which caused a temperature increase and volume expansion of the primary water. Water, successively, flowed into the pressurizer and the pressure in the primary system [63] increased. The subsequent actions taken by the operators, combined with equipments failure, caused consistent loss and boil-off of water in the vessel and the uncovering of the reactor core within 130 minutes from the beginning of the accident [64]. The absence of heat removal caused the exothermic reaction steam-cladding with consequent core melting. Figure 1.28 shows the configuration of the TMI-2 reactor after the accident: about 62 tons of melted material was formed, a cavity remained at the top part of the core below which 37 tons of melted material covered by a uniform crust were placed [65].

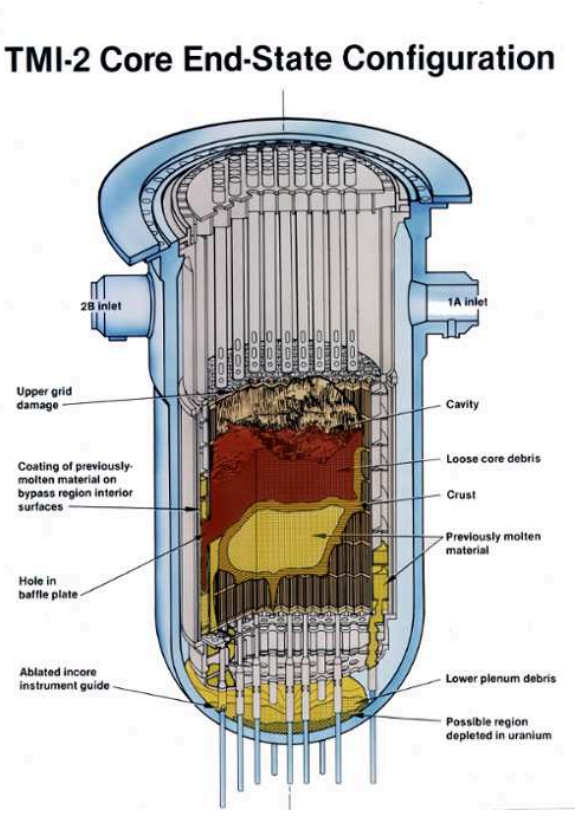

Figure 1.28 – Post-accident condition of the TMI-unit 2 reactor core. The yellow central part constitutes the melted core, whilst in gold is represented the fused crust. The red upper part depicts the loose debris [66]

Samples were extracted from the damaged reactor at Three Mile Island and characterised in the framework of a collaboration organised by OECD-NEA, managed by Idaho National Laboratory and which involved many European institutes. The samples belonging to the molten core and examined by the Institute for Transuranium Elements (ITU), now Joint Research Centre Karlsruhe, were found to be dense ceramic of almost equi-molar composition (U,Zr)O_2 for the main phase with Fe-rich secondary phases originating from the stainless steel constituents of the reactor [60]. The crust samples showed that the crust zone experienced temperatures ≤ 1773 K, as the steel and other structural materials did not melt completely. Metallic nodules with selectively oxidised Ni at the outer surface were also observed. Many uranium dioxide fuel pieces were found in the debris; moreover further investigations of the debris samples demonstrated that stainless steel reacted with the Zircaloy cladding, forming almost equi-molar compositions [60].

The Chernobyl accident

The accident at the 4th Unit of Chernobyl Nuclear Power Plant on 26 April 1986 caused the explosion with subsequent destruction of the reactor core with release of an enormous amount of solid and gaseous fission products in the environment. The four Chernobyl reactors were water cooled reactors of the Soviet RBMK design which employed slightly enriched uranium (2% ^{235}U) as fuel and a combination of graphite moderator and boiling water. The RBMK core is larger than the typical LWR core, because of the presence of graphite characterised by much higher diffusion and slowing down length for neutrons [64]. Another fundamental difference with western LWRs are the positive reactivity feedback and its instability behaviour at low power levels. When the water density decreases e.g. because of the boiling of the water coolant, the LWR experiences a large negative reactivity due to the fact that water itself constitutes the moderator, whereas for the RBMK this phenomenon does not occur. The RBMK reactor is also characterised by unstable operation at low power which forbids operations at power levels below the 20% of full power. On April the 25$^{\text{th}}$, 1986 it was decided to test the capability of the spinning turbine to provide enough electrical power to operate different parts in the power plant. After having reduced the power of 50%, as planned, the power continued to decrease until, because of a human error, it dropped to 30 MW (th). This in turn determined the filling of the core by water and Xe buildup, precluding de facto the planned test power. Other actions taken by the operator let the power increase, at first slowly, then faster and induced the operator to extract the emergency rods. This action was evidently taken too late as within few seconds the power was 100 times the full power. The reactor 4 was, then, suddenly destroyed. During this accident the uranium dioxide fuel interacted firstly with the Zircaloy cladding and subsequently with steel, serpentinite and concrete of the structure

incorporating also sand which determined the formation of the so-called lava like fuel containing materials (LFCM) or Chernobyl "lava". Chernobyl lava may be grouped into five categories [67]:

- Brown lava. This is a brown glassy material, containing many small metal spheres and pores.
- Black lava. Mass of coal-black colour characterised by high porosity.
- Slag or slag like granulated LFCM. This is a kind of ceramic solidified mass covered with glassy crust. Its colour is alternatively gray-magenta or dark-brown. This material is the result of the interaction between brown ceramic and water.
- Pumice. This type of LFCM is characterised by friable pieces, coming from the pressure suppression pool and was generated during the contact of hot lava with water.
- Melted and solidified metal

The Chernobyl lava flowed down to the reactor block basement and within few days after the accident, reached other rooms at lower levels of the reactor building. Samples of the Chernobyl lava were extracted from the reactor building [68]. Figure 1.29 shows the aspect of the solidified lava.

Figure 1.29 – : Solidified LFCM flowing out of the 4th steam-distribution valve in Room number 210/7.

The Fukushima accident

On March 11th, 2011 the east coast of Japan was subjected to an earthquake with magnitude 9.0, which caused an enormous tsunami. The earthquake damaged

the electric power supply lines to the Fukushima Daiichi nuclear power plant and the consecutive tsunami reached the two diesel engines which supply electrical power in case of emergency. The consequence was a loss of off-site and on-site electrical power, hence a loss of the cooling function at the three operating reactor units (Units 1,2 and 3) and at the spent fuel pools. Unfortunately all the security measures taken were not sufficient to avoid the accident: Units 1-3 overheated, the nuclear fuel melted and the hydrogen produced triggered explosions in the reactor buildings in Units 1,3 and partly 4 [69].

1.5.3 Decomissioning

Decommissioning and site remediation are important goals that must be achieved for the nuclear power plants after a severe accident. They enable the possibility to recover the affected areas guaranteeing a safe life to people living in proximity, but are not straightforward tasks. If the decommissioning of an undamaged nuclear power plant is planned, a series of actions is taken to ensure the safely removal of the fuel; moreover the status of any contamination is well known and documented. Post-accident decommissioning presents a completely different set of circumstances: the condition of the facility, fuel and equipment is unknown and determining the roadmap to face all these uncertain conditions requires long time and often development of new technology.
At the time of writing, none of the three power plants affected by the nuclear accident have been decommissioned: at the Three Mile Island site, the undamaged Unit 1 will be decommissioned within the next 20 years. The plan is to dismantle and completly remediate TMI-2 at the same time. Chernobyl Unit 4 is at the moment in a condition of safe storage and the plan is to complete its decommissioning for 2050. To establish the exact preconditions for the Fukushima Daiichi NPP decommissioning is not possible now, but the plan is to start with the fuel debris removal and perform an analysis to ensure safe storage and final decommissioning [69].
At Three Mile Island the defueling was achieved thanks to a core boring system whose functioning properties depend on the fuel debris mechanical properties, hence hardness and elastic modulus are extremely important in determining the performance of the boring machine. For this purpose, different research activities are on-going to evaluate compositions, phases, densities, microstructures, mechanical and thermal properties of corium. To accomplish the Fukushima Daiichi debris fuel removal the experience of the TMI-2 is fundamental, as there are similarities between the two accidents; however, there are also important differences [69]:

- The Fukushima reactors are BWR whereas the Three Mile Island reactor is

a PWR.

- The progression of the accident is different: the corium was released from the pressure vessel in Fukushima whereas it remained "in-vessel" in TMI.
- In Fukushima seawater was used in the reactors' pressure vessels as a cooler trying to avoid a complete reactors' meltdown.

The unicity of the conditions in each nuclear accident makes the decommissioning of these three NPPs a big challenge.

1.6 Conclusion

This first chapter introduces the main phenomena affecting nuclear fuel, which are object of study in the present research work. The focus is on the period of irradiation in reactor, the back end of the nuclear fuel cycle and the nuclear fuel conditions consequent to a nuclear accident. In case of normal irradiation, the determination of the fuel mechanical properties is critical for the evaluation of the fuel performance in reactor and to ensure the safety during the in-pile operations. Determination of the mechanical properties is also fundamental to guarantee a safe removal from the core of reactor and its safe management and disposal in a repository. The long term behaviour of the spent fuel can be estimated only by knowing its physical, chemical and mechanical properties based on measurements addressing geological time scale effects.
In case of nuclear accidents a challenging objective is that of restoring the pre-accident conditions and decommission the destroyed nuclear power plants. The first step is the recovery of the fuel debris which requires specific tools whose performance depends on the corium mechanical properties. The above-mentioned considerations highlight the relevance of studying the variation of the LWR nuclear fuel elastic properties during normal operations, storage, and under accidental conditions. This is the scope of the present work.

Chapter 2

Mechanical and thermal properties

Contents

2.1 Introduction

Chapter 2 provides the essential theoretical background to understand physical phenomena used to determine irradiated nuclear fuels and severly degraded fuels properties, investigated in the experimental part of thesis. Material's properties influence propagation behaviour of stress waves in matter e.g. in terms of velocity or amplitude. The determination of stress waves propagation velocity allows inferring material's elastic properties.
Chapter 2 gives an overview on the theory of elasticity and relations between elastic properties and stress waves propagation velocities, then introduces the theoretical

derivation of surface waves and their mathematical correlations with stress waves and material's elastic properties.
In conclusion, an overview of the theory connecting thermal and stress waves propagation velocities is given.

2.2 Theory of Elasticity

A force applied to a solid body produces a variation in its volume and shape, hence a displacement of its points from the original position. If we define $\mathbf{r}$ the position of a generic point in the body (with components x_i; i=1,2,3) and with $\mathbf{r}'$ its position after the deformation, the displacement is given by the displacement vector $\mathbf{u}$ [70]

$$\mathbf{u} = \mathbf{r} - \mathbf{r}' \tag{2.1}$$

The displacement vector components u_i are function of the coordinates x_i. If dl is the distance between two points prior to the deformation ($dl = \sqrt{dx_1^2 + dx_2^2 + dx_3^2} = \sqrt{d}x_i^2$), the distance after the deformation becomes dl', where $dl'^2 = (dx_i + du_i)^2$. Considering that $du_i = (\partial u_i/\partial x_k)dx_k$, dl'^2 can be expressed [70]

$$dl'^2 = dl^2 + 2u_{ik}dx_i dx_k \tag{2.2}$$

The term u_{ik} is the symmetrical strain tensor which is defined as:

$$u_{ik} = \frac{1}{2}\Big(\frac{\partial u_i}{\partial x_k} + \frac{\partial u_k}{\partial x_i} + \frac{\partial u_l}{\partial x_k}\frac{\partial u_l}{\partial x_i}\Big) \tag{2.3}$$

If $\frac{\partial u_i}{\partial x_k} << 1$, the quadratic term in 2.3 can be neglected and the strain tensor can be approximated by the infinitesimal strain tensor ε_{ik}:

$$u_{ik} \approx \varepsilon_{ik} = \frac{1}{2}\Big(\frac{\partial u_i}{\partial x_k} + \frac{\partial u_k}{\partial x_i}\Big) \tag{2.4}$$

When a force is applied to a solid body, internal forces are generated which tend to restore the original thermal and mechanical equilibrium state. These internal stresses, produced by the interaction among molecules, are determined by short range forces. The total force acting on one part of the body is the sum of the forces acting in all the related volume elements, then [70]:

$$\int F_i dV = \int \frac{\partial \sigma_{ik}}{\partial x_k} dV = \oint \sigma_{ik} df_k \tag{2.5}$$

df_i are the components of the surface element vector d**f** directed along the normal, σ_{ik} represents the stress tensor; indexes i and k define the direction of the normal to the plane subjected to the stress component and the direction of the stress component, respectively. The stress tensor likewise the strain tensor, is symmetric, hence $\sigma_{ik} = \sigma_{ki}$ [70].
The general form of the Hooke's law expresses each component of the elastic strain tensor as a linear combination of each component of the stress tensor [71]:

$$u_{ik} = s_{ikjl}\sigma_{jl} \quad i,k = 1,2,3 \tag{2.6}$$

s_{ikjl} are the elastic compliances in tensor notation. Conversely the stress tensor can be expressed as

$$\sigma_{ik} = c_{ikjl}\varepsilon_{jl} \tag{2.7}$$

c_{ikjl} are the elastic stiffness constants in tensor notation. Elastic compliances and stiffness constants are symmetric and this makes possible to pass from the tensor to the matrix notation, by substituting each pair of indices [71]:

tensor notation indices	11 22 33	23 32	13 31	12 21
matrix notation	1 2 3	4	5	6

If we consider isotropic, elastic media, the coefficients must be independent of the coordinate system chosen. Following this consideration an additional simplification can be introduced as [71]: $c_{12} = c_{13} = c_{23}$, $c_{44} = c_{55} = c_{66}$, $c_{11} = c_{22} = c_{33}$ and the rest of the coefficient are zero. In addition $c_{12} = c_{13} = c_{23} = \mu$ $c_{44} = c_{55} = c_{66} = \lambda$, then [71]:

$$c_{11} + c_{22} + c_{33} = \lambda + 2\mu \tag{2.8}$$

λ and μ are called Lamé's elastic constants; they define the elastic properties of an isotropic solid. In terms of Lamé's elastic constants Hooke's law can be rewritten as:

$$\sigma_{ij} = \lambda\delta_{ij}u_{kk} + 2\mu u_{ij} \tag{2.9}$$

where δ_{ij} represents the Kronecker delta[1].
Hooke's law can also be expressed in terms of Young's modulus of elasticity E; in particular if we consider an isotropic elastic body subjected to a stress σ_{zz}, the strain components are [21]:

$$u_{zz} = \frac{\sigma_{zz}}{E} \tag{2.10}$$

[1] $\delta_{ij} \begin{cases} 0, & \text{if } i \neq j \\ 1, & \text{if } i = j \end{cases}$

$$u_{xx} = -\nu u_{zz} = -\nu \frac{\sigma_{zz}}{E} \tag{2.11}$$

$$u_{yy} = -\nu u_{zz} = -\nu \frac{\sigma_{zz}}{E} \tag{2.12}$$

The term ν in 2.11 and 2.12 represents Poisson's ratio which defines the ratio of the transverse deformation to the longitudinal extension: $\nu = -u_{xx}/u_{zz}$. Poisson's ratio can assume values between -1 and 0.5, even though the most common materials have positive Poisson's ratios. Negative Poisson's ratio values are characteristic of the auxetics materials, which display a dilatation in the perpendicular direction of the applied tension if stretched.
Young's modulus is related to Lamé's parameter μ[2] and Poisson's ratio by [72]:

$$E = 2\mu(1 + \nu) \tag{2.13}$$

Another important elastic modulus is the bulk modulus K:

$$K = -V\partial P/\partial V \tag{2.14}$$

which is related to Poisson's ratio and Young's modulus by:

$$K = \frac{E}{3(1 - 2\nu)} \tag{2.15}$$

The negative sign in 2.14 indicates that a preassure increase determines a volume decrease. The Poisson's ratio expressed in terms of the Lamé's parameters is [72]:

$$\nu = \frac{\lambda}{2(\lambda + \mu)} \tag{2.16}$$

In an infinite isotropic elastic material two types of waves propagate: longitudinal and transverse waves. In the first case the particles are displaced in the same direction of waves motion whilst for transverse waves, particles displacement is normal to the propagation direction [73].
As the heat exchange during a time interval comparable to the period of oscillatory motion is negligible, then any parts of the body subjected to a deformation can be assumed to be insulated and the motion to be adiabatic [70]. By combining the internal stress force with the density and the acceleration, the equation of motion can be obtained [71]

$$\frac{\partial \sigma_{ij}}{\partial x_j} = \rho \ddot{u}_i \tag{2.17}$$

[2]The Lamé's parameter μ is often called Shear modulus and it is indicated with G

and Hooke's law becomes:

$$\sigma_{ij} = \mu\Big(\frac{\partial u_i}{\partial x_j} + \frac{\partial u_j}{\partial x_i}\Big) + \lambda\delta_{ij}\frac{\partial u_k}{\partial x_k} \tag{2.18}$$

Considering that for an isotropic solid $u_{ij} = \frac{1}{2}\Big(\frac{\partial u_i}{\partial x_j} + \frac{\partial u_j}{\partial x_i}\Big)$. Hence:

$$\Big(\frac{\partial \sigma_{ij}}{\partial x_j}\Big) = \mu\nabla^2 u_i + (\lambda+\mu)\frac{\partial(\nabla\cdot\mathbf{u})}{\partial x_i} = \rho\ddot{u}_i \tag{2.19}$$

The displacement can be expressed as sum of the gradient of a scalar ($\nabla\varphi$) and the curl of a vector function ($\nabla\times\mathbf{A}$). In case of pure longitudinal waves the second term is zero, then using the vector form and considering that $\nabla^2\mathbf{u} = \nabla\nabla\cdot\mathbf{u} - \nabla\times\nabla\times\mathbf{u}$, the equation of motion is [71]:

$$(\lambda+2\mu)\nabla^2\mathbf{u} = \rho\frac{\partial^2\mathbf{u}}{\partial t^2} \tag{2.20}$$

Hence, removing the gradient operator, the d'Alembert equation describing the wave propagation is:

$$\nabla^2\varphi = \Big(\frac{\rho}{\lambda+2\mu}\Big)\frac{\partial^2\varphi}{\partial t^2} \tag{2.21}$$

where $v_l = \Big(\frac{\lambda+2\mu}{\rho}\Big)^{1/2}$ is the longitudinal wave velocity. In case of pure transverse waves, the equation of motion is :

$$\nabla^2\mathbf{A} = \frac{\rho}{\mu}\Big(\frac{\partial^2\mathbf{A}}{\partial t^2}\Big) \tag{2.22}$$

where $v_t = \sqrt{\frac{\rho}{\mu}}$ with $\mathrm{v_t}$ transverse wave velocity.

In terms of the longitudinal and transverse velocities the relations 2.13 and 2.16 can be rewritten as:

$$E = \rho v_t^2\frac{3v_l^2 - 4v_t^2}{v_l^2 - v_t^2} \tag{2.23}$$

and

$$\nu = \frac{v_l^2 - 2v_t^2}{2(v_l^2 - v_t^2)} \tag{2.24}$$

2.3 Rayleigh waves

The theoretical existence of waves propagating near the free boundary of an elastic half-space was demonstrated in 1885 by Lord Rayleigh. Rayleigh waves are originated by the overlapping of longitudinal and transverse waves, travelling along the half-space with common phase velocity v_R [74]. If we consider a plane harmonic Rayleigh wave propagating along the boundary between a perfectly elastic, isotropic solid and vacuum, setting $x = v_R/v_t$ the following sextic equation, known as Rayleigh equation, can be written [75]:

$$\left(\frac{v_R}{v_t}\right)^6 - 8\left(\frac{v_R}{v_t}\right)^4 + 8\left(3 - 2\left(\frac{v_t}{v_l}\right)^2\right)\left(\frac{v_R}{v_t}\right)^2 - 16\left(1 - \left(\frac{v_t}{v_l}\right)^2\right) = 0 \qquad (2.25)$$

For any values of ν corresponding to the more common media ($0 < \nu < 0.5$) only one positive and real solution of equation 2.25 is the Rayleigh velocity v_R. The approximate solution given by Viktorov [75] is:

$$v_R = v_t \frac{0.87 + 1.12\nu}{1 + \nu} \qquad (2.26)$$

In the homogeneous half-space Rayleigh waves are non-dispersive and for values of Poisson's ratio in the abovementioned range, the Rayleigh waves velocity is between 0.87 v_t and 0.96 v_t.
Figure 2.1 shows the elliptical and retrograde movement of the solid particles due to the Rayleigh wave propagation on the surface of the solid. Figure 2.2 displays the dependence of the Rayleigh waves velocity amplitude on the penetration depth. From the figure appears clear how the normal component to the surface increases at the beginning but it decreases monotonically with depth, while the parallel component changes sign at depth $\sim 0.2\lambda_R$. After one wavelength the amplitudes are reduced of about the 80% of their maximum values.

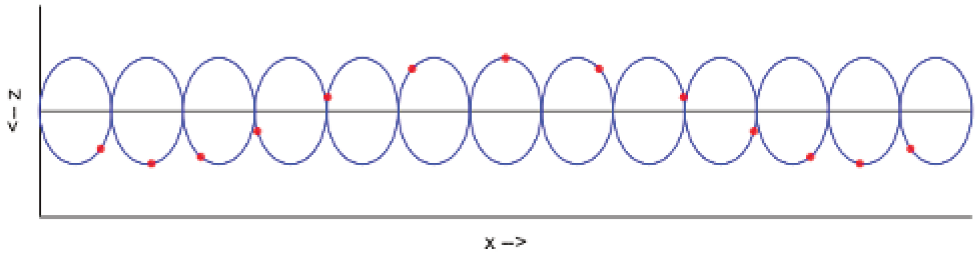

Figure 2.1 – Ellipsoidal movement of the particles due to the Raylegh wave propagation on x direction on the surface of the solid [76] simulated with GNU Octave 4.0

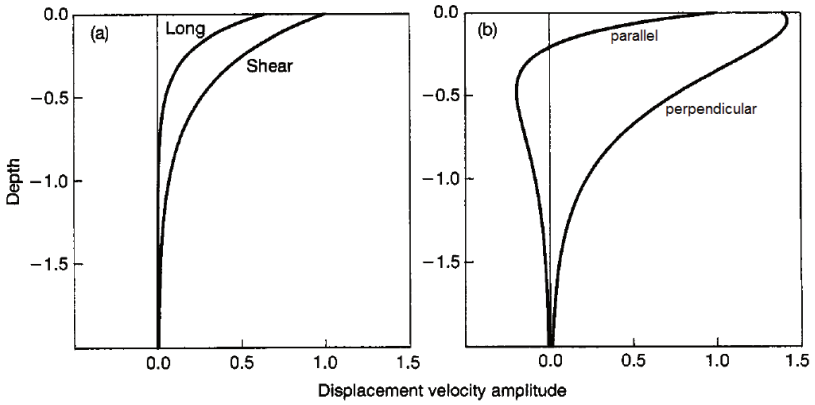

Figure 2.2 – Rayleigh wave components and displacement velocity components, in fused silica, as a function of depth (measured in units of Rayleigh wavelegths: $\lambda_R = v_R/f$, f = frequency) (a) longitudinal and shear components of the Rayleigh wave (b) displacement velocity components parallel and perpendicular to the surface. [74]

2.4 Young's modulus, Rayleigh wave velocity and Poisson's ratio

To calculate Young's modulus of materials by means of relation 2.23, at least two velocities must be known (out of longitudinal velocity, transverse velocity, Rayleigh velocity).
Laux [77] observed that if the Poisson's ratio of the material is known, Young's modulus can be calculated solely by means of the Rayleigh wave velocity [77] [78] thanks to [77]:

$$E = \frac{\rho v_R^2 (\nu + 1)^3}{2(0.56\nu + 0.435)^2} \tag{2.27}$$

which considers equation 2.26.
A linearity between Poisson's ratio and the parameter F(ν) with

$$F(\nu) = \frac{E}{\rho v_R^2} \tag{2.28}$$

was observed experimentally by Bayón et al. in [79]. Malischewsky and Tuan in [80] demonstrated that this linearity depends upon the mathematical form of the Rayleigh wave velocity and the Poisson's ratio; F(ν) can be derived by using an approximation of the Rayleigh wave velocity (Malischewsky's formula [81]) and in particular expressing:

$$\eta = \left(\frac{v_R}{v_t}\right)^2 \tag{2.29}$$

and

$$E = 2\rho(1+\nu)v_t^2 = \frac{2\rho(1+\nu)v_R^2}{\eta} \tag{2.30}$$

$$\zeta = \left(\frac{v_t}{v_l}\right)^2 = \frac{(1-2\nu)}{2(1-\nu)} \tag{2.31}$$

where η is:

$$\eta = \frac{2}{3}\left(4 - \sqrt[3]{h_3(\zeta)} + \frac{2(1-6\zeta)}{h_3(\zeta)}\right) \tag{2.32}$$

and, using the same notation as in [80]:

$$h_3(\zeta) = 17 - 45\zeta + h_1(\zeta) \tag{2.33}$$

$$h_1(\zeta) = 3\sqrt{33 - 186\zeta + 321\zeta^2 - 192\zeta^3} \tag{2.34}$$

By expanding in the interval $\nu \in [-1, 0.5]$ and by using relations 2.32-2.34, the function F =F(ν) can be obtained.
F(ν) is plotted in Figure 2.3: in the range of negative Poisson's ratio (auxetic materials), F is not a linear function of ν, but in the positive range (the majority of materials, including nuclear fuel), the relation is linear and is approximated by:

$$F(\nu) = 2.61803 + 1.3384\nu \tag{2.35}$$

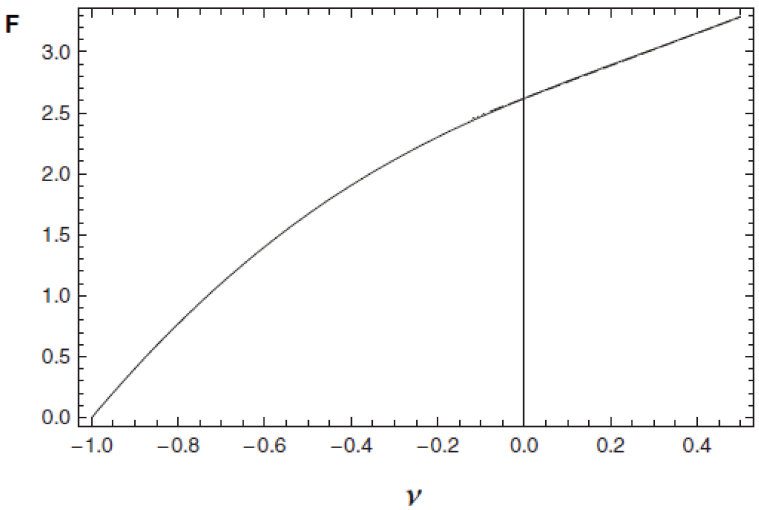

Figure 2.3 – Relation between the parameter F and the Poisson's ratio. In the positive range of Poisson's ratios, F can be approximated by a straight line [80].

Hence, if ν is $\sim$ 0.3 as for uranium dioxide, F(ν)=3.02 which agrees with

relation 2.27 ($E = 3.02\rho v_R^2$, if ν =0.3).

2.5 Plastic behaviour and hardness

Mechanical behaviour of solids is generally defined accordingly to their capability to deform reversibly, permanently or to fail under the application of a stress.
Elastic deformation is characterised by complete and instantaneous recovery of strain following the stress removal. If the stress applied to an elastic solid overcomes the rupture strength, the material is subjected to failure; for ceramics under uniform stress or near room temperature, this failure is often sudden and complete (brittle behaviour) [21]. Some materials experience a permanent deformation when a stress is applied, i.e. upon stress removal the deformation remains. In this case the material displays a plastic behaviour.
A measure of material's resistance to plastic deformations is given by the hardness, usually determined by indentation tests in which a load P is applied which causes a permanent deformation on the material. The shape of the deformation depends on the type of indenter used. In particular, generically the hardness number is defined as [82]

$$H = \frac{P}{A} \tag{2.36}$$

with A being the true area of contact for the Vickers indenter (pyramidal square based) or the projected area for Knoop indentation (rhomboid base). Figure 2.4 gives an example of Vickers indenter's imprint on the rim zone of a 67 GWd $\cdot$ t^{-1}M LWR fuel (Spino et al. [48]).

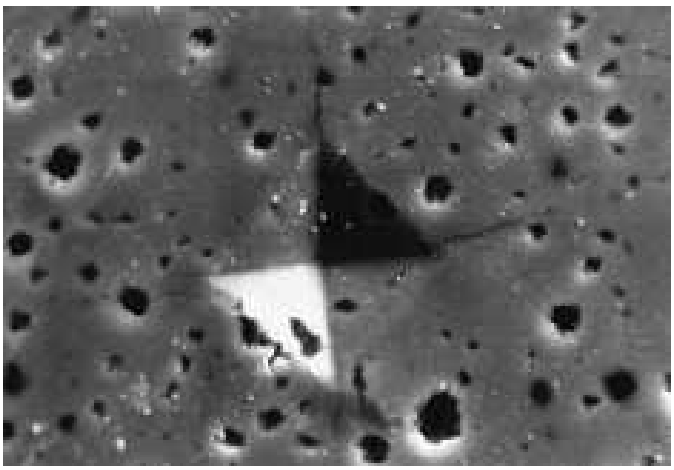

Figure 2.4 – Vickers indenter's imprint on the rim zone of a high burnup LWR fuel [48].

2.6 Plasticity of UO_2

The Knoop micro-hardness of polycrystalline sintered fresh uranium dioxide, with density approximately equal to 93.6% TD, was measured by Kutty et al. [83] which obtained a value of about 5.92 GPa in the dense region of the pellet.
Below about 1273 K, uranium dioxide is brittle and does show only little plastic deformation. A transition from brittle to ductile behaviour is observed at higher temperatures. The plastic deformation of uranium dioxide occurs mainly by gliding and climbing of dislocations and by grain boundary slip [84].
Radiation-induced defects hinder dislocation glides, reducing ductility. Such defects can be subdivided into inclusion-like and obstacles with dislocation properties. Bubbles, and precipitates belong to the first category. They have relatively short-range strain fields and their properties are stable under their interaction with dislocations.
Obstacles such as voids contribute significantly to radiation-induced hardening. Dislocation loops and stacking faults (with longer range of action the first, the second lower), can determine hardening of the material and their interaction with a gliding dislocation can change properties belonging to both the interacting defects [85].

2.7 Elastic properties of UO_2

The Young's modulus of uranium dioxide single crystals was studied by Wachtman et al. [86] and Fritz [87], using acoustic methods at room temperature. Wachtman obtained a maximum Young's modulus of 338 GPa in the $< 100 >$ direction and a minimum for the $< 111 >$. He calculated, then, the polycrystalline Young's modulus by using the Voigt-Reuss-Hill (VRH) average, where [88]

$$E_{Voigt} = f_1(c_{ij}) \tag{2.37}$$

$$E_{Reuss} = f_2(s_{ij}) \tag{2.38}$$

Hill demonstrated, using energy considerations, that 2.37 and 2.38 are upper and lower limits of the polycrystalline elastic modulus (in this case Young's modulus) and suggested to use their arithmetic mean to calculate the polycrystalline elastic modulus. Table 2.1 compares Young's modulus values for fully dense polycristalline uranium dioxide

Table 2.1 – Comparison of Young's modulus (E) values of fully dense uranium dioxide. Lang's value corrected for porosity has been taken from [86]. Laux's value has been determined by studying variation of Young's modulus as a function of porosity.

E (GPa)(Wachtman et al. (VRH)) [86]	E (GPa) Lang [86] [89]	E (GPa) Fritz [87]	E (GPa) Laux [77]
(Reuss= 217; Voigt = 244) 231	228	220.7	224 ± 1

Young's modulus values of fully dense uranium dioxide, reviewed by Martin, are available in [90].

2.8 Thermal properties

In non-metal materials lattice thermal conduction is the dominating mechanism for heat transfer. When a temperature gradient is present within a body, the thermal energy propagates thanks to wave packets; the major responsible for conduction is represented by the acoustic phonons [91]. The specific heat capacity of a solid was found in the early experiments of Dulong and Petit to be very similar for all materials. Hence, the amount of heat energy per molecule, necessary to raise the temperature of a solid by a given amount, seemed to be independent of its chemical composition [92]. Using the classic Dulong and Petit model it is not possible to explain the behaviour of the specific heat in the proximity of the absolute zero. Because of this discrepancy the vibrational theory of the specific heat has been developed; in particular Einstein before and Debye later introduced approximations which consider the interatomic forces as obeying Hooke's law [93]. Einstein considered a simple crystal as an aggregate of $3N_a$ (N_a= Avogadro constant) simple harmonic oscillators vibrating with the same frequency f and characterised by an energy state equal to an integer multiple of hf, where h is Planck's constant. By combining the Planck's energy quantisation and the Boltzmann distribution, Einstein expressed the total energy as [92]:

$$E_n = \frac{3N_a hf}{e^{(hf/k_B T)} - 1} \tag{2.39}$$

Where k_B is the Boltzmann's constant ($1.38\ 10^{-23}\ J \cdot K^{-1}$). The specific heat of a solid at constant volume can be determined as

$$C_v = \frac{dE_n}{dT} \tag{2.40}$$

Einstein's model was successively corrected by Debye who considered the system as $3N_a$ coupled vibration instead of $3N_a$ indipendent vibrations. The model of Debye reproduces the T^3 behaviour observed for the C_v at very low temperatures; moreover, it relates the specific heat to the solid elastic properties. By indicating with n the number of atoms in the molecule, the specific heat at constant volume expressed in $J \cdot kg^{-1} \cdot K^{-1}$ is [93]:

$$C_v = \frac{3Rn}{M} \cdot 3\left(\frac{T}{\Theta}\right)^3 \int_0^{\Theta/T} \frac{x^4 e^x}{(e^x - 1)^2} dx \tag{2.41}$$

In relation 2.41, R indicates the gas constant ($8.31\ J \cdot mol^{-1} \cdot K^{-1}$) and M the molar mass of the molecule. Θ represents the Debye temperature and is related to the longitudinal and transverse waves velocities [92, 94]:

$$\Theta = \frac{h}{k}\left(\frac{9N}{4\pi a^3\left(\frac{1}{v_l^3} + \frac{2}{v_t^3}\right)}\right)^{1/3} \tag{2.42}$$

where the mean acoustic velocity is defined as:

$$v_m = \left(\frac{1}{v_l^3} + \frac{2}{v_t^3}\right)^{-1/3} \tag{2.43}$$

N is the number of atoms in the unit cell and a the lattice parameter. Thermal expansion is related to the material elastic properties thanks to the dimensionless Grüneisen parameter γ, defined in terms of the adiabatic Bulk modulus K as [95]:

$$\gamma = \frac{\alpha K}{\rho C_p} \tag{2.44}$$

Where ρ indicates the material density, α the thermal lattice expansion coefficient [22, 26]:

$$\alpha = \frac{1}{V}\left(\frac{\partial V}{\partial T}\right)_P \tag{2.45}$$

C_p refers to the heat capacity at constant pressure:

$$C_p = C_v + \frac{\alpha^2 V_m T}{\beta} \tag{2.46}$$

with V_m the molar volume and β the coefficient of compressibility:

$$\beta = -\frac{1}{V}\left(\frac{\partial V}{\partial P}\right) = \frac{1}{K} \tag{2.47}$$

To determine the thermal conductivity of a ionic solid, the lattice vibrations are treated as a gas of phonons. The process of thermal energy transfer is stochastic: it diffuses through the specimen after a large number of collisions of phonons with each other or with the solid's defects. The phonons gas, which could be considered as isotropic [22, 26], is characterised by a mean phonons speed (u) and a mean free path (l), thus the thermal conductivity λ_c can be expressed as:

$$\lambda_c = \frac{1}{3}\rho C_v l \tag{2.48}$$

The phonons mean free path is mainly dominated by the geometrical scattering and by the scattering with other phonons. This latter would not exist if the force between atoms was harmonic. Hence, anharmonicity introduces the phonon-phonon scattering and limits the mean free path [22]. Phonons collisions characterised by an unchanged total crystal momentum after the collision, are not responsible for thermal resistivity because they do not vary the phonons' energy. Conversely, thermal resistivity is related to *umklapp* scattering: a three phonons process determining the total crystal momentum to change after the collision by a non-zero reciprocal lattice vector[3] (Figure 2.5). At very low temperatures, the free mean path should become very large, but the defects in the solid prevent this phenomenon, then the phonons mean free path can be expressed as [26]

$$l = \frac{1}{a + bT} \tag{2.49}$$

Thermal conductivity of nuclear fuel is extremely important for the prediction of the fuel performance during irradiation, the temperature profile along the radius of the pellet and the fission gas release. The thermal conductivity of a poor semiconductor such as UO_2 is dominated by phonons heat transport (phonon-defects and umklapp process) for temperatures below 1500 -1600 K [3] [96]. Thus, the thermal conductivity (λ_c) of uranium dioxide and MOX nuclear fuels can be expressed, thus, by the following empirical relation [97]:

$$\lambda_c = \frac{1}{A + BT} \tag{2.50}$$

[3]The reciprocal lattice is the Fourier transform of the direct lattice. The reciprocal lattice vector is a linear combination of the primitive vectors of the reciprocal lattice [22]

where A takes into account the phonon scattering by substitutional atoms, point and extended defects and B refers to the umklapp process.

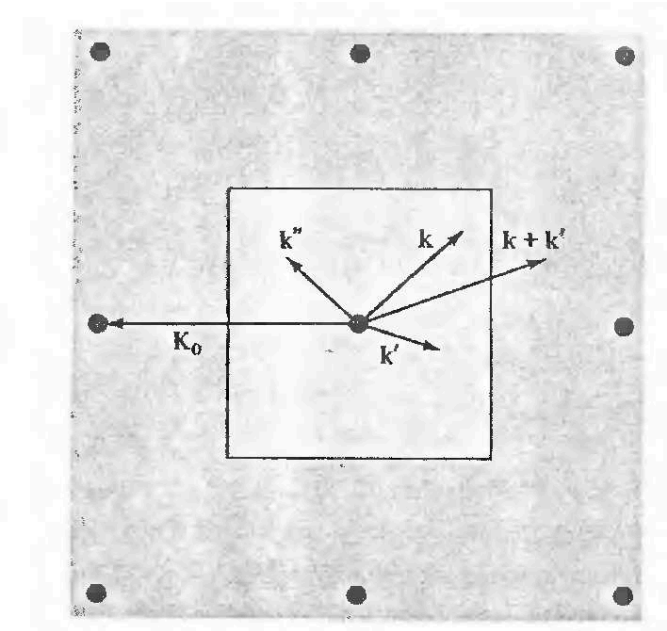

Figure 2.5 – Schematic of the umklapp process. The points represent reciprocal lattice points in a two dimensional square lattice. The colliding phonons with wave vectors respectively **k** and **k'** merge into a phonon whose wave vector is **k"** and $\mathbf{k"}+\mathbf{K_0}=\mathbf{k}+\mathbf{k'}$ (Ashcroft), with $\mathbf{K_0}$ is the reciprocal lattice vector [98].

At mesoscopic scale, the main parameters influencing λ_c are the microstructure (porosity, grain size, fission gas bubbles and additives distribution) and, eventually, precipitates. At the atomic scale, thermal conductivity depends on plutonium or other additives in lattice solution, soluble and insoluble fission products and fission gases dispersed as atoms, radiation damage, stoichiometry and fission density [97]. Actinides, rare earths, and transition metals can form mixed oxides with UO_2 or $(U,Pu)O_2$ and may act as phonon scattering centres because of the different bonding potential, ionic radius, or mass existing between impurities and substituted atoms. A measure of the total scattering coefficient is given by the differences in atomic mass and ionic radii and by the Grünesein constant, which defines the strain generated in the lattice by the difference in ionic radius.
The effect of insoluble or volatile fission products can be interpreted with the same equations as for the dissolved fission products [97]. Stoichiometry has a major effect on the thermal conductivity of fresh fuels, but the O/U ratio of UO_2 irradiated under LWR conditions remains close to 2.00 up to a burnup of 100 $GWd \cdot t^{-1}M$ [99–101]. Introducing additives like Gd or Cr, has a negative effect on the thermal conductivity with higher impact at low burnup [97].
Two important contributions for the determination of thermal conductivity of non

metallic crystals are those of Leibfried-Schlömann [102] and Julian [103], who considered acoustic phonons governing heat transport in crystalline solids.
The agreement with experimental results was within 20 % for those crystals with only one atom per primitive crystallographic cell, but worse for other type of crystalline solids, especially when more than one atom per cell is present [104].
Leibfried and Schlömann B parameter ($m \cdot W^{-1}$) for non metallic crystals is defined as [104]:

$$B = 0.01 \cdot \frac{\gamma^2}{5.72 \cdot 10^{-8} M \delta \theta_D^2} \tag{2.51}$$

where γ is the Grüneisen parameter, M = atomic mass of the lattice and δ^3 the volume of the primitive cell in Å^3. Julian corrected relation 2.51 with the following expression:

$$B = 0.01 \cdot \frac{2\gamma^2(1 - 0.514\gamma^{-1} + 0.228\gamma^{-2})}{5.72 \cdot 10^{-8} \cdot 0.849 M \delta \theta_\infty^2} \tag{2.52}$$

where

$$\theta_\infty^2 = \frac{5h^2}{3k^2} \frac{\int_0^\infty f^2 g(f) df}{\int_0^\infty g(f) df} \tag{2.53}$$

with: k= Boltzmann's constant, h= Planck's constant, f= phonon frequency and g(f)= phonon density of states function.
For crystals with only one atom in the primitive cell, θ_∞ represents the high temperature limit of Debye temperature for acoustic modes.
When the primitive crystallographic cell has more than one atom, in addition to the acoustic branch also the optic branch of phonons is present, although in many crystals their group velocity is low if compared with that of acoustic phonons, which makes optic phonons inefficient heat carriers [104].
In uranium dioxide and plutonium dioxide, despite optic phonons having a large group velocity their contribution to heat transport is negligible due to their anharmonicity, whereas longitudinal phonons are the main heat carriers [105].
Following these considerations, parameter B of thermal conductivity for uranium dioxide can be calculated by using the model developed by Leibfried and Schlömann and Julian, in particular by using the review of Slack [104], who generalised expressions 2.51 and 2.52 to crystalline solids with n atoms in the primitive crystallographic cell. Therefore, parameter B of thermal conductivity (m W^{-1}) for uranium dioxide can be determined by:

$$B = 0.01 \cdot \frac{2\gamma^2 n^{2/3}(1 - 0.514\gamma^{-1} + 0.228\gamma^{-2})}{5.72 \cdot 10^{-8} \cdot 0.849 \overline{M} \delta \theta_D^3} \tag{2.54}$$

2.9 Conclusion

Longitudinal and transverse waves (bulk waves) velocities in matter are strictly related to the material's elastic properties. Hence, Young's modulus, Bulk modulus and Shear modulus (Lamé's parameter μ) can be calculated by measuring the transverse and the longitudinal waves velocities in material. In the single parameter model, developed by Debye, the acoustic velocity does not depend upon the wave number and bulk waves velocities can be combined to obtain a mean sound velocity v_m which is directly related to the Debye temperature and the material's specific heat. The Debye temperature and the specific heat, therefore, can be calculated if transverse and longitudinal velocities in matter are known. If the quantistic description of sound interaction in matter is considered, phonons are also the main responsible for heat transport: the B coefficient of the thermal conductivity, related to three phonons umklapp scattering process, is consequently related to the bulk waves velocities of propagation.
The existence of mathematical relations between bulk waves velocities and Rayleigh wave velocity enables to calculate all the properties considered in Chapter 2 thanks to the single Rayleigh wave velocity measurement.
The relation existing between Young's modulus and Rayleigh wave velocity will be used in the entire experimental part of the thesis, whereas in section 4.6 Debye theory will be applied to determine Debye temperature and specific heat capacity of fresh uranium dioxide and chemical analogues of irradiated uranium dioxide, by using the Rayleigh wave. The mathematical expressions of v_t and v_l in terms of v_R, which enable the calculation of the mean acoustic velocity v_m, are also given in section 4.6.
Finally 2.54 is used in section 4.6 to determine the B coefficient of thermal conductivity solely by means of the Rayleigh wave velocity.

Chapter 3

Experimental techniques

Contents

3.1 Introduction

Chapter 3 introduces the experimental techniques used during the measurement campaigns related to the present Thesis.
After having exposed the theoretical working principles of high frequency acoustic microscopy, the cold and hot facilities of the European Commission Joint Research Centre Karlsruhe are described, in particular the hot-cell hosting the acoustic microscope dedicated to irradiated nuclear fuel measurements.
In addition to the high frequency acoustic microscopy, which represents the main technique used, available additional tecniques were used, in particular Vickers microhardness, reflection-mode echography, scanning electron microscopy and X-ray diffraction.
A brief description of the techniques used to complement the acoustic microscopy results, is given at the end of the chapter.

3.2 High frequency acoustic microscopy

Figure 3.1 shows a schematic of an acoustic microscope's sensor. A piezoeletric transducer mounted at the top of a high purity silica rod, previously metallised, converts the incoming sinusoidal signal into plane acoustic waves.
Acoustic waves are focused thanks to a spherical dioptre (acoustic lens) ground at the lower extremity of the rod. The lens is submerged in a coupling liquid and when the waves cross the spherical interface between the lens and the fluid they are refracted towards a focus on the axis of the lens. The very high refractive index encountered when acoustic waves pass from a solid to a liquid enables the waves to be focused by a single lens surface [74]. The amplitudes of the acoustic waves reflected back and detected by the piezoelectric transducer are related to the elastic properties of the sample. Hence, by converting the signal received in a greyscale[1] and by scanning mechanically the sample along a plane parallel to its surface (x-y in Figure 3.1) it is possible to construct an acoustic image. The image spatial resolution is determined by [74]

$$R = 0.51\lambda_{cl}/N.A. \tag{3.1}$$

Where λ_{cl} is the wavelength in the coupling liquid and N.A. is the numerical aperture of the lens. If the semi-angle subtended at the focus by the circumference of the lens aperture is Θ_0, then N.A. = sin Θ_0. Higher frequencies give better resolution.

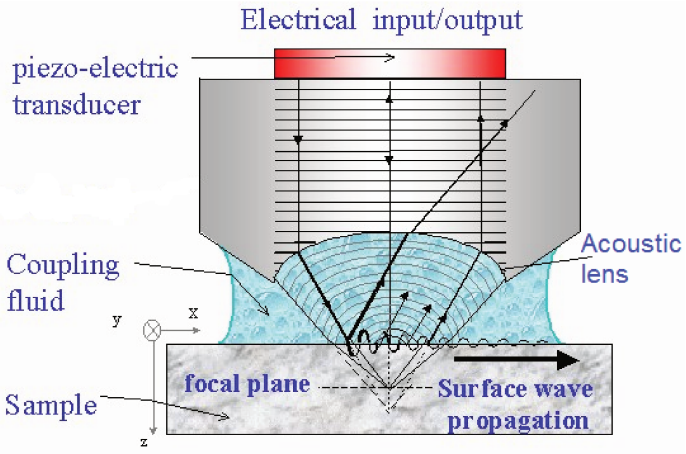

Figure 3.1 – Schematic of an acoustic microscope's sensor. At the top the piezoelectric transducer mounted on a high purity silica rod (delay line). At the bottom of the silica cylinder the acoustic lens which provides the focusing action.

[1] A greyscale image has grey values ranging from 0 to 255. Black corresponds to 0, whereas white to 255.

Figure 3.2 shows an example of surface image acquired at 140 MHz using methanol as coupling liquid: the spatial resolution is $\sim 6\mu m$. The image in 3.3, acquired at 60 MHz, has instead a spatial resolution $\sim 13\mu m$.

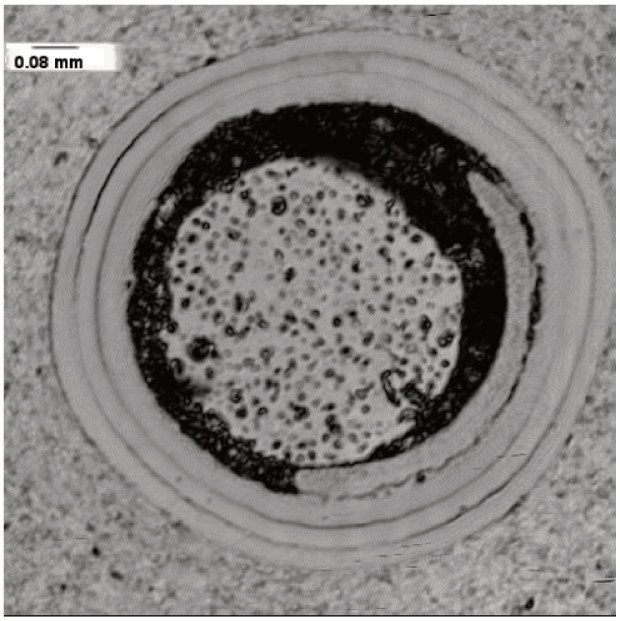

Figure 3.2 – Acoustic image (140 MHz) of an irradiated High Temperature Reactor coated particle, embedded in graphite matrix. The nucleus of the coated particle is uranium dioxide fuel contained in several coating layers (SiC and pyrocarbon), which are barriers for fission products release.

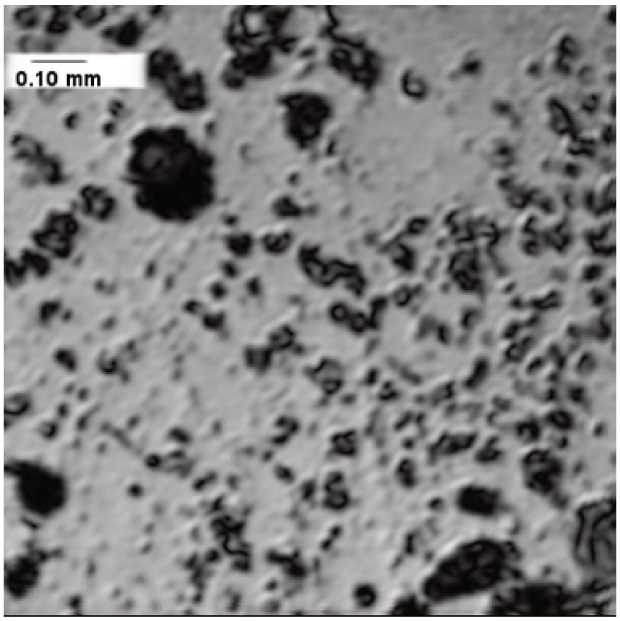

Figure 3.3 – Acoustic image (60 MHz) of a sample belonging to the Phebus test (FTP1)

As matter is not opaque to acoustic waves, acoustic microscopy gives the possibility to construct a sub-surface image by slightly defocusing below the surface of the sample [2]. Material elastic properties can be inferred by using the acoustic microscope in *Acoustic signature mode*, i.e. by gradually reducing the distance between the acoustic lens and the sample and determining an interference between the normal reflected waves and the Rayleigh surface waves generated by those waves incident at the critical angle (Snell-Descartes law):

$$\Theta_R = sin^{-1}\frac{v_{cl}}{v_R} \tag{3.2}$$

where v_{cl} is the velocity in the coupling liquid and v_R is the Rayleigh wave velocity. To satisfy the condition in 3.2 and to guarantee a low attenuation during the waves propagation, methanol represents a good coupling liquid ($v_{cl} \sim 1100\ m \cdot s^{-1}$) for uranium dioxide measurements. The piezoelectric voltages, generated by both reflected normal and Rayleigh waves, are summed in terms of amplitude and phase. During the defocusing their phases changes at different rates causing alternate constructive and destructive interference. The signal V(z) received is pseudo-periodic (Figure 3.4) with spatial period related to the Rayleigh waves velocity by:

$$\Delta z = \frac{\lambda_{cl}}{2(1 - cos\Theta_R)^2} \tag{3.3}$$

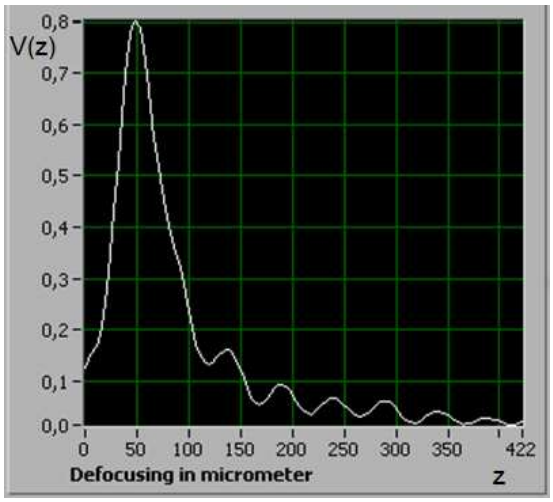

Figure 3.4 – V(z) obtained at 90 MHz in irradiated uranium dioxide using methanol as coupling liquid and 400 μm defocusing

[2]The maximum depth is limited by attenuation phenomena, which are proportional to the square of the applied frequency

The Rayleigh wave velocity ($\mathrm{m\,s^{-1}}$) can be calculated thanks to 3.3 and 3.2:

$$v_R = \frac{v_{cl}}{\sqrt{1-(1-\frac{v_{cl}}{2f\Delta z})^2}} \tag{3.4}$$

where Δz is the spatial period (m) and f the frequency applied (Hz).
In order to measure the period of the oscillation a Fourier transform is used, after having coupled the acoustic signature with a Gaussian function, to reduce the amplitude of the discontinuities at the boundaries of each finite sequence acquired (Blackman windowing). The acoustic signature mode enables the determination of the material local elastic properties, with a resolution depending on both the frequency and the defocusing depth. During the defocusing, in fact, the diameter of the insonified area increases in size (see Figure 3.5): for instance at 100 MHz the geometrical area's diameter is about 250 μm [77].

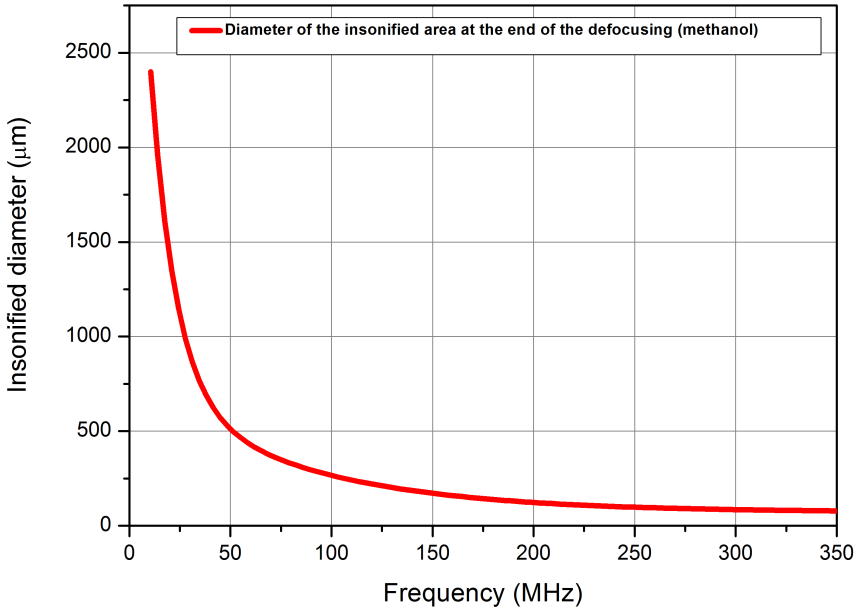

Figure 3.5 – Diameter of the insonified area at the end of the defocusing (about 400 μm) when the coupling liquid is methanol [77].

The resolution of this technique is higher than the geometrical area investigated due to a concentration of the acoustic energy in the centre and approximately half of the geometrical area insonified.

The acoustic microscope's system in the European Commission Joint Research Centre Karlsruhe[3] is schematically represented in Figure 3.6: the excitation signal is synthesised and split by a coupler and then it is partially sent to the acquisition board (reference signal); thanks to a switch a single burst is produced to excite the piezoelectric after amplification. The information received by the transducer is amplified, filtered, digitised and stored in a memory.

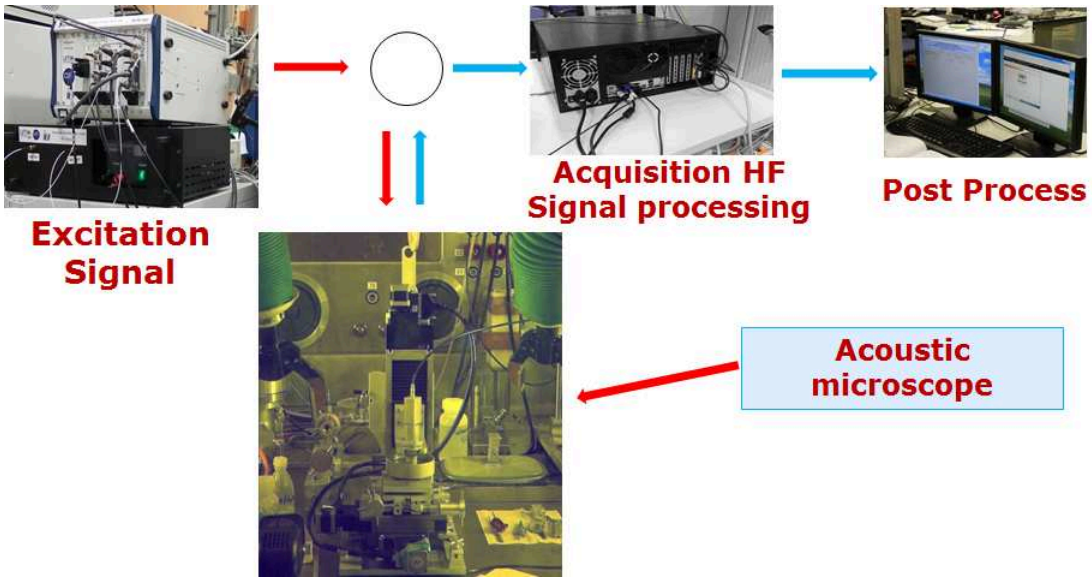

Figure 3.6 – Schematic of the acoustic microscopy setup in the hot-cell facility of the Joint Research Centre Karlsruhe: from the excitation signal generation to the data acquisition and storage.

A better insight of the acoustic microscope installed in hot-cell is illustrated in Figure 3.7: the stepper motors can be piloted by the remote control system, whilst every simple operation such as connecting cables to the sensor, putting the sample in place or adjusting the parallelism of the sample via micrometric screws, must be performed by means of tele-manipulators (Figure 3.8). The system has been designed to work in high irradiation field. The work in hot-cell requires high frequency cables of 10 m length and numerous connections which are responsible for a degradation of the signal requiring additional amplification, impedance adaptation and signal filtering.

[3]The acoustic microscope was installed in the Joint Research Centre hot-cell in the frame of Laux's PhD thesis [77]

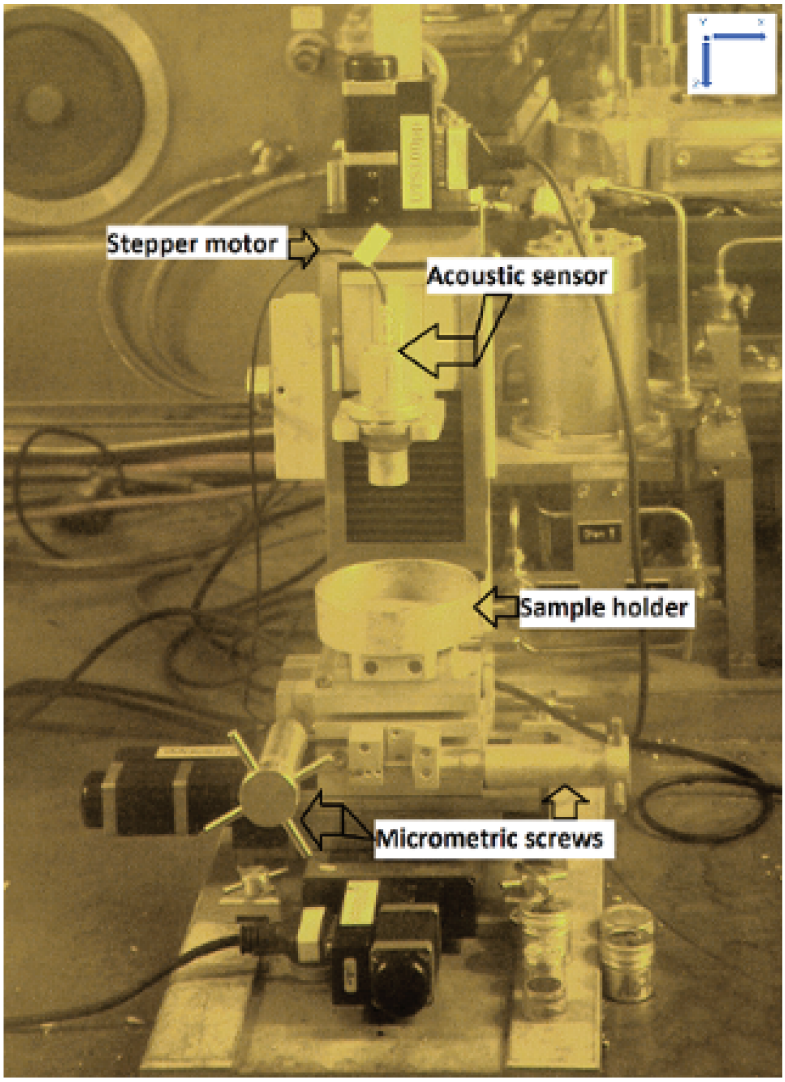

Figure 3.7 – View of the high frequency acoustic microscope in the hot-cell of the EC-JRC Karlsruhe. The acoustic sensor in the picture operates at 140 MHz. The stepper motors enable the control of the movement along the three axes with increments of respectively 1 μm and 0.1 μm along x-y and z. The micrometric screws enable the adjustment of the parallelism between the samples' surface and the acoustic sensor.

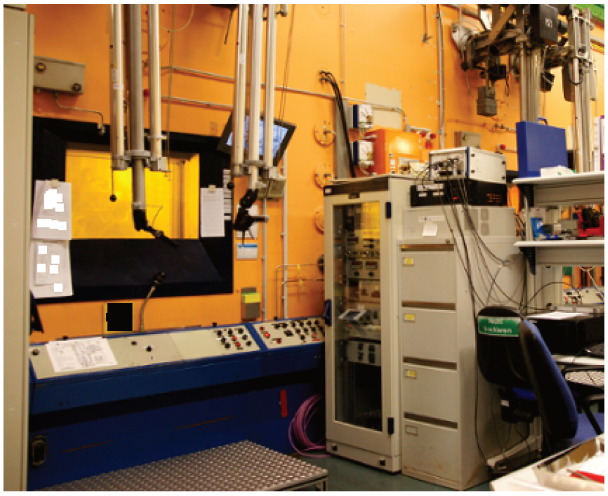

(a)

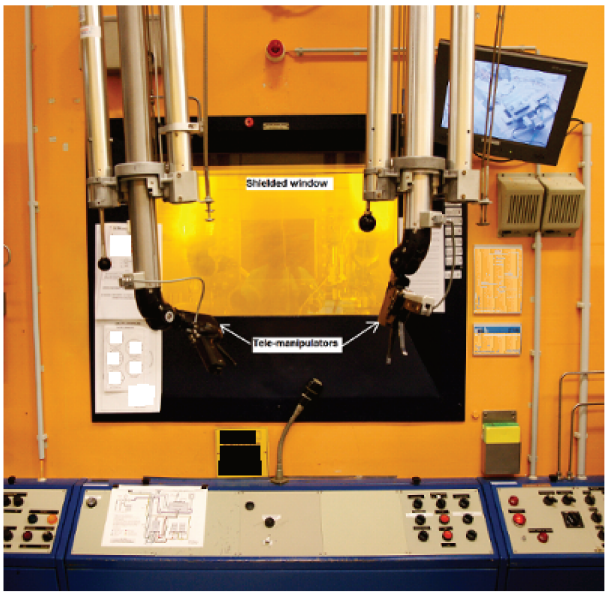

(b)

Figure 3.8 – (a) General view of the acoustic microscope hosting hot-cell, with the electronic remote control and data acquisition system (b) View of the acoustic microscope hosting hot-cell with the tele-manipulators and lead window (thickness $\sim$ 1 m). The wall (thickness $\sim$ 1 m) is made of barytes concrete to shield from the high gamma and neutron fields.

In the frame of the thesis experimental work a fresh uranium dioxide sample implanted with high energy ions and a chemical analogue of an irradiated uranium dioxide fuel were measured by means of an acoustic microscope installed outside the hot-cell (3.9). In this case a sensor working at 100 MHz was used; due to its

toxicity methanol was substitued by ethanol. Ethanol presents the disadvantage to be more attenuating, but acoustic velocity in ethanol is similar to acoustic velocity in methanol. Properties of these coupling liquids are listed in Table 3.1, whereas differences in acoustic signatures will be described in the experimental part of the thesis.

Table 3.1 – Comparison between acoustic properties of methanol and ethanol [106]

Coupling liquid	Temperature (K)	Velocity ($\mathrm{m\,s^{-1}}$)	Attenuation coefficient ($\mathrm{dB\,\mu m^{-1}\,GHz^{-2}}$)
Methanol	303	1088	0.262
Ethanol	303	1127	0.421

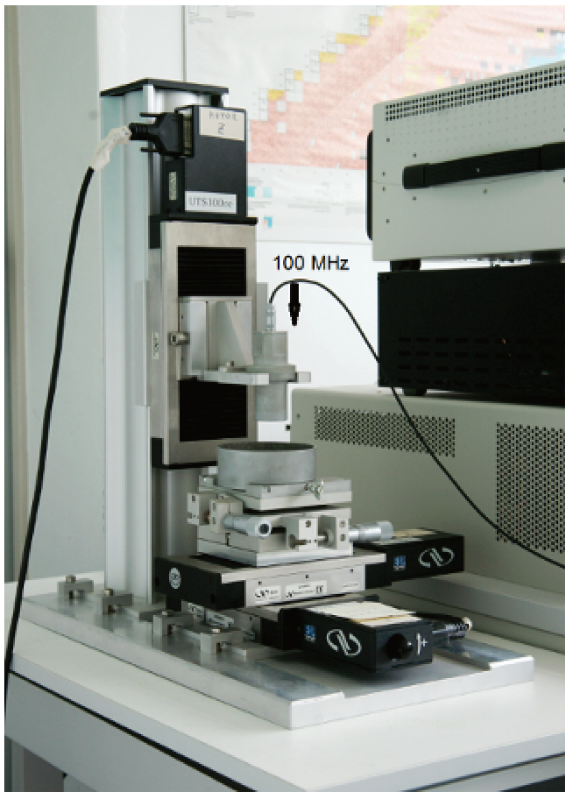

Figure 3.9 – Schematic of the acoustic microscopy setup in the hot-cell facility of the Joint Research Centre Karlsruhe: from the excitation signal generation until the data acquisition and storage.

3.3 Micro-echography

From equations 2.24 and 2.26 it follows that in addition to the Rayleigh wave velocity another bulk velocity (either v_l or v_t) is necessary to determine precisely the Poisson's ratio of material.
The simplest technique enabling the determination of the longitudinal velocity in nuclear material, as demonstrated by Roque [107], is the micro-echography which differs from the conventional echography for the smaller sensor's size, more suitable for the investigation of small samples. Classical echographic methods are based on the measurement of the time of flight: the time necessary for the acoustic waves to travel inside a sample of a specific thickness. A simple schematic of a reflection-mode echography system is depicted in Figure 3.10.

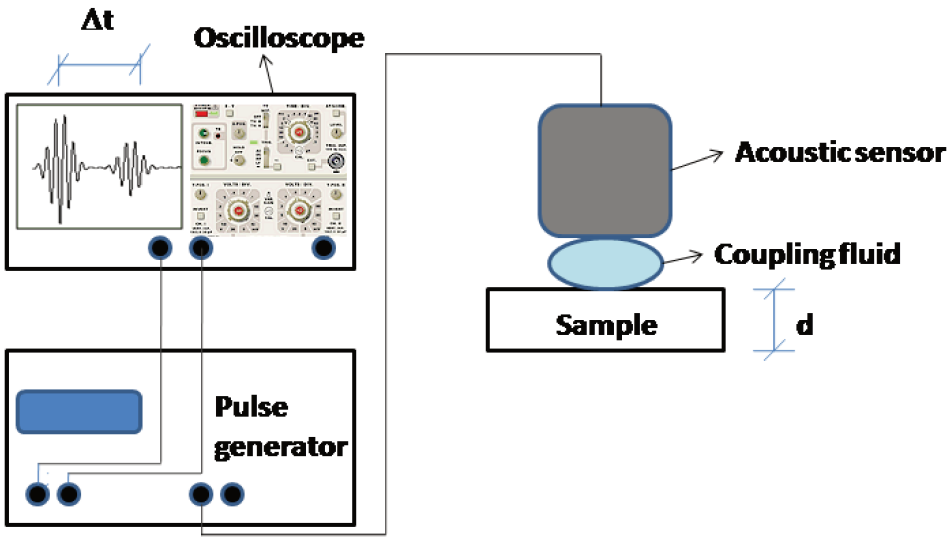

Figure 3.10 – Schematic of reflection-mode echography experimental setup.

If we indicate with d the sample thickness, with Δt the time between the echo reflected on the surface near the acoustic sensor and the echo reflected on the opposite side of the sample, v_l, the longitudinal velocity can be calculated from:

$$v_l = \frac{2d}{\Delta t} \tag{3.5}$$

The working frequency must be accurately chosen in order to guarantee a low attenuation of the signal (low frequency is preferable) and a precise determination of the time of flight (high frequency); moreover with higher frequency the ratio

wavelength - piezoelectric transducer diameter is smaller, which reduces diffraction in the transducer.
Figure 3.11 shows the reflected waves paths giving two different echoes e.g. like those visualised in Figure 3.12 and 3.13. Hull et al. [108] developed three different signal treatments for the time of flight determination; in particular the cross-correlation method has been used in the framework of this PhD theses [108].

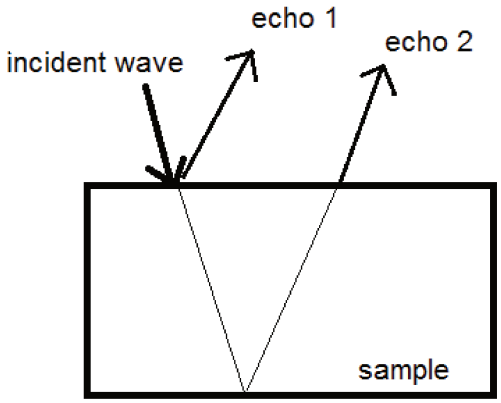

Figure 3.11 – Paths followed by the acoustic waves reflected on the two different surfaces of the sample reaching the piezoelectric at different times.

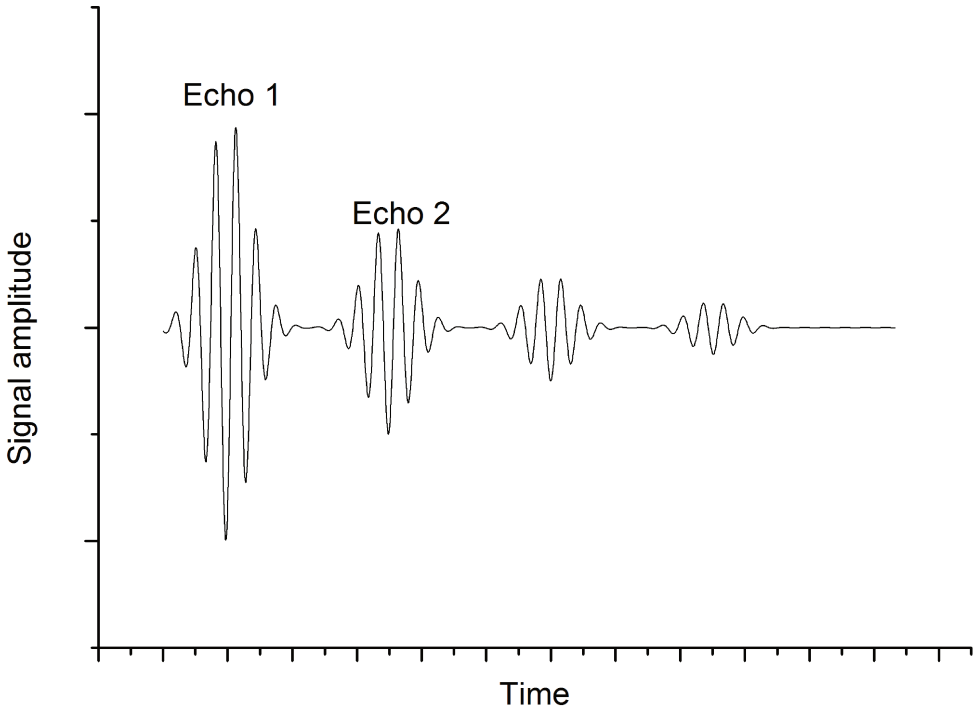

Figure 3.12 – Simulated echoes corresponding to the different surfaces' reflection of the acoustic wave.

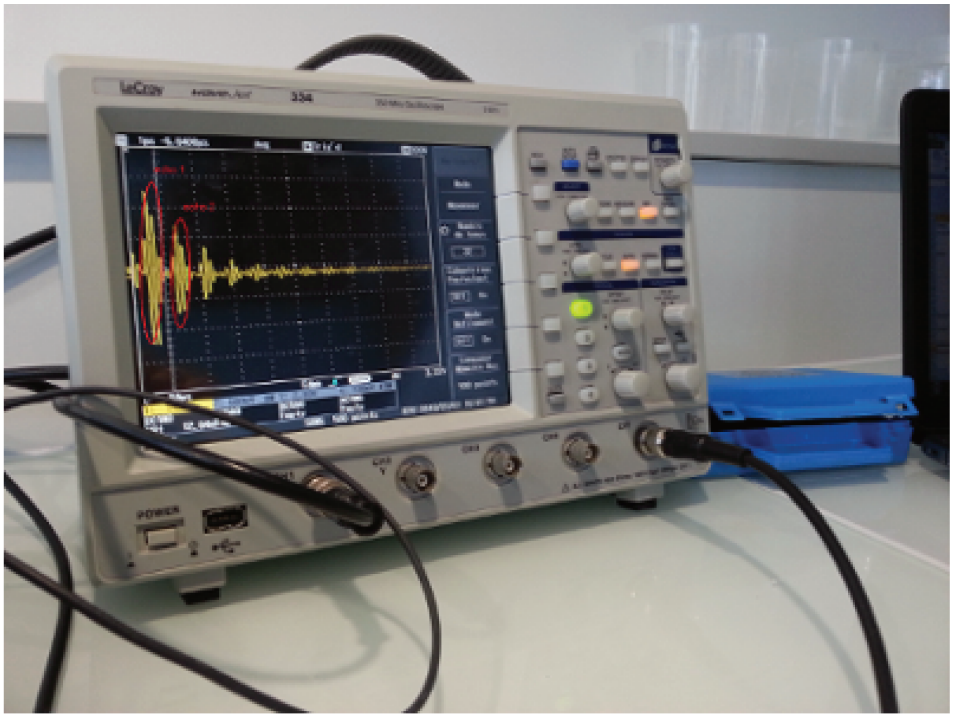

Figure 3.13 – Experimental echoes corresponding to the different surfaces' reflection of the acoustic wave on FARO sample (80 wt% UO_2 and 20 wt%ZrO_2).

3.4 Vickers indentation

In the present research work Vickers indentations tests were performed for the determination of the ratio Hardness-Young's modulus. Measurements were performed by forcing a squared pyramid with apex of 136° on the polished surface of a sample, leaving on it an impression. The Vickers microhardness HV (GPa) can be calculated by means of the relation proposed in the standard methods for advanced ceramics ASTM C1327-99 [109]

$$HV = 0.0018544\frac{P}{d^2} \tag{3.6}$$

where P(N) is the maximum applied load and d (mm) is the average length of the two diagonals of indentation.
Measurements were performed using a Micro-Duromat 4000E microhardness Vic-

kers tester, incorporated in a shielded LEICA Telatom 3 optical microscope (Figure 3.14).

Figure 3.14 – Shielded optical microscope (LEICA Telatom 3) equipped with a Micro-Duromat 4000E microhardness Vickers tester

3.5 X-ray diffraction

The lattice parameter was determined by X-ray diffraction. According to Bragg's law, if we consider a crystal with parallel lattice planes distant d, the path difference between reflected rays from consecutive planes determines a constructive

interference only if it contains an integer number of wavelengths, hence [22]:

$$2dsin\Theta = n\lambda \tag{3.7}$$

where Θ is the angle between the incident ray and the plane.
In the frame of this thesis a Bruker D8 Advance X-ray diffractometer has been used, mounted in the Bragg–Brentano configuration with a curved Ge monochromator and a copper tube (40 kV,40 mA). Lattice parameter was calculated by fitting the 2 Θ curves in the range 10°-120°.

Figure 3.15 – X-ray diffractometer Bruker D8 Advance, in Bragg-Bentano configuration and Ge-primary monochromator.

3.6 Scanning electron microscopy

High-resolution and depth-of-field images of irradiated fuel samples were acquired with a shielded JEOL 6400® scanning electron microscope (SEM) using MaxView® software package from SAMx.
In scanning electron microscopy high-energy electrons (typically 25-30 keV) interact with material's atoms, producing signals related to the topography and composition of the sample's surface. Signals are produced by secondary electrons, backscattered electrons, and characteristic X-rays and result from the interaction

with the sample at or near its surface. In its primary detection mode, secondary electron imaging, the SEM can produce very high-resolution images of a sample surface, revealing details down to about 1–5 nm in size. The instrument used in this work was mounted in a shielded glove-box allowing the examination of irradiated fuels.

Figure 3.16 – Scanning electron microscope in glove box.

Chapter 4

High Frequency acoustic microscopy as post irradiation examination technique

Contents

4.1 Introduction

The first part of this research work focuses on the determination of the local elastic properties of high burnup fuel by high frequency acoustic microscopy.
Micro-acoustic techniques were applied for the first time to uranium dioxide by Vincent Roque [110], who studied the variation of Rayleigh wave velocity in fresh uranium dioxide as a function of porosity, grain size and in presence of additives; finally he applied the technique to uranium dioxide irradiated in Chinon NPP, France. He defined some limitations and advantages of the technique, comparing also the performance of different coupling liquids in the investigation of uranium dioxide fuel.
Thanks to the acoustic microscope installation in the hot-cell of the Joint Research Centre Karlsruhe (in the frame of a collaboration with the University of Montpellier and with the support of EDF), Didier Laux [77] [78] continued the study of the variation of the elastic properties in irradiated uranium dioxide, by applying the technique to fresh uranium dioxide fuels, chemical analogues of irradiated fuel, special fuel irradiated in BR3 reactor and special irradiation discs belonging to the HBRP project (subsection 1.3.4).
Laux observed a global decrease of the Young's modulus in irradiated uranium dioxide [78] compared to fresh UO_2. The majority of samples belonging to his experimental campaign are characterised by homogeneous burnup and temperature profiles, hence they are not affected by the local heterogeneities in microstructure typical of commercial LWR fuels.

This chapter presents the results achieved in the present study by applying high frequency acoustic microscopy both on special irradiation discs and on commercial PWR fuels. The range of applications of the high frequency acoustic microscopy is extended: the local porosity of commercial PWR fuels has been determined only by means of the Rayleigh wave velocities allowing to tackle also the local variation of Young's modulus along the radius of high burnup irradiated pellets. Whenever possible, the local Young's modulus has been related to the micro-hardness profile to evaluate the ratio hardness/Young's modulus.
By studying the evolution of density as a function of burnup, an empirical model able to predict the variation of Young's modulus with the burnup, in the range 0-100 $GWd \cdot t^{-1}M$, is proposed. This model includes also the influence of dopants

on Young's modulus, which until now has been scarcely evaluated.
The model can be used in a fuel performance code, but also to evaluate the unknown average burnup of an irradiated LWR fuel, by measuring the Rayleigh wave velocity via acoustic microscopy.

4.2 Materials

4.2.1 Irradiated uranium dioxide nuclear fuels

In this work, high frequency acoustic microscopy measurements were carried out on commercial PWR fuel samples and on special irradiation discs belonging to the Nuclear Fuel Industry Research (NFIR) program [111]. The characteristics of the investigated samples are summarised in Table 4.1. The commercial PWR uranium dioxide fuels had initial enrichment $\sim$ 3.5-3.95% ^{235}U and initial density $\sim$ 95 - 96% TD, whereas the NFIR special irradiation discs had initial enrichment $\sim$ 20% ^{235}U and density $\sim$ 95 - 96.5% TD. The latter, were irradiated in Halden reactor under isothermal conditions, which, together with the thermalised neutronic spectrum, determined homogeneous burnup profiles.
Prior to the measurements, each sample in Table 4.1 was mounted in an aluminium sample holder (Figure 4.1 (a) and (b)), embedded in resin, then accurately ground and polished using diamond pastes with particle size from 12 μm to 1 μm).
Figure 4.2 shows a schematic of the special irradiation disc concept [112]: each uranium dioxide disc is held between two molybdenum discs, which ensures the homogeneous temperature profile.

Table 4.1 – Fuel samples investigated in the present study using high frequency acoustic microscopy .

Samples	Burnup range ($GWd \cdot t^{-1}M$)	Comments
UO_2	48 - 103.5	Special irradiation discs NFIR [113]. UO_2 (standard grains and large grains) and UO_2 doped with Gd_2O_3, Cr_2O_3, kaolinite
UO_2	100	Commercial PWR fuel
UO_2	80	Commercial PWR fuel [114]
UO_2	78	Commercial PWR fuel [115], [116]
UO_2	67	Commercial PWR fuel [117]

(a)

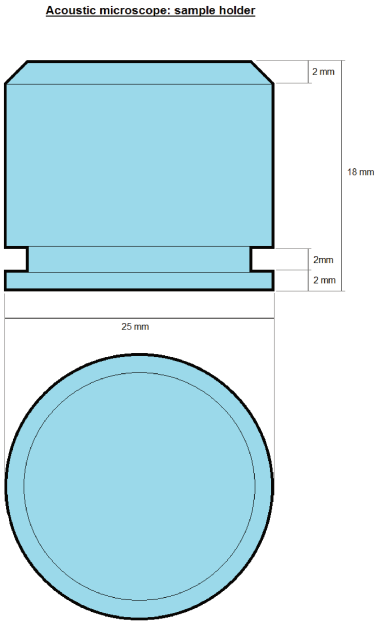

(b)

Figure 4.1 – (a) Aluminium sample holder (b) schematic of the aluminium sample holder

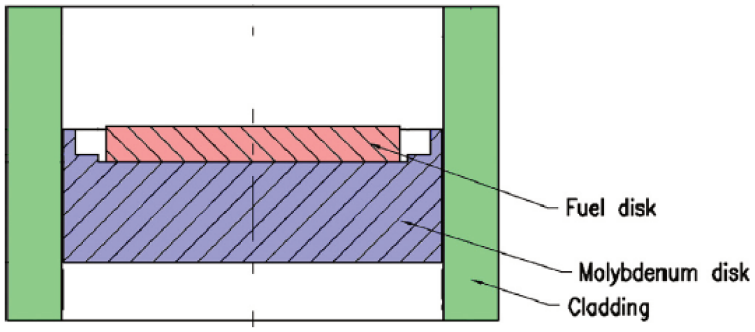

Figure 4.2 – Schematic of the special irradiation disc concept [112]

The commercial PWR uranium dioxide samples, either cross section or axial section of the original pellets, are all characterised by high density of cracks and restructured rim (High Burnup Structure), whose thickness is variable, but generally bigger for pellets with higher average burnup. Figure 4.3 shows an optical micrograph (16 x) of the sample with average burnup 100 GWd·t^{-1}M, where numerous cracks are crearly visible, Figure 4.4 (a) shows an acoustic image acquired at 60 MHz of the uranium dioxide sample with average burnup of 78 GWd·t^{-1}M. On the investigated sample a scratch was performed to reveal fracture surface morphology ((III) in Figure 4.4 (a)). The scratched portion was examined with

a scanning electron microscope (SEM) appearing fully restructured until $\sim$ 400-500 μm of distance from the cladding; a fracture surface SEM image is available in Figure 4.4 (b).

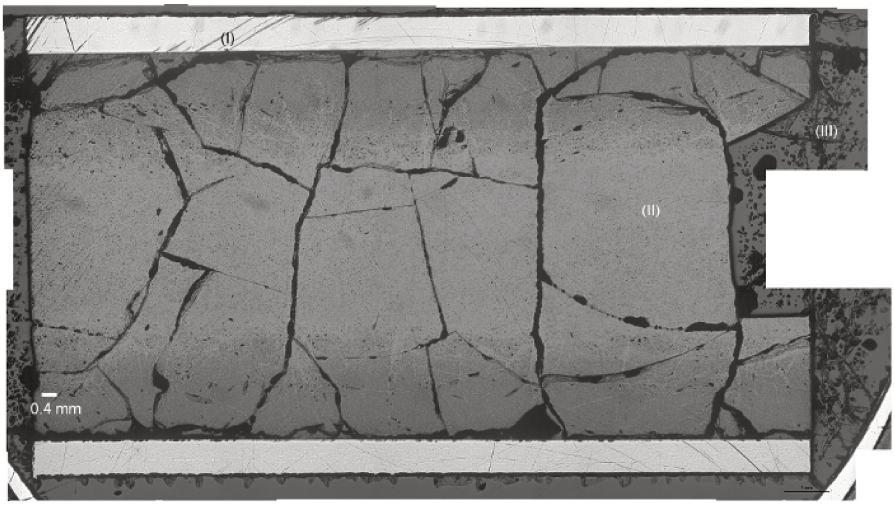

Figure 4.3 – Optical micrograph of the commercial irradiated fuel with 100 GWd·t^{-1}M average burnup. (I) Zr-based alloy cladding, (II) UO_2 fuel (III) embedding resin.

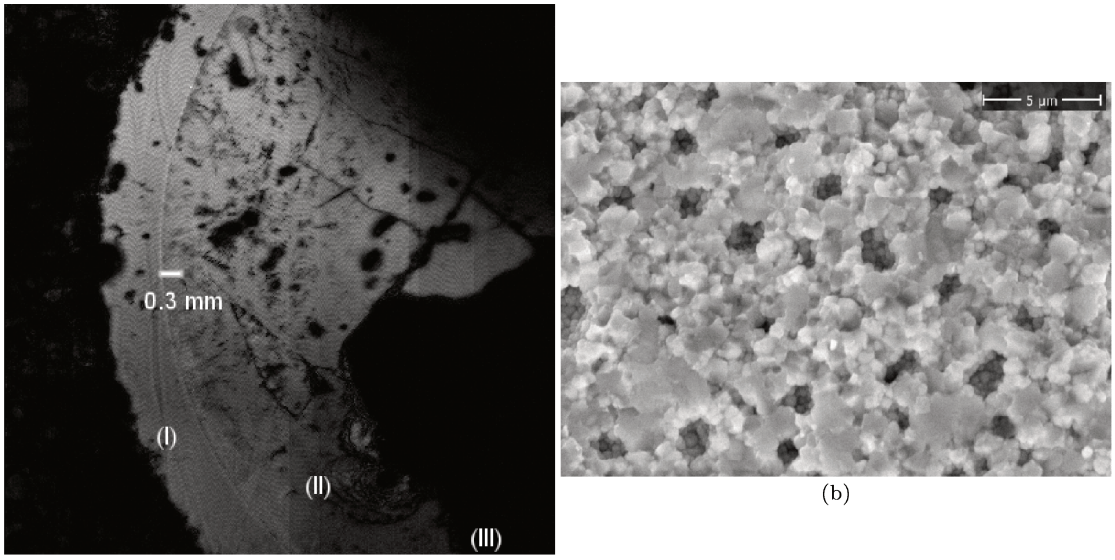

(a) (b)

Figure 4.4 – (a) acoustic image of half pellet cross section acquired at 60 MHz of the sample with 78 GWd·t^{-1}M; (I)Zr-based alloy cladding, (II)uranium dioxide fuel (III) portion of the fuel scratched for SEM investigation. (b)Fresh fracture scratched SEM image of fully restructured portion of the sample.

4.2.2 Fresh UO_2 and chemical analogue of irradiated UO_2

In the present work high frequency acoustic microscopy was employed to investigate relations between UO_2 elastic and thermophysical properties. Rayleigh wave velocity measurements were performed on a fresh uranium dioxide pellet (density $\sim$ 96% TD) and on a SIMFUEL sample synthesised by AECL [118] [119] [120], with simulated irradiation burnup of 60 GWd·t^{-1}M. SIMFUEL is obtained by doping fresh UO_2 with stable additives, with the aim at obtaining a phase structure and microstructural features representative of irradiated fuel. Due to the lack of volatile and gaseous species, the microstructure of SIMFUEL does not present gas bubbles, hence does not fully represent the real irradiated uranium dioxide fuel; moreover the HBS is not reproduced at all. The density of the SIMFUEL sample was measured by weighing it in air and in water (method based on the Archimedes' principle), which gave a density of 10250 kg·m^{-3}, in agreement with the range given in [119].
Fresh uranium dioxide pellet was investigated by high frequency acoustic microscopy at 60 MHz, using methanol as coupling liquid. Measurements were performed in hot-cell, even though the manipulation of unirradiated UO_2 does not require the same shielding as for irradiated nuclear fuels.
The investigation of SIMFUEL (60 GWd·t^{-1}M), instead was performed outside the hot-cell; the "cold" set-up with a sensor operating at 100 MHz was employed. Because of its toxicity, methanol was replaced by ethanol (v_{cl}= 1127 m s^{-1}) which caused higher attenuation of the signal, with a V(z) characterised by small amplitude oscillations; in any case four clear oscillations were generated, enabling a good accuracy in Rayleigh wave velocity determination (Figure 4.5).

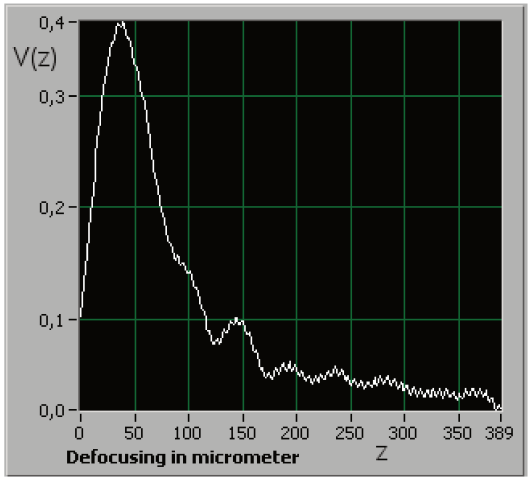

Figure 4.5 – V(z) obtained on SIMFUEL AECL with simulated burnup of 60 GWd·t^{-1}M using ethanol as coupling liquid. The oscillation amplitudes are sufficient and can be compared with those obtained by coupling methanol and uranium dioxide in Figure 3.4

4.3 Fuel matrix swelling and porosity via high frequency acoustic microscopy

4.3.1 Experimental validation of the relation between Rayleigh wave velocity and uranium dioxide density

The investigation of irradiated pellets presents significant complications in terms of availability of the samples, difficulties in obtaining an inspectable section and non-reversibility of the mount once the sample has been embedded. The latter implies that when the sample is prepared for ceramographic examination, the determination of the fuel density with immersion methods is precluded (i.e. methods based on the Archimedes principle).
The availabilities of methods enabling the determination of the density of embedded samples is a relevant point to improve the options for the post irradiation examination of irradiated fuel. Laux et al. [121] determined an empirical experimental law relating the density of the irradiated uranium dioxide fuels with the Rayleigh wave velocity, which unbinds the determination of the elastic properties by acoustic microscopy from other techniques.
As a starting point of this work, the law between the density and the Rayleigh wave velocity ($\rho = 3.3v_R + 2050$) has been validated and refined, thanks to a measurement campaign on NFIR special irradiation discs. Their densities was previously measured by weighing the sample in air and in 1,1,2,2-tetrabromoethane by immersion method [122]. Microstructural examinations of the samples, embedded in resin and mounted in sample holders (see Figure 4.6), were also previously performed in the frame of their post irradiation examination [122]: standard and large grains NFIR special irradiation discs presented the typical HBS structure.
The NFIR discs porosity was determined in the frame of the present study via SEM image analysis performed thanks to the shielded JEOL 6400® scanning electron microscope and to the MaxView® software package from SAMx. The images with a magnification of 600x were processed using Image-Pro Analyser®7.0 (MediaCybernetics, Rockville, MD, USA).
Acoustic microscopy measurements were performed on the samples of Table 4.2, by applying a frequency of 82 MHz (one of the resonance frequency of the acoustic sensor) and using methanol as coupling liquid. The densities were plotted as a function of the Rayleigh wave velocity together with data of [121] and then fitted by the relation proposed by Laux and co-workers [121] (see Figure 4.7).

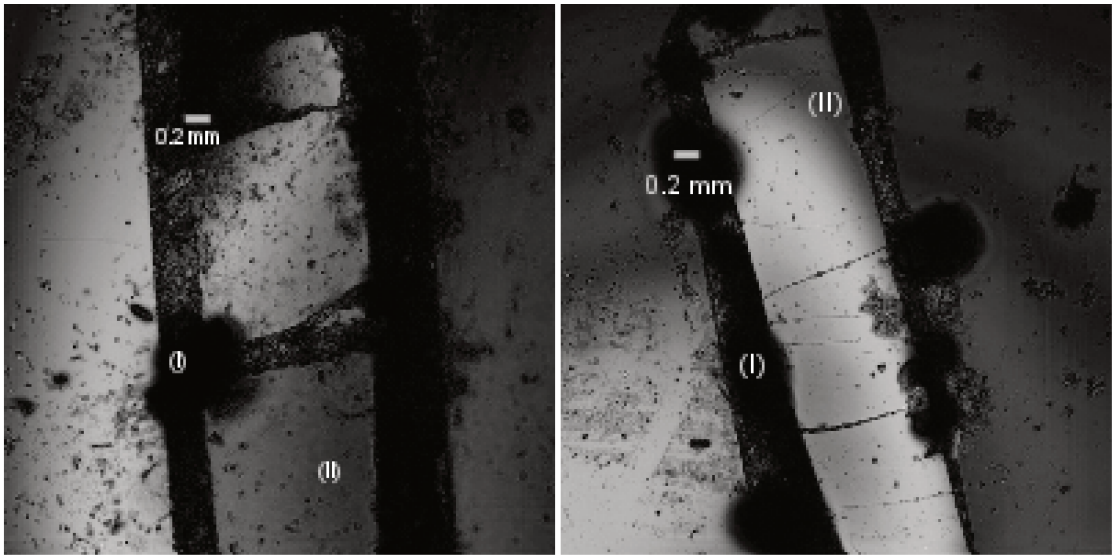

(a) (b)

Figure 4.6 – Acoustic images acquired at 140 MHz of: (a) large grain sample of 71.6 GWd·t^{-1}M average burnup and (b) kaolinite doped sample with 101 GWd·t^{-1}M average burnup.

The refined relation between density and porosity obtained is:

$$\rho = 3.3 \cdot v_R + 2037 \tag{4.1}$$

The adjusted[1] coefficient of determination R^2 for 4.1 is 0.53, but the average calculated bias between the densities, measured using the two techniques (acoustic microscopy and immersion method) is about 2%. The validity of relation 4.1 was also verified by calculating the densities of fresh fuels in references [110] and [77] from their reported porosity (p), thanks to the relation:

$$p = 1 - \frac{\rho}{\rho_{th}} \tag{4.2}$$

where ρ_{th} is the theoretical density TD. By fitting the data with 4.1 the adjusted coefficient of determination R^2 is 0.98.
The validity of relation 4.1 is thus proved by both the set of new experimental data and by the analysis of data from the literature. The relation is used throughout the thesis whenever the density is not known.

[1]See appendix A

Table 4.2 – NFIR unpublished data. Densities of the NFIR special irradiation discs determined by method based on the Archimedes' principle.

Samples	Burnup ($GWd \cdot t^{-1}M$)	Density $kg \cdot m^{-3}$
UO_2 standard grain (11.5 μm)	99.4	8820
UO_2 (doped with 2000 ppm Cr_2O_3)	96.7	9360
UO_2 large grain (29 μm)	99.4	9440
UO_2 (kaolinite doped)	101	9330
UO_2 large grain (29 μm)	71.6	9970
UO_2 standard grain (11.5 μm)	103.5	9320
UO_2 (doped with 2000 ppm Cr_2O_3)	48	10180
UO_2 standard grain (11.5 μm)	76.3	10030
UO_2 (doped with 8 wt% Gd_2O_3)	100	9260
UO_2 (0.25 wt% kaolinite doped)	81.2	9888

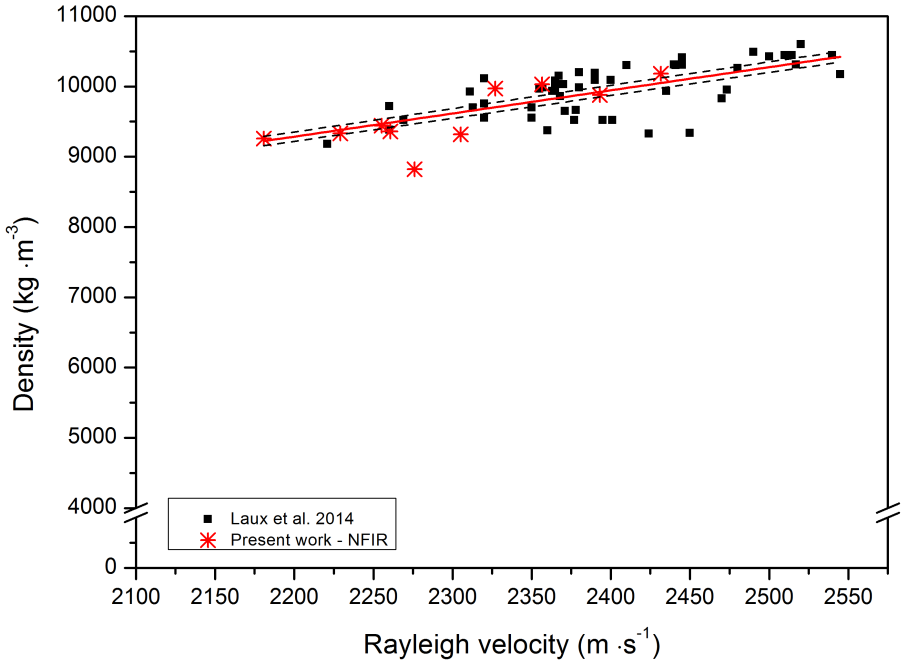

Figure 4.7 – Density of uranium dioxide fuels as a function of burnup. The red asterisks indicate the measurements performed in the present work on NFIR special irradiation discs, whereas the black squares refer to the measurements performed by Laux et al. [121]. Relation 4.1 is represented by the solid red line and its 95% of confidence level by the black dashed lines.

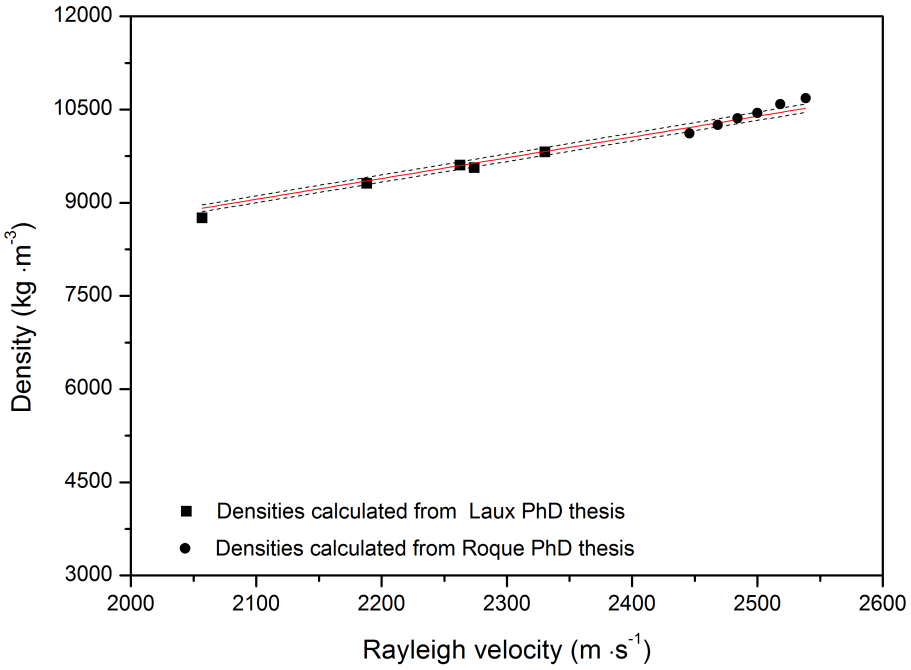

Figure 4.8 – Density of fresh uranium dioxide fuels calculated starting from the porosity values published in [110] and [77]. Relation 4.1 fitted to the data is represented by the solid red line (adjusted $R^2 = 0.98$). The dashed lines represent 95% of confidence level.

4.3.2 Determination of the fuel matrix swelling and porosity

As stated in 1.3.3, during the irradiation in nuclear reactor the volume of the nuclear fuel is subjected to swelling which is mainly caused by the precipitation of the insoluble fission products and, to a lesser extent, by the crystal volume increase due to irradiation defects.
Matrix swelling is defined as the fractional volume increase of the irradiated fuel matrix with respect to the fuel matrix volume before the irradiation [26] [32]. The total swelling, instead, is determined by the bulk volume increase due to the cumulative effect of matrix volume and porosity increases. The total fuel swelling can be expressed as in [32]:

$$total\ swelling = \frac{\Delta V^{total}}{V_0^{total}} = \frac{V^{total} - V_0^{total}}{V_0^{total}} \tag{4.3}$$

V_0^{total} and V^{total} are the initial and final bulk volumes. In terms of porosity we can write:

$$V_0^{total} = \frac{V_0^{matrix}}{1 - p_0} \tag{4.4}$$

$$V^{total} = \frac{V^{matrix}}{1 - p} \tag{4.5}$$

where p_0 and p are the initial and the final porosity of the nuclear fuel, respectively. To study the evolution of the matrix swelling with irradiation, the densities of the samples in Table 4.2 have been corrected for the porosity, hence their matrix density has been calculated, and then plotted as a function of burnup. In Figure 4.9 (a), the NFIR special irradiation discs's matrix densities, together with data from literature [32] [47, 118, 119, 121, 123], are plotted as a function of burnup; the best relation fitting the data (adjusted $R^2 = 0.5$) is:

$$\rho^{matrix} = \frac{\rho}{1 - p} = \rho_{th} \cdot (1 - 8 \cdot 10^{-4} \cdot burnup) \tag{4.6}$$

If relations 4.1, 4.3-4.6 are combined, the matrix swelling determined experimentally for irradiated uranium dioxide fuels, can be expressed as:

$$\frac{\Delta V^{matrix}}{V_0^{matrix}} = \frac{8 \cdot 10^{-4} \cdot burnup}{1 - 8 \cdot 10^{-4} \cdot burnup} \tag{4.7}$$

Figure 4.9 (b) shows the variation of the matrix swelling experimentally determined in the present experimental campaign. The matrix swelling as a function of burnup between 0 and 100 GWd·t^{-1}M results to be between 0.8 % and 1 % per 10 GWd·t^{-1}M. This means that the matrix swelling described by relation 4.7 is in very good agreement with the results published in the open literature [29] [30] [31] and is still valid up to 100 GWd·t^{-1}M.
The density of the uranium dioxide nuclear fuel decreases during the irradiation due to the combined effect of matrix swelling and porosity increase. If these phenomena are accurately separated, the matrix swelling of the fuel as a function of burnup can be determined and, in the same manner, the porosity of the irradiated nuclear fuel can be calculated.
The determination of the irradiated nuclear fuel porosity was performed on two irradiated samples and is presented in the following subsections.

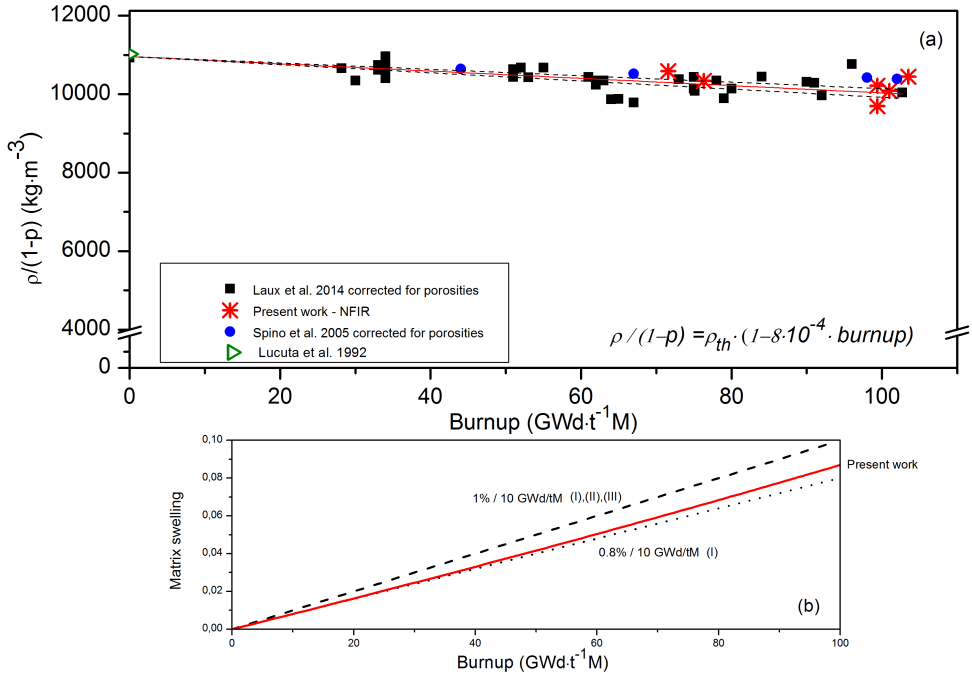

Figure 4.9 – (a) Matrix density versus burnup: red asterisks refer to NFIR data of the present work, blue circles to values published by Spino et al. in [32], black squares to data published by Laux et al. [121] corrected for porosities. The green triangle corresponds to unirradiated UO_2 measured by Lucuta et al. [118] (b) uranium dioxide fuel matrix swelling determined experimentally (red line) in comparison with the empirical laws published in literature. (I): [30], (II): [31] (III): [29].

Local porosity determination in irradiated uranium dioxide with 67 GWd·t^{-1}M

The investigated sample is a longitudinal section of a pellet taken from a commercial PWR fuel rod. The initial fuel enrichment was 3.95 % ^{235}U and the initial fuel density 10580 $\mathrm{kg \cdot m^{-3}}$. The pellet has an average burnup[2] of 67 GWd·t^{-1}M . Figure 4.10 shows an optical micrograph; for comparison, an acoustic image acquired at 140 MHz, 15 μm below the surface, is shown in Figure 4.11.
Rayleigh wave velocity measurements were performed along the radius of the pellet, trying to avoid big visible cracks, at steps of 200 μm, using methanol as coupling liquid. As in irradiated uranium dioxide there is a large number of discontinuity points that can affect the acoustic signature acting as scattering centres, the frequency was gradually reduced in order to enlarge the investigation area. V(z) was realized at 90 MHz, because at this frequency a high number of oscillations in the signal received by the piezoelectric was experimentally observed.

[2]See Table 4.1

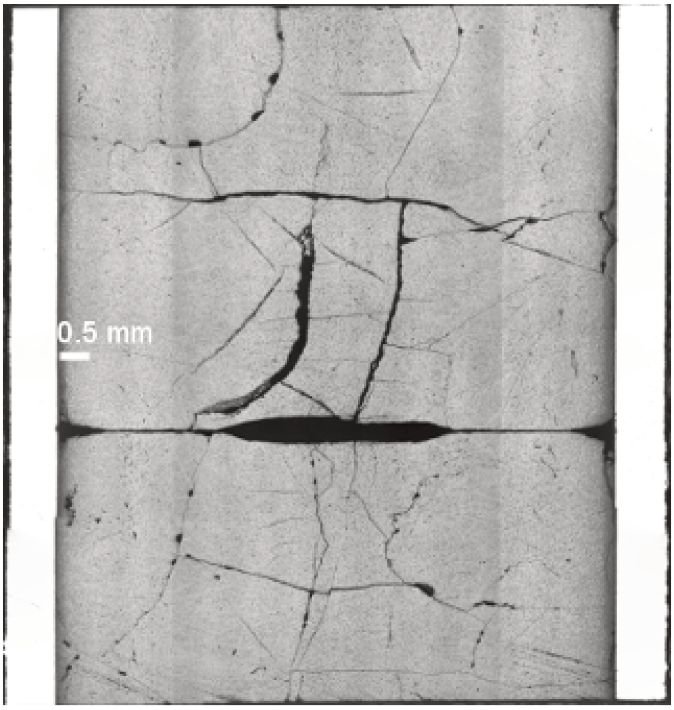

Figure 4.10 – Optical micrograph of the longitudinal section investigated via high frequency acoustic microscopy.

Figure 4.11 – Acoustic image of the longitudinal section of the investigated pellet, acquired at 140 MHz, 15 μm below the surface.

Fractional radial positions higher than 0.9 were not investigated, because the

pellet is subjected to a rapid increase of burnup at its edge, hence the spatial resolution of the available acoustic sensor cannot single out the differences in local properties at the rim. Every radial position examined corresponds to a specific local burnup; the burnup profile was calculated for this pellet using the TRANSURANUS fuel performance code [124] (Figure 4.12).

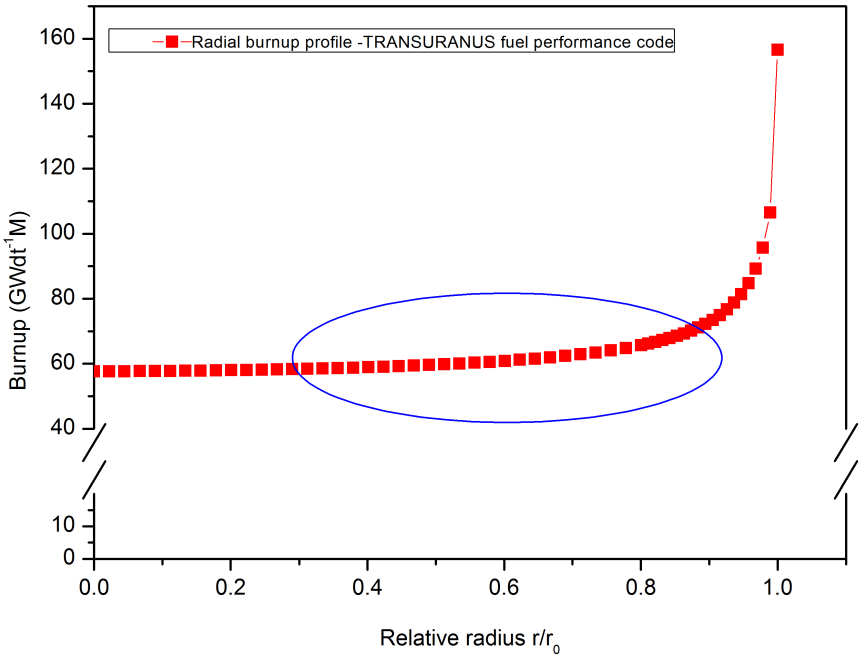

Figure 4.12 – Burnup profile along the radius of the 67 GWd·t^{-1}M pellet calculated with the TRANSURANUS fuel performance code [124]. The ellipse indicates the range of local burnup corresponding to the portion of radius investigated by acoustic microscopy. The exponential increase of the local burnup at the rim of the pellet is observable for radial positions greater than 0.9.

The porosity of the sample was determined by means of relations 4.1, 4.6 and the local values of burnup obtained with TRANSURANUS, thus:

$$p = 1 - \frac{3.3 \cdot V_R + 2037}{\rho_{th} \cdot (1 - 8 \cdot 10^{-4} \cdot burnup)} \tag{4.8}$$

The values measured along the radius of the pellet, corresponding to an area of about 200 μm, were then compared with the porosity previously determined using SEM image analysis (see [117] and [125]). The analysed images had a magnification of 500x and spatial resolution of 0.15 μm. In Figure 4.13 the local porosity determined by acoustic microscopy is plotted and compared to the porosity determined by SEM image analysis: the agreement between the two methods is excellent and

porosity values are comparable at all common radial positions investigated. Using both techniques, it is possible to observe a porosity increase close to $\frac{r}{r_0} = 0.6$, which corresponds to the boundary of the so called "dark-zone". This first approach to the determination of the irradiated uranium dioxide nuclear fuel porosity using acoustic microscopy, is promising and a validation of the method was thus subsequently performed.

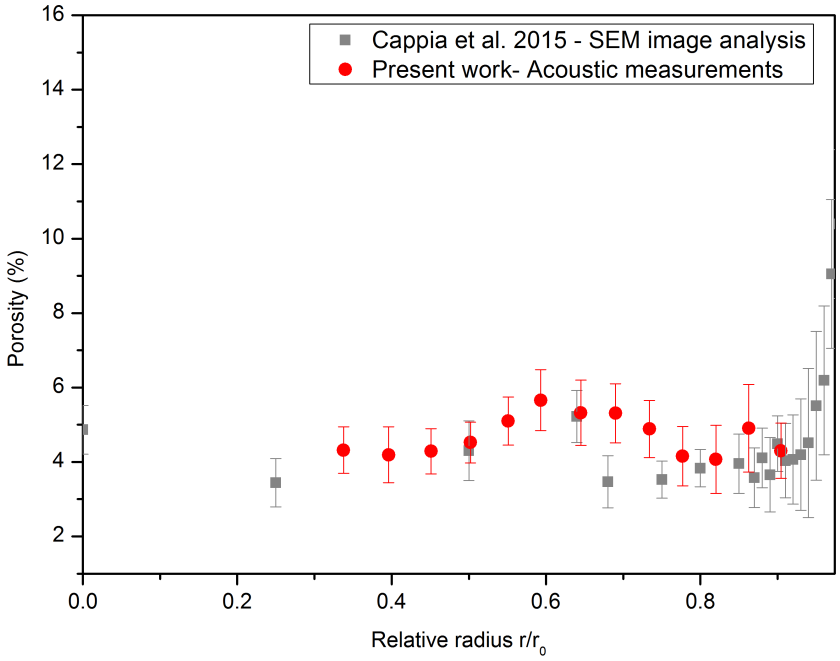

Figure 4.13 – Local porosity of the irradiated UO_2 pellet, with average burnup of 67 GWd·t^{-1}M calculated by high frequency acoustic microscopy (90 MHz) and compared with the porosity profile determined by SEM image analysis [117] [125]

.

Local porosity determination in irradiated uranium dioxide with 80 GWd·t^{-1}M

Relation 4.8 was also validated by measuring the local Rayleigh wave velocity along the pellet with 80 GWd·t^{-1}M [3]. For this measurement the sensor working at variable frequencies up to 140 MHz could not be used and a sensor working at 60 MHz, was used instead. This frequency gives acoustic images with lower resolution, but presents the advantage to be less sensitive to the discontinuity points

[3] See Table 4.1

(e.g. large pores, cracks), which normally constitute an obstacle for quantitative measurements on irradiated material and to reduce attenuation.
The pellet was from a commercial PWR rod at a position adjacent to the sample investigated by Spino and Papaioannou in [114] and had an initial enrichment of 3.8% ^{235}U. Rayleigh wave velocity measurements were performed at steps of about 400 μm, considering that this distance is larger than the spatial resolution of the technique at 60 MHz, using methanol as coupling liquid. The radial profile of burnup was calculated by Spino and Papaioannou [114] by means of the code Apollo-2. Data were fitted by an exponential relation (Figure 4.14) and the local values of burnup were introduced in equation 4.6, together with the measured local Rayleigh wave velocities and the local densities calculated with relation 4.1.

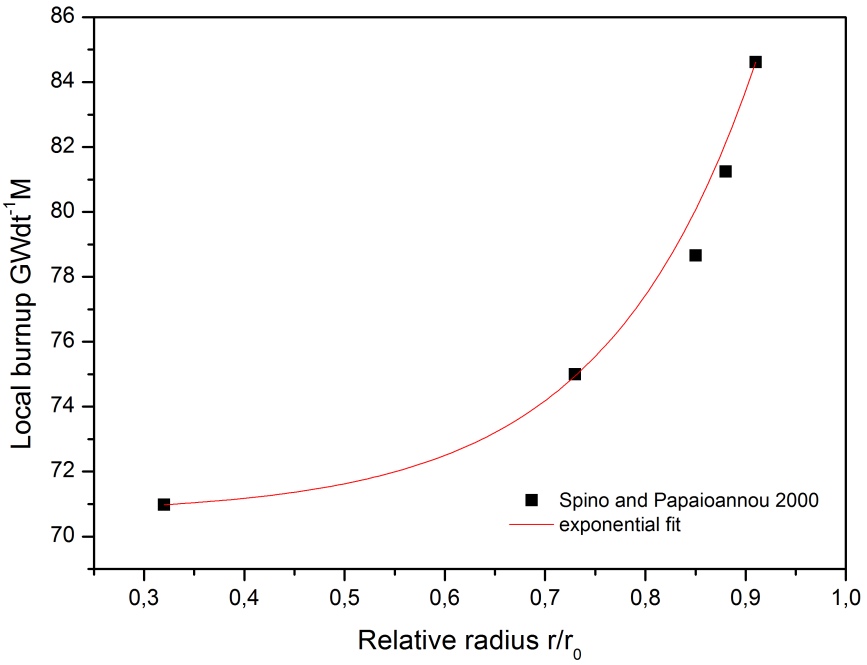

Figure 4.14 – Local burnup of pellet with average burnup of 80 GWd·t^{-1}M, calculated by means of Apollo-2 code by Spino and Papaioannou [114].

In Figure 4.15 the porosity determined at the examined radial positions of the pellet is compared to the porosities determined in [114] by optical image analysis. The local porosity determined by means of the Rayleigh wave velocities (by acoustic microscopy), is in excellent agreement with the local porosity determined via optical image analysis, also for this irradiated commercial PWR uranium dioxide pellet. Hence, this result confirms the validity of the relations proposed

and encourages their use for the post irradiation examination of irradiated nuclear fuel.

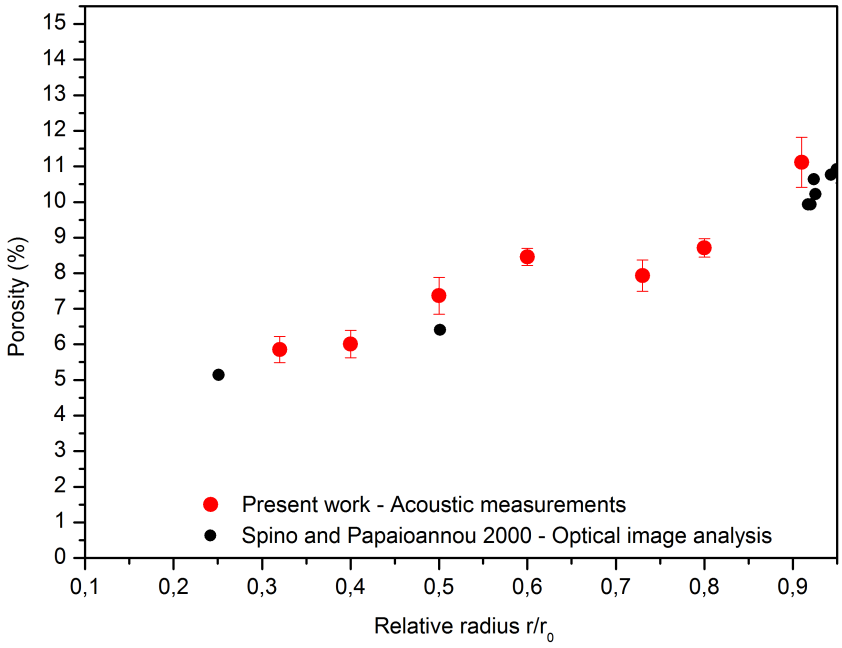

Figure 4.15 – Comparison between porosity determined by high frequency acoustic microscopy in the present experimental campaign and porosity determined by optical image analysis by Spino and Papaioannou [114].

4.3.3 Total swelling as a function of burnup

If the matrix swelling and porosity increase are not separated, the evolution of the irradiated nuclear fuel density with the burnup can be studied.
In Figure 4.16 the variation of the ratio bulk density-theoretical density (ρ/ρ_{th}) as a function of burnup is presented for the undoped UO_2 NFIR special irradiation discs (Table 4.2) and for UO_2 fuels with density previously measured using the Archimedes' principle; in particular, data for HBRP samples, SIMFUEL and special fuel irradiated in BR3 reactor [121] or published by Spino and co-workers [32] and by Bouloré [126] up to a burnup of 103.5 GWd·t^{-1}M are plotted. The relative density as a function of burnup, showed in Figure 4.16 can be expressed as:

$$\frac{\rho}{\rho_{th}} = 0.963 - 1 \cdot 10^{-4} \cdot (burnup)^{3/2} \tag{4.9}$$

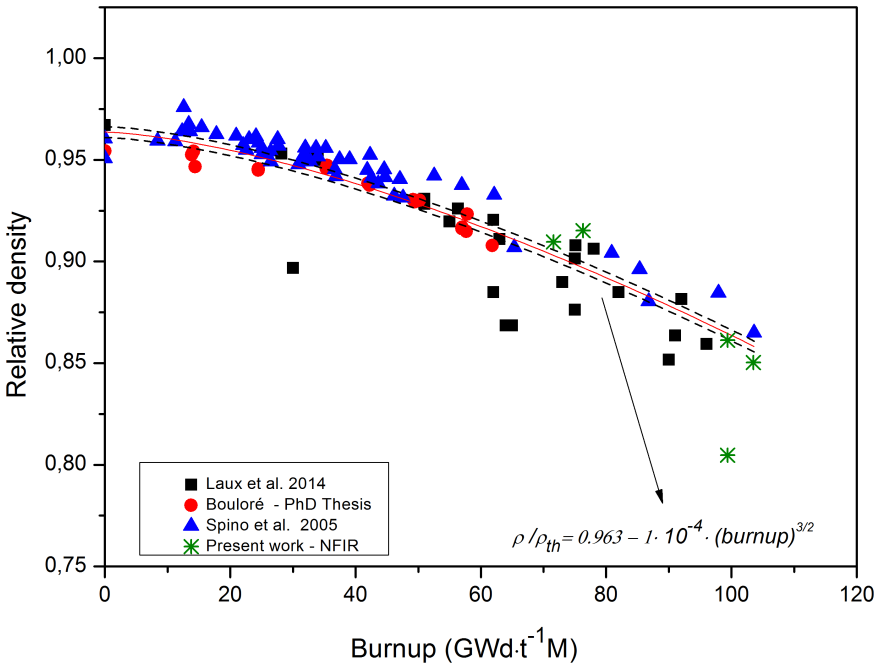

Figure 4.16 – Bulk density-theoretical density ratio of irradiated uranium dioxide fuel and unirradiated analogues as a function of burnup. Green asterisks: results obtained in the present work; blue triangles: samples measured by Spino et al. [32], red circles: density values of Bouloré in [126]; black squares: uranium dioxide data published by Laux et al. [121]. The red solid line is the fitting function (adjusted R^2 is 0.81), whereas the dashed lines correspond to 95% confidence level.

4.3.4 Summary

The experimental campaigns performed on both special irradiation discs and commercial PWR fuels[4], allow the achievement of three important results: *a*) the validation of a law correlating the Rayleigh wave velocity and the density of fresh and irradiated uranium dioxide, *b*) the determination of the matrix swelling as a function of burnup in the burnup range 0-100 GWd·t^{-1}M, *c*) the determination of the porosity in irradiated uranium dioxide fuel.
The main consequence is that using acoustic microscopy on a single side of a specimen it is possible to simultaneous investigate more than one property, thus reducing the requested characterisation time. Due to the high radiation dose which affects the integrity of electronic components and to the radiation protection prescriptions, time is a big constraint when working with irradiated material. Reducing

[4]see Table 4.1

the time necessary for assays, is thus highly beneficial to optimize operation and cost of the measurements.

4.4 Burnup effect on irradiated LWRs fuels Young's modulus

4.4.1 Young's modulus dependence on local burnup

The determination of Young's modulus can be performed by the single measurement of the Rayleigh wave velocity, as stated in section 2.4, if the Poisson's ratio is known. Laux et al. [77] [78] obtained a Poisson's ratio of about 0.3 for irradiated UO_2, which is very close to the value determined for fresh UO_2 [77] [90]. Hence, it is possible to assume a constant Poisson's ratio in irradiated uranium dioxide fuel and, by using 2.27 or relations 2.28 and 2.35 ($F(\nu) \sim 3.0$), Young's modulus of UO_2 can be expressed as:

$$E = 3.0\rho v_R^2 \tag{4.10}$$

or, if combined with 4.1 E can be calculated solely by measuring the Rayleigh wave velocity:

$$E = 9.9v_R^3 + 6111v_R^2 \tag{4.11}$$

Relation 4.11 was used to calculate the local Young's modulus (E) of the irradiated uranium dioxide with 67, 78, 80 and 100 GWd·t^{-1}M, with the aim of identifying variations associated with the microstructure restructuring into HBS. As stated in subsection 1.3.4, the radius of the pellet can be subdivided into roughly three regions: a central region where the structure is comparable with that of unirradiated uranium dioxide, at least in terms of grain size, a transition region where recrystallization (or polygonisation) begins and next to micrometric size grains the submicrometric grains are clearly visible and the fully restructured rim.
In Figure 4.17 a TEM micrograph of a HBRP special irradiation disc irradiated to 72 GWd·t^{-1}M at 923 K, gives an example of transition zone. In HBRP, as in NFIR discs, the burnup profile is quite flat, therefore the disc uniform burnup of about 72 GWd·t^{-1}M coincides with its local burnup.
Figure 4.17 (a) and (b) shows a zone of the sample where restructuration did not occur; in (b) TEM micrograph resolves fuel dislocations, but no signs of restructuration can be observed. In Figure 4.17 (c) and (d), intermediate grains with gas bubbles and small grains ($\sim$ 100 nm) bubble-free are present, proving the possible co-existence of restructured and unrestructured areas also at the microstructural

level.
In Figure 4.18 a HBRP disc with 55 GWd·t^{-1}M and Tirr = 683 K is examined. The TEM micrographs show clear unrestructured zones ((a), (b), (c))) and (d) zones where the grains have the typical HBS size.
The formation of high burnup structure is limited by the couple of values (*local burnup*, *temperature*); relevant thresholds have been identified by Sonoda et al. [127] to be (55-82 GWd·t^{-1}M, T $\leq$1373 $\pm$ 373 K); incipient HBS could have an impact on the fuel mechanical properties and is, thus, object of interest.

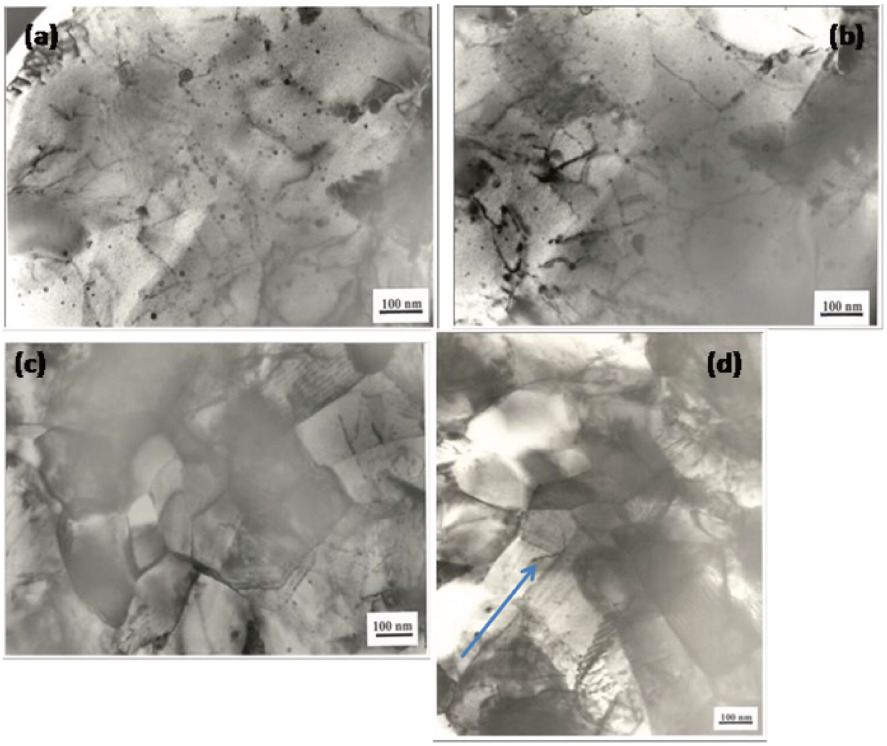

Figure 4.17 – TEM bright field images of a HBRP special irradiation disc with burnup of 72 GWd·t^{-1}M.

Figure 4.19 shows the variation of Young's modulus as a function of the local burnup for the samples with average burnup of 67, 78, 80 and 100 GWd·t^{-1}M. In the local burnup range investigated ($\sim$ 57-120 GWd·t^{-1}M) a global decrease of Young's modulus is observed, but it is worthwhile to stress that between 70 GWd·t^{-1}M and $\sim$ 90 GWd·t^{-1}M, the decrease is larger and Young's modulus has the same trend for the pellets with average burnup of about 80 GWd·t^{-1}M.
The pellet irradiated at 78 GWd·t^{-1}M, examined using SEM, presents an incipient HBS structure starting from $\frac{r}{r_0}$=0.4-0.5. For the pellet irradiated at 80 GWd·t^{-1}M, SEM examinations are not available, but the similar trend of Young's modulus as a function of the local burnup would suggest a similar microstructure in the common radial positions investigated

This fact would suggest that in the range of local burnup 70-90 GWd·t^{-1}M, Young's modulus is affected by the restructuring and its variation could be dependent upon the percentage of microstructure modified. Due to a lack of quantitative information on the microstructure an estimation cannot be performed, but these results would encourage a further and more systematic study in the above-mentioned burnup range to better explain these results.

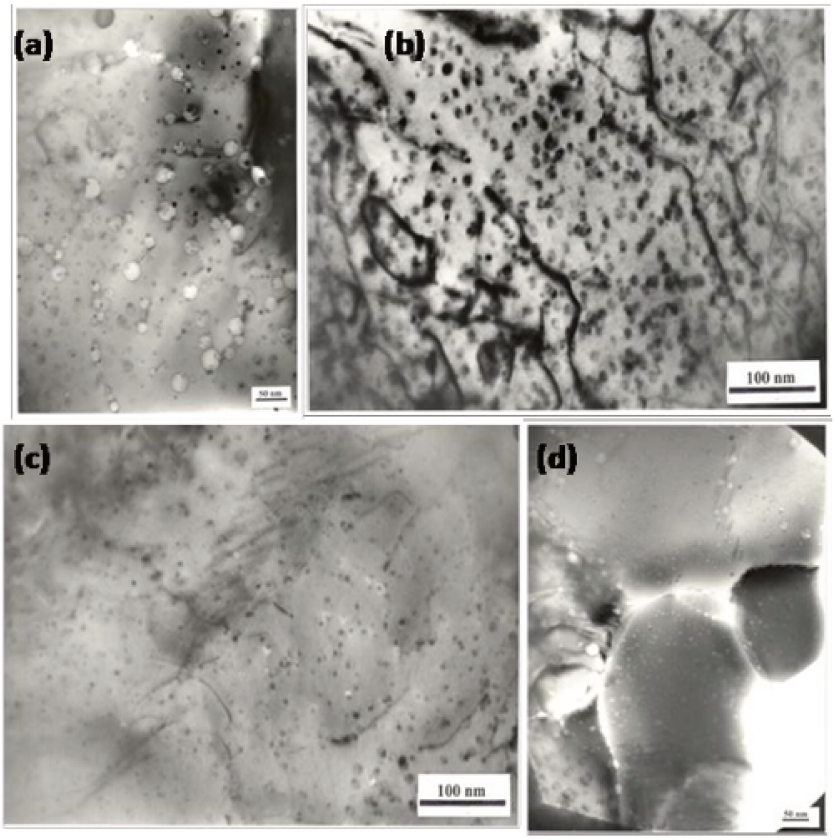

Figure 4.18 – TEM bright field images of a HBRP special irradiation disc with burnu of 55 GWd·t^{-1}M.

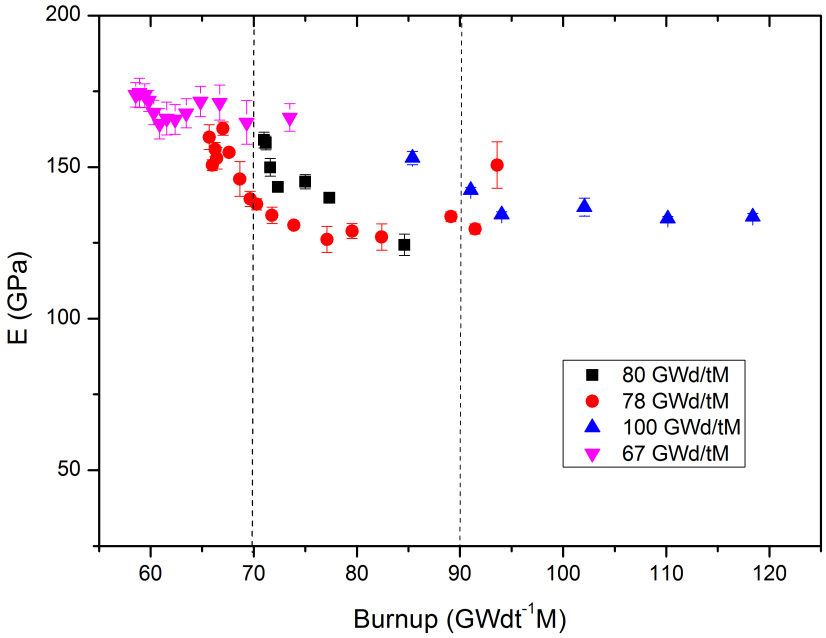

Figure 4.19 – Young's modulus versus local burnup for the commercial PWR uranium dioxide nuclear fuels of Table4.1.

4.4.2 Empirical model for Young's modulus as a function of the average burnup

Fuel performance codes employ direct correlations with Young's modulus to forecast in-pile nuclear fuel behaviour and life-time, thus to guarantee a safe operational fuel life. The global variation of Young's modulus as a function of the average burnup was studied in the present research work and an empirical law able to predict the evolution of E with the increasing burnup was determined. The empirical law extends the range of applications of the acoustic microscopy, as it can be used to evaluate the average burnup of irradiated nuclear fuels from the Rayleigh wave velocity.

To correlate Young's modulus and burnup of irradiated UO_2, experimental results obtained with samples of Table 4.1 were combined to data published in literature. The available experimental data were not covering the low burnup range, therefore relation 4.1 was used to derive the Rayleigh wave velocity from reported densities for low burnup and integrated in 4.11 to calculate Young's modulus. In particular, the following data have been used in the low burnup range: standard UO_2 fuel

from Assmann and Manzel [31] in the range $\sim$ 13-44 GWd·t^{-1}M and densities from Figure 3 of Harada and Doi [128], in the range $\sim$ 8-53 GWd·t^{-1}M (Figure 3 of [128] plots densities from standard grain UO_2 from [129] [130]).
The model considers the evolution of undoped uranium dioxide Young's modulus as a function of burnup. The dependence for UO_2 fuel containing additives is also considered. The measured Young's modulus of the Gd-doped NFIR special irradiation disc (Table 4.2) was corrected for its Gd-content. Corrections were also applied for Gd and Ce doped HBRP special irradiation discs measured by Laux and co-workers [77] [121]. In particular, on the basis of observations performed by Baron [131] and Watson [132]:

$$E((U,Gd)O_2) = E(UO_2) - 3.3(\%Gd) \tag{4.12}$$

Young's moduli of Ce-doped UO_2 HBRP special irradiation discs were corrected by fitting data of Yamada et al. [94] with the following relation (adjusted R^2= 0.9):

$$E((U,Ce)O_2) = E(UO_2) - 2.88(mol\%Ce) - 0.074(mol\%Ce)^2 \tag{4.13}$$

A correction was not applied for kaolinite doped specimens[5], mostly due to the very low dopant content (dopant content $<$ 0.5 wt%) and to the lack of reported relations between its content and Young's modulus. Rayleigh wave velocity as a function of Cr_2O_3 concentration, in fresh uranium dioxide, appears to be almost constant up to 1300 ppm in the study performed by Vincent Roque [107]; consequently a trend for Young's modulus variation is not observed. In the case of NFIR special irradiation discs, Cr_2O_3 concentration is 2000 ppm, which is outside the range examined by Roque but is in any case a low concentration and variations of Young's modulus are not expected; therefore E of chromium-doped samples was not corrected.
By combining relations 4.1, 4.11 and the relation describing the variation of density with burnup 4.9, the evolution of Young's modulus as a function of burnup can be described by:

$$E = -3.63{\cdot}10^{-10}{\cdot}burnup^{4.5} + 9.13{\cdot}10^{-6}{\cdot}burnup^{3} - 7.62{\cdot}10^{-2}{\cdot}burnup^{1.5} + 214 \tag{4.14}$$

Figure 4.20 shows the experimental results of the present research work plotted together with Young's modulus data from the literature. The fitting of 4.14 to the data (adjusted R^2=0.85), the corresponding 95% confidence level and its corresponding prediction band are also plotted. In particular. The Young's moduli from literature belong to:

[5]See Table 4.2

- Samples measured by Laux et al. [78] [121] using acoustic microscopy , in particular: fresh UO_2 fuels, chemical analogues of irradiated fuels (SIMFUEL [118] [119]), HBRP special irradiation discs [45] [46] [47], a MOX special irradiation disc [133] and special UO_2 fuel (8.6 % ^{235}U, grain size = 15-20 μm) irradiated in BR3 reactor [123] [134] [135];

- unirradiated UO_2 fuels in the porosity range 0-5%, measured with ultrasonic techniques by Phani et al. [136];

- two irradiated UO_2 samples measured with Knoop indentation by Spino [137]

. Over the whole range of burnup considered, namely 0-103 GWd·t^{-1}M, the reduction of average Young's modulus is $\backsim$ 33 %. Data estimated in the low burnup range would indicate a maximum Young's modulus increase due to densification of about 20 GPa. Data are more scattered between 60 GWd·t^{-1}M and 95 GWd·t^{-1}M: higher E values are observed for datapoints from special irradiation samples, namely HBRP-1, HBRP-2, HBRP-3 with E $\sim$ 174 GPa at about 90 GWd·t^{-1}M .
It is worthwhile to consider that HBRP-1 and HBRP-2 (irradiation temperature = 1000 K and 1333 K) show the HBS configuration, whereas HBRP-3 (irradiation temperature = 1493 K) is non-restructured [47].
In the same burnup range, Young's modulus values at or outside the lower limit of the prediction band correspond to two samples irradiated in the BR3 reactor, to a commercial PWR fuel and to HBRP-4 (E $\sim$ 145 GPa at about 70 GWd·t^{-1}M and 160 GPa at about 60 GWd·t^{-1}M). The fuel of the BR3 reactor is a special fuel irradiated under simulated LWR conditions [134], hence subjected to the typical LWR temperature gradients. BR3 fuel samples maintain the original grain size almost up to the interface with cladding, showing incipient high burnup structure only from $\frac{r}{r_0}$= 0.99 [123] [134] [135]. Samples irradiated in commercial PWR present, as stated in the previous section, a mid-pellet region characterised by the initial development of HBS (transition region) and full restructuring at the pellet rim. HBRP-4, extracted from a rod irradiated at 1373 K and pressurised with about 40 GPa of Ar, does not present evidence of high burnup structure [47].
Following the above considerations, it is difficult to explain these "outlier" values by making considerations based on the influence of irradiation conditions such as temperature or on the presence of high burnup structure.
The empirical law proposed describes satisfactorily (adjusted R^2=0.85) the evolution of Young's modulus with the increasing burnup, despite the data scattering. Data scattering could be due to the heterogeneous microstructure, to differences in chemical composition and irradiation history or simply to the measured samples conditions and configurations (most of the HBRP special irradiation discs were splitted in fragments or even powdered, especially at the highest burnup values).

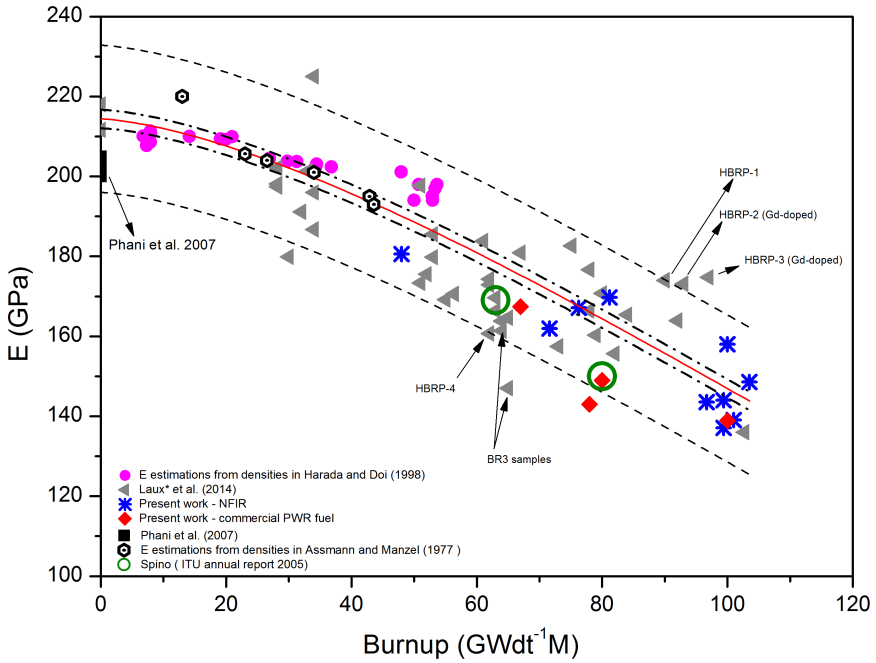

Figure 4.20 – Young's modulus of the investigated samples as a function of burnup. Blue asterisks and red rhombi: NFIR special irradiation discs and samples from the commercial PWR fuel, respectively. Magenta full circles: estimated Young's moduli from densities in [128]. Empty small circles: estimations from densities in [31]. Black squares: fresh uranium dioxide samples measured by Phani et al. [136]. Grey triangles: data from Laux et al. [121]; the asterisk in the legend indicates that corrections were applied for Gd and Ce doped HBRP samples. Green empty large circles : Knoop indentation results reported by Spino in [137]. The dot-dashed lines represent 95% of confidence level, whilst the external dashed lines indicate 95% prediction band. Data in common with Figure 4.16 have not been used during the fitting and in the calculation of the adjusted coefficient of determination (adjusted $R^2 = 0.85$).

4.5 Correlation between Young's modulus and Vickers microhardness

With the purpose of finding possible empirical relations between Young's modulus and hardness, using high frequency acoustic microscopy also to probe the hardness of irradiated uranium dioxide, Vickers microhardness (H_v) was measured along the radius of the pellet irradiated at 67 GWd·t^{-1}M [117].
Room temperature measurements were performed under N_2 protective atmosphere, employing a load of 0.98 N, loading rate of $9.8{\cdot}10^{-3}$ N $\cdot$ s^{-1} and a hold time at the maximum load of 12 s.

In Figure 4.21 Vickers microhardness values are plotted together with Young's moduli obtained at the same radial positions; the trends of microhardness and Young's modulus radial profiles are almost super-imposable: both decrease up to 0.6 fractional radial position and increase thereafter picking around 0.75. These results would suggest that, in ceramic uranium dioxide, Vickers microhardness is related to Young's modulus, and that by knowing the latter, microhardness can be estimated thanks to the ratio H/E.

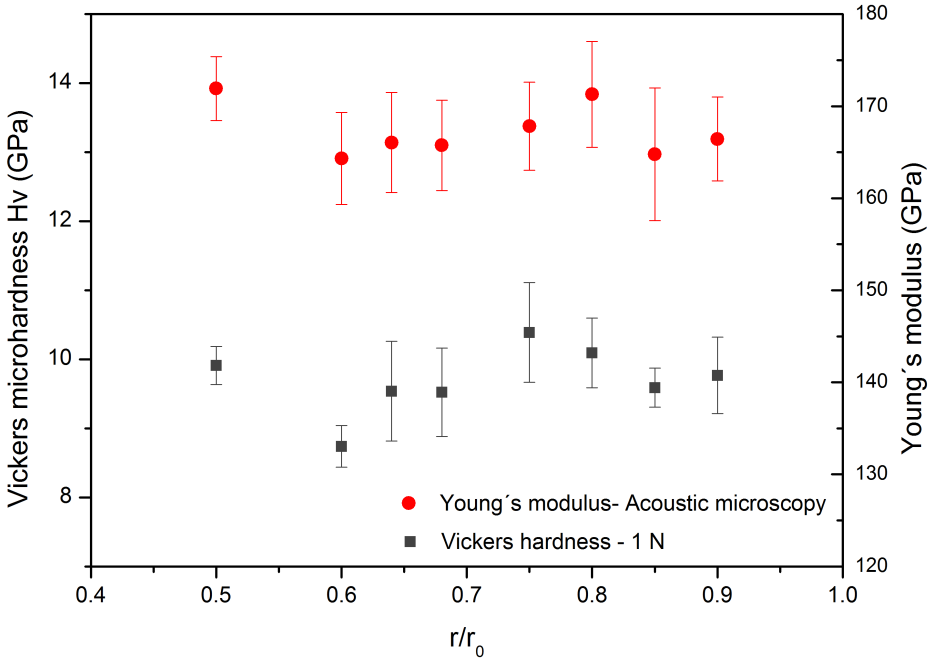

Figure 4.21 – Comparison between the Young's modulus profile and the hardness profile along the radius of the pellet with 67 GWd·$^{-1}$M [117].

In this particular case, the average value of the ratio H/E = 0.058 ± 0.002 [125] [117]. This correlation is in good agreement with the values found by Spino et al. [137] performing Knoop indentation on uranium dioxide with an average burnup of 60 GWd·t^{-1}M and 80 GWd·t^{-1}M (H/E = 0.054 and 0.056 respectively). Average Vickers microhardness for the examined pellet is H_v = 9.69 GPa, which is higher than the hardness obtained for fresh UO_2 in previous works (e.g. Kutty et al. [83] in section 2.6), but it is consistent with the increasing values of hardness in the central regions of 40-70 GWd·t^{-1}M fuel observed by Spino et al. in irradiated uranium dioxide [48]
When comparing the obtained H/E ratio with published data on unirradiated analogues, relatively large discrepancies are noticed. In particular there is not good agreement with the experimental results by Pujol et al. [138] obtained on

unirradiated SIMFUEL [138], namely H/E = 0.026 for simulated 3 at.% burnup and H/E = 0.024 for simulated 8 at.% burnup. Kutty et al. [83] found a value closer to the results obtained by Pujol et al. [138]: 0.0263 measuring the dense region of sintered UO_2 pellets, 0.0298 in porous patch, 0.0304 in the highly porous region of sintered UO_2 with 93 % TD.
The discrepancy observed between results obtained on irradiated and unirradiated fuel samples is mostly due to irradiation effects: porosity of uranium dioxide fuel increases during the irradiation, reducing the load-bearing area perpendicular to the applied stress, and in turn, producing hardness decrease [48]. Point defects produced by irradiation, on the other hand, cause hardness increase which has been observed in uranium dioxide fuel as a consequence of the auto-irradiation[6]. The different value of the ratio H/E ratio obtained in the present experimental campaign on irradiated fuel stresses the importance to consider all the effects acting on the fuel in reactor, which cannot be fully reproduced by unirradiated simulants. The values obtained for the investigated pellet with lowest average burnup, were confirmed for the pellet with average burnup of 100 $GWd\cdot^{-1}M$. Vickers microhardness was measured in a parallel experimental campaign [139] using a load of 0.98 N. In Figure 4.22, the Vickers hardness - Young's modulus ratio is quite constant for the local burnup range 90-113 $GWd\cdot t^{-1}M$ and has an average value of H/E of 0.056± 0.001 for the pellet at 100 $GWd\cdot t^{-1}M$.

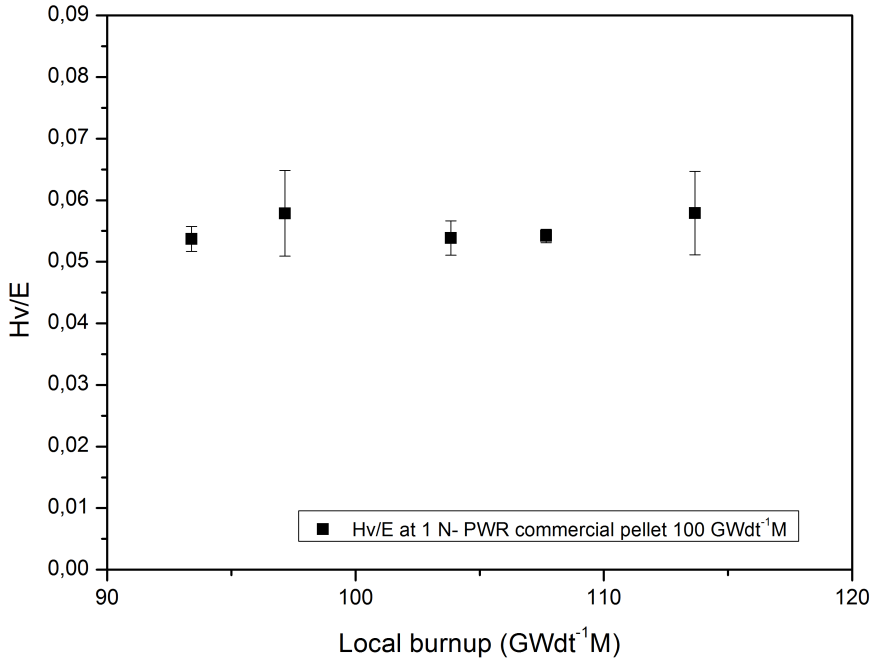

Figure 4.22 – H/E for commercial PWR pellet with average burnup of 100 $GWd\cdot^{-1}M$ [139].

[6]see section 1.4

4.6 Rayleigh velocity for thermal properties determination

In this section uranium dioxide thermal properties are investigated using the mathematical relations between acoustic velocities and thermal parameters. In particular, the evolution with the simulated burnup, of the full dense[7] UO_2 specific heat capacity C_p and B coefficient of thermal conductivity, is studied.
The Debye theory of specific heat relates heat capacity of materials to the transverse and longitudinal modes of propagation of acoustic waves, hence heat capacity to material's elastic properties. Debye theory assumes the solid to be an elastic continuum in which all the sound waves travel at the same velocity; Debye model is valid at low temperatures, when heat capacity is proportional to T^3, hence in proximity of 0 K.
Although discrepancies exist between the mean acoustic velocity v_m (equation 2.43) calculated at 0 K and at room temperature, the error in using room temperature elastic constants is low for a large number of materials [88] [140].
Elastic properties are also related to the mechanism responsible for heat transport in crystalline solids: as stated in section 2.8, thermal conductivity for an oxide ceramic as uranium dioxide depends on phonons contribution and can be expressed by relation 2.50 ($\lambda_c = \frac{1}{A+BT}$) for a broad range of temperatures. The parameter A is the sum of thermal resistance due to phonon scattering by point defects, impurities and extended defects; the product BT is related to the three phonons umklapp scattering. In the framework of the PhD thesis the applicability of 2.54 has been verified by determining all the parameters using the Rayleigh wave velocity; the methodology was at first validated on fresh uranium dioxide.[8]
Grüneisen parameter and Debye temperature were calculated by means of Rayleigh wave velocity corrected for full dense uranium dioxide: the measured average Rayleigh wave velocity was corrected by means of relation 4.1, in particular:

$$\rho_1 = 3.3 v_{R1} + 2037 \tag{4.15}$$

and

$$\rho_0 = 3.3 v_{R0} + 2037 \tag{4.16}$$

By combining 4.15 and 4.16 we obtain:

$$v_{R0} = \frac{1}{3.3}\left((3.3 v_{R1} + 2037)\frac{\rho_0}{\rho_1} - 2037\right) \tag{4.17}$$

[7] with zero porosity
[8] See subsection 4.2.2

where the density at zero porosity of the unirradiated uranium dioxide coincides with its theoretical density.
From the average Rayleigh wave velocity of 2482 m·s^{-1} the transverse and longitudinal velocities were calculated with:

$$v_t = \sqrt{\frac{\mu}{\rho}} \tag{4.18}$$

and

$$v_l = \sqrt{\frac{\lambda + 2\mu}{\rho}} \tag{4.19}$$

where the Lamé's parameter μ can be determined with [72]:

$$\mu = \frac{E}{2(\nu + 1)} \tag{4.20}$$

To calculate the coefficient B of this pellet, Poisson's ratio of unirradiated uranium dioxide was used, in particular values reviewed by Martin [90] were averaged, giving ν =0.3155, which was introduced in 2.27 and coupled with 4.20 to obtain v_t:

$$v_t = v_R \sqrt{\frac{3.04}{2(\nu + 1)}} \tag{4.21}$$

The Lamé's parameter λ expressed in terms of ν and μ is:

$$\lambda = \mu \frac{2\nu}{1 - 2\nu} \tag{4.22}$$

The longitudinal velocity, obtained by combining 2.27, 4.19 and 4.22 is:

$$v_l = v_R \sqrt{\frac{3.04(1 - \nu)}{(\nu + 1)(1 - 2\nu)}} \tag{4.23}$$

From the values of the longitudinal and the transverse velocities obtained, it was possible to calculate Debye temperature, specific heat capacities at constant volume (C_v) and at constant pressure (C_p) and finally the Grüneisen parameter (γ), thanks to relations 2.41-2.47. By means of Slack's relation 2.54, the coefficient B was deduced; in calculation the lattice parameter of the sample was unknown, hence a_0 = 5.4704 Å measured by Grønvold [141] was used.
Normally, thermal conductivity refers to 95% dense UO_2, hence B parameter must be corrected for 5% of porosity to be compared with values obtained with other techniques or published in literature. For this reason, Brandt and Neuer's rela-

tion [142] between thermal conductivities of full dense uranium dioxide and porous uranium dioxide, was used:

$$\lambda_0 = \frac{\lambda_p}{1 - \alpha p}, \quad \alpha = 2.58 - 0.5t \tag{4.24}$$

where p is the porosity fraction, λ_p the thermal conductivity of porous UO_2 and t= T(°C)/1000.
Table 4.3 lists the above-mentioned thermophysical parameters obtained in this experimental campaign.

Table 4.3 – Thermophysical properties at 300 K of unirradiated UO_2 determined using the measured Rayleigh wave velocity at 60 MHz.

θ_D(K)	C_v(J·kg^{-1}K^{-1})	C_p(J·kg^{-1}K^{-1})	γ	B (m·W^{-1})
390.9	254.9	256.6	2.1	$2.80 \cdot 10^{-4}$

Thermophysical parameters in Table 4.3 can be compared with data published in literature, in particular θ_D of UO_2 measured by Willis is $377 \pm 10K$ [143], C_p recommended by Fink [144] is about 237 J·kg^{-1}K^{-1} and $\gamma = 2$ (Pillai et al. [96] from Momin and Karkhanavala [145]).
B in Table 4.3 can be directly compared to the experimental value of $2.44 \cdot 10^{-4}$ m·W^{-1} obtained by measuring the thermal diffusivity of an analogue UO_2 sample (in terms of synthesis method and structure). The measurement was performed at the Joint Research Centre Karlsruhe using the "laser-flash" technique described in a publication of Ronchi et al. [146].
Bias between B calculated using Slack's model [104] and the experimental laser flash technique is about 15%; this discrepancy could be explained if we consider that both Poisson's ratio and lattice parameter were not measured, instead values published in literature were used, although the Poisson's ratio in calculation of Bulk modulus shall be accurately determined. The fresh UO_2 pellet measured in this experimental campaign is characterised by a non perfectly homogeneous distribution of density: the local density varies along a distance comparable with the resolution of the instrument at 60 MHz (see Figure 4.23). This in turn increases the uncertainties on the Rayleigh wave velocities (uncertainties are ~ 2 %).
Slack's model was also applied to SIMFUEL [118] [119] with simulated burnup of about 60 GWd·t^{-1}M. The thermophysical parameters for this sample are listed in Table 4.4. In addition to the sample measured, Rayleigh velocities of SIMFUEL at 0, 30 and 80 GWd·t^{-1}M, calculated from [121], were used to determine specific heat capacities and parameter B. Lattice parameters and densities measured and

published by Lucuta et al. [118] [119] were used in calculation, Poisson's ratio was maintained 0.3155, as for unirradiated uranium dioxide.

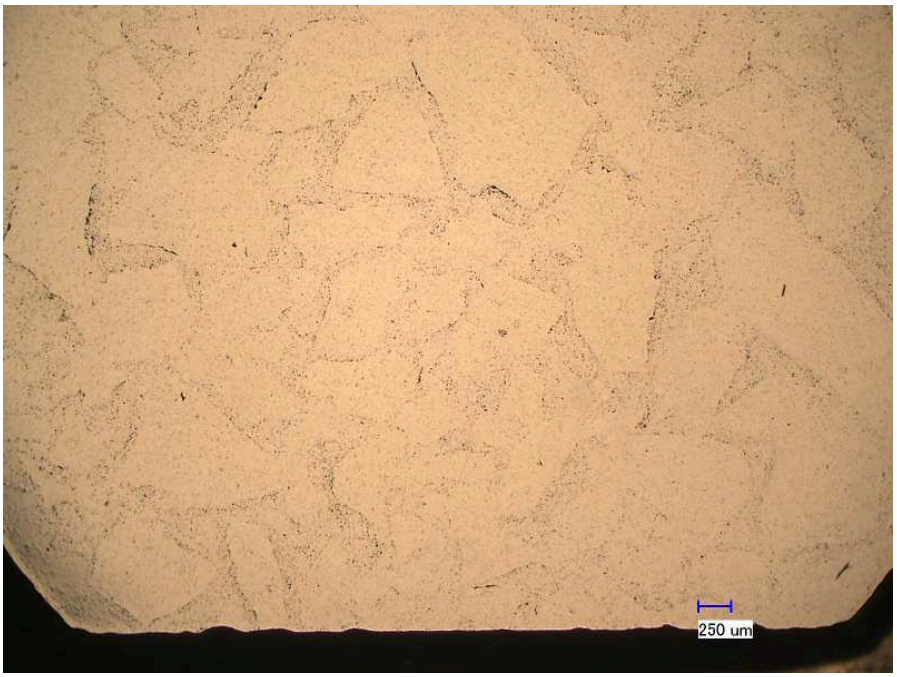

Figure 4.23 – Optical micrograph of the fresh UO_2 measured in the present experimental campaign

Table 4.4 – Thermophysical properties at 300 K of SIMFUEL (simulated burnup 60 GWd·t^{-1}M) determined using the measured Rayleigh wave velocity at 100 MHz.

θ_D(K)	C_v(J·kg^{-1}K^{-1})	C_p(J·kg^{-1}K^{-1})	γ	B (m·W^{-1})
381.1	255.9	257.2	2.0	$2.75 \cdot 10^{-4}$

In Figure 4.24, B coefficients determined in this experimental campaign are compared with values obtained by Lucuta et al. [118] which are represented by the relation:

$$B = (2.2 - 0.0005\ burnup) \cdot 10^{-4} \tag{4.25}$$

with burnup expressed in GWd·t^{-1}M. The average bias between values obtained by Lucuta and co-workers [118] and this work is about 20-30 %, but it is worthwhile highlighting that the parameter B decreases slightly with the increasing simulated burnup, in the range 30-80 GWd·t^{-1}M, in agreement with relation 4.25.

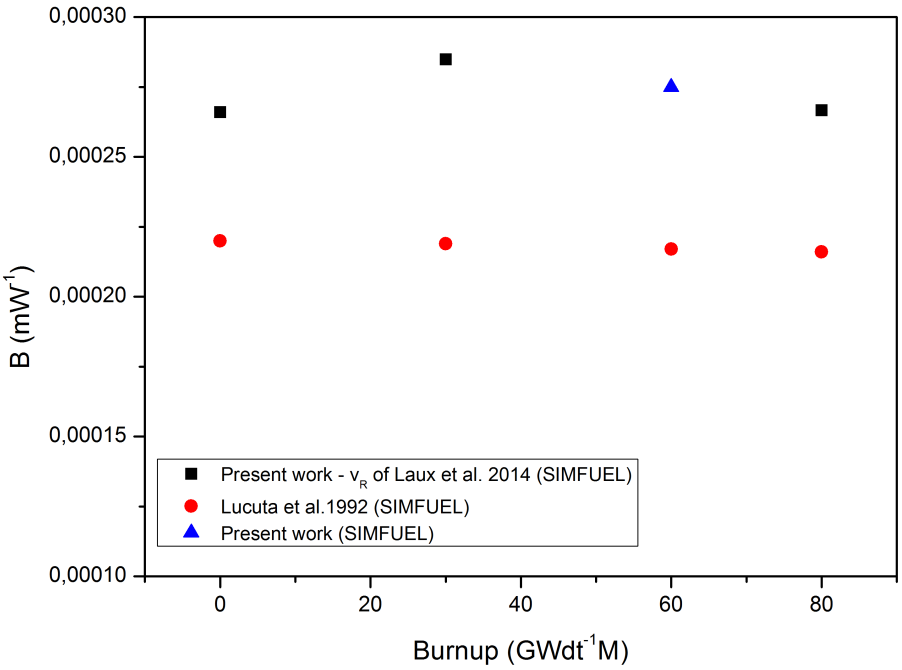

Figure 4.24 – B parameter of thermal conductivity calculated in the present experimental campaign: blue triangle refer to B calculated by means of Rayleigh wave velocity measured on SIMFUEL with burnup of 60 GWd·t^{-1}M; black squares refer to B calculated by using Rayleigh wave velocities deduced from [121]. Red circles refer to B parameter measured by Lucuta et al. [118]

A comparison between C_p calculated using Rayleigh wave velocity and C_p measured by Lucuta et al. [118] is available in Figure 4.25. The bias between C_p of the present work and of [118] is about 8% for the unirradiated UO_2, 6% for 30 GWd·t^{-1}M and about 5% for 80 GWd·t^{-1}M. The sample with simulated burnup of 60 GWd·t^{-1}M measured in the present work was not included because specific heat capacity for this burnup is not reported.
C_p increases by about 2% for the sample at simulated 30 GWd·t^{-1}M and about 4% at 80 GWd·t^{-1}M in Lucuta [118], whereas C_p is practically constant in the present work between 0 and 80 GWd·t^{-1}M. Matzke et al. [120] re-measured specific heat capacities of above-mentioned samples at different temperatures, but due to the lack of data at 300 K a comparison cannot be performed. At the closest temperature available, 400 K, values are consistent with data of Lucuta et al. [118], but the simulated burnup effect has a lower impact on the specific heat capacity. A difference in specific heat capacity is not experienced between 0 and 30 GWd·t^{-1}M and a difference of about 0.7% characterises the sample at 80 GWd·t^{-1}M, which would be in agreement with the results obtained in the present work.
Present work hence, agrees with precedent experimental research works in observing an almost negligible burnup effect on the specific heat capacity.

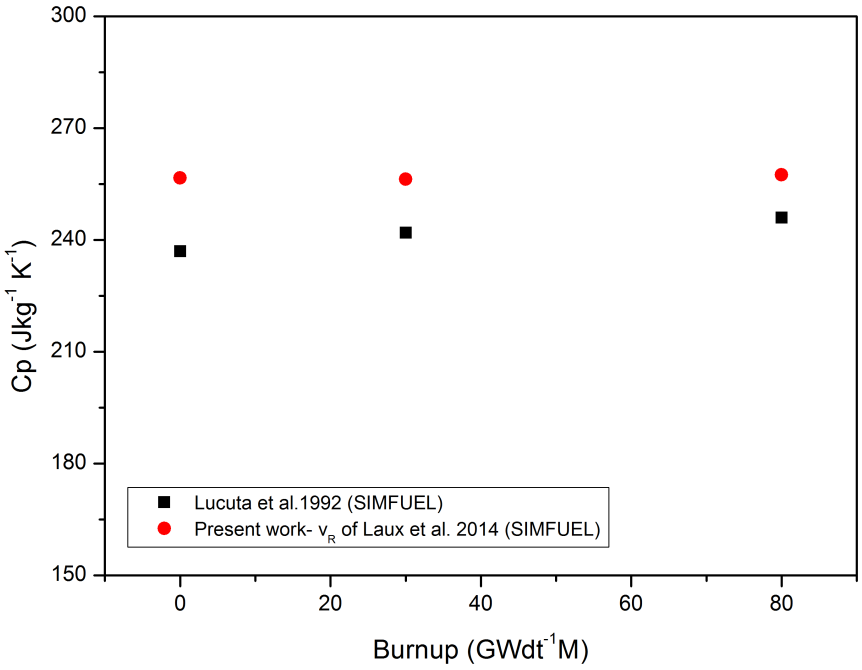

Figure 4.25 – Specific heat capacity at constant pressure. Red circles: C_p calculated in the present work using Rayleigh wave velocities deduced in [121]. Black squares: C_p measured by Lucuta et al. [118]

4.7 Summary

Section 4.4 is focused on the Young's modulus dependence on local and average burnup of irradiated nuclear fuels. In subsection 4.4.1, Young's modulus local variations are assessed along the radii of irradiated uranium dioxide pellets in the range of local burnup $\sim$ 57-120 GWd·t^{-1}M. A global decrease is observed in the range investigated, even though E decrease is more significant between 60 GWd·t^{-1}M and 90 GWd·t^{-1}M. This range of burnup corresponds to the transition region of the uranium dioxide pellet with an average burnup of 78 GWd·t^{-1}M; the decrease of Young's modulus, therefore, could be associated to the microstructure modification in the transition region. A confirmation of these results requires further studies which should particularly consider the areas of the pellet where the original microstructure starts evolving in HBS.
In subsection4.4.2 the variation of Young's modulus as a function of the average burnup is studied in the wide burnup range 0-100 GWd·t^{-1}M, by combining experimental results obtained via acoustic microscopy and data available in literature. In this study, the effect of dopants in fuel containing additives is also considered:

in particular correction factors based on the literature are introduced for Young's modulus of Gd-doped and Ce-doped nuclear fuel. Corrections are not applied in the case of kaolinite and chromium-doped uranium dioxide, considering the low concentration of these latter additives and the lack of available relations between E and their concentrations. Young's modulus of irradiated LWR fuels decreases of about 33 % between 0 and 100 GWd·t^{-1}M. By combining the empirical relations between Rayleigh wave velocity and density 4.1, density and average burnup 4.9, and Young's modulus and Rayleigh wave velocity 4.11, an empirical model describing the evolution of Young's modulus as a function of burnup is finally proposed. Section 4.5 considers the experimental campaign performed in order to determine a correlation between Young's modulus and Vickers microhardness for irradiated uranium dioxide nuclear fuel.
In the burnup range $\sim$ 60-113 GWd·$^{-1}$M, the ratio between Vickers microhardness and Young's modulus is found to be constant, but almost 100% higher than the ratio measured in unirradiated uranium dioxide or in chemical analogues of irradiated fuels [83].
The higher H/E ratio demonstrates that chemical analogues cannot completely simulate the behaviour of irradiated fuel: in particular the swelling due to porosity increase is missing, as well as point and extended defects produced during irradiation in reactor or during storage.
The existence of a correlation between hardness and Young's modulus for ceramic uranium dioxide could find an explanation in the elastic component of the deformation during indentation tests which characterises brittle ceramic materials [147]. In the present research work the correlation has been investigated only empirically, thanks to a joint measurement campaign [139] and a parallel Vickers microhardness measurement campaign on the same sample (100 GWd·$^{-1}$M) [139].
Considering the constant value H/E (about 0.056), Rayleigh wave velocity measurements could be used also to probe the hardness of irradiated uranium dioxide fuels, enabling fast post irradiation examination or providing an additional technique for the validation of results.
In section 4.6, correlations between Rayleigh wave velocity in material and its thermal properties are investigated. Rayleigh wave velocity is used to calculate the Debye temperature (Θ_D), the specific heat at constant volume and at constant pressure (C_v, C_p) and the Grüneisen parameter (γ) of both fresh uranium dioxide and chemical analogues of irradiated uranium dioxide (SIMFUEL [118] [119] [120]). The agreement with the Debye temperature and the Grüneisen parameter of fresh uranium dioxide in literature is excellent, whereas there is a bias of $\sim$ 8% between C_p recommended by Fink [144] and the value obtained by acoustic microscopy.
Θ_D, C_p and γ were used to calculate the B coefficient of thermal conductivity thanks to the model developed by Leibfried and Schlömann [102], refined by Ju-

lian [103] and revised by Slack [104].
The value of the coefficient B for fresh uranium dioxide is 15% higher than B measured by the laser flash technique on an analogue sample.
The same parameters were calculated for chemical analogues of irradiated uranium dioxide and the results would suggest a negligible burnup effect on the specific heat capacity at constant pressure. The coefficient B, decreseas slightly as a function of the simulated burnup up to 80 $GWd \cdot t^{-1}M$, in agreement with the trend observed by Lucuta et al. [118] [119] and Matzke et al. [120]. The coefficient B calculated using high frequency acoustic microscopy is 20%-30% higher than B measured by Lucuta and co-workers [118].
In future it is envisaged to study in depth the variation of Poisson's ratio as a function of burnup in order to adjust the results obtained in the present research work.

4.8 Conclusion

In Chapter 4 the elastic properties and microstructural features of irradiated nuclear fuels, in particular UO_2 were studied. In the frame of the related experimental campaign, the results obtained on uranium dioxide samples, irradiated under different irradiation conditions and broad burnup range, enabled to propose an empirical model to describe the evolution of Young's modulus as a function of the burnup. Moreover, by studying the variation of the density with the burnup, the evaluation of the local porosity and the total fuel swelling was possible. The results obtained in Chapter 4 were integrated in the fuel performance code TRANSURANUS. The empirical model that is proposed here can either be incorporated in other fuel performance codes, or used to derive the average unknown burnup of an irradiated uranium dioxide fuel. Moreover, the present study gives the possibility to estimate, thanks to the Rayleigh wave velocity, the hardness of the nuclear fuel. Another important result is the correlation between elastic and thermal properties. This correlation allowed to derive important thermal parameters solely by means of the Rayleigh wave velocity.

Chapter 5

Ageing effect and radiation damage

Contents

5.1 Introduction

The aim of the second part of the thesis is the investigation of the auto-irradiation effect on nuclear fuel. Nuclear fuels are subjected to radiation damage[1] during their life in reactor and after their discharge from the core and disposal in storage; this phenomenon influences physical, thermal and mechanical properties of both in-reactor and spent fuel.
Many publications have treated the production of lattice defects and consequent variation of lattice parameter in irradiated UO_2. Weber [34] studied the variation of lattice parameter under alpha-irradiation and its recovery during annealing at

[1] See subsection 1.3.2

different temperatures [28], Nakae et al. [148] determined the volume change due to fission in UO_2 at two different fission doses (about 10^{14} and 10^{18} fissions $\cdot$ cm^{-3}), Kato et al. [149] studied variation of lattice parameter of MOX samples stored for over thirty years, Prieur the variation of diameters in (U,Am)O_{2+x} pellets [9] and Wiss et al. [35] studied both variation of lattice parameter and Vickers microhardness under simulated storage conditions. Lattice parameter increase, hence lattice volume expansion was determined in all the abovementioned works.
Limited studies on the variation of uranium dioxide elastic properties due to charged particle irradiation, in particular alpha irradiation, are available in literature: Elbakhshwan and co-workers [150] determined, via nano-indentation and finite element modeling, hardness, yield strength and Young's modulus variation as a function of Kr^+ irradiation dose (at 600 keV), observing a decrease of Young's modulus up to about 10^{14} ions$\cdot$ cm^{-2} followed by a Young's modulus increase at higher irradiation doses. Debelle et al. [151] studied the variation of stress and strain when implanting 20 keV He in uranium dioxide single crystals and they observed an increase of stress and normal strain magnitudes as a function of damage level (dpa) followed by a relaxation.
In the present experimental campaign ^{238}Pu-doped UO_2 and MOX have been investigated by X-ray diffraction, to evaluate the variation of lattice parameter, and by high frequency acoustic microscopy to study the impact of auto-irradiation on elastic modulus. Alpha-doped UO_2 can simulate the behaviour of uranium dioxide fuel after many years of storage thanks to the fast accumulation of damage due to the addition of short-lived alpha-emitters. Storage effect is also evaluated on commercial PWR fuels described in Chapter 4. The effect of ion implantation on Young's modulus of UO_2 has also been investigated by high frequency acoustic microscopy.

5.2 Materials

To determine the variation of lattice parameter due to alpha self-irradiation and the impact that auto-irradiation and implantation have on Young's modulus, the samples listed in Table 5.1 were investigated. Two uranium dioxide samples were doped with $\sim$ 0.1 and 10 wt% of PuO_2 (Pu-01 and Pu-10 respectively) containing 66.7 % ^{238}Pu (half life = 87.74 y), to simulate in laboratory time scale irradiation effects produced during long-term storage of spent fuel. To ensure homogeneity in mixing Pu and UO_2 matrix, powders were synthesised by a sol–gel technique, based on coprecipitation from a nitric acid solution and then they were pressed and sintered at 1973 K in Ar/H_2 [152], obtaining pellets with 92-94% TD. The

microscopy examinations of both samples did not show Pu-rich phases or Pu agglomerates; the average grain size was slightly smaller than 10 μm, which is the typical grain size of UO_2 fuel [152]. Figure 5.1 (a) shows an acoustic image of the UO_2 sample doped with 0.1 wt% of Pu (Pu-01), acquired at 60 MHz using methanol as coupling liquid. On the right, Figure 5.1 (b) shows the sample mounted on the holder. The higher damage level of the sample doped with 10% of Pu (Pu-10) is qualitatively observable in Figure 5.2 (a) where an acoustic image, acquired under the same conditions as Figure 5.1 (a), depicts an highly cracked structure and in Figure 5.2 (b), which shows the sample mounted on the holder after several years of storage[2].

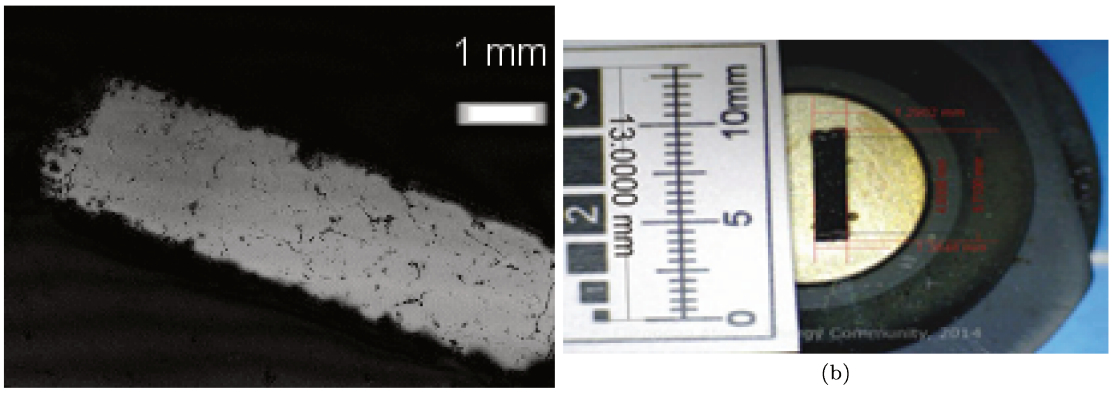

(a) (b)

Figure 5.1 – (a) Acoustic image of Pu-01, acquired at 60 MHz (b) The same sample mounted on a holder.

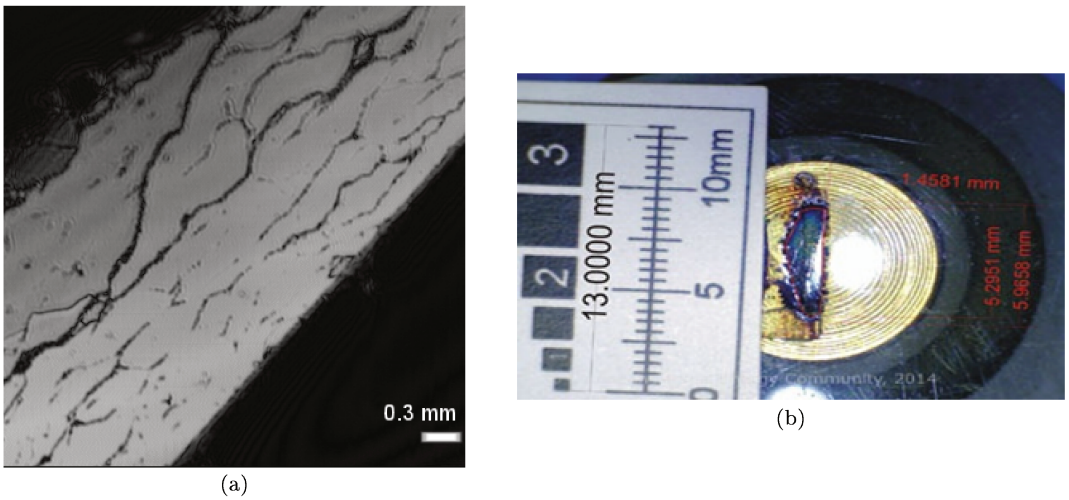

(a) (b)

Figure 5.2 – (a) Acoustic image of Pu-10, acquired at 60 MHz (b) The same sample mounted on a holder.

[2]Pictures of Pu-doped specimens on sample holders were acquired several years before acoustic measurements

Two MOX samples were analysed in the present campaign: in particular the pellet of Figure 5.3 with $(U_{1-x},Pu_x)O_{2.000}$, where x= 23.8% (Phenix [153]) and a sample characterised by 45 wt% of Pu, known as TRABANT2 (Figure 5.4). TRABANT2 was prepared via sol-gel method [154] and is characterised by a slight substoichiometry (O/M = 1.990).

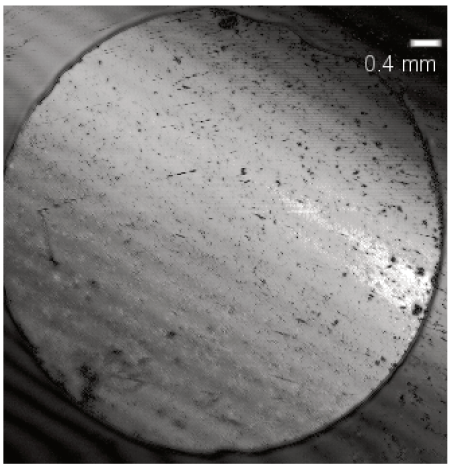

Figure 5.3 – Acoustic image of the Phenix pellet acquired at 60 MHz using methanol as coupling liquid.

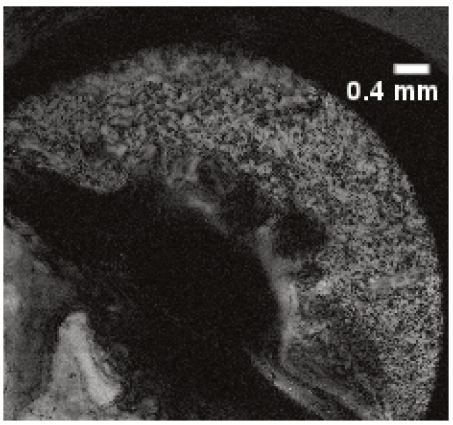

Figure 5.4 – Fragment of Trabant2 pellet measured via high frequency acoustic microscopy at 60 MHz, with methanol as coupling liquid.

Auto-irradiation was also studied on commercial PWR fuels: in particular using two of the specimens of Table 4.1 with average burnup of 80 and 100 $GWd{\cdot}t^{-1}M$ and an additional longitudinal section of the rod irradiated at 80 $GWd{\cdot}t^{-1}M$ which was examined before and after heating treatment.
The effect of irradiation damage on Young's modulus was finally completed by measuring an implanted uranium dioxide specimen with ^{238}U irradiated in Uni-

versal Linear Accelerator, Gesellschaft für Schwerionenforschung, Darmstadt, Germany [155].

Table 5.1 – Fuel samples investigated using X-ray diffraction (XRD) and high frequency acoustic microscopy (AM) in the present study. The age of the implanted sample is not relevant.

Samples	Age (years)	Comments	Technique
Pu-01	19	$^{238}U_{0.999}Pu_{0.001}O_2$	AM
Pu-10	19	$^{238}U_{0.9}Pu_{0.1}O_2$	XRD and AM
UO_2	23	Commercial PWR fuel. Average burnup = 80 GWd·t^{-1}M; see Chapter 4	AM
UO_2	14	Commercial PWR fuel. Average burnup = 100 GWd·t^{-1}M; see Chapter 4	AM
UO_2	23	Commercial PWR fuel. Average burnup $\sim$ 80 GWd·t^{-1}M)	AM
Phenix	18	$^{238}U_{0.762}Pu_{0.238}O_2$	AM
TRABANT 2	18	$^{238}U_{0.55}Pu_{0.45}O_{1.990}$	XRD and AM
UO_2	-	Implanted with ^{238}U Energy=2.7 GeV fluence= 5·10^{10} ions·cm^{-2}	AM

Samples in Table 5.1 were carefully polished prior to the measurements.

5.3 Lattice parameter variation

Lattice parameters of Phenix, Pu-10 and TRABANT2 samples were measured by X-ray diffraction acquiring scans from 20° to 120° using 0.0086 step-intervals and counting steps of 5 s. Figure 5.5 gives an example of an XRD spectrum obtained with TRABANT2; the sample appears monophasic (FCC structure) with a lattice parameter of 5.4512 Å.

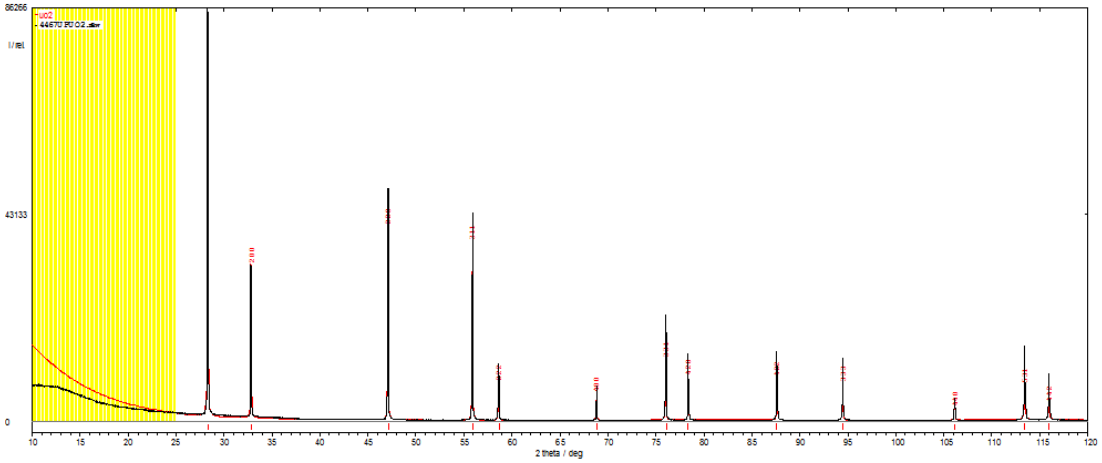

Figure 5.5 – XRD spectrum of TRABANT2 sample.

If defects clustering is excluded, the variation of the lattice parameter due to irradiation damage, in a cubic structure crystal, can be expressed in terms of dpa as indicated by Weber [34]:

$$\frac{\Delta a}{a_0} = C(1 - e^{-D \cdot dpa}) \tag{5.1}$$

where the constant C is proportional to the average number of Frenkel's pair, in particular their local production rate, and it is inversely proportional to their annealing rate. The constant D is related to the defects annealing rate and the exponential form derives from the tendency to have defects production rate equal to defects annealing rate (saturation) at long times. The variation of lattice parameter was calculated starting from UO_2 lattice parameter[3], and PuO_2 lattice parameter (5.3958 Å), following Vegard's law and correcting for the oxygen vacancies as described by the equation [156] [157]:

$$a = a_0 + 0.32x \tag{5.2}$$

Lattice parameter in 5.2 is expressed in Å and x is the negative deviation from the

[3]See section 4.6

stoichiometric condition O/M= 2.000.
The variation of lattice parameter for the three samples measured in the present experimental campaign was related to the dpa produced during the storage time[4], calculated by means of SRIM code [16] with displacements energy of 20 and 40 eV (for O and U respectively). The number of displacements produced by a recoil nucleus and by the emitted alpha particle is about 1750. Results obtained are plotted in Figure 5.6, together with previous data of Wiss et al. [35] and are fitted by relation 5.1. For comparison Figure 5.6 shows also the variation of lattice parameter obtained with uranium dioxide and plutonium dioxide by Weber [158]. Parameters C and D obtained using equation 5.1 are: C= 0.43 and D= 3.98 with an adjusted determination coefficient $R^2 = 0.81$. The saturation value, C, is 0.43%, which is smaller than 0.632% obtained by Wiss et al. [35], or 0.8% determined by Weber on single UO_2 crystals [34]. The saturation value is instead closer to the work performed by Weber on UO_2 polycrystals [158] (0.3%-0.5%) and Kato et al. [149](0.29%).

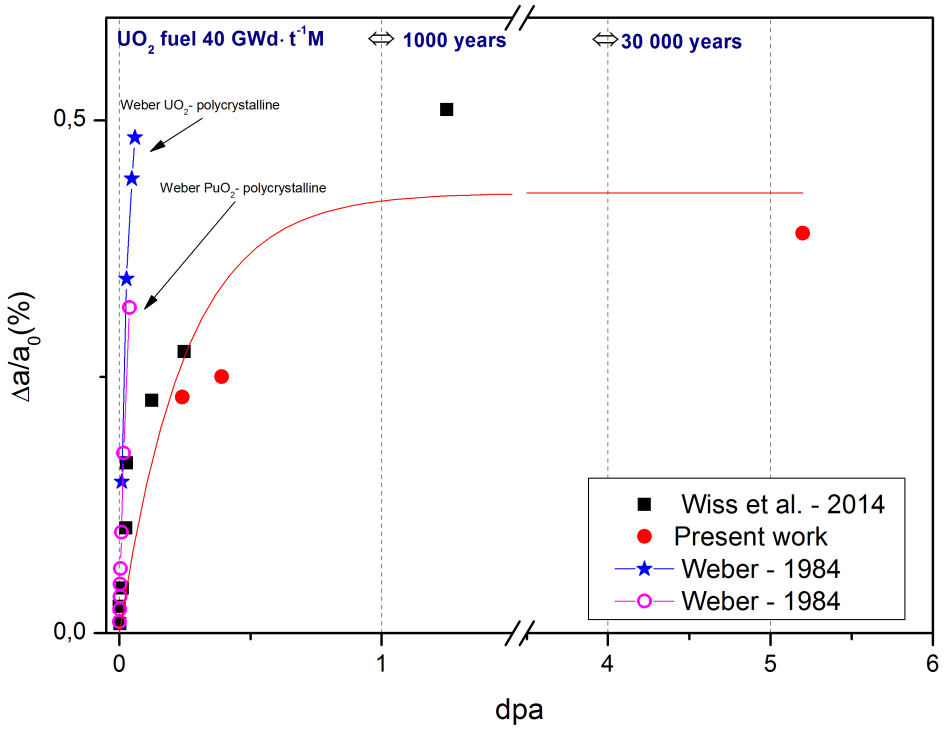

Figure 5.6 – Lattice parameter variation, measured by means of X-ray diffraction, as a function of the cumulated alpha-irradiation damage (dpa). The dpa were calculated using SRIM [16]. Red circles refer to the measurements of the present work, black squares refer to data by Wiss et al. (2014). Pink empty circles and blue stars refer to measurements performed by Weber [158] respectively on UO_2 and PuO_2. The arrows indicate the dpa produced in a LWR UO_2 after 1000 and 30 000 years, respectively.

[4]See Table 5.1

The present study confirms lattice expansion trend according to formation and annealing of point defects kinetic, followed by saturation; however, it does not discriminate between the ballistic effect due to the irradiation process and the He formation. As stated in subsection 1.3.3, He is rather insoluble in uranium dioxide and He-gas bubbles form with consequent large strains generation [159].
To determine the annealing temperatures for irradiation induced lattice defects and to compare the results with those obtained by Weber [28], isothermal and isochronal annealings were performed in a parallel experimental campaign, on Pu-01 and Pu-10 at 600 K, 900 K, 1100 K and 1500 K. Each sample was mantained at the desired temperature for about 30-40 min and subsequently lattice parameter was measured at room temperature as previously described.
Figure 5.7 shows the decrease in terms of relative lattice parameter for Pu-10 and Pu-01 after each thermal treatment; results are normalised to the lattice parameter at 300 K after several years in storage.

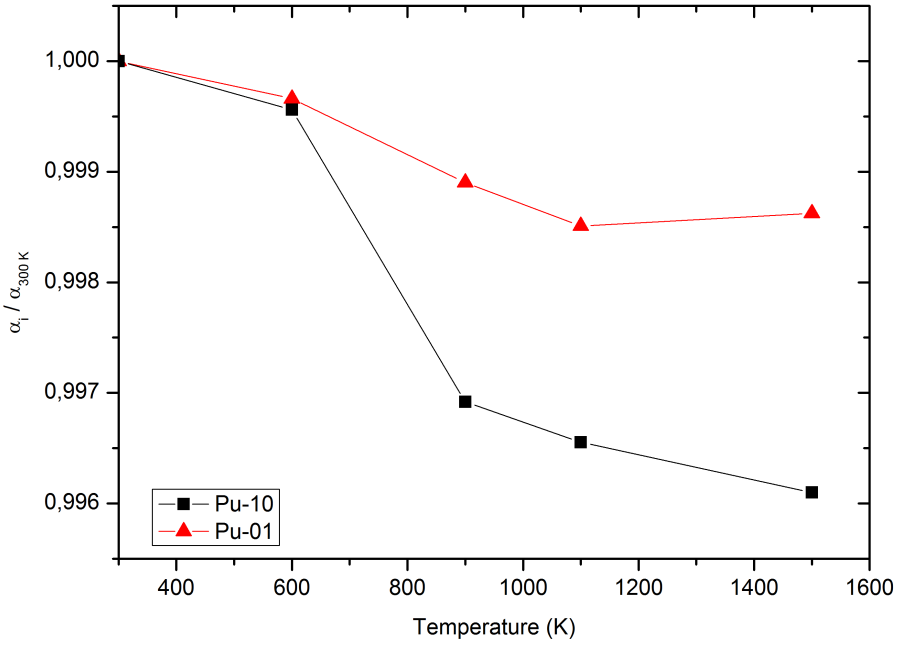

Figure 5.7 – Variation of the lattice parameter of samples Pu-01 (red triangles) and Pu-10 (black squares) after annealing treatments. α_i represents the lattice parameter measured at step i, while α_{300K} defines the lattice parameter measured at 300 K before the annealing cycles.

There is a good agreement with results obtained by Weber [28]: three steps are obtained for lattice parameter recovering, at approximately the same temperatures (570 K, 850K and 1100-1500 K). From Figure 5.7, it is possible to observe that annealing is predominant at the second step (850 K), temperature corresponding to the migration and recombination of U vacancies.

5.4 Alpha damage effect on Young's modulus

To evaluate the impact of auto-irradiation on elastic properties, Young's modulus of samples in Table 5.2 was measured and related to the dpa produced during storage. Alpha damage was calculated as described in the previous section, with the exception of spent fuel where the alpha particles produced during storage were estimated on the basis of fuel rods post-irradiation decay calculation using Web-Korigen [55] and Decay Engine++ of Nucleonica [56]. The radionuclides inventory corresponding to the average burnup was assumed to be representative of the same local burnup. This assumption, in addition to the rods average burnup being higher than the validation range of the code [160], introduces uncertainties to the results.
Alpha-damage effect on Young's modulus was considered for the pellet with average burnup of 80 GWd·t^{-1}M at the radial positions measured with higher and lower burnup ($\frac{r}{r_0}$= 0.9: local burnup ∼84 GWd·t^{-1}M; $\frac{r}{r_0}$= 0.3: local burnup ∼70 GWd·t^{-1}M). For the data analysis the variation of Young's modulus due to Pu addition in the matrix, must be considered; however, literature presents few spread sets of data [90]. This spread could reside in the lack of separation of auto-irradiation and Pu addition effects in literature. For this reason a MOX fuel pellet was measured before and after annealing, in order to evaluate simultaneously the decay effect and the chemical composition effect (difference between Young's modulus of fresh (U,Pu)O_2 and fresh UO_2.
For this purpose Phenix, a pellet of $(U_{0.762}Pu_{0.238})O_2$ with O/M = 2.000 and ∼95% TD [153], was measured by acoustic microscopy at 60 MHz, using methanol as coupling liquid. The sample was successively heated at 1515 K, in Ar/H_2 (temperature ramp rate = 15 K·min^{-1}) for 20 min to anneal Frenkel's defects formed during the storage time and then re-measured at the same conditions. After having verified the Poisson's ratio to be close to 0.3 [90] [161], relation 4.10 was used to calculate Phenix Young's modulus. Young's modulus increases by ∼5% after the annealing (see Table 5.2).

Table 5.2 – Phenix [153] Young's modulus measured before and after annealing at 1500 K via acoustic microscopy at 60 MHz

E non-annealed (GPa)	E annealed (GPa)
195.2 ± 1.5	204.6 ± 1.9

The intrinsic Young's modulus[5] was calculated by correcting the Rayleigh wave

[5]E corrected for porosity (representative of the solid matrix)

velocity for porosity (equation 4.17) and considering that after storage density decrease due to lattice volume expansion must be considered. Variation of density in auto-irradiated samples can be expressed as:

$$\rho_f = \rho_i \cdot \left(\frac{1}{1 + \frac{\Delta V}{V_i}} \right) \tag{5.3}$$

where ρ_f defines the density after several years of storage and ρ_i, the density measured at the time of sample synthesis. If the variation of volume is determined only by the crystal lattice expansion, i.e. if the precipitation of He gas bubbles is not considered, the relative volume variation is:

$$\frac{\Delta V}{V_i} \simeq \frac{3a_0^2 \delta a}{a_0^3} \tag{5.4}$$

a_0 is the lattice parameter at the time of synthesis and δa the variation of lattice parameter measured in section 5.3.
Intrinsic E of the annealed Phenix is about 3-10% higher than intrinsic E of UO_2 ($E_0 \sim$ 247 GPa for fresh MOX and $E_0 \sim$ 239 GPa for full dense UO_2 using 4.16 to calculate Rayleigh velocity at zero porosity, while comparing with the value of Young's modulus of UO_2 measured in the section 4.6 the difference is about 10%: $E_0 \sim$ 224 GPa for UO_2). The increase of Young's modulus due to Pu measured here confirms that observed by De Novion and co-workers [162]. De Novion and co-workers measured Young's modulus for UO_2 and MOX at different stoichiometric conditions with two different Pu content: 15% and 76%. If values at O/M= 2.000 are fitted by a straight line, the following relation is found (adjusted R^2= 0.96):

$$E_{MOX} = E_{UO_2} + 0.3(\%Pu) \tag{5.5}$$

Hence for a concentration of 23.8 wt%, E_0 increases of $\sim$ 3%. The problem of correction for Pu content was significant for TRABANT2 (Pu = 45 wt%); also in this case a correction based on relation 5.5 was used.
Another correction had to be applied to spent fuel's results, as the effect of fission products on Young's modulus must be subtracted. Laux [77] observed for SIMFUEL samples a Young's modulus decrease, in the range of simulated burnup 0-100 GWd·t^{-1}M, which could be expressed by (adjusted R^2= 0.93):

$$E_{SIMFUEL} = E_{UO_2} \cdot (1 - 2 \cdot 10^{-3} \cdot burnup) \tag{5.6}$$

with burnup in GWd·t^{-1}M. Young's modulus values of the commercial PWR fuels examined in this section, were corrected accordingly with 5.6.
Intrinsic Young's moduli of samples in Table 5.1 are plotted versus dpa in Figure

5.8, together with the intrinsic Young's modulus of fresh UO_2 measured in section 4.6 and that determined by Wachtman [86] for comparison. The results suggest a decrease of Young's modulus due to alpha-irradiation up to 0.42 dpa. In calculation of intrinsic Young's modulus of TRABANT2, the substoichiometric condition was not considered, although De Novion et al. [162] demonstrated a slight decrease of E when $O/M \neq 2.000$; in any case this difference should be within the large uncertainties characterising TRABANT2 Young's modulus.
Pu-10 has instead a large Young's modulus, higher than the intrinsic value of fresh uranium dioxide. This value could appear an outlier, but if the work of Elbakhshwan et al. [150] is considered, it is plausible that Young's modulus decreases within a specific range of displacements per atoms and then starts increasing. This explanation is supported both by the increase of extended defects observed by Jonnet [163] and by the relaxation phenomena experienced by uranium dioxide implanted with He at increasing fluences, in the experiment performed by Debelle et al. [151].

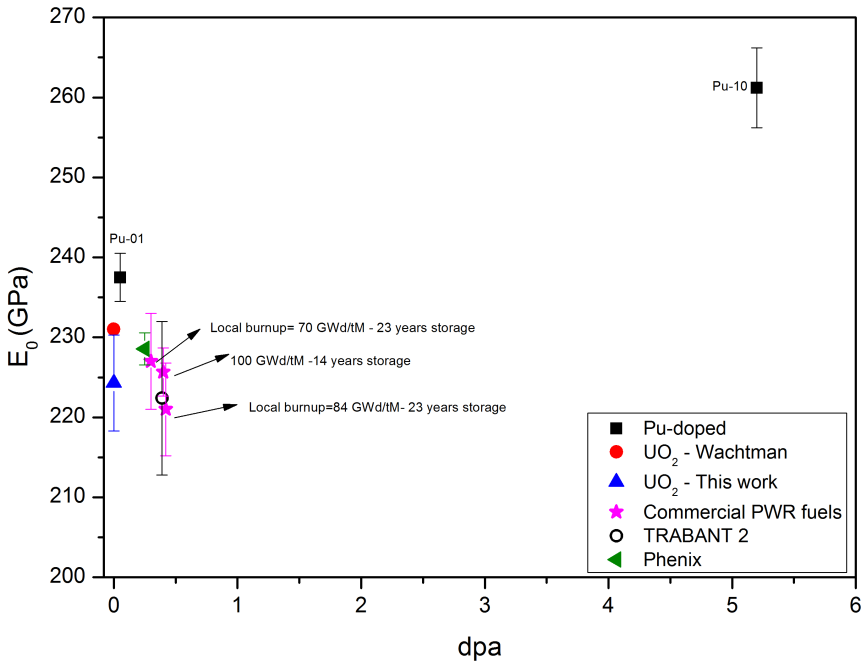

Figure 5.8 – Young's modulus variation as a function of dpa calculated using SRIM [16] and DECAY ENGINE++ of Nucleonica [56]. In case of spent fuel samples (magenta stars) the inventory at the end of irradiation was determined with webKorigen++ [56]. Young's modulus of fresh UO_2 published by Wachtman [86] is represented by the full red circle, whereas the blue vertical triangle represents the value obtained in the present work. The empty black circle refers to TRABANT2, the horizontal green triangle to Phenix and the black squares to Pu-01 and Pu-10.

Jonnet studied density and size of dislocation loops formed in Pu-10 after 4 years and 7 years of storage (respectively 1.1 and 2 dpa), finding an increase of the mean loop radius and loops density in three years of storage [163]. The density increase in dislocation loops experienced by Pu-10 at different alpha-damage levels, is depicted in Figure 5.9, where five TEM bright fields images show dislocation loops evolution at different accumulated decay damage.
Relaxation behaviour was observed by Debelle and co-workers [151] for UO_2 single crystals irradiated with He ions. They observed stress and strain magnitude increase up to a threshold irradiation damage level (3 dpa), followed by a relaxation of the generated in-plane stress and normal strain (a magnitude decrease) in the implanted layer above this damage level. This phenomenon has been explained as a consequence of the extended defects increase (such as dislocation loops [164]) which causes the irradiated layer not to respond anymore elastically to the radiation damage, being plastically deformed.
Young's modulus of Pu-01 sample, corrected both for porosity and Pu content, is affected by a density decrease caused by the lattice expansion of ~ 0.24 % and the consequent estimated variation of E, which could be obtained by combining 4.1, 4.11 and 5.1, is within the error bars ($\sim 1\%$). Therefore, it is possible to conclude that Young's modulus of Pu-01 should be comparable with that of unirradiated full dense UO_2.
This conclusion is corroborated by considering that the UO_2 theoretical Young's modulus, obtainable by using relation 4.1 and 4.11, is about 239 GPa. On the other hand the value obtained by Wachtman [86] on UO_2 single crystals is slightly lower and, considering the error bars, it is consistent with Young's modulus of fresh uranium dioxide presented in section 4.6. The large error bars for the fresh UO_2 (blue triangle in Figure 5.8) are most probably due to the heterogeneity of the density distribution of the particular investigated sample.
Following the latter considerations, the variation of Young's modulus due to alpha-damage is calculated by comparing with Pu-01 Young's modulus or with Young's modulus measured by Wachtman [86]. Observing Figure 5.8, the following considerations can be done:

- Intrinsic Young's modulus for Phenix non-annealed sample (corrected for the Pu content using equation 5.5) is about 4% lower than intrinsic Young's modulus for Pu-01, which agrees with the increase of 5% measured after annealing. If Young's modulus of fresh uranium dioxide measured in the present work and obtained by Wachtman [86] are taken as a reference, Young's modulus of Phenix is instead comparable with that of fresh uranium dioxide. However, this last conclusion would be in disagreement with the annealing result.

- The lowest Young's modulus is observed for the spent fuel with local burnup

of 84 GWd·t^{-1}M after 23 years: E is $\sim$ 7% lower than E of Pu-01 (4 % lower than that of the datapoint for fresh UO_2). If the measurement uncertainties are considered, these differences agree with the recovery observed after thermal treatment of the pellet extracted from the same rod and with similar average burnup, described in the next section.

- Notwithstanding the large error bars, the TRABANT2 Young's modulus is consistent with the trend observed in the range 0-0.42 dpa

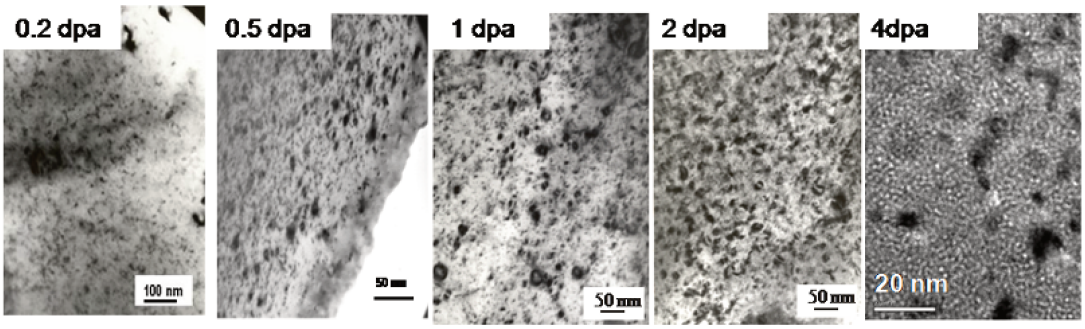

Figure 5.9 – TEM bright field image of Pu-10 acquired at different times after the synthesis. The Figure show the increase of dislocation loops density for increasing damage levels (from 0.2 to 4 dpa). Images corresponding to 1.1 and 2 dpa belong to [163]. At high damage level, nanometric bubbles become visible (see especially the 4 dpa image).

Microstructure and mechanical properties of irradiated fuel at discharge from the reactor evolve during low temperature storage due to the cumulative effect of decay damage and He generation. Alpha irradiation, determines lattice swelling and a reduction of Young's modulus after several years in storage. A cumulated alpha damage of 0.8 dpa corresponds to 90 years of alpha auto-irradiation for a spent fuel with 100 GWd·t^{-1}M average burnup and about 800 years for a spent fuel with average burnup of 40 GWd·t^{-1}M , 4 dpa instead corresponds to 4 100 and 30 000 years respectively. These accumulated defects will produce swelling of the nuclear fuel in addition to the in-reactor swelling and must be taken into account.

5.5 Thermal annealing

To investigate ageing effects on spent fuel, a longitudinal section of a pellet taken from the same rod with average burnup of 80 GWd·t^{-1}M[6], was cut in two half longitudinal sections: one was immediately ground, polished and measured by

[6]See Table 4.1

high frequency acoustic microscopy, the second was annealed and then measured under the same conditions (60 MHz, methanol as coupling liquid). The purpose of the experiment was to determine Young's modulus variations along the radius of the pellet before and after a thermal treatment.
To perform the experiment a small oven (Figure 5.10) was adapted and introduced in a hot-cell.

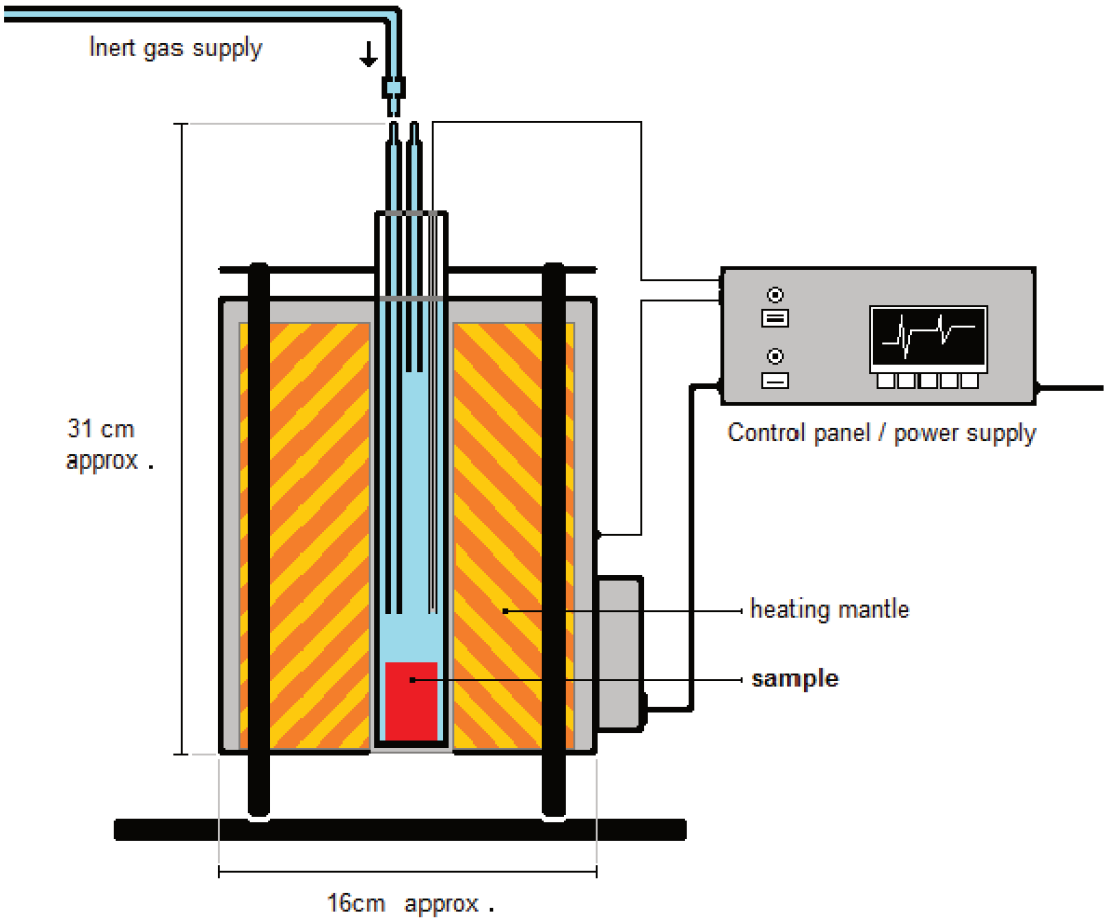

Figure 5.10 – Schematic of the furnace used for thermal annealing in hot-cell.

The annealing was performed at 850 K for one hour in Ar, considering that at this temperature most of the lattice defects are annealed; higher temperatures were avoided also because they could damage the sample due to the in-reactor low irradiation temperature at the rim.
For the annealing in hot-cell, the oven was equipped with an external cage (to avoid possible contacts with the few warm spots) and with a thermocouple (to monitor continuously the temperature thanks to the external controller). The he-

ating ramp during the thermal treatment had to be controlled manually as the controller gives only the possibility to monitor the temperature; 850 K was reached within ∼1 h.
After the annealing the sample was examined by SEM (see Figures 5.11 (a) and (b)), to inspection the rim microstructure and verify the absence of handling damages.
Rayleigh wave velocity measurements were performed along the radius of the pellet, for both specimens, at steps of approximately 400 μm, then Young's modulus was calculated by means of relation 4.11. Local Young's modulus values obtained for the two different configurations are compared in Figure 5.12 where a generally higher E is observed for the annealed sample, although differences in average values are almost within the measurement uncertainties for $\frac{r}{r_0} \leq 0.5$. These results would suggest that, for the damage level/timescale considered, storage alpha-irradiation is significant at the rim, but it is less relevant moving towards the centre of the pellet. The latter consideration is consistent with the higher Pu concentration at the pellet edge due to the resonance epithermal neutron capture of ^{238}U, which generates a higher local alpha-activity.

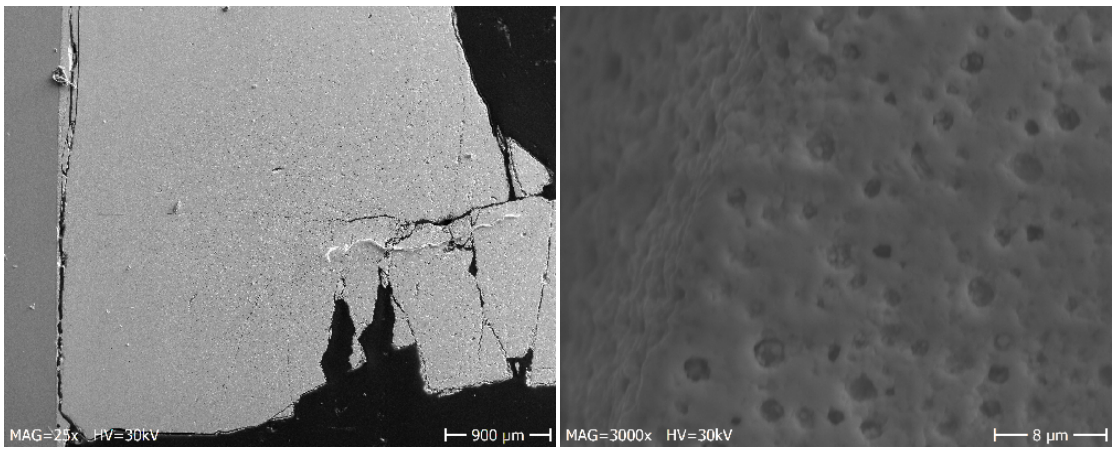

(a) (b)

Figure 5.11 – (a) SEM micrograph of the pellet's half longitudinal section (burnup ∼ 80 GWd·t^{-1}M) after heating treatment (b) SEM micrograph of the rim of the same pellet.

An example of Pu distribution along the radius of a high burnup pellet (102 GWd·t^{-1}M) is given in Figure 5.13. The local Pu concentration, determined by Walker et al. [115] using EPMA, increases exponentially at the periphery, while it is quite constant up to a fractional radial position of 0.8, hence Pu and local burnup profiles are very similar[7].
Due to the fact that in this experimental campaign relative Young's modulus

[7]The burnup profile of the pellet examined in this section should be similar to that of Figure 4.14

variations are considered, no corrections are applied for the local porosity, avoiding the introduction of additional uncertainties due to correction factors.
Table 5.3 shows the local difference in Young's modulus due to auto-irradiation at each radial position considered, if the increase after heating is attributed to storage-defects annealing. Differences are calculated in respect with the post-heating treatment values.
If the variation of E at $\frac{r}{r_0}$= 0.9 is compared with the decrease in Young's modulus achieved in the analogue pellet with similar burnup (see Figure 5.8), an agreement in Young's modulus variation is observed (estimated ΔE for the local burnup of 84 GWd·t^{-1}M is about 4-7%, if compared to fresh UO_2). After annealing, differences in Young's modulus values are not detected at the local burnup of $\sim$ 70 GWd·t^{-1}M (approximate relative radius =0.3) as variations are within the uncertainties of the measurement. In the previous section, excluding the error bars, a variation between 2 and 5% was observed; however this difference is reduced if the error bars of the datapoint at 70 GWd·t^{-1}M (Figure 5.8) are considered.

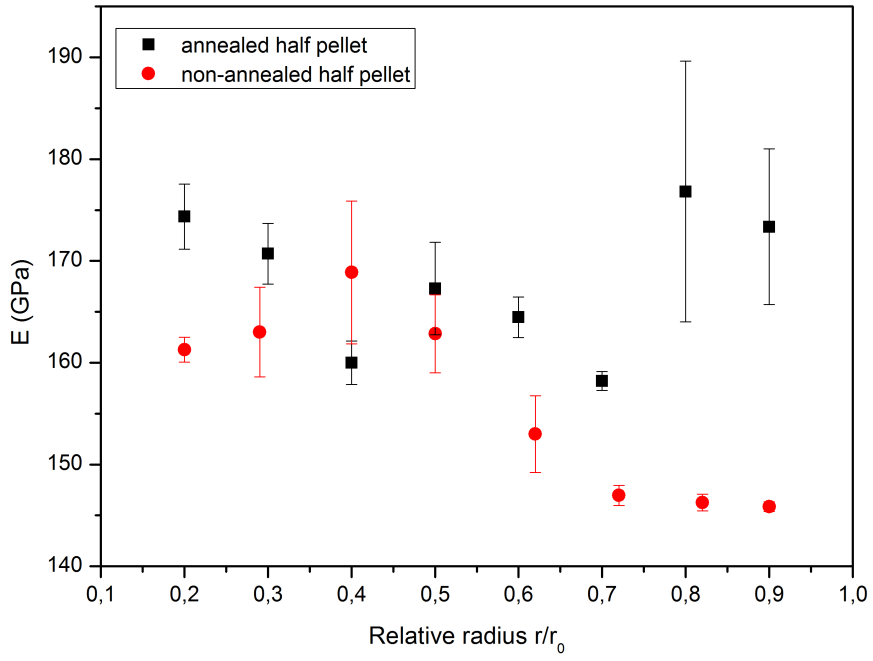

Figure 5.12 – Local Young's modulus measured along the radius of a pellet with average burnup of $\sim$ 80 GWd·t^{-1}M. Black squares correspond to the annealed half pellet, whereas red circles refer to the remaining non-annealed half.

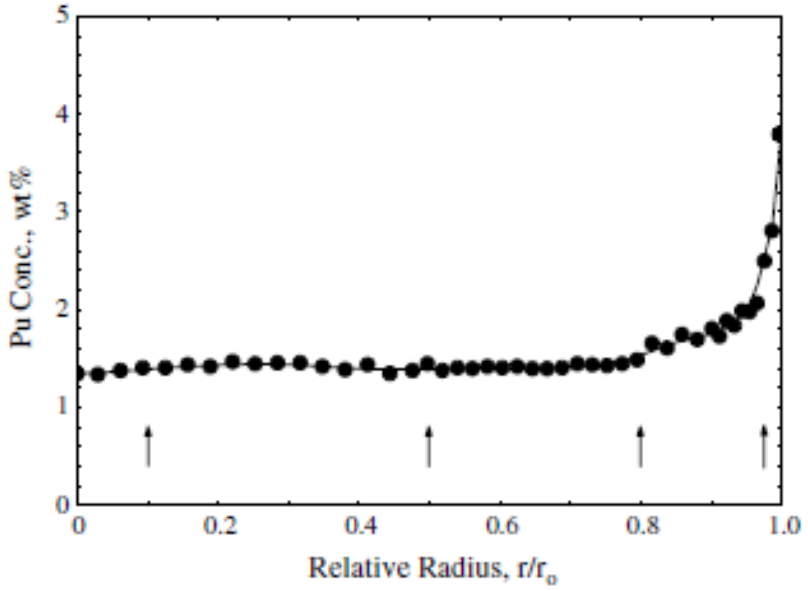

Figure 5.13 – Pu concentration radial profile along a pellet of 102 GWd·t^{-1}M [115]

Table 5.3 – Local Young's modulus difference between the annealed and non-annealed half pellets with average burnup of $\sim$ 80 GWd·t^{-1}M, measured with respect to the annealed half.

$\frac{r}{r_0}$	Young's modulus variation (%)
0.9	15.9 ± 4.0
0.8	17.3 ± 6.5
0.7	7.1 ± 1.2
0.6	7.0 ± 3.4
0.5	2.7 ± 4.9
0.4	-5.6 ± 5.8
0.3	4.5 ± 4.2
0.2	7.5 ± 2.4

5.5.1 Summary and conclusion

Spent fuel physical and mechanical properties evolve during storage in a repository as a consequence of fission products decay, actinides decay and the subsequent radiation damage and helium accumulation. Spent fuel, in comparison to in-reactor fuel, is characterised by lower temperature (in dry storage condition, max T $\sim$ 673 K [165]) which makes thermal diffusion and annealing less effective. After decay of

the short-lived fission products, the spent fuel is subjected mainly to alpha auto-irradiation damage and radiogenic helium accumulation at near ambient condition and these processes will continue throughout storage and geological disposal.
The necessity to discharge, transport and store nuclear fuel requires the accurate prediction of physical and mechanical properties, in order to understand spent fuel behaviour on a time-scale which could exceed 100 years.
In the present study variation of lattice parameter and Young's modulus as a function of the cumulated alpha-damage is presented: increase of lattice parameter followed by saturation is confirmed and the value obtained at saturation (0.43%) is in agreement with results of the published literature obtained with polycrystal UO_2 or MOX [149] [158] .
The study is based on high frequency acoustic measurements on actinides-doped samples, which are used to simulate spent fuel after thousands of years, MOX samples and real high-burnup spent fuel samples measured after a maximum of 23 years in storage. Variation of Young's modulus due to alpha auto-irradiation was studied in two different manners: by determining the variation of intrinsic Young's modulus as a function of the cumulated alpha-damage and by measuring Young's modulus before and after thermal treatments at minimum 850 K, temperature that enables the recovering of the majority of lattice defects as observed by Weber [28] and as confirmed in a parallel experimental campaign of this study.
Intrinsic Young's modulus decreases with the increasing alpha-damage, at least until 0.42 dpa; however, at $\sim$ 5 dpa, Young's modulus obtained is higher than that for fresh UO_2. The variation of Young's modulus due to alpha auto-irradiation finds explanation in both the variation of interatomic distances due to the presence of point defects and to the variation of crystal volume which produces swelling of uranium dioxide. The additional swelling caused by precipitation of He-bubbles is not considered in the present analysis, but a priori should cause additional Young's modulus decrease.
Young's modulus relaxation observed at $\sim$ 5 dpa could be attributed to the occurrence of restructuring processes e.g. the exceeding of a specific dislocation loops density.
The observed trend would agree with the finite element modeling results of Elbkhshwan and co-workers [150] who modeled the variation of Young's modulus of UO_2 thin films under irradiation at different fluences of Kr^+ ions. Young's modulus measured after the annealing at 1515 K of a MOX sample confirms the recoverability of most of the damage due to alpha auto-irradiation.
Measurements performed after annealing of an irradiated high burnup pellet show a generally higher Young's modulus in respect to measurements performed on the same pellet before annealing; this is particularly significant at the pellet rim. This result finds explanation in the higher Pu concentration at the periphery of the

pellet in comparison to its centre. Hence, variation of Young's modulus in spent fuel is not uniform along the radius of the pellet. This aspect must be taken into account when handling and storing spent fuel, especially because also in a repository the integrity of cladding is of primary importance to prevent fission products release. The fuel rod cladding represents again the first barrier against emission in the atmosphere, even if the storage casks are designed to contain the fission products. Further annealing studies are needed to validate results obtained for the first time during this experimental campaign.

5.6 Swift heavy ions irradiation of UO_2 and impact on Young's modulus

During irradiation in reactor, light or heavy fission fragments with energies of about 70 - 100 MeV, lose energy within the nuclear fuel producing heat and radiation damage in the UO_2 matrix. In the experimental campaign performed, the effect of irradiation with swift heavy ions on uranium dioxide Young's modulus was studied by measuring Rayleigh wave velocity along the surface of a UO_2 sample irradiated with ^{238}U ions. Irradiation was performed at 2.7 GeV [166], with a ions fluence of $5{\cdot}10^{10}$ ions·cm^{-2}, at room temperature. The sample was investigated using the cold setup at a frequency of 100 MHz, with ethanol as coupling liquid. V(z), as in the case of SIMFUEL, presented lower amplitude oscillations, but the presence of more than five oscillations (Figure 5.14) guaranteed an accurate Rayleigh wave velocity measurement.

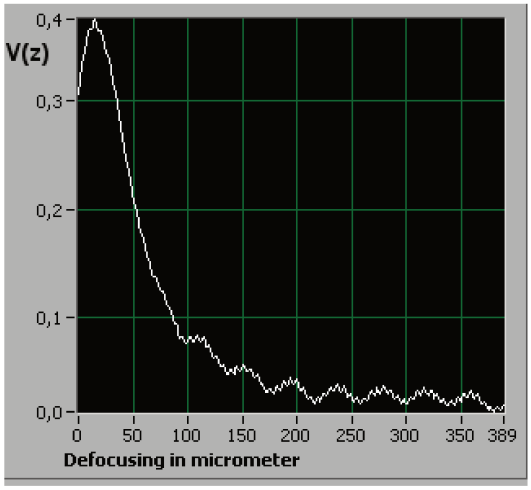

Figure 5.14 – Acoustic signature obtained at 100 MHz in UO_2 ($\sim$ 99% TD), implanted with ^{238}U ions of 2.7 GeV; irradiation fluence of $5{\cdot}10^{10}$ ions·cm^{-2}.

Prior to the measurement a SRIM simulation [16] was performed to ensure that the Rayleigh wavelength at 100 MHz was inside the implanted layer, avoiding the Rayleigh waves to interact also with the unirradiated layer. In particular, at 100 MHz, λ_R is ~ 27 μm, which gives also the order of magnitude of Rayleigh wave penetration inside the sample. The range of ^{238}U in 99% TD UO_2, calculated with SRIM, is 49.6 μm (see Figure 5.15), but the size of damaged layer could be larger due to the generation of secondary collision cascades. Tracks formed by the high energy ions during the penetration of uranium dioxide sample are observable in Figure 5.16. Tracks are typically consisting of a heavily disordered lattice with Schottky defects. The core of the track is formed by vacancies with a periphery characterized by clouds of interstitials.

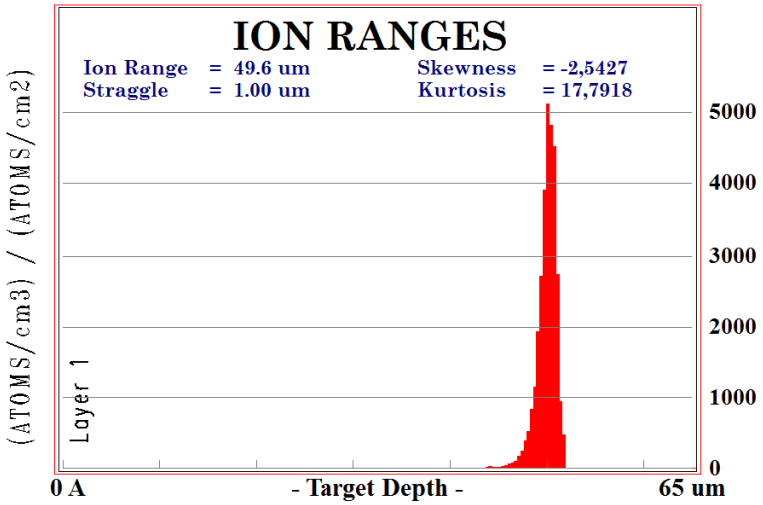

Figure 5.15 – Range of ^{238}U ions of 2.7 GeV in UO_2 (99% TD) calculated by means of SRIM code [16].

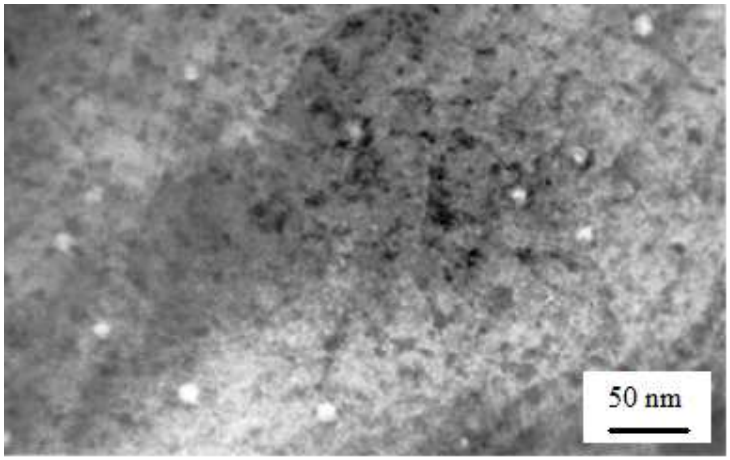

Figure 5.16 – TEM micrograph of the uranium dioxide sample implanted with ^{238}U ions of 2.7 GeV, irradiation fluence of $5 \cdot 10^{10}$ ions·cm^{-2}.

In the case of interaction of swift heavy ions with matter an estimation of the damage cannot be given in terms of dpa because, as stated in subsection 1.3.1, these ions lose the majority of their energy via inelastic collisions, whereas dpa considers only displacements produced by elastic collisions. Due to the lack of a consistent scale, a comparison with alpha irradiated samples is not performed. In any case, this study gives a first approach to the matter, underlying also problems to be considered in future. Implanted samples could exhibit some differences in comparison to bulk irradiated samples, for instance Debelle and co-workers [151], observed an additional strain due to the unirradiated substrate reaction to the strain produced by the implantation layer.
Table 5.4 shows Young's modulus measured on the implanted side of the specimen and compares it to Young's modulus measured on the non-implanted side. Data obtained for the non-implanted side are quite scattered due to the lack of polishing on this side, but the calculated average Young's modulus is in agreement with the value obtained for fresh UO_2 in section 4.6, if the same porosity of 1 % is considered (217 ± 5 GPa).

Table 5.4 – Young's modulus of implanted and non-implanted UO_2 (2.7 GeV ^{238}U ions onto UO_2 with 99% TD).

Implanted side - E(GPa)	Non implanted side - E(GPa)
172.7 ± 0.6	212.9 ± 10.7

From Table 5.4, a decrease of Young's modulus of ∼ 19 % is observed in the implanted layer. This behaviour, although not quantitatively comparable, is consistent with the trend shown in Figure 5.8.
In reactor, fission products energies are lower if compared to the present experiment and fission fragments masses are also smaller than ^{238}U; in particular the stopping power is lower (see Figure 5.17): the maximum stopping power for the interaction with fission fragments is about 18-20 MeV µm^{-1} (for their initial energy), while the stopping power is about ∼ 67 MeV µm^{-1} when the projectile is ^{238}U at 2.7 GeV. In the study performed by Matzke and co-workers [166] and Wiss et al. [167] on implanted samples, the threshold stopping power for formation of tracks visible at TEM investigation in uranium dioxide, would be ∼ 22-29 MeV µm^{-1} when the interaction occurs with ions of energies comparable with those of fission products. On the other hand, Snezes [168] found a threshold of 8.66 MeV µm^{-1} for fission fragments typical energies and 20.4 MeV µm^{-1} for high velocity ions. Fission fragments energy losses are slightly below the threshold fixed by [166] and [167], but above the threshold indicated by Szenes [168].
Following the latter considerations, fission fragments interaction with uranium dioxide might conduct to a Young's modulus variation consistent with the case considered in the present measurement campaign.

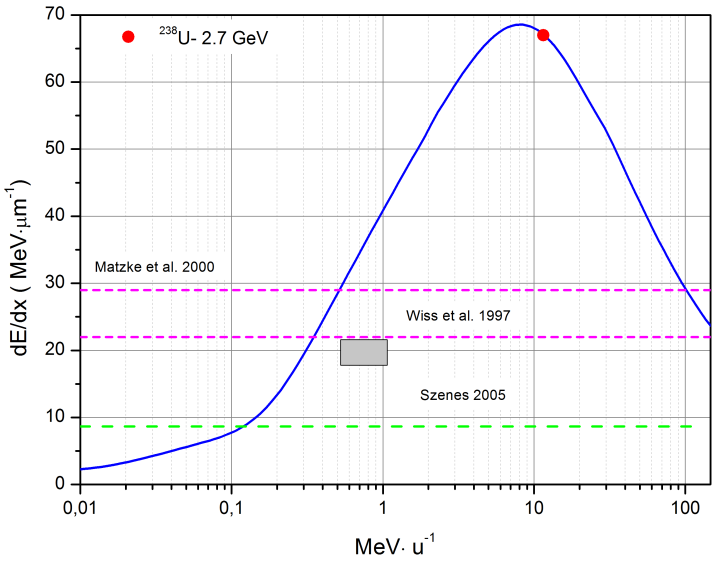

Figure 5.17 – Electronic stopping power for ^{238}U ions interaction with UO_2 (99%TD) versus energy expressed as MeV u^{-1} (blue curve). The electronic stopping power for the 2.7 GeV ^{238}U ions' case is indicated by the red full circle. The grey rectangle shows the typical fission products energies losses at their initial energies, which are below the threshold for visible tracks formation found by Matzke and co-workers [166] (magenta dashed line), closer to the threshold observed by Wiss et al. [167] (violet dashed line) and above the threshold estimated by Szenes [168] (green dashed line).

5.7 Conclusion

In Chapter 5 the variation of Young's modulus due to the production of radiation damage is presented. The study performed focuses on the detection and separation of the components contributing to elastic properties variation, in particular when irradiation damage is caused by elastic interaction with nuclei, as in the case of alpha-decays, or by inelastic collisions with material's electrons (swift heavy ions irradiation). In the case of auto-irradiation due to alpha decay, Young's modulus decreases in a specific range of dpa (up to 0.42 dpa) and at $\sim$ 5 dpa is higher than that of fresh UO_2. Acoustic microscopy measurements performed after a thermal treatment of a commercial PWR pellet (with damage level $\sim$ 0.3-0.45 dpa) show that Young's modulus increases after the annealing and the recover, more evident at the periphery of the pellet, is consistent with the decrease estimated for the analogue pellet with comparable damage level.
A decrease of Young's modulus is also observed in the layer of UO_2 implanted with high energy ions (^{238}U at 2.7 GeV), in section 5.6. This study, whose aim is the

determination of the Young's modulus variation due to the interaction with swift heavy particles, cannot give direct information on the effect that fission fragments interaction with the uranium dioxide matrix, has on the UO_2 Young's modulus. However, it is a single effect study, where temperature effect on the radiation damage is excluded and represents a first evaluation of the high energy losses impact on Young's modulus. In future more systematic studies are envisaged to properly forecast the above-mentioned effect; in particular by evaluating Young's modulus variation due to room temperature irradiation with ions of mass and energies comparable with those of the fission products. Another key point is the comparison of radiation damage effect on Young's modulus when the irradiating particles have different energies, masses and fluences.

Chapter 6

Severely degraded fuels

Contents

6.1 Introduction

During a severe accident in a Light Water Reactor (LWR), the exothermic oxidation of the Zircaloy at temperature above 1473 K, is responsible for the cladding and subsequently fuel melting, which results in the production of corium. In the past, several studies were performed in order to understand the corium physical and thermo-physical properties with the aim to model the corium behaviour at different stages of the accident. In this context, the FARO programme [61] was launched in order to obtain information on the quenching behaviour of corium having a composition of 80 wt% UO_2 - 20 wt% ZrO_2 when poured into water. Another important set of available data is related to the Three Miles Island Unit 2 (TMI-2) reactor accident samples studies [60] in the framework of a collaboration organised by OECD-NEA, managed by Idaho National Laboratory and including many European institutes.

Recently, following the accident at Fukushima Daiichi and the necessity to plan corium debris removal and damaged reactors decommissioning, the interest has been focused on the determination of the mechanical properties of corium, with the aim to optimize type and design of defueling tools and to program adequate recovery plans.
Data on fuel debris mechanical properties are scanty and even less is available in literature on the elastic properties.
In the present research work, Young's modulus of severely degraded fuels was determined by measuring Rayleigh wave velocity on prototypic corium and then using results obtained to better interpret those achieved using acoustic microscopy for the very first time on samples extracted from TMI-2. Moreover, for the first time, the same approach was applied to a sample of Chernobyl "lava" giving a first dataset which could enable understanding mechanical properties of lava-like fuel containing material and give additional information on the accident.

6.2 Materials

To study elastic properties of corium, the starting point was considered to be a simple system such as prototypic corium material. Materials belonging to the FARO experiments L-19 and L-24 were investigated by Matzke and Rondinella [61] at the Joint Research Centre Karlsruhe (previously Institute for Transuranium Elements) to analyse properties before and after the interaction between corium and water with the aim to understand mechanisms behind hydrogen production. Two FARO L-24 samples, in particular non-quenched corium re-solidified in the furnace after the discharge (material No.2), were selected and examined in the present work. Figure 6.1 shows an acoustic image of one of the two FARO L-24 samples (FARO-A) acquired in one of the IES laboratories of the University of Montpellier at 150 MHz, using methanol as coupling liquid. Matzke and Rondinella [61] observed, after annealing in Ar/H_2 at 1673 K, consistent weight increase of non-quenched samples L-24 material No.2, hence they deduced an uptake of oxygen during the annealing due to a slight sub-stoichiometric state.
Figure 6.2 shows oxygen potential measurements performed by Matzke and Rondinella [61] on FARO samples: the oxygen potential of FARO L-24 material No.2 is indeed lower than oxygen potential of stoichiometric UO_2, also after annealing. This set of data would corroborate the hypothesis of substoichiometric condition, although a comparison with the oxygen potential of stoichiometric $(U,Zr)O_2$ would give a definitive answer. In the present experimental campaign it was decided to anneal one FARO sample (FARO-B), with the aim of detecting Young's modulus

differences between the annealed and non-annealed samples. FARO-B was annealed at 1923 K for 6 h in Ar/H_2 (heating ramp rate = 8 K/min) and at the end of the process it lost $\sim$ 0.08 % of its original weight.

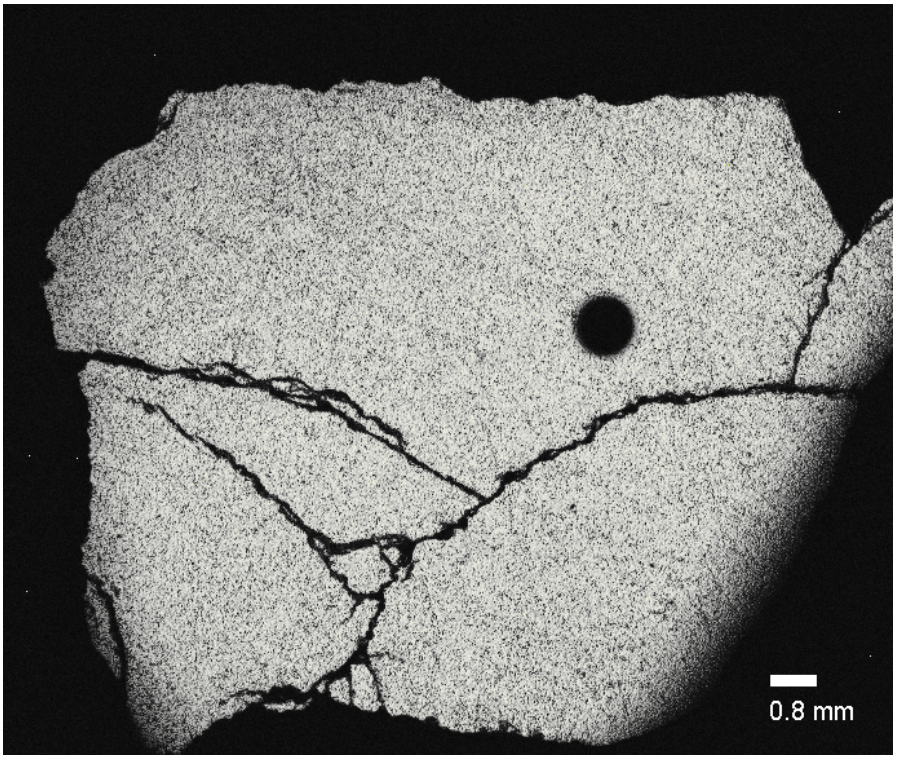

Figure 6.1 – Acoustic image acquired at 150 MHz of the sample belonging to FARO L-24 material No.2 [61], non-annealed (FARO-A).

X-ray diffraction investigations on both FARO samples revealed a non-homogeneous solid solution $U_{1-y}Zr_yO_{2\pm x}$, with cubic structure and an average lattice parameter of 5.352 Å; considering that both FARO samples have the same average lattice parameter, O/M should be also very similar, even though for X-ray diffraction measurements it is necessary to investigate a small fragment of the sample, which could be not representative.
In addition to FARO L-24, two other samples synthesised at the European Commission Joint Research Centre Karlsruhe [169] [170], with higher ZrO_2 content (45 mol% UO_2 - 55 mol% ZrO_2 (S1) and 20 mol% UO_2 - 80 mol% ZrO_2 (S2)) were measured. Both samples were prepared using powder metallurgical process, namely in mixing together UO_2 and ZrO_2 powders, press the mixture and sinter at 1873 K in Ar/H_2 for several hours [169] [170].

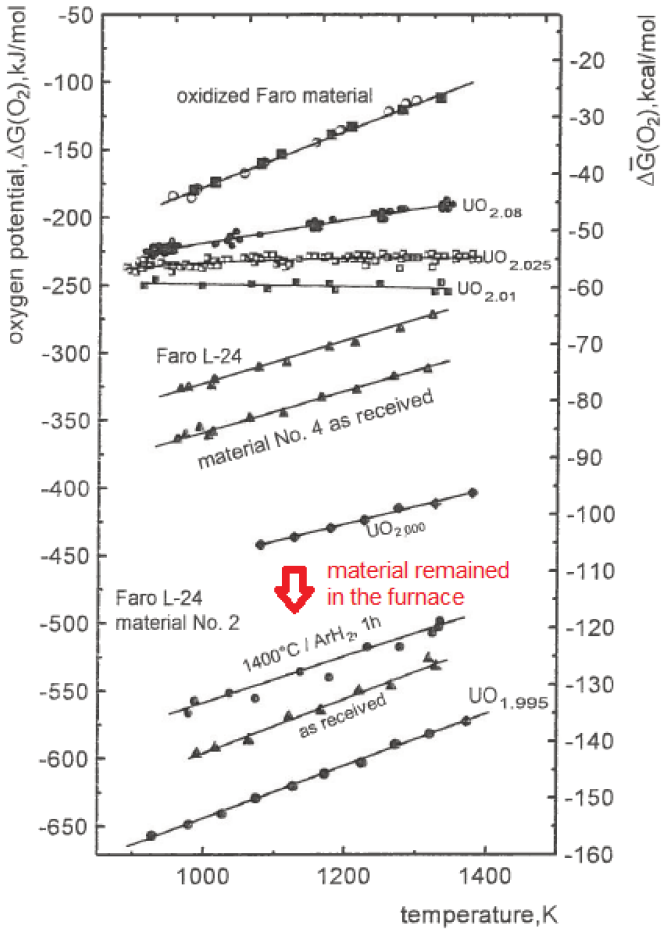

Figure 6.2 – Oxygen potential measured on FARO samples by Matzke and Rondinella [61].

The density of FARO-A, FARO-B, S1 and S2 was measured by the immersion method, i.e. by weighting them in air and in water (see Table 6.1). Given the cubic structure of FARO samples, porosity was obtained by calculating theoretical density with:

$$TD_{(U,Zr)O_2} = \frac{4((1-y)M_{UO_2} + yM_{ZrO_2})}{N_a \cdot ((1-y)a^3_{UO_2} + ya^3_{ZrO_2})} \tag{6.1}$$

where M represents the molecular mass, N_a is the Avogadro constant and a the lattice parameter. Lattice parameter for uranium dioxide is 5.4704 Å [141] and for cubic zirconium dioxide is 5.135 Å [171].
XRD measurements of samples belonging to the same batches of S1 and S2 determined the co-exhistence of different structures with prevalence of fcc for S1 and tetragonal and monoclinic for S2 [169] [170]. For these two samples it was decided

to calculate theoretical density using relation 6.1 and the cubic lattice parameter, given that monoclinic and tetragonal structures represent respectively lower and upper bounds for ZrO_2 theoretical density (TD cubic ZrO_2= 6081 $kg\,m^{-3}$ [172], TD monoclinic ZrO_2= 5087 $kg\,m^{-3}$ [173] and TD tetragonal ZrO_2= 6100 $kg\,m^{-3}$).

Table 6.1 – Densities measured by means of immersion method of prototypic corium samples examined in the present experimental campaign

Sample	Density ($kg\,m^{-3}$)	%TD
FARO-A	9238	98
FARO-B	9177	97.4
S1	7687	91
S2	6409	89

In addition to prototypic corium, three samples bored out of the solidified mass at TMI-2 ('core bore rocks') were investigated by high frequency acoustic microscopy, in particular G12-P2-E, G12-P6-E and G12-P10-A, which were extracted from the central fully melted core (see Figure 6.3).

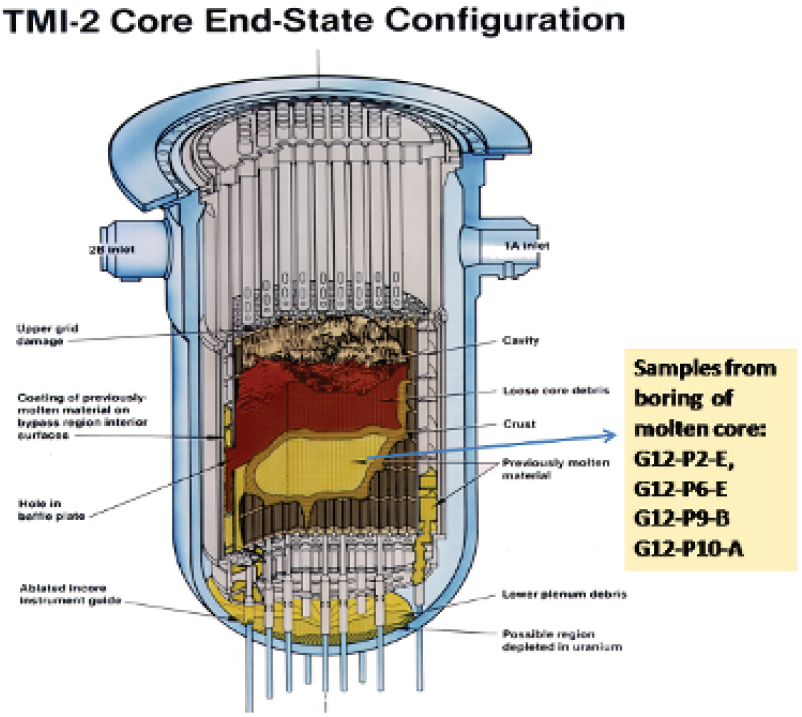

Figure 6.3 – Schematic of the final configuration of TMI-2 and extracted core rocks examined at the Joint Research Centre Karlsruhe.

These samples were investigated in the past by Bottomley and Coquerelle [174] and properties found can be summerised as follows:

- G12-P6-E (ρ = 7660 kg m^{-3}). The sample is a ceramic rock with a high proportion of ferrous phase. Eutectic is formed by Zr-rich phases (42 wt% Zr, 37 wt% U, 20 wt% O) and U-rich phases (75 wt%U, 10 wt%Zr, 14 wt%).
- G12-P2-E (ρ = 7380 kg m^{-3}). The sample has a similar composition to G12-P6-E.
- G12-P10-A (ρ = 8680 kg m^{-3}). The sample contains U-rich phases (75 wt% U, 11 wt%Zr) and Zr-rich phases (42 wt % Zr, 38 wt% U). The sample's average composition is $\sim$ 70 wt% UO_2 - 28 wt% ZrO_2; its porosity is lower if compared with the other bore rocks. A few ferrous phases were detected. Oxygen-metal ratio (O/M) of uranium dioxide was estimated by means of X-ray diffraction, considering an empirical law relating O/M and lattice parameter: O/M = 2.14 (fully oxidized sample).
  An optical micrograph (16x) and an acoustic image of G12-P10-A (60 MHz, methanol as coupling liquid) are shown in Figure 6.4.

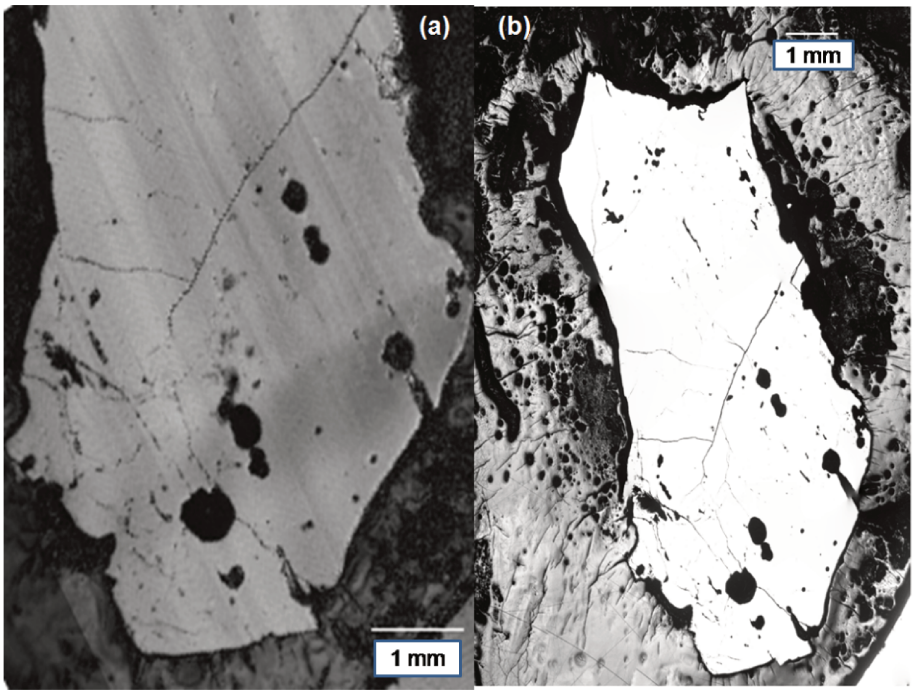

Figure 6.4 – (a) Surface acoustic image of core rock G12-P10-A, acquired at 60 MHz using methanol as coupling liquid (b) optical micrograph (16x) of sample G12-P10-A.

To conclude the study on the severely degraded fuels, high frequency acoustic microscopy was applied to a Chernobyl brown lava sample (Figure 6.5). Young's

modulus was calculated by using the black lava density of 2760 $\mathrm{kg\,m^{-3}}$, measured by immersion method.

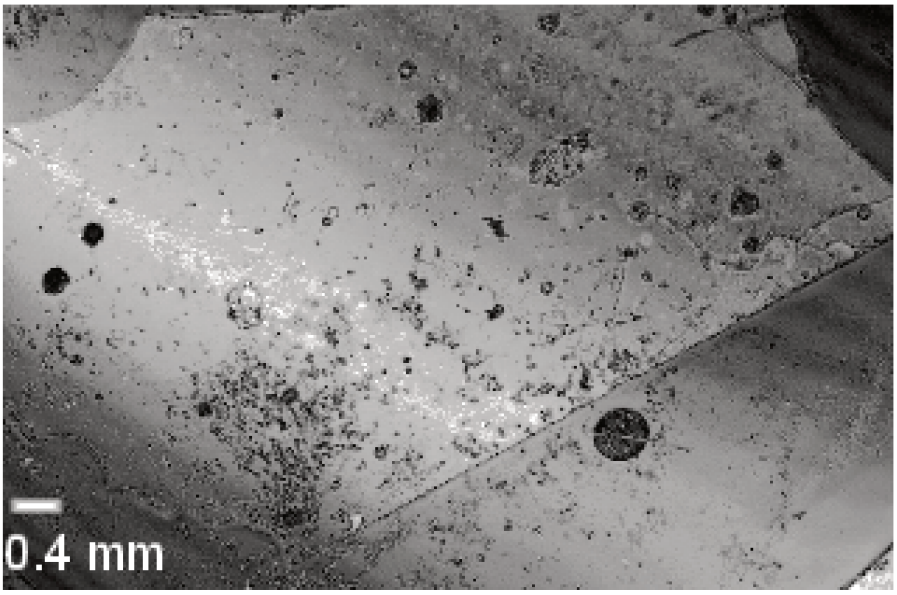

Figure 6.5 – acoustic image (60 MHz) of Chernobyl brown lava sample investigated in the present experimental campaign

6.3 Determination of Young's modulus of prototypic corium and TMI-2 samples

The determination of Young's modulus based solely on the measurement of Rayleigh wave velocity requires the Poisson's ratio to be known. To estimate Poisson's ratio of (U,Zr)O_2, both longitudinal and Rayleigh wave velocities were measured on FARO-A and FARO-B by coupling echography in reflection mode (5 MHz, bandwidth of 4 MHz) and acoustic microscopy (90 MHz).
Figure 6.6 shows the time domain response of the piezoeletric transducer during the measurement of FARO-A longitudinal velocity, using the time of flight method. The Poisson's ratio of FARO-A and FARO-B, determined by coupling Rayleigh wave and longitudinal wave velocities, is ~ 0.3, close to typical values of uranium dioxide (see Table 6.2); this allows determining Young's modulus of (U,Zr)O_2 with composition similar to FARO L-24 samples by using relation 4.10. Poisson's ratio of S1 and S2 could not be verified, therefore it was assumed a constant Poisson's ratio for them of 0.3.

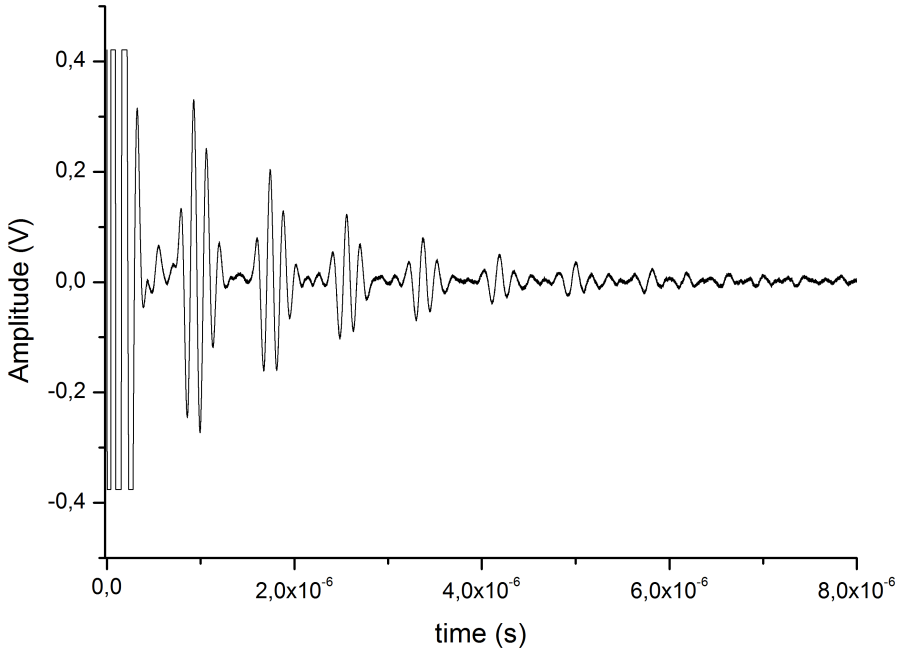

Figure 6.6 – Time domain response of the piezoelectric transducer during the echography measurements performed on FARO-A

Table 6.2 – Poisson's ratio of FARO-A and FARO-B

Sample	Poisson's ratio
FARO-A	0.294
FARO-B	0.331

Young's modulus was calculated using relation 2.23 for FARO-A and FARO-B and using the approximate relation 4.10 for S1 and S2. For prototypic corium relation 4.1 between density and Rayleigh wave velocity is not conserved, hence intrinsic Young's modulus could not be calculated with the method described in the previous sections.
Variation of zirconium dioxide Young's modulus as a function of porosity was determined by Smith and Crandall [175]; by fitting data with a straight line it is

possible to find the following relation (adjusted R^2=0.99) :

$$E_{ZrO_2} = E_0 * (1 - 2p) \tag{6.2}$$

This relation fits datapoints obtained by Laux [77], expressing Young's modulus of fresh uranium dioxide versus porosity in the porosity range 2%-20% with an adjusted coefficient of determination R^2 of 0.93. Due to the good fitting for both zirconium dioxide and uranium dioxide, relation 6.2 was used to correct for porosity the Young's moduli of FARO-A, FARO-B, S1 and S2. Figure 6.7 (a) shows Young's modulus of corium samples versus ZrO_2 content expressed as molar fraction, together with Young's modulus of fresh UO_2 determined by Wachtman et al. [86] and Young's modulus of pure monoclinic ZrO_2 measured by Smith and Crandall [175]; datapoints are then compared to Young's moduli measured using pulse-echo method, available in the JAEA R&D review 2015 [176] and referring to Hoshino et al. [177]

Young's modulus of corium samples measured in the present experimental campaign decreases linearly with the increasing zirconia content, up to a concentration of 80 mol% ZrO_2, this decrease is better visualised in Figure 6.7 (b), where data of the present experimental campaign, together with Young's modulus of fresh uranium dioxide of Wachtman et al. [86], are fitted by the linear relation (adjusted R^2= 0.92)

$$E_{(U,Zr)O_2} = E_{UO_2} - 0.82(x_{ZrO_2}) \tag{6.3}$$

where x is the molar fraction of zirconium dioxide.

Results obtained on corium samples are in agreement with literature data for a concentration of zirconium dioxide of 55 mol%, but a large discrepancy is observed at 35 mol%. This difference can hardly be explained without information on the samples, especially on the porosity. Considering all results it is possible to affirm that increasing zirconia content determines Young's modulus decrease in the range 0- 60 mol%

FARO-B in Figure 6.7 (a) has a lower Young's modulus in respect with FARO-A. This discrepancy could be explained by a different O/M ratio or to a probable variation in average composition: the fragments investigated using XRD present almost superimposable spectra, but they can be not representative of the bulk. Matzke and Rondinella, moreover, observed deviations from the nominal U/Zr ratio of 0.8/0.2, with compositions ranging from $(U_{0.86},Zr_{0.14})O_2$ to $(U_{0.75},Zr_{0.25})O_2$ [61]; a different composition would partially explain the lower Young's modulus of FARO-B, but without further measurements a conclusion cannot be drawn. The Poisson's ratio of 0.3 determined on the FARO samples was used to calculate the average Young's modulus of G12-P2-E, G12-P6-E and G12-P10-A samples extracted from the TMI-2 reactor core.

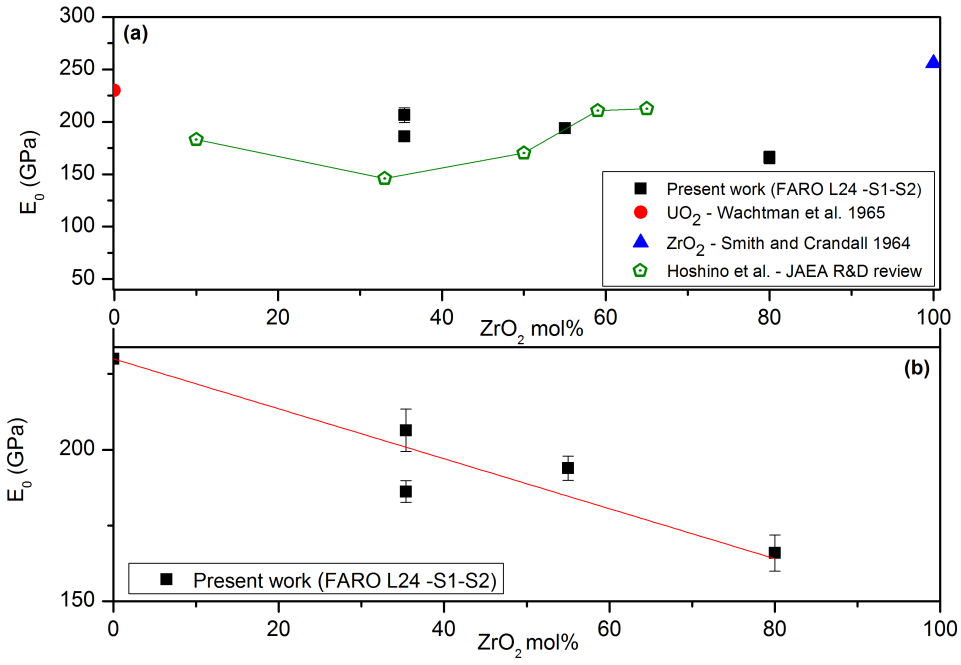

Figure 6.7 – Young's modulus of corium samples as a function of zirconium dioxide content. (a) Black squares refer to FARO-A, FARO-B, S1 and S2; red full circle to Young's modulus of uranium dioxide as obtained by Wachtman et al. [86]; blue triangle to intrinsic Young's modulus of monoclinic zirconium dioxide measured by Smith and Crandall [175]. The open green circles refer to data published in JAEA R&D review 2015 [176] referring to Hoshino et al. [177]. (b) Close-up of data obtained in the present experimental campaign of FARO-A, FARO-B, S1 and S2, which would indicate a linear decrease of Young's modulus for zirconium dioxide content up to 80 mol%.

Table 6.3 lists the results obtained whereas Figure 6.8 compares Young's modulus values of the three rocks investigated. A correction for the porosity is not performed at this stage, due to the fact that TMI-2 rocks are not purely $(U_{1-x}Zr_x)O_2$, but additional phases and compounds are present (e.g. ferrous phases, Al_2O_3). In addition to TMI-2 Young's modulus values, Figure 6.8, presents also a comparison with Young's modulus of S1, which has a density (7687 $kg\,m^{-3}$) very similar to G12-P6-E (7666 $kg\,m^{-3}$) and close to G12-P2-E (7380 $kg\,m^{-3}$). Young's modulus of G12-P2-E is consistent with Young's modulus value measured on the synthesised corium sample S1, whereas G12-P6-E has a Young's modulus $\sim 9\%$ lower than S1. Nothwithstanding the higher density, Young's modulus of G12-P10-A is comparable with Young's modulus of G12-P2-E and S1. Bottomley and Coquerelle [174] observed fewer ferrous phases in G12-P10-A with respect to G12-P2-E and G12-P6-E, but the impact of these ferrous phases on corium Young's modulus is unclear at the moment, especially considering that G12-P6-E and G12-P2-E have similar content of ferrous phases (even though not equal) and similar densities, but

different Young's modulus. Another aspect that needs further investigation is the impact of oxygen-metal ratio on Young's modulus: Bottomley and Coquerelle [174] calculated O/M for UO_2 in G12-P10-A $\sim$ 2.14 which represents a significative deviation from stoichiometry. The ratio O/M should be investigated also for the other samples measured in the present experimental campaign to see if differences exist which could explain the scatter of the results.

Table 6.3 – Young's modulus of core bore rocks extracted from the TMI-2 reactor core

Sample	Young's modulus (GPa)
G12-P2-E	167.0 ± 9.2
G12-P6-E	142.4 ± 5.5
G12-P10-E	164.8 ± 1.9

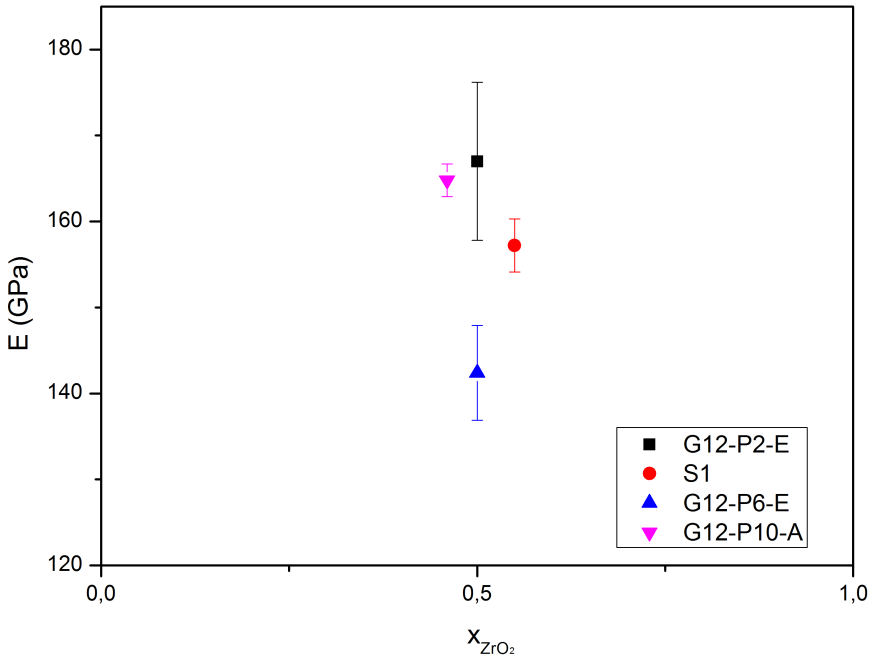

Figure 6.8 – Young's modulus of TMI-2 core bore samples, measured using acoustic microscopy at 60 MHz in comparison with Young's modulus of the synthesised corium sample with similar composition (S1).

6.4 Determination of Young's modulus of Chernobyl brown lava

One sample of the Chernobyl brown lava was investigated by acoustic microscopy at 60 MHz. The areas examined are indicated in Figure 6.9.

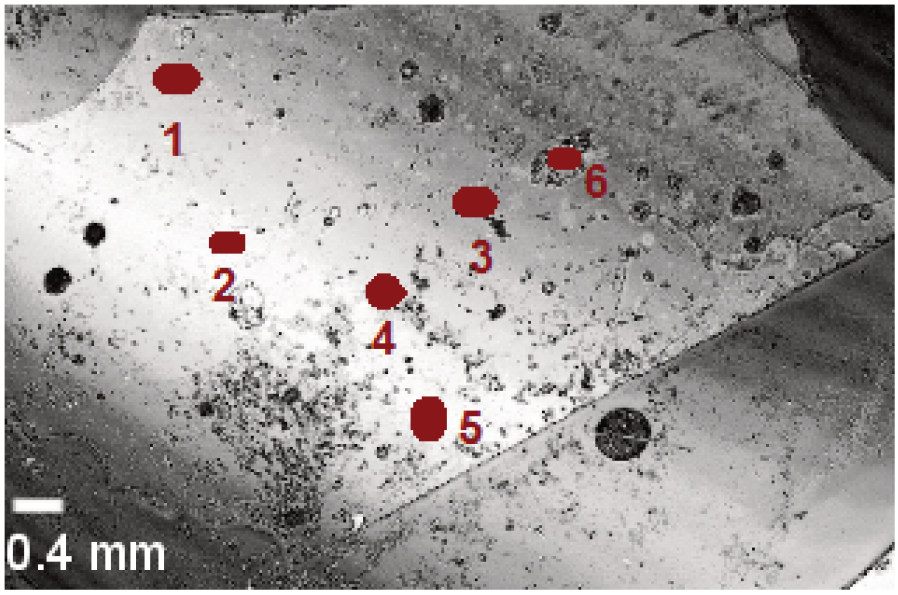

Figure 6.9 – Sample of Chernobyl brown lava investigated using high frequency acoustic microscopy. The red circles indicate the areas of measurement.

Brown lava has a composition that is very different to TMI-2 core rocks, as it is mainly composed by SiO_2 [178], therefore it was assumed a Poisson's ratio of SiO_2 in particular a value of 0.165, which represents the average of values published by Spinner [179] and McSkimin [180]. Table 6.4 lists Young's modulus values determined in the different regions of the sample, together with the average Young's modulus for Chernobyl brown lava and the corresponding uncertainty in the mean. Using a Poisson's ratio of 0.165, Young's modulus can be calculated using the following relation:

$$E = 2.84\rho v_R^2 \tag{6.4}$$

As $F(\nu)$[1]$= 2.8$ instead of 3.0 of uranium dioxide, it is evident that the error performed in calculating Young's modulus using 6.4 should be within 6%, if Poisson's ratio is slightly greater than 0.165.
Due to the uncertainities in density measurement and to the fact that the density

[1]See section 2.4

of a black lava sample was used in calculation, it is clear that an important source of error could be associated to the density value.

Table 6.4 – Young's modulus of Chernobyl brown lava in the six regions investigated and average calculated Young's modulus.

Region	Young's modulus (GPa)
region 1	71.9
region 2	71.3
region 3	73.8
region 4	38.9
region 5	68.5
region 6	72.7
Average	**66.2 ± 5.0**

6.5 Conclusion

Chapter 6 presents the results obtained by extending the range of applications of high frequency acoustic microscopy to the severely degraded fuels, produced as a consequence of a nuclear accident.
Samples from real severe accidents and from laboratory simulations were analysed. The first step of the research was investigating Poisson's ratio and successively, Young's modulus of prototypic corium, which offers the advantage to be material of controlled known composition.
Poisson's ratio calculated for corium samples with composition 80 wt% UO_2 and 20 wt% ZrO_2 is analogue to UO_2 Poisson's ratio (~ 0.3).
Young's modulus of prototypic corium, measured in the present work, decreases as a function of zirconium dioxide content, up to a concentration of 80 mol%. This result would be slightly in disagreement with results published in literature [176]; however, due to a lack of information on samples characteristics and measurement conditions in [176], an explanation to the discrepancy cannot be given. If the present study is simultaneously considered with the study in [176], it is possible to affirm that Young's modulus of corium with composition $U_{1-y}Zr_yO_2$ decreases at least up to a content in zirconium dioxide of 60 mol%.
After having performed an annealing treatment on a corium sample, a discrepancy is also observable between Young's modulus of annealed and non-annealed samples with the same nominal composition. This difference could be addressed to a different oxygen-metal ratio, if observations performed by Matzke and Rondi-

nella [61] are considered, but XRD investigations showed a very similar structure, with very close lattice parameter, which would imply that Young's modulus difference is more probably determined by a slighly different composition between the two samples.
Young's moduli of TMI-2 core rock specimens are comparable within 9% with Young's modulus of synthesised corium with equimolar composition , if comparable densities are considered. Differences in Young's modulus among the individual TMI-2 specimens could be determined by the variable ferrous phases content. G12-P10-A, has a low content of ferrous phases and displays the lowest Young's modulus, despite the fact its density is greater than the density of all the samples considered. Another aspect which needs further investigation is the determination of O/M for all the samples considered in the present experimental campaign and the assessment if differences in O/M could partially explain differences in the results.
Globally Young's modulus of TMI-2 melted core rock specimen is in the range 140-170 GPa.
High frequency acoustic microscopy was applied also to a Chernobyl lava, in particular brown lava. In this case the melted fuel is mainly constitued by silicates and Young's modulus measured on a brown lava sample, by using Poisson's ratio of SiO_2, is almost half of the value obtained for TMI-2 samples and comparable with the value of glass ($\sim$ 70 GPa).

Chapter 7

Conclusion

The focus of the present research work is the application of the high frequency acoustic microscopy to the investigation of the nuclear fuel elastic properties, considering three possible conditions: the irradiation in reactor, its storage or the disposal in interim or geological repositories and the extreme conditions characterising a nuclear accident.
The evaluation of the fuel performance in reactor, to fulfill the safety standards under normal operational conditions, requires the mechanical properties to be known. The degradation of the nuclear fuel mechanical properties must be predicted to ensure safe handling transport and treatment of spent fuel after its discharge from the reactor: radiation damage processes, do not terminate once the fuel is removed from the core of the reactor, they continue as a consequence of the radioactive decays, in particular the actinides'alpha decays. This auto-irradiation phenomenon may affect the integrity of the spent fuel rod, enhancing the risk of fission products release and contamination of the casks. This may complicate fuel recovery operations after storage and would require special handling and facilities to be available.
The third case considered in the frame of the present research work, is the investigation of the complex material produced as a consequence of a nuclear accident which involves melting of fuel and cladding and other structural materials, hence the formation of corium. The importance of the determination of corium elastic properties consists of being able to provide data helpful for the design of adequate defueling tools and debris removal from damaged facilities.The decommissioning of damaged NPPs requires radiological remediation and ad hoc procedures .
Moreover, since the corium mechanical properties are influenced by the cooling rate, their analysis could be useful in understanding the mechanism and the conditions governing the accident progression and its aftermath.
The experimental campaign performed on various types of irradiated nuclear fuels and analogues, has allowed achieving important results:

- The evaluation of Young's modulus for a large number of nuclear fuels irradiated under different conditions. The results enabled to derive the Young's modulus dependence on the porosity, incorporated in the fuel performance code TRANSURANUS, and to extend this to account for the local burnup.
- The determination of an empirical model able to predict the evolution of Young's modulus of irradiated uranium dioxide as a function of the average burnup, which can be used in other fuel performance codes or to estimate the unknown average burnup of irradiated UO_2.
- The estimation of the nuclear fuel swelling in the range 0-100 GWd $\cdot$ t^{-1}M.
- The extension of the range of applications of the high frequency acoustic microscopy. In particular, this study demonstrated the simultaneous evaluation of the porosity and the hardness of irradiated UO_2 fuels, by measuring the Rayleigh wave velocity.

Moreover, the empirical model correlating burnup and Young's modulus, includes also correction factors which account for additives content in the fuel. However, further studies are needed to fully determine the evolution of Young's modulus with dopants content, in particular as a function of Gd_2O_3, CeO_2 and Cr_2O_3 concentrations. The study should be performed both on fresh and irradiated fuel, with the aim to investigate the effect of the additives, before, during/after irradiation. The correlation between elastic and thermal properties, has highlighted the possibility of obtaining different thermal parameters by means of the Rayleigh wave velocity. This correlation might imply the possibility to derive a semi-empirical model linking the evolution of Young's modulus, as a function of fuel composition and irradiation history with the evolution of the thermal conductivity.
The irradiation damage effect on the nuclear fuel elastic properties was tackled in the second part of the thesis. After having studied the evolution of the lattice parameter caused by the irradiation damage up to its saturation level, the impact of auto-irradiation damage on Young's modulus was studied. Different effects had to be considered and properly separated: the variation of Young's modulus due to the simple addition of Pu and the effects caused by the presence of porosity or fission products. If the number of displacement per atoms is considered, Young's modulus decreases up to $\sim$ 0.45 dpa, but at very high dpa level ($\sim$ 5) Young's modulus becomes much higher than that of fresh uranium dioxide. The Young's modulus decrease, observable at low dpa values, is related to the formation of point defects. The large Young's modulus recovery and increase observed for the alpha-doped analogue at 5 dpa could be caused by an increase of extended defects which are responsible for a relaxation effect. The occurrence of restructuring

processes affecting the Pu-doped microstructure at $\sim$ 5 dpa should be also verified. To validate this assumption, further systematic studies are needed: more data for Young's modulus shall be obtained in the displacement per atom range between 0.42 and 5 dpa; TEM image analysis shall be coupled to opportune thermal treatments and high frequency acoustic microscopy measurements, in order to derive a quantitative explanation of the phenomenon. In future, the study of auto-irradiation effect should be performed on homogeneous samples in terms of composition and porosity with the aim to reduce possible artifacts introduced by the different correction factors applied in the frame of the present work. In addition, the variation of Young's modulus as a function of Pu content must be performed on fresh or annealed samples.
Young's modulus decreases also for UO_2 irradiated with accelerated ^{238}U ions of high energy. In this case a quantitative comparison with the results obtained on alpha-doped samples was not feasible due to the difference in terms of energy, mass and stopping power; for the same reason a conclusion cannot be drawn on the effect induced by fission fragments interaction with uranium dioxide. However, this study represents a single effect study and shows the decrease of Young's modulus as a consequence of the interaction between high energy heavy ions and uranium dioxide, at room temperature. Qualitatively it confirms the Young's modulus decrease observed as a function of the accumulated alpha-decay damage. In future this study shall be repeated under irradiation conditions more comparable with those characteristic of fission fragments, applying higher frequencies than 100 MHz. TEM image analysis shall be coupled to the acoustic measurements with the objective to observe if threshold effects in terms of tracks density could be detected.
The third part of the thesis represents a preliminary study on the elastic properties of severely degraded fuels . The Poisson's ratio of the (U,Zr)O_2 with 80% UO_2 and 20% ZrO_2 is comparable with the Poisson's ratio of UO_2 (0.3). Young's modulus calculated using this Poisson's ratio decreases if the content in ZrO_2 increases. The results obtained by measuring the prototypic corium reproduce partially the values obtained for the Three Mile Island samples. The TMI-2 core bore sample with a density similar to that of the synthesised corium (with almost equimolar composition) exhibits a Young's modulus only $\sim$ 9% lower. Considering that the Three Mile Island core bore rocks contain ferrous phases and other compounds such as Al_2O_3, further studies are needed to include the effect of more complex compounds containing additional phases. Variation of Young's modulus for (U,Zr)O_2 must also be studied considering:

- The coexistence of different structures (monoclinic, cubic and tetragonal).
- The ratio O/M.

- The variation of Young's modulus after interaction with water and sea-water.

Regarding the present study on the Chernobyl's brown lava, it showed that its Young's modulus is comparable with that of simple glass. This result was obtained by using an estimated Poisson's ratio for SiO_2 and the measured density of a Chernobyl black lava sample. In future studies the accuracy of the determination of Young's modulus of Chernobyl brown lava can be improved by directly measuring the Poisson's ratio value (e.g. via echography) and its density.

Appendix A

Adjusted coefficient of determination R^2

In order to estimate how well a model predicts the dependent variable in regression analysis, the coefficient of determination R^2 is widely used.
$0 \leq R^2 \leq 1$; $R^2 = 1$ represents a perfect model fit whereas $R^2 = 0$ indicates no fit. The total variation $\sum(y_i - \bar{y})^2$ of the dependent variable y has two components [181]: a variation that is explainable by the regression equation and a variation that cannot be explained by the regression equation. Therefore the total variation can be expressed as:

$$\sum(y_i - \bar{y})^2 = \sum(\hat{y}_i - \bar{y})^2 + \sum(y_i - \hat{y}_i)^2 \tag{A.1}$$

where y_i represents the measured data. The first term $\sum(\hat{y}_i - \bar{y})^2$ in equation A.1 represents the variance explained by the regression function and the second term $\sum(y_i - \hat{y}_i)^2$ represents the unexplained variation. The ratio between the explained variation and the total variation measures the goodness of the regression function [181]:

$$R^2 = \frac{\sum(\hat{y}_i - \bar{y})^2}{\sum(y_i - \bar{y})^2} \tag{A.2}$$

The coefficient of determination increases when the number of predictors increases: if more variables are added to the regression model, the coefficient of determination will increase, even though none of the additional independent variables affects the dependent variable. R^2 is sensitive to the number of predictors and this fact hinders the comparison between two regression models with a different predictors number. The dependence is removed by using the adjusted coefficient of determination,

which is defined as [181]:

$$adjusted\ R^2 = 1 - \left((1 - R^2)\frac{n-1}{n-p-1}\right) \tag{A.3}$$

where n indicates the sample size and p the number of predictors (total number of explanatory variables in the model excluding the constant term).

Bibliography

[1] WNA, Nuclear power in the world today (2017).
URL http://www.world-nuclear.org/information-library/current-and-future-generation/nuclear-power-in-the-world-today.aspx

[2] M. Schneider, A. Froggatt, et al., World nuclear industry status report 2016.

[3] Morss, Lester R. and Edelstein, Norman M. and Fuger, Jean, The Chemistry of the Actinide and Transactinide Elements (Set Vol. 1-6): Volumes 1-6, Springer Science & Business Media, 2010, Ch. 34, pp. 3665–3811. doi:http://dx.doi.org/10.1007/1-4020-3598-5.

[4] IAEA-TECDOC-1613, Nuclear fuel cycle information system, Tech. rep., IAEA - TECDOC SERIES (2009).

[5] IAEA, OECD-NEA, Uranium 2007: Resources, production and demand, Tech. rep., OECD Nuclear Energy Agency and the International Atomic Energy Agency (2008).

[6] H. Matzke, Radiation effects in nuclear fuels, Springer Netherlands, Dordrecht, 2007, pp. 401–420. doi:10.1007/978-1-4020-5295-8_14.

[7] CEA, Nuclear fuels, a nuclear energy division monograph, Commissariat à l'énerge atomique, Éditions du Moniteur, 2009.

[8] Guerin Y., Noirot J., Parrat D., International school in nuclear engineering - Nuclear fuels for light water reactors and fast reactors (Réf. P967/10/V2), 2016, Ch. 1, p. 10.

[9] D. Prieur, Élaboration de combustible a base d'oxydes d'uranium et d'americium: modélisation thermodynamique et propriétés des materiaux, Ph.D. thesis, Université de Limoges (2011).

[10] H. Bailly, D. Menessier, C. Prunier, The nuclear fuel of pressurized water reactors and fast reactors design and behaviour, CEA, 1999.

[11] H. Kleykamp, The chemical state of the fission products in oxide fuels, Journal of Nuclear Materials 131 (2–3) (1985) 221 – 246. doi:http://doi.org/10.1016/0022-3115(85)90460-X.

[12] D. Evans, R., The atomic nucleus, 1955, McGrawHill, New York.

[13] C. Leroy, P.-G. Rancoita, Electromagnetic interaction of radiation with matter - chapter 2, in: Principles of radiation interaction in matter and detection, World Scientific, Hackensack, USA, 2009, pp. 31 – 216.

[14] J. F. Ziegler, J. P. Biersack, The Stopping and Range of Ions in Matter, Springer US, Boston, MA, 1985, pp. 93–129. doi:10.1007/978-1-4615-8103-1_3.

[15] W. D. Loveland, D. J. Morrissey, G. T. Seaborg, Interaction of radiation with matter, in: Modern Nuclear Chemistry, John Wiley & Sons, Inc., 2005, pp. 497–535. doi:10.1002/0471768626.ch17.

[16] J. Ziegler, J. Biersack, M. Ziegler, SRIM - The stopping and range of ions in matter (2013).
URL http://srim.org/

[17] T. Wiss, 2.18 - Radiation effects in UO_2, in: R. J. Konings (Ed.), Comprehensive Nuclear Materials, Elsevier, Oxford, 2012, pp. 465 – 480. doi:http://dx.doi.org/10.1016/B978-0-08-056033-5.00039-2.

[18] A. Chroneos, M. Rushton, R. Grimes, 1.02 - Fundamental point defect properties in ceramics, in: R. J. Konings (Ed.), Comprehensive Nuclear Materials, Elsevier, Oxford, 2012, pp. 47 – 64. doi:http://dx.doi.org/10.1016/B978-0-08-056033-5.00002-1.

[19] L. E. Murr, Handbook of Materials Structures, Properties, Processing and Performance, Springer International Publishing, Cham, 2015, pp. 1–11. doi:http://dx.doi.org/10.1007/978-3-319-01815-7_2.

[20] M. Razeghi, Defects -chapter 14, in: Fundamentals of Solid State Engineering, Springer US, Boston, MA, 2006, pp. 551–571. doi:10.1007/0-387-28751-5.

[21] J. B. Wachtman, W. R. Cannon, M. J. Matthewson, Types of mechanical behaviour, Chapter 2 - Elasticity, Chapter 3, in: Mechanical Properties of Ceramics, John Wiley & Sons, Inc., 1996, pp. 23–35.

[22] C. Kittel, Phonons II. Thermal Properties - Chapter 5, in: Introduction to Solid State Physics, John Wiley & Sons, Inc, 2005, pp. 106–129.

[23] K. Nordlund, A. E. Sand, F. Granberg, S. J. Zinkle, R. Stoller, R. S. Averback, T. Suzudo, L. Malerba, F. Banhart, W. J. Weber, F. Willaime, S. Dudarev, D. Simeone, Primary radiation damage in materials - nuclear science nea/nsc/doc(2015)9, Tech. rep. (2015).

[24] S. Zinkle, 1.03 - Radiation-induced effects on microstructure*, in: R. J. Konings (Ed.), Comprehensive Nuclear Materials, Elsevier, Oxford, 2012, pp. 65 – 98. doi:http://doi.org/10.1016/B978-0-08-056033-5.00003-3.

[25] R. Smallman, R. Bishop, Chapter 4 - Defects in solids, in: R. Smallman, R. Bishop (Eds.), Modern Physical Metallurgy and Materials Engineering (Sixth Edition), Butterworth-Heinemann, Oxford, 1999, pp. 84 – 124. doi:http://dx.doi.org/10.1016/B978-075064564-5/50004-5.

[26] D. R. Olander, Fundamental aspects of nuclear reactor fuel elements, Tech. rep., California Univ., Berkeley (USA). Dept. of Nuclear Engineering. Technical Information Center, Office of Public Affairs, Energy Research and Development Administration (1976).

[27] H. Matzke, A. Turos, Ion implantation studies of UO_2 and UN, Journal of Nuclear Materials 188 (1992) 285 – 292. doi:http://dx.doi.org/10.1016/0022-3115(92)90486-5.

[28] W. Weber, Thermal recovery of lattice defects in alpha-irradiated UO_2 crystals, Journal of Nuclear Materials 114 (2) (1983) 213 – 221. doi:http://dx.doi.org/10.1016/0022-3115(83)90259-3.

[29] D. Franklin, J. Roberts, L. Che-Yu, Low temperature swelling and densification properties of LWR fuels, Journal of Nuclear Materials 125 (1) (1984) 96 – 103. doi:http://dx.doi.org/10.1016/0022-3115(84)90518-X.

[30] OECD-NEA, Scientific issues of fuel behaviour, fission product swelling, Tech. rep. (1995).

[31] H. Assmann, R. Manzel, The matrix swelling rate of UO_2, Journal of Nuclear Materials 68 (3) (1977) 360 – 364. doi:http://doi.org/10.1016/0022-3115(77)90266-5.

[32] J. Spino, J. Rest, W. Goll, C. Walker, Matrix swelling rate and cavity volume balance of UO_2 fuels at high burn-up, Journal of Nuclear Materials 346 (2–3) (2005) 131 – 144. doi:http://dx.doi.org/10.1016/j.jnucmat.2005.06.015.

[33] J. Spino, D. Papaioannou, Lattice contraction in the rim zone as controlled by recrystallization: Additional evidence, Journal of Nuclear Materials 372 (2–3) (2008) 416 – 420. doi:http://dx.doi.org/10.1016/j.jnucmat.2007.03.173.

[34] W. Weber, Ingrowth of lattice defects in alpha irradiated UO_2 single crystals, Journal of Nuclear Materials 98 (1–2) (1981) 206 – 215. doi:http://dx.doi.org/10.1016/0022-3115(81)90400-1.

[35] T. Wiss, J.-P. Hiernaut, D. Roudil, J.-Y. Colle, E. Maugeri, Z. Talip, A. Janssen, V. Rondinella, R. J. Konings, H.-J. Matzke, W. J. Weber, Evolution of spent nuclear fuel in dry storage conditions for millennia and beyond, Journal of Nuclear Materials 451 (1–3) (2014) 198 – 206. doi:http://dx.doi.org/10.1016/j.jnucmat.2014.03.055.

[36] V. V. Rondinella, T. Wiss, The high burn-up structure in nuclear fuel, Materials Today 13 (12) (2010) 24 – 32. doi:http://dx.doi.org/10.1016/S1369-7021(10)70221-2.

[37] P. V. Uffelen, R. J. M. Konings, C. Vitanza, J. Tulenko, Analysis of reactor fuel rod behavior - chapter 13, in: D. G. Cacuci (Ed.), Handbook of Nuclear Engineering, Springer US, Boston, MA, 2010. doi:10.1007/978-0-387-98149-9_13.

[38] J. Spino, K. Vennix, M. Coquerelle, Detailed characterisation of the rim microstructure in PWR fuels in the burn-up range 40–67 GWd/tM, Journal of Nuclear Materials 231 (3) (1996) 179 – 190. doi:http://dx.doi.org/10.1016/0022-3115(96)00374-1.

[39] H. Kleykamp, Post-irradiation examinations and composition of the residues from nitric acid dissolution experiments of high-burnup LWR fuel, Journal of Nuclear Materials 171 (2) (1990) 181 – 188. doi:http://dx.doi.org/10.1016/0022-3115(90)90364-S.

[40] C. Walker, T. Kameyama, S. Kitajima, M. Kinoshita, Concerning the microstructure changes that occur at the surface of UO_2 pellets on irradiation to high burnup, Journal of Nuclear Materials 188 (1992) 73 – 79. doi:http://dx.doi.org/10.1016/0022-3115(92)90456-U.

[41] K. Une, K. Nogita, S. Kashibe, M. Imamura, Microstructural change and its influence on fission gas release in high burnup UO_2 fuel, Journal of Nuclear Materials 188 (1992) 65 – 72. doi:http://doi.org/10.1016/0022-3115(92)90455-T.

[42] C. Walker, S. Bremier, S. Portier, R. Hasnaoui, W. Goll, SIMS analysis of an UO_2 fuel irradiated at low temperature to 65 MWd/kgHM, Journal of Nuclear Materials 393 (2) (2009) 212 – 223. doi:http://doi.org/10.1016/j.jnucmat.2009.06.017.

[43] J. Spino, K. Vennix, M. Coquerelle, Detailed characterisation of the rim microstructure in PWR fuels in the burn-up range 40–67 GWd/tM, Journal of Nuclear Materials 231 (3) (1996) 179 – 190. doi:http://doi.org/10.1016/0022-3115(96)00374-1.

[44] D. Baron, M. Kinoshita, P. Thevenin, R. Largenton, Discussion about HBS transformation in high burn-up fuels, Nuclear Engineering and Technology 41 (2009) 199 – 214. doi:10.5516/NET.2009.41.2.199.

[45] M. Kinoshita, T. Sonoda, S. Kitajima, A. Sasahara, E. Kolstad, H. Matzke, V. Rondinella, A. Stalios, C. Walker, High burnup rim project (III). Completed scope and results, American Nuclear Society, 2000, pp. 590–603.

[46] M. Kinoshita, T. Sonoda, S. Kitajima, A. Sasahara, E. Kolstad, H. Matzke, T. Kameyama, T. Matsumura, E. Kolstad, V. Rondinella, H. Ronchi, C., J.-P., T. Wiss, F. Kinnart, J. Ejton, D. Papaioannou, H. Matzke, High burnup rim project (II). Irradiation and examination to investigate rim-structured fuel, American Nuclear Society, 2000, pp. 207–213.

[47] CRIEPI, Final report of high burnup rim project, Tech. rep., Central Research Institute of Electric Power Industry (2001).

[48] J. Spino, J. Cobos-Sabate, F. Rousseau, Room-temperature microindentation behaviour of lwr-fuels, part 1: fuel microhardness, Journal of Nuclear Materials 322 (2–3) (2003) 204 – 216. doi:http://dx.doi.org/10.1016/S0022-3115(03)00328-3.

[49] D. Pizzocri, F. Cappia, L. Luzzi, G. Pastore, V. Rondinella, P. V. Uffelen, A semi-empirical model for the formation and depletion of the high burnup structure in UO_2, Journal of Nuclear Materials 487 (2017) 23 – 29. doi:http://doi.org/10.1016/j.jnucmat.2017.01.053.

[50] IAEA, Storage and disposal of spent fuel and high level radioactive waste, Tech. rep.
URL https://www.iaea.org/About/Policy/GC/GC50/GC50InfDocuments/English/gc50inf-3-att5_en.pdf

[51] ENSI, Installations de gestion des déchets, inspection fédérale de la sécurité nucléaire ifsn (2017).

URL https://www.ensi.ch/fr/installations-nucleaires/installations-de-gestion-des-dechets/

[52] B. Bonin, The scientific basis of nuclear waste management, in: D. G. Cacuci (Ed.), Handbook of Nuclear Engineering, Springer US, Boston, MA, 2010, pp. 3253–3419. doi:10.1007/978-0-387-98149-9_28.

[53] P. Carbol, D. Wegen, T. Wiss, P. Fors, 5.16 - spent fuel as waste material, in: R. J. Konings (Ed.), Comprehensive Nuclear Materials, Elsevier, Oxford, 2012, pp. 389 – 420. doi:http://dx.doi.org/10.1016/B978-0-08-056033-5.00106-3.

[54] Impact of high burnup uranium oxide and mixed uranium–plutonium oxide water reactor fuel on spent fuel management, IAEA Nuclear Energy Series No. NF-T-3.8.
URL http://www-pub.iaea.org/books/iaeabooks/8428/Impact-of-High-Burnup-Uranium-Oxide-and-Mixed-Uranium-Plutonium-Oxide-Water-Reactor-Fuel-on-Spent-Fuel-Management

[55] U. Fischer, H. Wiese, Improved and consistent determination of the nuclear inventory of spent PWR-fuel on the basis of time-dependent cell-calculations with korigen, Tech. rep., Kernforschungszentrum Karlsruhe GmbH (Germany (1983).

[56] J. Magill, J. Galy, R. Dreher, D. Hamilton, M. Tufan, C. Normand, A. Schwenk-Ferrero, H. Wiese, Nucleonica: a nuclear science portal, in: International Conference on Nuclear Data for Science and Technology, EDP Sciences, 2007, pp. 89–92.

[57] A. Sonzogni, Nudat 2.6, national nuclear data center, Brookhaven national laboratory.

[58] International Atomic Energy Agency and OECD Nuclear Energy Agency, INES the international nuclear and radiological event scale, IAEA, 2013.

[59] F. Fichot, J. M. Seiler, K. Trambauer, C. Mueller, Chapter 2 - In-vessel core degradation, in: B. R. Sehgal (Ed.), Nuclear Safety in Light Water Reactors, Academic Press, Boston, 2012, pp. 89 – 183. doi:http://dx.doi.org/10.1016/B978-0-12-388446-6.00002-2.

[60] P. Bottomley, C. Walker, D. Papaioannou, S. Bremier, P. Pöml, J.-P. Glatz, S. van Winckel, P. van Uffelen, D. Manara, V. Rondinella, Severe accident research at the Transuranium Institute Karlsruhe: A review of past experience

and its application to future challenges, Annals of Nuclear Energy 65 (2014) 345 – 356. doi:http://doi.org/10.1016/j.anucene.2013.11.012.

[61] H. Matzke, V. V. Rondinella, Investigation of specimens from the FARO tests l-19 and l-24, Tech. rep., European Commission, Joint Research Centre, Institute for Transuranium Elements (1998).

[62] D. Magallon, H. Hohmann, Experimental investigation of 150-kg-scale corium melt jet quenching in water, Nuclear Engineering and Design 177 (1) (1997) 321–337. doi:http://dx.doi.org/10.1016/S0029-5493(97)00201-X.

[63] NSAC, Epri-NSAC-80-1, analysis of Three Mile Island-unit 2 accident, Tech. rep., Nuclear Safety Analysis Center (1980).

[64] B. R. Sehgal, Chapter 1 - Light water reactor safety: A historical review, in: B. R. Sehgal (Ed.), Nuclear Safety in Light Water Reactors, Academic Press, Boston, 2012, pp. 1 – 88. doi:http://doi.org/10.1016/B978-0-12-388446-6.00001-0.

[65] V. Tyrpekl, Material effect in the fuel-coolant interaction: structural characterization of the steam explosion debris and solidification mechanism, Ph.D. thesis, Université de Strasbourg; Université Charles de Prague (République Tchèque) (2012).

[66] Nuclear Regulatory Commission, TMI-2 core end-state configuration (2007). URL http://www.nrc.gov/images/reading-rm/photo-gallery/20071114-006.jpg

[67] A. Borovoi, S. Gavrilov, G. Pretzsch, Development of the data base: Nuclear fuel and radioactive waste, environmental impact, and radiological situation in Chernobyl npp 4th block "shelter", in: J. Kolejka (Ed.), Role of GIS in Lifting the Cloud Off Chernobyl, Springer Netherlands, Dordrecht, 2002, pp. 67–76. doi:10.1007/978-94-010-0518-0_5.

[68] P.Pöml, B. Burakov, T. Geisler, C. Walker, M. Grange, A. Nemchin, J. Berndt, R. Fonseca, P. Bottomley, R. Hasnaoui, Micro-analytical uranium isotope and chemical investigations of zircon crystals from the Chernobyl "lava" and their nuclear fuel inclusions, Journal of Nuclear Materials 439 (1–3) (2013) 51 – 56. doi:http://doi.org/10.1016/j.jnucmat.2013.03.031.

[69] IAEA, The Fukushima daiichi accident, technical volume 5/5, post accident recovery, Tech. rep., International Atomic Energy Agency (2015).

[70] E. M. Lifshitz, A. M. Kosevich, L. P. Pitaevskii, Chapter I - Fundamental equations, in: E. M. Lifshitz, A. M. Kosevich, L. P. Pitaevskii (Eds.), Theory of Elasticity (Third Edition), third edition Edition, Butterworth-Heinemann, Oxford, 1986, pp. 1 – 37. doi:http://dx.doi.org/10.1016/B978-0-08-057069-3.50008-5.

[71] R. Truell, C. Elbaum, B. B. Chick, Propagation of stress waves in solids - Chapter 1, in: R. Truell, C. Elbaum, B. B. Chick (Eds.), Ultrasonic Methods in Solid State Physics, Academic Press, 1969, pp. 1 – 52. doi:http://dx.doi.org/10.1016/B978-1-4832-3318-5.50006-7.

[72] J. B. Wachtman, Jr, Elastic Deformation of Ceramics and Other Refractory Materials, in: Proceedings of a Symposium, Gaithersburg, U.S., National Bureau of Standard, April 1968, pp. 139–168.

[73] R. G. Maev, Scanning Acoustic Microscopy. Physical Principles and Methods. Current Development, in: Acoustic Microscopy - Fundamentals and Applications, Wiley-VCH Verlag GmbH & Co. KGaA, 2008, pp. 9–19. doi:10.1002/9783527623136.ch1.

[74] G. A. Briggs, O. V. Kolosov, A little elementary acoustics - Chapter 6, in: Acoustic Microscopy, Oxford University Press, 2009, pp. 74–97.

[75] I. A. Viktorov, Rayleigh and Lamb Waves: Physical Theory and Applications, Plenum press, 1970, Ch. 1, pp. 1–67.

[76] C. Greene, Rayleigh wave animation (2012).
URL https://ch.mathworks.com/matlabcentral/fileexchange/35770-rayleigh-wave-animation

[77] D. Laux, Caractérisation mécanique de combustibles nucléaires à fort taux de combustion par méthodes micro-acoustiques, Ph.D. thesis, Montpellier 2 (2002).

[78] D. Laux, D. Baron, G. Despaux, A. Kellerbauer, M. Kinoshita, Determination of high burn-up nuclear fuel elastic properties with acoustic microscopy, Journal of Nuclear Materials 420 (1–3) (2012) 94 – 100. doi:http://doi.org/10.1016/j.jnucmat.2011.09.010.

[79] A. Bayón, F. Gascón, F. J. Nieves, Estimation of dynamic elastic constants from the amplitude and velocity of Rayleigh waves, The Journal of the Acoustical Society of America 117 (6) (2005) 3469–3477. doi:10.1121/1.1898663.

[80] P. G. Malischewsky, T. T. Tuan, A special relation between Young's modulus, Rayleigh-wave velocity, and Poisson's ratio, The Journal of the Acoustical Society of America 126 (6) (2009) 2851–2853. doi:http://dx.doi.org/10.1121/1.3243464.

[81] P. M. Auning, A note on Rayleigh-wave velocities as a function of the material parameters, Geofisica International-Mexico- 43 (3) (2004) 506.

[82] D. Chicot, A. Tricoteaux, et al., Mechanical properties of ceramic by indentation: Principle and applications, in: Ceramic Materials, INTECH Open Access Publisher, 2010.

[83] T. Kutty, A. Sengupta, C. Ganguly, Indentation technique for mechanical property evaluation of ceramic nuclear fuel, European. Appl. Res. Rept.-Nucl. Sci. Technol. 7 (1990) 1473–1486.

[84] D. Vollath, Uranium Dioxide UO_2- Chapter4, Springer-Verlag Berlin Heidelberg GmbH, Germany, 1985.

[85] Y. Osetsky, D. Bacon, 1.12 - Atomic-level dislocation dynamics in irradiated metals, in: R. J. Konings (Ed.), Comprehensive Nuclear Materials, Elsevier, Oxford, 2012, pp. 333 – 356. doi:http://doi.org/10.1016/B978-0-08-056033-5.00028-8.

[86] J. B. Wachtman. Jr., M. L. Wheat, H. J. Anderson, J. Bates, Elastic constants of single crystal UO_2 at 25° C, Journal of Nuclear Materials 16 (1) (1965) 39 – 41. doi:http://doi.org/10.1016/0022-3115(65)90089-9.

[87] I. J. Fritz, Elastic properties of UO_2 at high pressure, Journal of Applied Physics 47 (10) (1976) 4353–4358. doi:10.1063/1.322438.

[88] O. L. Anderson, A simplified method for calculating the debye temperature from elastic constants, Journal of Physics and Chemistry of Solids 24 (7) (1963) 909 – 917. doi:http://doi.org/10.1016/0022-3697(63)90067-2.

[89] S. M. Lang, Properties of high-temperature ceramics and cermets. Elasticity and density at room temperature, Tech. rep., DTIC Document (1958).

[90] D. Martin, The elastic constants of polycrystalline UO_2 and (U, Pu) mixed oxides: a review and recommendations, High temperatures-high pressures 21 (1) (1989) 13–24.

[91] J. Yang, Theory of Thermal Conductivity, in: T. M. Tritt (Ed.), Thermal Conductivity: Theory, Properties, and Applications, Springer US, Boston, MA, 2004, pp. 1–20. doi:10.1007/0-387-26017-X_1.

[92] R. Eisberg, R. Resnick, Quantum statistics - Chapter 11, in: Quantum physics of atoms, molecules, solids, nuclei, and particles, John Wiley, New York, 1974.

[93] F. Seitz, The specific heats of simple solids - Chapter 3, in: The modern theory of solids, McGraw-Hill New York, 1940, pp. 99–136.

[94] K. Yamada, S. Yamanaka, T. Nakagawa, M. Uno, M. Katsura, Study of the thermodynamic properties of (U, Ce)O_2, Journal of Nuclear Materials 247 (1997) 289 – 292. doi:http://dx.doi.org/10.1016/S0022-3115(97)00076-7.

[95] F. D. Stacey, Theory of thermal and elastic properties of the lower mantle and core, Physics of the Earth and Planetary Interiors 89 (3–4) (1995) 219 – 245. doi:http://dx.doi.org/10.1016/0031-9201(94)03005-4.

[96] C. Pillai, A. George, Thermal conductivity of uranium dioxide, Journal of Nuclear Materials 200 (1) (1993) 78 – 81. doi:https://doi.org/10.1016/0022-3115(93)90011-M.

[97] D. Staicu, 2.17 - Thermal properties of irradiated UO_2 and MOX, in: J. M. Rudy Konings (Ed.), Comprehensive Nuclear Materials, Elsevier, Oxford, 2012, pp. 439 – 464. doi:http://dx.doi.org/10.1016/B978-0-08-056033-5.00038-0.

[98] N. Ashcroft, N. Mermin, Anharmonic Effects in Crystals - Chapter 25, in: Solid State Physics, Holt, Rinehart and Winston, 1976.

[99] K. Une, Y. Tominaga, S. Kashibe, Oxygen potentials and lattice parameter of irradiated BWR fuel, Journal of Nuclear Science and Technology 28 (5) (1991) 409–417. doi:http://dx.doi.org/10.1080/18811248.1991.9731376.

[100] H. Matzke, Oxygen potential in the rim region of high burnup UO_2 fuel, Journal of Nuclear Materials 208 (1) (1994) 18 – 26. doi:http://dx.doi.org/10.1016/0022-3115(94)90193-7.

[101] J. Spino, P. Peerani, Oxygen stoichiometry shift of irradiated LWR-fuels at high burn-ups: Review of data and alternative interpretation of recently published results, Journal of Nuclear Materials 375 (1) (2008) 8 – 25. doi:http://dx.doi.org/10.1016/j.jnucmat.2007.10.007.

[102] G. Leibfried, E. Schlömann, A. der Wissenschaften, M.-p. Klasse, Wärmeleitung in elektrisch isolierenden Kristallen, von Günther Leibfried und Ernst Schlömann, Vandenhoeck und Ruprecht, 1954.

[103] C. L. Julian, Theory of heat conduction in rare-gas crystals, Phys. Rev. 137 (1965) A128–A137. doi:10.1103/PhysRev.137.A128.

[104] G. A. Slack, The thermal conductivity of nonmetallic crystals, Solid State Physics 34 (1979) 1 – 71. doi:http://dx.doi.org/10.1016/S0081-1947(08)60359-8.

[105] Q. Yin, S. Y. Savrasov, Origin of low thermal conductivity in nuclear fuels, Phys. Rev. Lett. 100 (2008) 225504. doi:10.1103/PhysRevLett.100.225504.

[106] G. A. Briggs, O. V. Kolosov, Resolution - Chapter 3, in: Acoustic Microscopy, Oxford University Press, 2009, pp. 74–97.

[107] V. Roque, Caractérisation par méthodes micro-acoustiques de pastilles de dioxyde d'uranium, Ph.D. thesis, Montpellier 2 (1999).

[108] D. R. Hull, P. Mercury, Ultrasonic velocity measurement using phase-slope and cross-correlation methodsmicroform, [Washington D.C., U.S.] : NASA, 1984.

[109] C1327-99, Standard test method for Vickers indentation hardness of advanced ceramics, Tech. rep., ASTM (1999).

[110] V. Roque, Caractérisation par méthodes micro-acoustiques de pastilles de dioxyde d'uranium, Ph.D. thesis, Montpellier 2 (1999).

[111] S. K. Yagnik, T. Tverberg, E. Kolstad, J. A. Turnbull, D. Baron, M. Kinoshita, Fuel (UO_2) R&D: needs, approaches and results, in: Water Reactor Fuel Performance Meeting. Seoul, Republic of Korea, 2008.

[112] J. Noirot, Y. Pontillon, S. Yagnik, J. Turnbull, T. Tverberg, Fission gas release behaviour of a 103 GWd/tHM fuel disc during a 1200 °C annealing test, Journal of Nuclear Materials 446 (1–3) (2014) 163 – 171. doi:http://doi.org/10.1016/j.jnucmat.2013.12.002.

[113] EPRI, High burn-up properties of the fuel variants irradiated in IFA-649, final report, Tech. rep. (1995).

[114] J. Spino, D. Papaioannou, Lattice parameter changes associated with the rim-structure formation in high burn-up UO_2 fuels by micro X-ray diffraction, Journal of Nuclear Materials 281 (2) (2000) 146–162. doi:http://dx.doi.org/10.1016/S0022-3115(00)00236-1.

[115] C. Walker, V. Rondinella, D. Papaioannou, S. V. Winckel, W. Goll, R. Manzel, On the oxidation state of UO_2 nuclear fuel at a burn-up of around 100 MWd/kgHM, Journal of Nuclear Materials 345 (2–3) (2005) 192 – 205. doi:http://doi.org/10.1016/j.jnucmat.2005.05.010.

[116] R. Manzel, C. Walker, EPMA and SEM of fuel samples from PWR rods with an average burn-up of around 100 MWd/kgHM, Journal of Nuclear Materials 301 (2–3) (2002) 170 – 182. doi:http://doi.org/10.1016/S0022-3115(01)00753-X.

[117] M. Marchetti, D. Laux, F. Cappia, M. Laurie, P. Van Uffelen, V. V. Rondinella, T. Wiss, G. Despaux, High frequency acoustic microscopy for the determination of porosity and Young's modulus in high burnup uranium dioxide nuclear fuel, IEEE Transactions on Nuclear Science 63 (2016) 1520–1525. doi:10.1109/TNS.2016.2552241.

[118] P. Lucuta, H. Matzke, R. Verrall, H. Tasman, Thermal conductivity of SIMFUEL, Journal of Nuclear Materials 188 (1992) 198 – 204. doi:http://dx.doi.org/10.1016/0022-3115(92)90471-V.

[119] P. Lucuta, R. Verrall, H. Matzke, B. Palmer, Microstructural features of SIMFUEL-simulated high-burnup UO_2-based nuclear fuel, Journal of Nuclear Materials 178 (1) (1991) 48–60. doi:http://dx.doi.org/10.1016/0022-3115(91)90455-G.

[120] H. Matzke, P. Lucuta, R. Verrall, J. Henderson, Specific heat of UO_2-based simfuel, Journal of Nuclear Materials 247 (1997) 121 – 126, thermodynamics of Nuclear Materials. doi:http://dx.doi.org/10.1016/S0022-3115(97)00069-X.

[121] D. Laux, W. de Weerd, D. Papaioannou, S. Kitajima, V. Rondinella, G. Despaux, Scanning acoustic microscope for mechanical characterization and density estimation of irradiated nuclear fuel, Progress in Nuclear Energy 72 (2014) 63–66. doi:http://dx.doi.org/10.1016/j.pnucene.2013.07.018.

[122] NFIR, Final-Report, High Burn-Up Properties of the Fuel Variants Irradiated in IFA-649, Tech. rep., Electric Power Research Institute (2013).

[123] J. Spino, Post irradiation examination of fuel rods BR3-N118, Tech. rep., Joint Research Centre, Institute for Transuranium Elements (1998).

[124] K. Lassmann, Transuranus: a fuel rod analysis code ready for use, Journal of Nuclear Materials 188 (1992) 295 – 302. doi:http://dx.doi.org/10.1016/0022-3115(92)90487-6.

[125] F. Cappia, M. Marchetti, A. Schubert, P. Van Uffelen, D. Papaioannou, R. Màcian-Juan, V. Rondinella, Microhardness and local properties of high burnup UO_2 in Proc. Conf. Topfuel, 2015, pp. 334–340.

[126] A. Bouloré, Étude et modélisation de la densification en pile des oxydes nucleaires UO_2, Ph.D. thesis, Institut National Polytechnique de Grenoble, École Nationale Supérieure des Mines de Saint-Étienne (2001).

[127] T. Sonoda, M. Kinoshita, I. Ray, T. Wiss, H. Thiele, D. Pellottiero, V. Rondinella, H. Matzke, Transmission electron microscopy observation on irradiation-induced microstructural evolution in high burn-up UO_2 disk fuel, Nuclear Instruments and Methods in Physics Research Section B: Beam Interactions with Materials and Atoms 191 (1–4) (2002) 622 – 628. doi:https://doi.org/10.1016/S0168-583X(02)00622-5.

[128] Y. Harada, S. Doi, Irradiation behavior of large grain UO_2 fuel rod by active powder, Journal of Nuclear Science and Technology 35 (6) (1998) 411–418. doi:10.1080/18811248.1998.9733883.

[129] S. Doi, S. Abeta, A. Irisa, S. Inoue, Topical meeting on LWR fuel performance, Vol. 2, Avignon, France, 1991, p. 588.

[130] Irisa, Y., et al, Topical meeting on LWR fuel performance, Williamsburg, USA, 1988, p. 102.

[131] D.Baron, B.Meslin., Effet de l'adjonction de gadolinium sur le comportement thermomécanique du combustible REP. Document interne., Tech. rep. (1996).

[132] R.H.Watson, NFIR-Properties of the Urania-Gadolinia System (Part 2). NFIR-RP04. Final Report, Tech. rep. (1987).

[133] B. S., W. De Weerd, D. Papaioannou, V. V. Rondinella, Irradiation effects on properties and structure evolution in MOX fuel: fuel density, JRC scientific and technical reports, tmp0043/m2/r2, Tech. rep. (2011).

[134] J. Spino, D. Baron, M. Coquerelle, A. Stalios, High burn-up rim structure: evidences that xenon-depletion, pore formation and grain subdivision start at different local burn-ups, Journal of Nuclear Materials 256 (2–3) (1998) 189 – 196. doi:http://dx.doi.org/10.1016/S0022-3115(98)00060-9.

[135] J. Spino, D. Papaioannou, Lattice contraction in the rim zone as controlled by recrystallization: Additional evidence, Journal of Nuclear Materials 372 (2–3) (2008) 416 – 420. doi:http://dx.doi.org/10.1016/j.jnucmat.2007.03.173.

[136] K. Phani, D. Sanyal, A. Sengupta, Estimation of elastic properties of nuclear fuel material using longitudinal ultrasonic velocity – a new approach, Journal of Nuclear Materials 366 (1–2) (2007) 129 – 136. doi:http://dx.doi.org/10.1016/j.jnucmat.2006.12.045.

[137] J. Spino, Determination of the Young Modulus of Irradiated Fuels by Knoop Indentation, in: Joint Research Centre, Institute for Transuranium Elements. Annual report, 2005, p. 50.

[138] M. Pujol, M. Idiri, L. Havela, S. Heathman, J. Spino, Bulk and Young's modulus of doped UO_2 by synchrotron diffraction under high pressure and Knoop indentation, Journal of Nuclear Materials 324 (2–3) (2004) 189 – 197. doi:https://doi.org/10.1016/j.jnucmat.2003.10.002.

[139] F. Cappia, D. Pizzocri, M. Marchetti, A. Schubert, P. V. Uffelen, L. Luzzi, D. Papaioannou, R. Macián-Juan, V. Rondinella, Microhardness and Young's modulus of high burn-up UO_2 fuel, Journal of Nuclear Materials 479 (2016) 447 – 454. doi:https://doi.org/10.1016/j.jnucmat.2016.07.015.

[140] O. L. Anderson, Determination and some uses of isotropic elastic constants of poly-crystalline aggregates using single-crystal data, in: Lattice Dynamics, Vol. III-part B of Physical acoustics, Academic Press, 1965, pp. 43–95. doi:https://doi.org/10.1016/B978-0-12-395669-9.50009-6.

[141] F. Grønvold, High-temperature X-ray study of uranium oxides in the UO_2-U_3O_8 region, Journal of Inorganic and Nuclear Chemistry 1 (6) (1955) 357 – 370. doi:http://dx.doi.org/10.1016/0022-1902(55)80046-2.

[142] R. Brandt, G. Neuer, Thermal conductivity and thermal radiation properties of UO_2, Journal of Non-Equilibrium Thermodynamics 1 (1) (1976) 3–24. doi:https://doi.org/10.1515/jnet.1976.1.1.3.

[143] B. T. M. Willis, Neutron diffraction studies of the actinide oxides. ii. thermal motions of the atoms in uranium dioxide and thorium dioxide between room temperature and 1100 °, Proceedings of the Royal Society of London A: Mathematical, Physical and Engineering Sciences 274 (1356) (1963) 134–144. doi:10.1098/rspa.1963.0118.

[144] J. Fink, Thermophysical properties of uranium dioxide, Journal of Nuclear Materials 279 (1) (2000) 1 – 18. doi:http://dx.doi.org/10.1016/S0022-3115(99)00273-1.

[145] A. Momin, M. Karkhanavala, Temperature dependence of the Grueneisen parameter and lattice vibrational frequencies of UO_2 and ThO_2 in the range 298 to 2300 K, High Temp. Sci.; (United States) 10:1.

[146] C. Ronchi, M. Sheindlin, D. Staicu, M. Kinoshita, Effect of burn-up on the thermal conductivity of uranium dioxide up to 100.000 MWd t^{-1}, Journal of Nuclear Materials 327 (1) (2004) 58 – 76. doi:https://doi.org/10.1016/j.jnucmat.2004.01.018.

[147] M. Sakai, The Meyer hardness: A measure for plasticity?, Journal of Materials Research 14 (9) (1999) 3630–3639. doi:10.1557/JMR.1999.0490.

[148] N. Nakae, T. Kirihara, S. Nasu, Irradiation induced volume change in UO_2, Journal of Nuclear Materials 74 (1) (1978) 1 – 9. doi:https://doi.org/10.1016/0022-3115(78)90526-3.

[149] M. Kato, A. Komeno, H. Uno, H. Sugata, N. Nakae, K. Konashi, M. Kashimura, Self-radiation damage in plutonium and uranium mixed dioxide, Journal of Nuclear Materials 393 (1) (2009) 134 – 140. doi:https://doi.org/10.1016/j.jnucmat.2009.05.020.

[150] M. S. Elbakhshwan, Y. Miao, J. F. Stubbins, B. J. Heuser, Mechanical properties of UO_2 thin films under heavy ion irradiation using nanoindentation and finite element modeling, Journal of Nuclear Materials 479 (2016) 548 – 558.

[151] A. Debelle, A. Boulle, F. Garrido, L. Thome, Strain and stress build-up in He-implanted UO_2 single crystals: an X-ray diffraction study, Journal of Materials Science 46 (2011) 4683–4689. doi:10.1007/s10853-011-5375-1.

[152] V. V. Rondinella, H. Matzke, J. Cobos, T. Wiss, α-radiolysis and α-radiation damage effects on UO_2 dissolution under spent fuel storage conditions, MRS Proceedings 556. doi:10.1557/PROC-556-447.

[153] D. Staicu, , E. Dahms, D. Manara, T. Wiss, O. Dieste Blanco, B. Cremer, P. Raison, M. Marchetti, D. Robba, N. Chauvin, P. Martin, Measurement of properties of fresh FR MOX fuel - deliverable d741, Tech. rep., European Commission - Joint Research Centre and Commissariat à l'énerge atomique (2017).

[154] D. Haas, J. Somers, F. Charollais, C. Fuchs, S. Fourcaudot, Fabrication and characterization of MOX fuels with high plutonium content using alternative processes, in: MOX Fuel Cycle Technologies for Medium and Long Term Deployment (Proc. Symp. Vienna, 1999), C&S Papers Series No, Vol. 3, 1999, pp. 523–530.

[155] H. Matzke, P. Lucuta, T. Wiss, Swift heavy ion and fission damage effects in UO_2, Nuclear Instruments and Methods in Physics Research Section B: Beam Interactions with Materials and Atoms 166–167 (2000) 920 – 926. doi:https://doi.org/10.1016/S0168-583X(99)00801-0.

[156] C. Duriez, J.-P. Alessandri, T. Gervais, Y. Philipponneau, Thermal conductivity of hypostoichiometric low Pu content (U,Pu)O_{2-x} mixed oxide, Journal of Nuclear Materials 277 (2–3) (2000) 143 – 158. doi:https://doi.org/10.1016/S0022-3115(99)00205-6.

[157] T. Ohmichi, S. Fukushima, A. Maeda, H. Watanabe, On the relation between lattice parameter and O/M ratio for uranium dioxide-trivalent rare earth oxide solid solution, Journal of Nuclear Materials 102 (1) (1981) 40 – 46. doi:http://dx.doi.org/10.1016/0022-3115(81)90544-4.

[158] W. J. Weber, Alpha-irradiation damage in CeO_2, UO_2 and PuO_2, Radiation Effects 83 (1-2) (1984) 145–156. doi:10.1080/00337578408215798.

[159] T.-H. Nguyen, A. Debelle, A. Boulle, F. Garrido, L. Thomé, V. Demange, Mechanical response of UO_2 single crystals submitted to low-energy ion irradiation, Journal of Nuclear Materials 467, Part 2 (2015) 505 – 511. doi:https://doi.org/10.1016/j.jnucmat.2015.10.046.

[160] U. Fischer, H. Wiese, Improved and consistent determination of the nuclear inventory of spent PWR-fuel on the basis of time-dependent cell-calculations with KORIGEN, Tech. rep., Kernforschungszentrum Karlsruhe GmbH (Germany (1983).

[161] H. Nakamura, M. Machida, M. Kato, Lda+ u study on plutonium dioxide with spin-orbit couplings, Progress in Nuclear Science and Technology 2 (2011) 16–19. doi:10.1016/j.jallcom.2012.03.117.

[162] C. De Novion, B. Amice, Y. Guerin, A. Groff, A. Padel, Propriétés mecaniques de ceramiques à base d'uranium and de plutonium, in: International Conference on Plutonium and other actinides; Santa Fe, N. Mex., USA, 1970, p. 15.

[163] J. Jonnet, A contribution to the understanding of the high burn-up structure formation in nuclear fuels, Ph.D. thesis, Vandoeuvre-les-Nancy, INPL (2007).

[164] A. Debelle, A. Boulle, F. Rakotovao, J. Moeyaert, C. Bachelet, F. Garrido, L. Thomé, Influence of elastic properties on the strain induced by ion irradiation in crystalline materials, Journal of Physics D: Applied Physics 46 (4) (2013) 045309. doi:http://dx.doi.org/10.1088/0022-3727/46/4/045309.

[165] L. Johnson, M. Niemeyer, G. Klubertanz, P. Siegel, P. Gribi, Calculations of the temperature evolution of a repository for spent fuel, vitrified high-level waste and intermediate level waste in opalinus clay, Tech. rep., nagra (2002).

[166] H. Matzke, P. Lucuta, T. Wiss, Swift heavy ion and fission damage effects in UO_2, Nuclear Instruments and Methods in Physics Research Section B: Beam Interactions with Materials and Atoms 166 (2000) 920 – 926. doi:http://dx.doi.org/10.1016/S0168-583X(99)00801-0.

[167] T. Wiss, H. Matzke, C. Trautmann, M. Toulemonde, S. Klaumünzer, Radiation damage in UO_2 by swift heavy ions, Nuclear Instruments and Methods in Physics Research Section B: Beam Interactions with Materials and Atoms 122 (3) (1997) 583–588. doi:10.1016/S0168-583X(96)00754-9.

[168] G. Szenes, Ion-induced amorphization in ceramic materials, Journal of Nuclear Materials 336 (1) (2005) 81 – 89. doi:http://dx.doi.org/10.1016/j.jnucmat.2004.09.004.

[169] C. Boshoven, M. Cologna, H. Hein, D. Kassim, E.and Manara, M. Murray-Farthing, S. Stohr, A. Seibert, V. Tyrpekl, Status report on the synthesis and characterisation of (U,Zr)O_2 compounds - deliverable 54520141, Tech. rep., European Commission - Joint Research Centre - Institute for Transuranium Elements (2014).

[170] A. Seibert, D. Staicu, , M. Cologna, C. Boshoven, H. Hein, E. Kassim, M. Murray-Farthing, E. Dahms, D. Robba, A. Küst, S. Stohr-Nourry, Second status report on the synthesis and characterisation of (U,Zr)O_2 compounds - deliverable 54520151, Tech. rep., European Commission - Joint Research Centre - Institute for Transuranium Elements (2015).

[171] R. Ploc, The lattice parameter of cubic ZrO_2 formed on zirconium, Journal of Nuclear Materials 99 (1) (1981) 124 – 128. doi:http://dx.doi.org/10.1016/0022-3115(81)90146-X.

[172] Y. Chang, H. Wang, Q. Zhu, P. Luo, S. Dong, Theoretical calculation and analysis of ZrO_2 spherical nanometer powders, Journal of Advanced Ceramics 2 (1) (2013) 21–25. doi:10.1007/s40145-013-0036-2.

[173] S. Ran, L. Winnubst, W. Wiratha, D. H. Blank, Sintering behavior of 0.8 mol%-CuO-doped 3Y-TZP ceramics, Journal of the American Ceramic Society 89 (1) (2006) 151–155. doi:10.1111/j.1551-2916.2005.00679.x.

[174] P. D. Bottomley, M. Coquerelle, Metallurgical examination of bore samples from the Three Mile Island unit 2 reactor core, Nuclear Technology 87 (1) (1989) 120–136.

[175] C. F. Smith, W. B. Crandall, Calculated high-temperature elastic constants for zero porosity monoclinic zirconia, Journal of the American Ceramic Society 47 (12) (1964) 624–627. doi:10.1111/j.1151-2916.1964.tb13120.x.

[176] Hoshino et al., Evaluation of the mechanical properties of the fuel debris, in: JAEA R&D Review 2015, JAEA, Japan, 2015, p. 24.

[177] Hoshino et al., Mechanical properties of fuel debris for defueling toward decommissioning, proceedings of 23rd international conference on nuclear engineering, ICONE23-2111, 2015, p. 6.

[178] S. T. Barlow, D. J. Bailey, A. J. Fisher, M. C. Stennett, C. L. Corkhill, N. C. Hyatt, Synthesis of simulant 'lava-like' fuel containing materials (lfcm) from the Chernobyl reactor unit 4 meltdown, MRS Advances 2 (11) (2017) 609–614. doi:10.1557/adv.2016.642.

[179] S. Spinner, Elastic moduli of glasses by a dynamic method, Journal of the American Ceramic Society 37 (5) (1954) 229–234. doi:10.1111/j.1151-2916.1954.tb14029.x.

[180] H. J. McSkimin, Measurement of ultrasonic wave velocities and elastic moduli for small solid specimens at high temperatures, The Journal of the Acoustical Society of America 31 (3) (1959) 287–295. arXiv:http://dx.doi.org/10.1121/1.1907714, doi:10.1121/1.1907714.

[181] O. Harel, The estimation of R^2 and adjusted R^2 in incomplete data sets using multiple imputation, Journal of Applied Statistics 36 (10) (2009) 1109–1118. doi:10.1080/02664760802553000.

Index

Resumé

Ce travail de recherche vise à étudier les propriétés élastiques par microscopie acoustique du combustible nucléaire dans trois situations particulières: combustible en utilisation normale en réacteur nucléaire, combustible stocké après la période d'irradiation et combustible en conditions extrêmes suite à un accident nucléaire. Les mesures réalisées sur les échantillons irradiés ont conduit à plusieurs résultats majeurs: validation d'une loi corrélant la vitesse des ondes de Rayleigh à la densité du dioxyde d'uranium irradié ou frais; détermination de la porosité dans le combustible irradié; évaluation du gonflement de la matrice en fonction du taux de combustion dans la gamme 0-100 $GWdt^{-1}M$; développement d'un modèle empirique capable de prévoir la variation de module de Young en fonction du taux de combustion en prenant même en compte la teneur en dopants (Gd_2O_3, CeO_2) ; quantification de l'évolution du module de Young du combustible suite à l'endommagement en stockage ; premières mesures sur du corium. Enfin, grâce au lien entre les propriétés thermiques et élastiques, différentes propriétés thermiques de l'UO_2 ont été calculées en mesurant la vitesse de l'onde de surface de Rayleigh seule.

Propriétés élastiques des combustibles nucléaires sous conditions extrêmes

Elastic properties characterization of nuclear fuels under extreme conditions

Abstract

The focus of the present thesis is the determination of the elastic properties of nuclear fuel using high- frequency acoustic microscopy. The nuclear fuel is considered under three different conditions: during its normal life in reactor, after its discharge and disposal in interim or long-term storage and subsequently to its severe degradation caused by a nuclear accident. Measurements performed on irradiated fuels allowed to validate a law between the density of fresh and irradiated fuel and the Rayleigh wave velocity; the determination of the irradiated fuel porosity and matrix swelling in the broad burnup range 0-100 $GWdt^{-1}M$; the development of an empirical model capable of predicting the evolution of Young's modulus versus burnup correcting also for the additives content (Gd_2O_3, CeO_2); Young's modulus evolution due to alpha-decay damage as in-storage condition; first corium measurements. Moreover, several UO_2 thermal parameters were calculated only by means of the Rayleigh wave velocity thanks to the link between thermal and elastic properties.

Mots-clés: Microscopie acoustique, combustible nucléaire, propriétés élastiques, propriétés mécaniques, dégâts par rayonnement, corium

Keywords: Acoustic microscopy, nuclear fuel, elastic properties, mechanical properties, radiation damage, corium